Akita University

Mineralogy and geochemistry of the Berong and Intex Ni-Co laterite deposits, Philippines

A thesis submitted for the degree of PhD
Graduate School of International Resource Sciences

by
ID 6517105

Tupaz Carmela Alen Jayme

September 28, 2020

Akita University

ABSTRACT

Ni laterites developed above ultramafic rocks contain a significant amount of Ni, and to some extent, Co and Sc. Several works have been conducted to understand the formation of Ni laterite deposits in New Caledonia, Indonesia, Australia, among places. However, few studies have examined the nature of the different serpentine veins formed in the bedrock and saprolite horizon. More importantly, there is a current lack of information regarding the genesis of Ni laterite deposits in the Philippines. In this study, two Ni-Co laterite deposits from Berong, Palawan, and Intex, Mindoro, Philippines, are investigated. These profiles are typically divided from bottom to top into (i) serpentinized ultramafic bedrock (ii) saprolite horizon and (iii) limonite horizon. The primary olivine in the bedrock contains a substantial amount of NiO (up to 0.38 wt%) indicating this is the principal source of the ore in the saprolite and limonite horizons. Three types of serpentine veins are identified in the ultramafic bedrock. A minor amount of talc is found in the bedrock, which is marked by a low amount of NiO with a concentration of up to 0.07 wt%. Nickel is mainly hosted by garnierites (i.e. serpentine-like, talc-like and sepiolite-like) in the saprolite horizon. Six types of serpentine veins are identified in the Berong deposit, whereas five types of these veins are investigated in the Intex deposit. These serpentines show variable NiO concentrations of up to 6.65 wt%. Garnierite mineralization in the Berong deposit is characterized mainly by sepiolite-falcondoite and pimelite-kerolite series and hold a strikingly high amount of Ni (up to 34.86

Akita University

wt%). Goethite and Mn-oxyhydroxides host high amount of Ni in the limonite horizon with concentrations of up to 2.15 wt% NiO and 23.89 wt% NiO, respectively. Lithiophorite-asbolane intermediate and asbolane are the most common Co-bearing Mn-oxyhydroxides in the studied deposits. The degree of weathering of ultramafic rocks and laterite profiles plays an important role on the enrichment of Ni in laterites. The Berong deposit contains a higher bulk amount of Ni in laterites compared with the Intex deposit, which is attributed to the different degrees of weathering of the laterites. The Berong laterites experienced more advanced degree of weathering in contrast to the Intex laterites. During chemical weathering, Mg and Si are leached from the bedrock resulting in the enrichment of elements (Fe, Al, Ni) in the weathered horizons. All the profiles display increased amounts of Sc, and to some extent, REE and these elements have a close association with Fe- and Mn-oxyhydroxides in the limonite horizon. The chondrite-normalized REE patterns illustrate positive and negative Ce anomalies at the transition boundary between the limonite and saprolite horizons. The genesis of the Berong and Intex laterite deposits are consistent with the per descendum models proposed by previous authors. The studied laterite profiles evolved into two distinct processes: (i) development of the saprolite and limonite horizons and (ii) formation of secondary silicate minerals (garnierite), Mn-oxyhydroxides and silica

Akita University

TABLE OF CONTENTS

Akita University

Akita University

Akita University

LIST OF TABLES

Akita University

Akita University

Akita University

LIST OF FIGURES

Akita University

Akita University

Akita University

Akita University

ACKNOWLEDGEMENT

For I know the plans I have for you," declares the LORD, "plans to prosper you and not to harm you, plans to give you hope and a future.

Jeremiah 29:11

To the Almighty Father, I am grateful for the wisdom and strength you have bestowed upon me for the past years. Your words have been my motivation to reach my dream despite the difficult times I encountered along the way. The Ph.D. journey is indeed a challenging experience, but with faith, hard work, and perseverance, nothing is impossible.

I alone cannot accomplish this without the support of several people that surround me. I am thankful to my thesis supervisor, Prof. Yasushi Watanabe, for his constant encouragement since day one. His profound insights helped me at various stages of my research.

I would like to express my gratitude to Dr. Kenzo Sanematsu for his training and assistance during the preparation and analyses of samples at the facility of the Geological Survey of Japan (GSJ). A special thank you to Dr. Takuya Echigo for his supervision throughout the duration of my stay at Akita University. I acknowledge the support of Nobukazu Soma and his staff from the Mineral Resources Research Group at GSJ.

To my thesis panel, Prof. Tsukasa Ohba and Prof. Andrea Agangi, thank you for the comments and suggestions, which helped significantly improved the thesis manuscript. I highly appreciate the support provided by Dr. Ryohei Takahashi and Dr. Hinako Sato during the ICP-MS analysis of thesis samples. Thank you to all my laboratory mates of the Mineral Resources and Tectonics Research Group for your input and help while I am doing my analysis.

This research would not be possible without the financial assistance of the Leading Program at Akita University, and approval of field investigation by the Berong Nickel Corporation and Intex Resources Philippines Inc. I am thankful to Jam Galang for the acquisition of resources, and to sir Marc Zamora, sir Bernard Magsino and ma'am Carolyn Sacdalan for their assistance during sample collection.

Friends play an important role in achieving a balanced academic and social life. Thank you to James Refran, Sophia Frias, Pearlyn Manalo, Amoh Kooganne, AV Cirineo, Labone Godirilwe, Zula Zul, Lloyd Bravo, Paolo Martizzi, Rina Harata, Mpho Keeditse, To Bounliyong, and Larona Teseletso, for the happy

Akita University

memories, particularly when we celebrate someone's birthday, graduation, New Year's Day or simply when we eat lunch or dinner at the cafeteria.

To my Filipino aunts in Akita, tita Minerva Taguchi, tita Veronica, tita Mariz, and tita Lei Chavez, a special thank you for all the support. I am grateful to ma'am Buena Calabia- Segwaben and sir Tony Segwaben for welcoming me into your home, every time I visit Tsukuba. Most importantly, your prayers and endless encouragement helped me to make it through.

A very special thank you to Shane O Neill for not giving up on me, especially during the dark times. Thank you for proofreading my papers as well. You have been there through ups and downs, and I am blessed to have you in my life.

Finally, I would like to thank my sister, Ralen Tupaz, relatives and friends back home for their never-ending support. Thank you so much, mama Arlene, for looking after me throughout this journey. You will always be in my heart.

Akita University

CHAPTER 1

Introduction

1.1 Introduction

Laterites are the residual products of strong chemical weathering of rocks exposed at the surface of the Earth (Elias, 2002). Over the past years, laterites have been regarded as significant host to economic ore deposits, namely bauxite, iron ore, and nickel laterite deposits, and to a lesser extent, lateritic gold deposits (Evans, 1993). The weathering profiles of laterites are generally developed under humid climate conditions, in regions with tectonic stability and low erosion rates (Brand et al., 1998).

The world's resources of Ni are derived from two types of deposits: the magmatic sulfide deposits and the nickeliferous laterite deposits. In 1982, Ni production came mostly from magmatic ores accounting for about 65% (DeYoung et al., 1986). However, recent reports by Butt and Cluzel (2013) revealed that laterites make up 60% to 70% of the world's Ni resources and are mainly found in New Caledonia, Australia, Cuba, Indonesia and the Philippines (Fig. 1). The global terrestrial Ni resources are hosted in Ni laterite deposits, which are the products of intense weathering of ultramafic rocks such as dunite, harzburgite and their serpentinized equivalents (Golightly, 1981). These rocks initially contain 0.2 to 0.4 wt% Ni but as lateritisation progresses, Mg and Si are removed and Ni, iron (Fe), cobalt

(Co), manganese (Mn), aluminum (Al), chromium (Cr), titanium (Ti), copper (Cu), zinc (Zn), zirconium (Zr) are concentrated (Brand et al., 1998). Nickel and Co are enriched by a factor of 3 to 30 times than the parent ultramafic rocks (Elias, 2002). The mine production of Ni occurs mainly in Australia, Brazil, Canada, Indonesia, New Caledonia, Russia, and the Philippines. In 2018, however, there was an enormous decrease in production that transpired in the Philippines because most of the mining companies failed to meet the environmental standards (USGS, 2018).

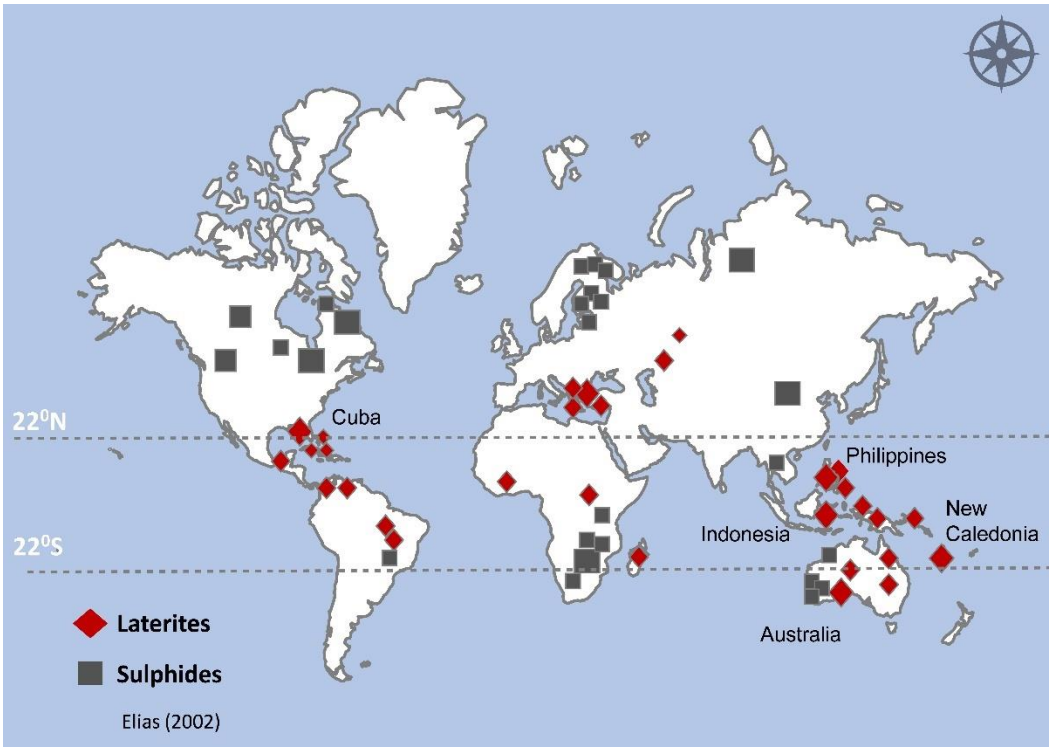

Fig. 1 Global distribution of laterites and sulphides. Modified from Elias (2002).

The typical Ni laterite profile in the Philippines is divided from the bottom to top: (i) unaltered or serpentinized bedrock, (ii) saprolite horizon, and (iii) limonite horizon (Fig. 2). Occasionally, goethite or hematite ferricrete covers

the uppermost limonite horizon (Marsh and Anderson, 2011). With respect to the mineralogical features of Ni laterites, these are divided into hydrous magnesium (Mg)-silicate, clay and oxide types (Brand et al., 1998; Gleeson et al., 2004; Freysinnet, 2005).

	MgO wt%	Fe_2O_3 wt%	NiO wt%	Co_2O_3 wt%
Red (upper limonite) Red-yellow (lower limonite) Loose (dry), friable and sticky (wet) Rich in secondary silica (5-8 m) and Mn-oxyhydroxides (10-15m)	0.20-2.07	30.8-69.8	0.22-1.14	0.01-0.85
Yellow Mixture of earthy (soft saprolite) and blocky rocks (hard saprolite)	20-35	7.43-30.3	2.17-7.77	0.01-0.25
Serpentinized peridotite	41	6.5	0.40	0.01

Fig. 2 A photo of a Ni laterite profile showing the concentrations of major oxides (MgO, Fe_2O_3) and minor elements (NiO and Co_2O_3) in the bedrock and the different weathered horizons in the Berong deposit, Palawan, Philippines.

Numerous works have been carried out towards investigating the mineralogical and geochemical characteristics of Ni laterites mainly in Australia (Putzolu et al., 2018), Brazil (Colin et al., 1990), New Caledonia (Dublet et al., 2012; Villanova-de-Benavent et al., 2014), Indonesia (Golightly, 1979; Fu et al., 2014), Cuba and the Dominican Republic (Aiglsperger et al., 2016). However, limited studies have been conducted to

Akita University

determine the distribution of Ni and Co in the Philippine laterite deposits. Previous work by Fan and Gerson (2011) studied Ni speciation in the saprolite and limonite ores from Pujada, Philippines, and they reported that Ni in the limonite ore is mostly associated with phyllomanganate and the rest is incorporated into goethite. Nickel in the saprolite ore is hosted by serpentine, and the remaining is adsorbed within phyllomanganate.

This study provides detailed documentation of the primary and secondary minerals in the bedrock, and ore minerals in the saprolite and limonite horizons of the Ni-Co laterite deposits in the Philippines. Two laterite deposits from Berong, Palawan, and Intex, Mindoro, Philippines are considered because these have differing Ni concentrations in the weathered horizons. Several factors affect the distribution and enrichment of Ni in laterite deposits. With these conditions, this study also aims to clarify the impact of the degree of weathering on the enrichment of Ni in these deposits. An increasing number of studies examined the occurrence of Co in laterite deposits owing to its importance in the production of rechargeable batteries and superalloys (USGS, 2019). The chemical composition of the Mn-oxyhydroxides are reported to investigate the geochemical behavior of Ni and Co within the laterite profiles.

It is well documented that hydrous Mg silicate deposits contain a considerable amount of Ni. In this type of deposit, Ni is hosted by talc, secondary serpentine, or an intimate mixture of these minerals, commonly known as garnierite (Brand et al., 1998). Furthermore, few studies have

Akita University

explored the nature of Ni-rich serpentine in laterites, particularly in the saprolite horizon (Cluzel and Vigier, 2008; Villanova-de-Benavent et al., 2014; Tauler et al., 2017). This work examines the nature and spatial relations between the previous serpentinization and the Ni-bearing serpentines in the saprolite horizon. Such information provides further understanding on the behavior of Ni as serpentinization progresses. Field observations, mineralogical, and chemical features of the primary, secondary, and ore-bearing phases are integrated to ultimately understand the complex formation of the Berong and Intex Ni-Co laterite deposits.

1.2 Mine Production and Use of Nickel

Mine production of Ni originates primarily from countries including Indonesia, the Philippines, New Caledonia, Russia, Australia, Canada, China, and Brazil (Fig. 3). There has been an increasing demand for refined nickel, stainless steel, nickel pig iron, and nickel chemicals. Production of lower-priced nickel pig iron is favored in contrast to refined nickel and stainless steel. Currently, a significant increase in nickel chemicals, specifically nickel sulfate, is utilized in the manufacturing of batteries (USGS, 2019).

Stainless steel accounts for the two-thirds of Ni usage and mostly supplies to various industries, including construction, transportation, and food processing. In 2013, China is the top global producer of stainless steel with a record of 14.3 million tons, whereas the U.S. steel industry generated 1.54 million tons. In the same year, however, Ni prices further decreased

from $17,729 to $13,725. Despite the price drop, there was a projected long-term demand for austenitic stainless steel (USGS, 2014). Nickel is recently consumed in the production of batteries, which are essential for electric vehicles and energy storage applications (USGS, 2019).

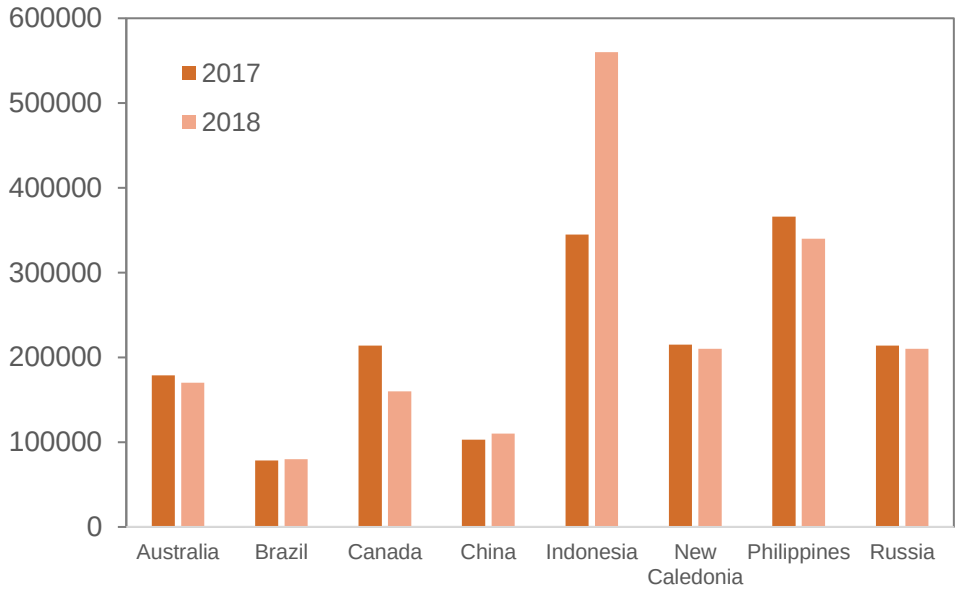

Fig. 3 World mine production of nickel from 2017 to 2018. Production based on U.S. Geological Survey, Mineral Commodity Summaries, 2019

1.3 Mine Production and Use of Cobalt

Most of the cobalt production is in Congo (Kinshasa), accounting for more than 60% and is mined either as a by-product of Ni or copper (Cu). Other countries with considerable reserves and mine production of cobalt occur in Australia, Canada, Cuba, Madagascar, New Caledonia, the Philippines, and Russia (Fig. 4). Based on the World Mine Production report from 2013 to 2017 (Brown et al., 2019), some countries do not recover Co.

One example is the copper mining in Poland, and Co is not produced as a by-product.

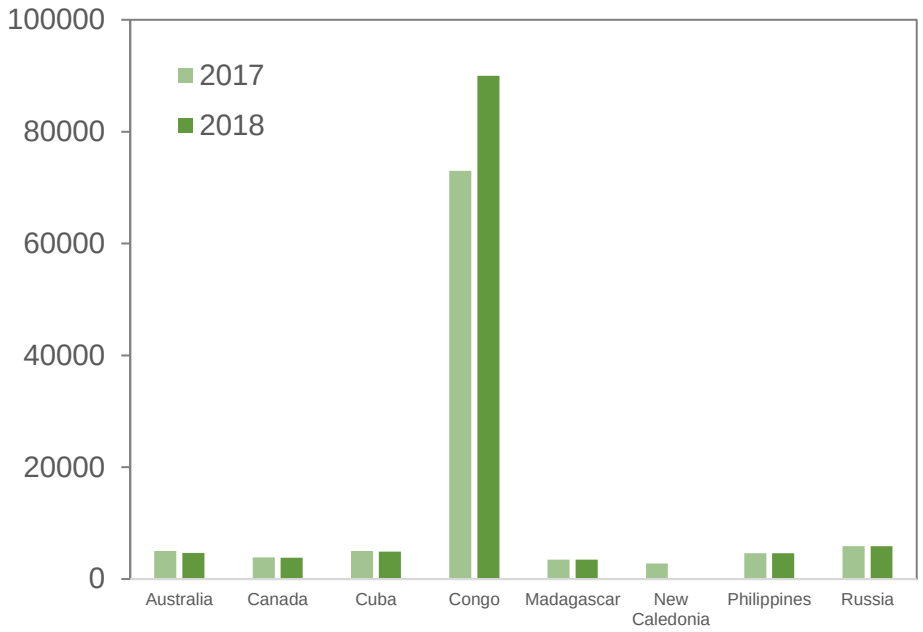

Fig. 4 World mine production of cobalt from 2017 to 2018. Production based on U.S. Geological Survey, Mineral Commodity Summaries, 2019.

In the past few years, the global production of cobalt has been higher than its consumption resulting in lower prices. A recent report, however, revealed that the prices have been increasing because of the robust demand of consumers in aerospace sectors and production of rechargeable batteries, particularly lithium-ion batteries. It is expected that there will be a decrease in the global consumption of Co in batteries and in turn, Ni will replace Co (USGS, 2019).

Akita University

1.4 Research Problems

Despite the increasing number of studies related to Ni laterite deposits in New Caledonia, Indonesia, Australia, among other countries, there are limited studies that focus on investigating the occurrence and paragenesis of the different serpentine veins in the bedrock and saprolite. Furthermore, there is a dearth of information about the ore minerals that host a significant amount of Co, particularly in the Philippine laterites. The quantification of critical metals (Sc and REE) in the Philippine deposits is also limited. More importantly, there is a current lack of studies in existence that provide information related to the formation and evolution of the Ni-Co laterite deposits in the Philippines.

1.5 Significance of the study

The present work highlights not only the characteristics of garnierite but also the nature of various serpentine veins in the bedrock and saprolite horizon, hence, providing a detailed picture of how Ni is initially leached from the bedrock, and later enriched during weathering. Nickel laterite deposits have been the target mainly for Ni resources, but recent works are also examining the occurrence of Co and Sc in these deposits. The increasing number of projects is driven by the growing demand for rechargeable batteries and raw materials needed for sustainable energy development (USGS, 2018). In this study, the knowledge gain regarding the effect of the degree of weathering is significant in understanding the distribution of Ni and Co concentrations in the saprolite and limonite. The

Akita University

comprehensive mineralogical and geochemical investigation of the laterite profiles from Berong and Intex deposits could provide additional insight into the complex formation of Ni lateritic deposits.

1.6 Objectives of the study

The main objective of this study is to investigate the formation and evolution of the Berong and Intex Ni-Co laterite deposits by combining field observations, mineralogical, and geochemical data. The following are the specific objectives of this study:

a) To gather field data and observe the occurrence of serpentine veins and garnierite in the weathered horizons of the laterite profiles.

b) To examine the characteristics and paragenetic sequence of the serpentine veins in the bedrock and saprolite horizon by optical microscopy and Raman spectroscopy.

c) To obtain the textural features and chemical composition of the primary, secondary, and ore minerals in the bedrock and weathered horizons by optical microscopy, X-ray Diffraction (XRD) and Electron Probe Microanalyses (EPMA).

d) To determine the whole rock chemistry of the major and minor elements by X-ray Fluorescence (XRF) analysis, and trace element concentrations of Sc and REE using Inductively Coupled Plasma Mass Spectrometry (ICP-MS) analysis.

e) To compare the similarities and differences between the two deposits.

Akita University

1.7 Scope and Limitation

For this study, two Ni-Co laterite deposits from Berong, Palawan, and Intex, Mindoro, Philippines, were investigated. Three outcrops were examined for the Berong deposit, whereas three drill cores were explored for the Intex deposit. These outcrops and drill cores were chosen based on the availability of complete and in-situ laterite profiles in the field. The raw maps used to make geologic maps were either acquired from the mining company or the Mines and Geoscience Bureau (MGB), a government agency in the Philippines.

Most of the sample preparation, including polished thin sections and polished samples, was conducted at the facility of the Graduate School of International Resource Sciences, Akita University. Observations under the microscope, pH, XRD, Raman, and ICP-MS analyses were also accomplished in the university. The preparation of eleven polished samples, EPMA and XRF analyses were done at the facility of the Geological Survey of Japan (GSJ), National Institute of Advanced Science and Technology (AIST) in Tsukuba, Japan.

1.8 Outline of the Thesis

The succeeding chapters discuss the following:

(i) Chapter 2 explains the tectonic setting of the Philippines and regional geology of the two study areas.

Akita University

(ii) Chapter 3 presents the mineralogy and geochemistry of the Berong Ni-Co laterite deposit, Palawan, Philippines. The highlight of this chapter is to show the different types of serpentine veins identified in the bedrock and saprock, and the occurrence of garnierite, Fe- and Mn-oxyhydroxides in laterites. Finally, the chapter proposes a dynamic model of laterization of the Berong deposit, Philippines.

(iii) Chapter 4 determines the effect of the degree of weathering of ultramafic rocks and laterites on the enrichment of Ni in the Intex deposit. The plots of Ultramafic Index of Alteration (UMIA) and Index of Lateritization (IOL) are utilized to illustrate the difference in the extent of lateritization between the two deposits and how this difference affected the increased concentration of Ni in the Berong deposit compared with Intex deposit.

(iv) Chapter 5 quantifies the concentrations of Sc and REE in the bedrock, saprolite, and limonite samples of the Berong and Intex deposits. The main aim is to provide preliminary information regarding their bulk abundance that could be significant in the exploration of critical metals.

(v) Chapter 6 summaries the similarities and differences between the Berong and Intex Ni-Co laterite deposits in the Philippines.

(vi) Chapter 7 presents the conclusions and recommendations of this Ph.D. research project

1.9 Research framework

Figure 5 shows the framework of the study, and this will serve as a guide to accomplish the above-stated objectives:

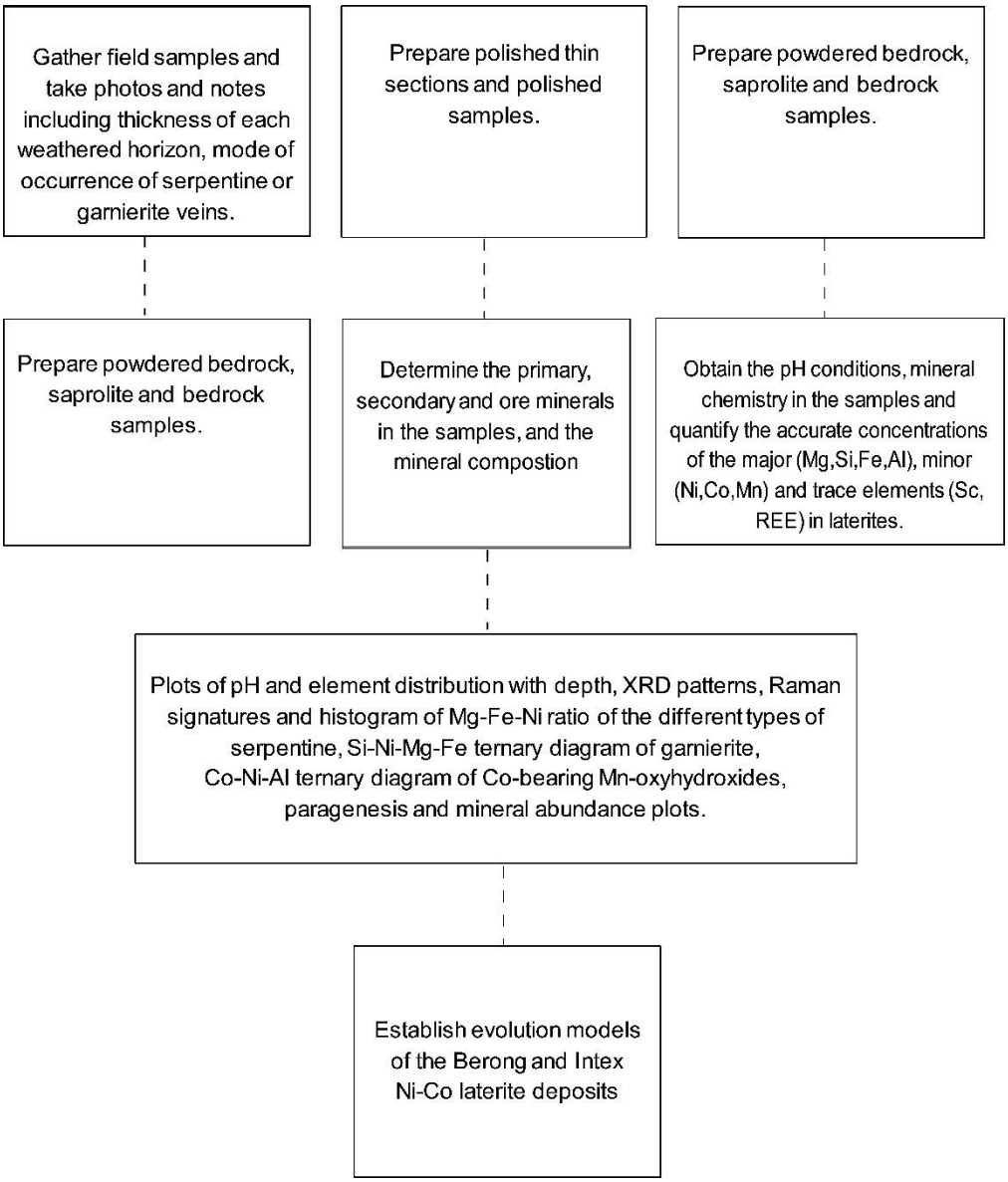

Fig. 5 Summary of framework achieved in this study.

2.0 References

Aiglsperger, T., Proenza, J. A., Lewis, J. F., Labrador, M., Svojtka, M., Rojas-Purón, A., Ďurišová, J., 2016. Critical metals (REE, Sc, PGE) in Ni laterites from Cuba and the Dominican Republic. Ore Geol Rev. *73*, 127-147.

Brand, N.W., Butt, C.R.M., Elias, M., 1998. Nickel laterites: classification and features. AGSO J. Aust. Geol. Geophys. 17, 81-88.

Brown, T.J., Idoine, N.E., Raycraft, E.R., Hobbs, S.F., Shaw, R.A., Everett, P., Kresse, C., Deady, E.A., Bide, T., 2019. World Mine Production 2013-2017. British Geological Survey, Keyworth, Nottinghamshire, England.

Butt, C.R.M., Cluzel, D., 2013. Nickel laterite ore deposits: Weathered serpentinites. Elements. 9, 123-128.

Cluzel, D., Vigier, B., 2008. Syntectonic mobility of supergene nickel ores of New Caledonia (Southwest Pacific). Evidence from garnierite veins and faulted regolith. Resour. Geol. 58, 161-170.

Colin, F., Nahon, D., Trescases, J.J., Melfi, A.J., 1990. Lateritic weathering of pyroxenites at Niquelandia, Goias, Brazil: the supergene behavior of nickel. Econ. Geol. 85, 1010-1023.

DeYoung, J. H., 1986. International Strategic Minerals Inventory Summary Report--nickel. Department of the Interior, USGS. 930, 1-15.

Dublet, G., Juillot, F., Morin, G., Fritsch, E., Fandeur, D., Ona-Nguema, G., Brown, G.E., 2012. Ni speciation in a New Caledonian lateritic regolith: A quantitative X-ray absorption spectroscopy investigation. Geochim. Cosmochim. Acta. 95, 119-133.

Elias, M., 2002. Nickel laterite deposits – geological overview, resources, and exploitation. Giant Ore Depos. Charact. Genes. Explor. CODES Spec. Publ. 4, 205-220.

Evans, A.M., 1993. Ore geology and industrial minerals: an introduction, third ed. Blackwell Science, Oxford. 262-271.

Fan, R., Gerson, A.R., 2011. Nickel geochemistry of a Philippine laterite examined by bulk and microprobe synchrotron analyses. Geochim. Cosmochim. Acta. 75, 6400-6415.

Fu, W., Yang, J., Yang, M., Pang, B., Liu, X., Niu, H., Huang, X., 2014. Mineralogical and geochemical characteristics of a serpentinite-derived laterite profile from East Sulawesi, Indonesia: Implications for the lateritization process and Ni supergene enrichment in the tropical rainforest. J. Asian Earth Sci. 93, 74-88.

Freyssinet, P., Butt, C.R.M., Morris, R.C., Piantone, P., 2005. Ore-forming processes related to lateritic weathering. Econ. Geol. 100th Anniv. 681-722.

Gleeson, S.A., Herrington, R.J., Durango, J., Velásquez, C.A., Koll, G., 2004. The mineralogy and geochemistry of the Cerro Matoso S.A. Ni Laterite deposit, Montelíbano, Colombia. Econ. Geol. 99, 1197-1213.

Golightly, J.P., Arancibia, O.N., 1979. The chemical composition and infrared spectrum of nickel-and iron-substituted serpentine from a nickeliferous laterite profile, Soroako, Indonesia. The Can Mineral. 17, 719-728.

Golightly, J.P., 1981. Nickeliferous laterite deposits. Econ Geol 75th Anniv. 710-735.

Marsh, E., Anderson, E., Gray, F., 2011. Ni-Co laterites–a deposit model. US Geol Surv. 2-3.

Putzolu, F., Balassone, G., Boni, M., Maczurad, M., Mondillo, N., Najorka, J., Pirajno, F., 2018. Mineralogical association and Ni-Co deportment in the Wingellina oxide-type laterite deposit (Western Australia). Ore Geol. Rev. 196, 282-296.

Tauler, E., Lewis, J. F., Villanova-de-Benavent, C., Aiglsperger, T., Proenza, J. A., Domènech, C., Galí, S., 2017. Discovery of Ni-smectite-rich saprolite at Loma Ortega, Falcondo mining district (Dominican Republic): geochemistry and mineralogy of an unusual case of “hybrid hydrous Mg silicate–clay silicate” type Ni-laterite. Miner. Deposita. 52, 1011-1030.

U.S. Geological Survey, 2014, Mineral commodity summaries 2014: U.S. Geol. Surv. 196, 108-109.

U.S. Geological Survey, 2018. Mineral commodity summaries 2018: U.S. Geol. Surv. 200. 50-51.

U.S. Geological Survey, 2019, Mineral commodity summaries 2019: U.S. Geol. Surv. 200. 112-113.

Villanova-de-Benavent, C., Proenza, J.A., Galí, S., García-Casco, A., Tauler, E., Lewis, J.F., Longo, F., 2014. Garnierites and garnierites: Textures, mineralogy, and geochemistry of garnierites in the Falcondo Ni-laterite deposit, Dominican Republic. Ore Geol. Rev. 58, 91-109.

Akita University

CHAPTER 2

Tectonic and Geological Setting

This section presents the tectonic setting of the Philippines and geological setting of the two study areas in the Philippines, namely Berong, Palawan and Victoria, Mindoro. The stratigraphy of the different formations within the mine or exploration area is also described in detail.

2.1 Tectonic Setting of the Philippines

The Philippines is located on a complex plate boundary between the Philippine Sea Plate and the eastern margin of the Eurasian Plate, typically expressed as subduction zones, collision zones, and marginal sea basin openings. It consists of insular arcs, ophiolitic suites and continental rocks which have a Eurasian affinity (Aurelio and Peña, 2004).

Multiple subduction zones surround the archipelago, namely, the west- and east-dipping subduction zones. These subduction zones are accommodated by the Philippine Fault Zone, which cuts the entire length of the archipelago (Fig. 6). The Philippine Trench and East Luzon Trough are the west-dipping subduction zones, whereas Manila Trench, Negros Trench, and Cotabato Trench are the east-dipping subduction zones. The Philippine Trench formed from the western subduction of the Philippine Sea Plate under the eastern Philippine arc (Fitch, 1970; Cardwell et al., 1980).

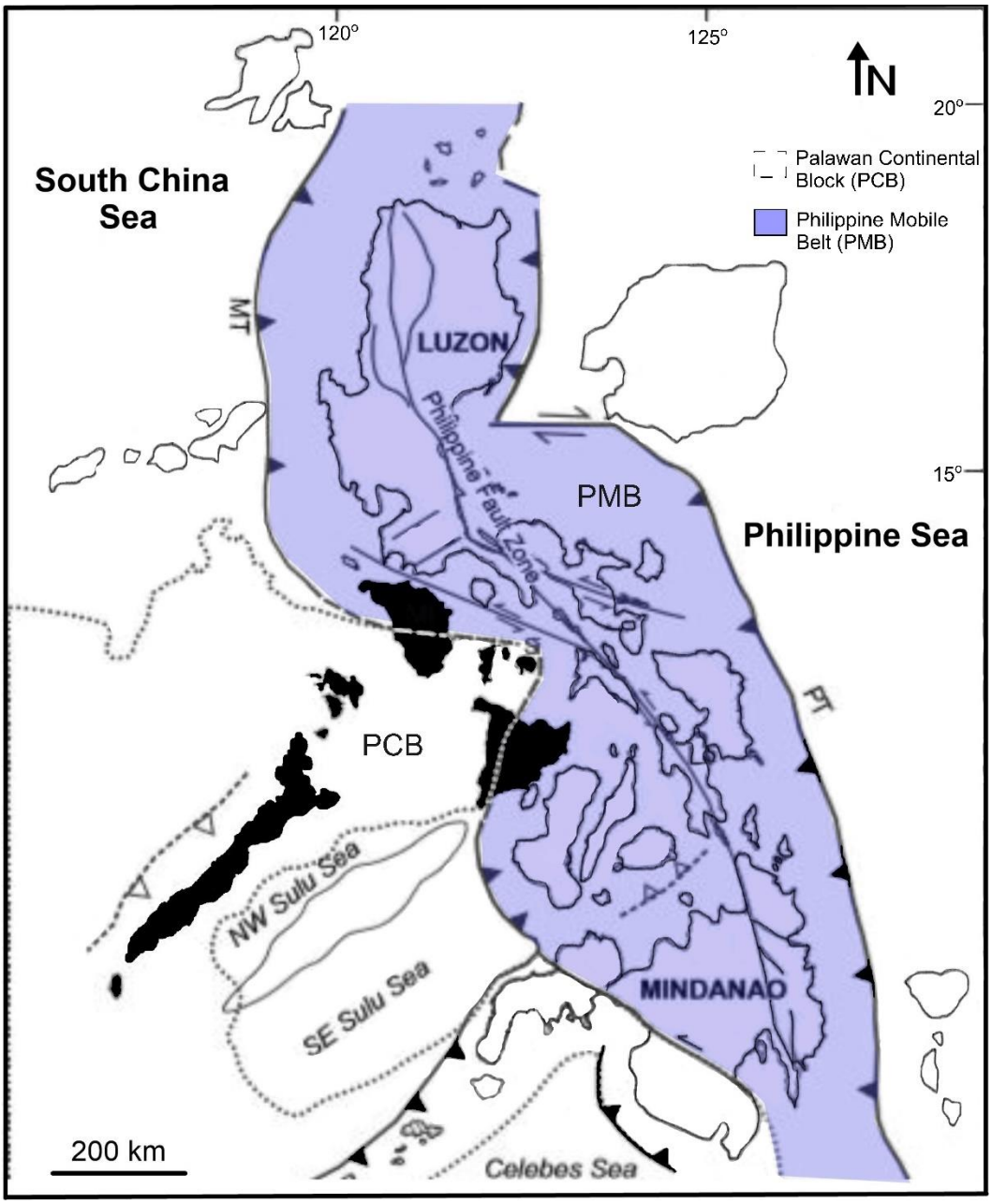

Fig. 6 The Philippines is bounded by two major subduction zones, the Philippine Trench (PT) and Manila Trench (MT), which is accommodated by the Philippine Fault Zone. Separated by dashed lines indicate the seismically active, Philippine Mobile Belt (PMB), and the aseismic block – Palawan Continental Block (PCB). Modified from Yumul et al. (2009).

Akita University

East Luzon Trough, on the other hand, is considered a new subduction zone to the east of Luzon Island (Karig, 1973; Lewis and Hayes, 1983). Opposite the East-Luzon trough is the Manila Trench, which represents the subduction of the oceanic crust of the South China Sea under the Luzon Arc (Karig, 1973; Cardwell et al., 1980). The Negros Trench passes the western coasts of the Panay and Negros Islands. Similar to the East Luzon Trough, the Cotabato Trench is also young, as indicated by its undeveloped Benioff zone.

The archipelago is divided into two major geologic blocks: The Philippine Mobile Belt (PMB) (seismically active block) and the Palawan Continental Block (PCB) (aseismic block) (Hamilton, 1979) (Fig. 6). The collision between the two blocks had influenced the geologic evolution of the Philippines (Yumul et al., 2009). The northern and southern part of the archipelago is marked by three active collision zones, such as the Taiwan, Mindoro-Panay, and Moluccas Sea collisions (Aurelio and Peña, 2004). Taiwan is an active orogenic belt derived from the collision of the western edge of the Philippine Sea Plate with the continental margin of Eurasia. This arc-continental collision marked the re-organization of the Philippine Sea Plate four million years ago (Barrier and Angelier, 1986). The Miocene collision between the NPB and PMB resulted in the arc-continental collisional deformation within Mindoro Island. In the Moluccas Sea, located south of Mindanao Island, an oceanic plate is subducting to the east and west directions (Roeder, 1977; Cardwell et al., 1980). The subduction is a

Akita University

manifestation of the convergence of the two active volcanic arcs, Sangihe and Halmahera. The arc-arc collision is a present-day example of the emplacement of ophiolite formed from the curvature of the fold axis of the oceanic plate (McCaffrey, 1991).

2.2 Geological setting

2.2.1 Palawan, Philippines

Palawan is separated into two parts, namely, the northern and southern/central blocks. These blocks were divided according to their structural and stratigraphic difference. The North Palawan is originally part of mainland Asia that was rifted in the course of the opening of the South China Sea and had similar stratigraphic grouping with southern Mindoro, northwest Panay and Romblon Island Group. The south and central blocks, on the other hand, consist of ophiolitic rocks and Cenozoic clastic sediments (Fig. 7). Previous work by Hamilton (1979) indicated that the Ulugan Bay Fault, a strike-slip fault, separates the northern block from the southern/central block. However, the occurrence of this fault was later negated, and instead, the boundary was placed along the Sabang Thrust which is a low to intermediate dipping structural line situated north of the Ulugan Bay Fault (Mitchell, 1985). It is then recognized that Palawan was a rifted block from the South China Sea (Hinz and others, 1983; Pineda and others, 1992). It was reported that the obliqueness of tilting during the collision of the Palawan Block and Philippine Mobile Belt resulted in the contrasting lithology and structures between the two blocks.

In southern Palawan, the local formations within the area of Barangay Berong are the Palawan Ophiolite and Dalrympole Amphibolite. Palawan Ophiolite is composed of Beaufort Ultramafic Complex, Stavely Gabbro, and Espina Formation (Fig. 8).

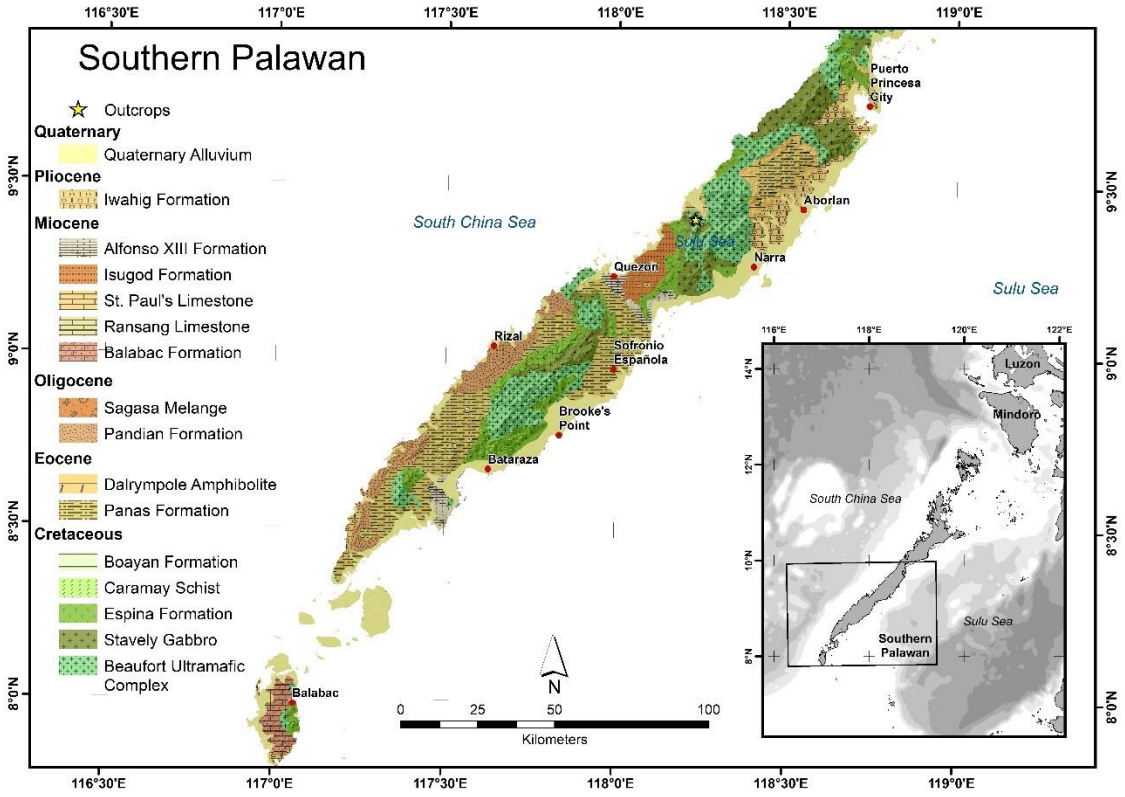

Fig. 7 Geologic map of the southern Palawan, Philippines. Palawan Ophiolite Complex consists of Beaufort Ultramafic Complex, Stavely Gabbro, and Espina Formation (green shaded regions) formations.

2.2.1.1 Beaufort Ultramafic Complex

The ultramafic rocks of the Beaufort Ultramafic Complex are the main components of the ophiolitic body, which are mainly exposed from Puerto Princesa in central Palawan to Bataraza located in the southernmost section of the island. These rocks are both unaltered and serpentinized

Akita University

peridotite and pyroxenite. The complex is principally composed of harzburgite with cumulate dunite (Mitchell, 1985). Dunite occurs as dikes or stocks and intrudes the harzburgite, while the pyroxenite is commonly found in stratiform layers (Aurelio and Peña, 2004).

2.2.1.2 Dalrympole Amphibolite

The Dalrympole Amphibolite is the metamorphic basement of the ophiolite suite, consisting of greenschist, amphibolite, quartz-mica schist, and quartzose schist. The amphibolite has a thickness of a several tens of meters, and most of the exposures can be found at Dalrympole Point on the western side of Nasuedan Beach. The metamorphic age of this unit is Middle Eocene to Late Eocene based on the results of K-Ar dating of amphibolite (Raschka et al., 1985).

2.2.1.3 Stavely Gabbro

The Stavely Gabbro overlies the Beaufort Ultramafic Complex and consists of medium to coarse-grained olivine gabbro and troctolite, which are mostly exposed in the west of Nara, south of Berong, in the west coast of Long Point and the rivers of Malinao and Balsahan. Gabbro is often characterized by coarse-grained crystals of mainly plagioclase feldspars, pyroxene with a moderate amount of hornblende (Mitchell, 1985).

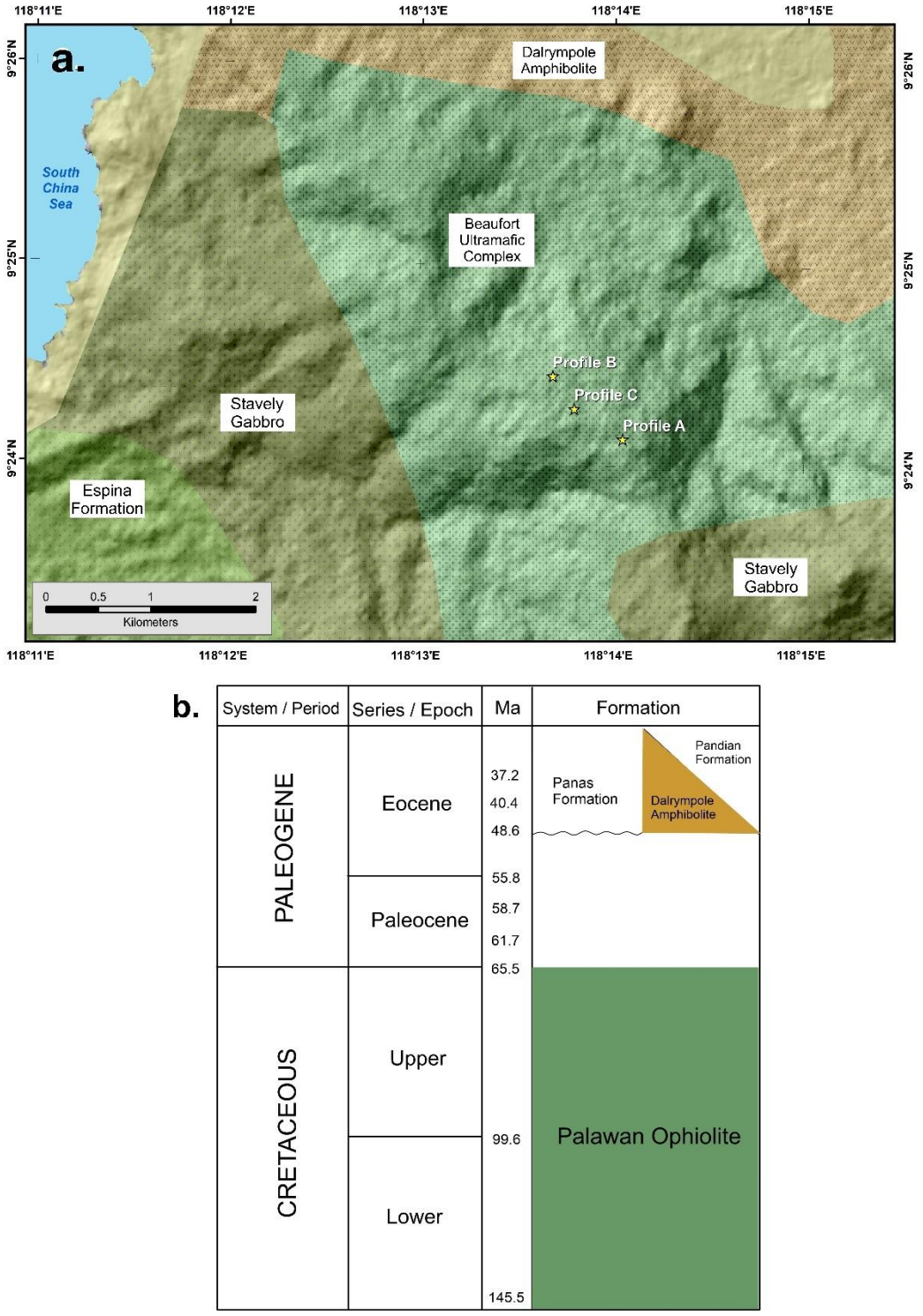

Fig. 8 Geologic map of the southern Palawan showing the local formations in the area of Barangay Berong, Palawan, Philippines. b) Stratigraphic column displaying the formations within the Mineral Productivity Sharing Agreement (MPSA) of the Berong mine.

Akita University

2.2.1.4 Espina Formation

The spilitic basalt with intercalated chert and sandstone constitutes the Espina Formation, which is the sedimentary cover of the mafic and ultramafic rocks. The chert is manganese bearing and appears reddish to brownish gray. Brown to gray fossiliferous limestone is associated with the ophiolitic sequence (Wolfart et al., 1986). These rocks are well exposed at Espina Point in Balabac island of the southern block. Paleocene and Neogene clastic sedimentary rocks overlie these ophiolitic rocks (Almasco et al., 2000).

2.2.2 Mindoro, Philippines

The Mindoro island is located in the western-central Philippines (Figure 9a). Several workers agreed that the islands of Mindoro are composed of two distinct tectonostratigraphic terranes (Karig, 1973; Mitchell, 1985; Sarewitz and Karig. 1986). The southwestern part of Mindoro is a fragment of the Palawan Microcontinental Block, which was rifted in the course of the opening of the South China Sea in the Eocene. While the northeastern part of the Mindoro block emanated from Luzon arc terrane which developed as an extension to the north-east Borneo in the plate tectonic reconstruction of Hall (2002) (Petersen et al., 2010).

Previous studies reported that the indentation of the oceanic leading edge of the Palawan Continental Block and the Philippine Mobile Belt and subsequent subduction most likely started during the early Miocene. Then the collision between the two blocks ended during the Pliocene (Bellon and

Akita University

Yumul, 2001; Yumul et al., 2003, 2005; Canto et al., 2012). This collision event resulted in seismic gaps, volcanic arc gaps, steep slabs, emplacement of the ophiolite, cusping and microblock (Marchadier and Rangin 1990; Jumawan et al., 1998; Yumul et al., 2008). Seismic gaps are segments that have not been active for a long time and may produce powerful earthquakes (Rong et al., 2003). Volcanic arc gaps, on the other hand, occur when one of the features are lacking including source materials for the volcanics, heat source, and a stress state (McGeary et al., 1984). The wide thrust or suture zone that traversed the island from north-west to south-east is related to the Miocene collision and the ophiolite emplacement and sedimentary rocks in Mindoro (Sarewitz and Karig, 1986; Rangin, 1991; Yumul et al., 2003). This suture zone hosts the ultramafic rocks with ophiolite origin and the intensive weathering of these rocks ultimately resulted in the development of the nickel laterite deposits on the island (Petersen et al., 2010).

The oldest rocks in Mindoro are on the southwestern side, consisting of sandstone, shale, mudstone with limestone, and conglomerate (Corby et al., 1951). These rocks constitute the Jurassic Mansalay Formation (Fig. 9b). The age of the formation is late Middle to early Late Jurassic based on ammonites, which are the main fossils in the area (Andal et al., 1968). Caguray Formation unconformably overlies the Mansalay Formation (Fig. 9b). Miranda (1980) reported exposures of main sandstone, shale,

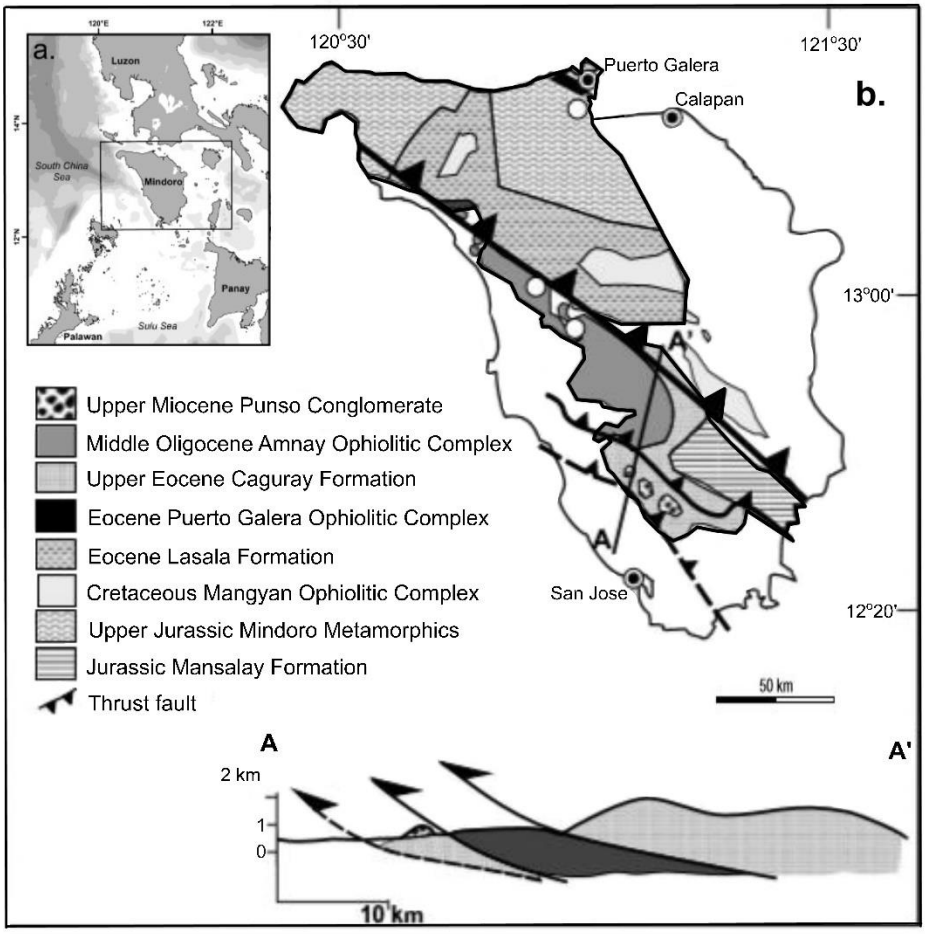

Fig. 9 a) Location map of the Mindoro Island. b) Geologic map displaying the various formations in the island. Adapted from Yumul et al. (2008).

mudstone with the minor occurrence of conglomerate and limestone along Caguray River and in San Jose town, Occidental Mindoro. The Mindoro Metamorphics in the northeastern section of the island consists of metamorphosed ophiolitic rocks, sedimentary and volcanic rocks, and quartz diorite. Intrusive bodies are also exposed in northern Mindoro comprising of granodiorite stocks and dikes, and dioritic bodies (Aurelio and Peňa, 2004). The Punso Conglomerate unconformably overlies older formations and nannofossils in siltstone suggest a Late Miocene age

Akita University

(Marchadier and Rangin, 1990). This formation is relatively thick, reaching up to 1500 m and consisting of conglomerate interbedded with shale, sandstone and mudstone (Eleston and Melendres, 1953). These rocks are well exposed along the Labangan River and Lumintao River. The study area in northeastern Mindoro encompasses two formations namely the Mangyan Ophiolitic Complex and Lasala Formation (Fig. 10).

2.2.2.1 Mangyan Ophiolitic Complex

There are three known ophiolite belts in Mindoro islands; the Eocene Lubang-Puerto Galera Complex, the Cretaceous Mangyan Complex, and the mid-Oligocene Amnay Complex (Fig. 9) (Hashimoto and Sato, 1968; Rangin et al., 1985; Karig et al., 1986). The multiple collisions that occurred from Early to Middle Miocene resulted in the generation of various ophiolites in the island (Yumul et al., 2003, 2005). Earlier works by Mitchell (1985) and Boudier et al. (1988) proposed that Mangyan Ophiolitic Complex was emplaced immediately after its formation based on the occurrence of amphibolite sole below the ultramafic rocks.

2.2.2.2 Lasala Formation

The Late Eocene Lasala Formation is composed dominantly of interbedded sandstone and shale with mudstone, conglomerate, limestone, basalt, and dikes (Fig. 4). The individual beds of sandstone and shale, on the other hand, are up to 2 m thick. The clasts of conglomerate consist mainly of basalt and chert. The exposure of a 100 m thick limestone

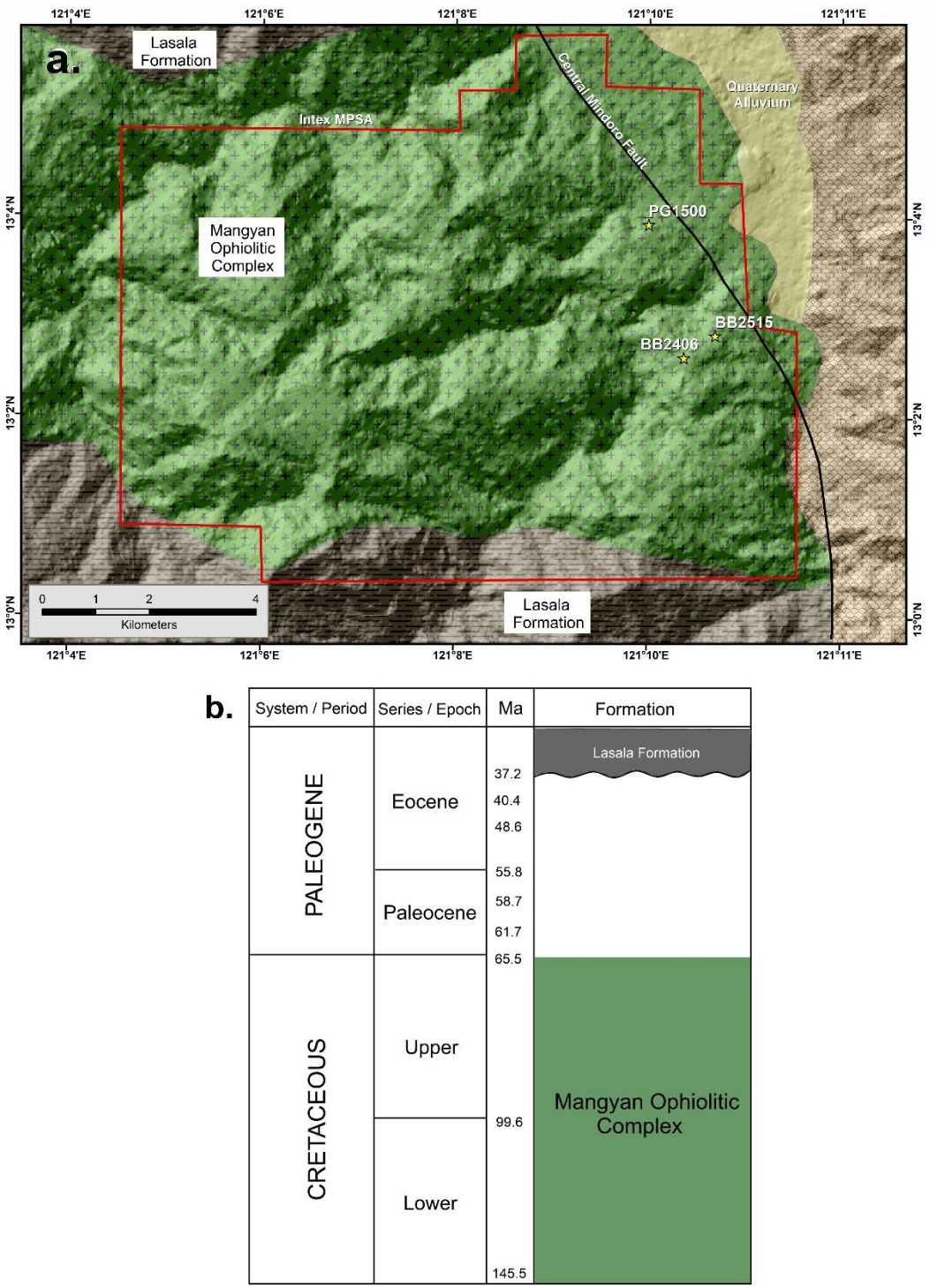

Fig. 10 a) Geologic map of the northeastern section of Mindoro, highlighting the local formations in the vicinity of Intex deposit. b) Stratigraphic column showing the formations within the Mineral Productivity Sharing Agreement (MPSA) of the Intex Resources mining company.

Akita University

separates Lasala Formation and Halcon Metamorphic Complex. The clastic sequence of this formation unconformably overlays the Halcon Metamorphic Complex. The indicated age of the formation was initially determined through paleontological analyses of foraminifera (Hashimoto and Sato, 1968). The work of Faure et al. (1989) reported similar age based on the occurrence of different species of foraminifera including *Amphistegina radiata, Operculina cf. saipanensis, Pellatispira mirabilis* (Umgrove), *Rotalidae species* and *S pherogypsina* species.

2.3 References

Almasco, J.N., Rodolfo, K., Fuller, M., Frost, G., 2000. Paleomagnetism of Palawan, Philippines. J. Asian Earth Sci. 18, 369-389.

Andal, D. R., Esguerra, J. S., Hashimoto, W., Reyes, B. P., Sato, T., 1968. The Jurassic Mansalay Formation, southern Mindoro, Philippines. Geology and Palaeontology of Southeast Asia. 4, 179-197.

Aurelio, M., Peña, R., 2004. Geology and mineral resources of the Philippines. Mines and Geosciences Bureau, Department of Environment and Natural Resources. 1, 27-30.

Barrier, E., & Angelier, J., 1986. Active collision in eastern Taiwan: the Coastal Range. Tectonophysics. 125, 39-72.

Bellon, H., Yumul, G.P., 2001. Miocene to Quaternary adakites and related rocks in Western Philippine arc sequences. Comptes Rendus l'Académie des Sci. - Ser. IIA - Earth Planet. Sci. 333, 343-350.

Boudier, F., Ceuleneer, G., Nicolas, A., 1988. Shear zones, thrusts and related magmatism in the Oman ophiolite: initiation of thrusting on an oceanic ridge. Tectonophysics. 151, 275-296.

Canto, A.P.B., Padrones, J.T., Concepcion, R.A.B., Perez, A.D.C., Tamayo, R.A., Dimalanta, C.B., Faustino-Eslava, D. V., Queaño, K.L., Yumul, G.P., 2012. Geology of northwestern Mindoro and its offshore

Akita University

islands: Implications for terrane accretion in west Central Philippines. J. Asian Earth Sci. 61, 78-87.

Cardwell, R. K., Isaacks, B. L., Karig, D. E., 1980. The spatial distribution of earthquakes, focal mechanism solutions, and subducted lithosphere in the Philippine and northeastern Indonesian islands. The Tectonic and Geologic Evolution of Southeast Asian Seas and Islands. *23*. 1-35.

Corby, G. W., 1951. Geology and oil possibilities of the Philippines. Department of Agriculture and Natural Resources Technical Bulletin, Philippines. 21, 362.

Faure, M., Marchadier, Y., Rangin, C., 1989. Pre-Eocene Synmetamorphic Structure in the Mindoro-Romblon-Palawan Area, West Philippines, and implications for the history of southeast Asia. Tectonics. 8, 963-979.

Fitch, T.J., 1972. Plate convergence, transcurrent faults, and internal deformation adjacent to Southeast Asia and the western Pacific. J. Geophys. Res. 77, 4432-4460.

Gervasio, F.C., 1967. Age and nature of orogenesis of the Philippines. Tectonophysics. 4, 379-402.

Hamilton, W., 1979. Tectonics of the Indonesian Region. U.S. Geol. Surv. Prof. Paper. 1078, 345.

Hashimoto, W., Sato, T., 1968. Contribution to the geology of Mindoro and neighboring islands, the Philippines. Geology and Paleontology of Southeast Asia. 5, 192-210.

Jumawan, F., 1998. Using geochemistry as a tool in determining the tectonic setting and mineralization potential of an exposed upper mantle-crust sequence: Example from the Amnay Ophiolitic Complex in Occidental Mindoro, Philippines. J. Geol. Soc. Geology and Paleontology of Southeast Asia Philipp. 53, 24-48.

Karig, D.E., 1973. Plate convergence between the Philippines and the Ryukyu islands. Mar. Geol. 14, 153-168.

Lewis, S.D., Hayes, D.E., 1983. The tectonics of northward propagating subduction along eastern Luzon, Philippine Islands. Tecton. Geol. Evol. Southeast Asian seas islands. Part 2. 27, 57-78.

Marchadier, Y., Rangin, C., 1990. Polyphase tectonics at the southern tip of the Mnaila trench, Mindoro-Tablas Islands, Philippines. Tectonophysics. 183, 273-287.

McCaffrey, R., 1991. Earthquakes and ophiolite emplacement in the Molucca Sea Collision Zone, Indonesia. Tectonics. 10, 433-453.

McGeary, S., Nur, A., Ben-Avraham, Z., 1985. Spatial gaps in arc volcanism: The effect of collision or subduction of oceanic plateaus. Tectonophysics.119, 195-221.

Mitchell, A.H.G., 1985. Geology of the Central Palawan: United Nations-Bureau of Mines and Geosciences, Internal Technical Report. 6, 1-45.

Petersen, J.S., Jensen, S.M., Blomsterberg, J., Audet, MA., 2010. Mineral Resources of the Mindoro Nickel-Laterite Project, the Philippines: NI 43-101 Technical Report, Unpublished Technical Report. 1-10.

Rangin, C., 1991. The Philippine Mobile Belt: a complex plate boundary. J. Southeast Asian Earth Sci. 6, 209-220.

Raschka, H., Nacario, E., Rammlmair, D., Samonte, C., Steiner, L., 1985. Geology of the ophiolite of central Palawan Island, Philippines. Ofioliti (Italy). 10, 375-390.

Roeder, D., 1977. Philippine arc system-Collision or flipped subduction zones? Geology. 5, 203-206.

Rong, Y., Jackson, D.D., Kagan Y.Y. 2003. Seismic gaps and earthquakes. Jour. Geophys. Research. 108, 2471-2484.

Sarewitz, D.R., Karig, D.E., 1986. Stratigraphic framework of western Mindoro Island, Philippines. Journal of the Geological Society Philippines. 40, 3-51.

Wolfart, R., Cepek, P., Graman, F., Kemper, E., Porth, H., 1984. Stratigraphy of Palawan Island, Philippines. Federal Institute for Geosciences and Natural Resources, Hannover. 16, 19-48.

Yumul Jr, G. P., Dimalanta, C. B., Tamayo Jr, R. A., Maury, R. C., 2003. Collision, subduction and accretion events in the Philippines: a synthesis. Island Arc. 12, 77-91.

Yumul, G. P., Dimalanta, C. B., Tamayo, R. A., 2005. Indenter-tectonics in the Philippines: Example from the Palawan Microcontinental Block-Philippine Mobile Belt Collision. 55, 189-198.

Yumul, G. P., Dimalanta, C. B., Maglambayan, V. B., Marquez, E. J., 2008. Tectonic setting of a composite terrane: a review of the Philippine island arc system. Geosci. 12, 7.

Yumul, G.P., Dimalanta, C.B., Marquez, E.J., Queaño, K.L., 2009. Onland signatures of the Palawan microcontinental block and Philippine mobile belt collision and crustal growth process: A review. J. Asian Earth Sci. 34, 610-623.

Akita University

CHAPTER 3

Mineralogy and geochemistry of the Berong Ni-Co laterite deposit, Palawan, Philippines

Abstract

Intense weathering of the serpentinized peridotite resulted in the formation of the Berong Ni-Co laterite deposit in Palawan (Philippines). The studied laterite profiles are divided from base to top into: (i) serpentinized bedrock, (ii) saprolite horizon, and (iii) limonite horizon. Olivine in the peridotite contains a significant amount of Ni (average 0.38 wt% NiO), thus representing the main source of the ore in the laterite horizons. Six types of Ni-bearing serpentines (up to 6.65 wt% NiO) in the saprock are discriminated based on their textures and Raman signatures. Garnierite (a mixture of serpentine-, kerolite- and sepiolite-like clays) typically occurs as coatings or fracture fillings in the saprock and is characterized by strikingly high NiO content up to 34.86 wt%. Goethite and Mn-oxy-hydroxides (i.e. lithiophorite-asbolane intermediates) are the principal hosts of Ni in the limonite (up to 2.15 wt% NiO and 23.89 wt% NiO, respectively) with the latter also being the main Co carriers (up to 12.59 wt% CoO). The whole-rock XRF data show typical trends observed in other Ni laterite deposits, where Mg and Si are depleted toward the surface, and the transition metals (i.e. Fe, Al, Ni, Co, and Mn) are retained in the weathered horizons. The saprolite horizon is particularly enriched in Ni, while the lower section of the limonite horizon is enriched in Co. The mildly acidic environmental condition

Akita University

(pH ≤ 6.57) in the limonite horizon was found to enhance the mobilization and re-distribution of Ni from the limonite towards the lower section of the profiles. Geological observations, coupled with mineralogical and geochemical data, show that the Berong Ni-Co laterite deposit formed in two weathering processes: (i) development of the saprolite horizon and the limonite horizon, and (ii) the late precipitation of secondary phyllosilicates (i.e. garnierite), Mn-oxy-hydroxides and silica.

3.2 Introduction

Ni-Co laterite ores are derived from the strong chemical weathering of mafic or ultramafic rocks containing Ni-bearing olivine (Golightly, 1981; Freyssinet et al., 2005; Butt and Cluzel, 2013). Such a process eliminates the mobile constituents of the peridotite (Mg, Si), whereas the immobile components (Fe, Al, Cr, Ni, Mn, Cu, and Co) are retained and concentrated in the laterite (Eliopoulos et al., 2012). A typical laterite profile generally consists either of unaltered or serpentinized peridotites at the bottom, overlain by a saprolite horizon containing relicts of the parent rocks with secondary minerals such as serpentine, goethite, and hydrous Mg-Ni phyllosilicates (Freyssinet et al., 2005). In many deposits, the transition between the saprolite and the oxide-dominated zone of the laterite (hereafter “limonite”) is marked by a smectite-rich boundary (Butt and Cluzel, 2013 and references therein). In this context, the limonite horizon is developed at the top of the profile and consists of goethite, hematite, maghemite, gibbsite and Mn-oxy-hydroxides. The topmost section of the

Akita University

horizon is the iron-cap (i.e., ferricrete) and is commonly enriched with hematite and goethite (Samama, 1986; Freyssinet et al., 2005).

Based on the major Ni ore assemblage, Ni-laterite deposits are typically classified into the following three categories: i) oxide laterite deposits (also called “limonitic ores”) dominated by Fe-Mn-oxy-hydroxides, ii) clay silicate deposits that consist mainly of Ni-rich smectites, and iii) hydrous Mg silicate deposits that contain mostly garnierite-like mineralization (Brand et al., 1998; Freyssinet et al., 2005; Butt and Cluzel, 2013). Major Ni laterite deposits are widely distributed in humid tropics including New Caledonia, Indonesia, the Philippines, Brazil, Colombia, Cuba, Central Africa and the Dominican Republic. Despite this, Ni laterites are also found at higher latitudes (e.g. Australia, Greece, Urals, etc.), where the current climatic regime does not match with the optimal environmental conditions enhancing lateritization, and thus they represent fossil paleo-weathering profiles (Thorne et al., 2012; Herrington et al., 2016).

Previous works on the Ni laterite deposits have investigated the mineralogy and distribution of Ni along laterite profiles developed on ultramafic rocks or on their serpentinized counterparts (Brand et al., 1998; Gleeson et al., 2004; Yongue-Fouateu et al., 2006; Dzemua et al., 2011; Fu et al., 2014). Recent works have studied the speciation of Ni, Co, Mn, and Sc to explain the evolution and concentration of these elements through the laterite profiles (Dublet et al., 2012; Fan and Gerson, 2015; Chasse et al., 2017; Ratié et al., 2018). However, little detailed mineralogical analysis has

Akita University

been conducted to characterize the paragenetic sequence of serpentine veins, particularly in the saprolite horizon (Cluzel and Vigier, 2008; Villanova-de-Benavent et al., 2014, 2016; Tauler et al., 2017). Recent work by Muňoz et al. (2019) investigated the relationship between the weathering reactions occurring at the weathering front and the enrichment of Ni in the saprock, demonstrating the correlation between the strong pH gradient, and the concentration of Ni in serpentine minerals.

In this study, we explore the nature and paragenetic sequence of the different types of serpentine veins identified in the harzburgite bedrock and saprock of the three Ni-Co laterite profiles found in the Berong deposit in Palawan, Philippines. The investigation aims to explain the behavior and local enrichment of Ni in serpentine. This study also aims to investigate the occurrence of garnierite and Mn-oxyhydroxides in the Berong deposit. The textures and chemical composition of the garnierite from the saprolite horizon, and lithiophorite-asbolane intermediate from the limonite horizon are provided. Finally, the combined data from field observations, mineralogy, and geochemistry are presented in order to gain a better understanding of the lateritization process and to build a dynamic model for the metallogenesis of the Berong deposit.

Akita University

3.3 Geological setting

3.3.1 Regional geology

The Palawan Island, situated on the western flank of the Philippine archipelago (Fig. 11a), is divided into a northern block and a southern block. The northern block, a part of the continental fragment of Asia, was separated by the rifting of the South China Sea and collided to the western edge of the Philippine Mobile Belt (PMB) in the Miocene (Holloway, 1981). Subsequently, the drifted fragment formed the continental North Palawan Block (NPB) (Taylor and Hayes, 1983). The collision-related signatures between NPB and PMB are preserved in the islands of Mindoro, Romblon, and Panay and result in the exposure of the ophiolitic sequences in these islands (Yumul et al., 2009).

The southern block mainly consists of ophiolitic rocks with Cenozoic clastic sedimentary rocks (Fig. 11b) (Mitchell, 1985). The Cretaceous to Eocene Palawan Ophiolite Complex consists of ultramafic rocks (Beaufort Ultramafic Complex), gabbro (Stavely Gabbro), pillow basalts, chert and red mudstone (Espina Formation) (Raschka et al., 1985; Encarnation et al., 1995). The ultramafic rocks of the Beaufort Ultramafic Complex consist of both unaltered and serpentinized peridotite and pyroxenite. The complex is composed of harzburgite with cumulate dunite (United Nations Development Programme, 1985). Dunite occurs as dikes or stocks and intrudes the harzburgite, while the pyroxenite is commonly found in

Akita University

stratiform layers (Aurelio and Peña, 2004). The Dalrympole Amphibolite is the basement of the ophiolite suite, consisting of greenschist, amphibolite, quartz-mica schist, and quartzose schist. Stavely Gabbro overlies the Beaufort Ultramafic Complex and consists of olivine gabbro and troctolite, which are composed of coarse-grained plagioclase and pyroxene with a minor amount of hornblende (United Nations Development Programme, 1985). The spilitic basalt with intercalated chert and sandstone constitutes the Espina Formation, which is the sedimentary cover of the mafic and ultramafic rocks. Brown to gray fossiliferous limestone is associated with the ophiolitic sequence (Wolfart et al., 1986). The Paleocene and Neogene clastic sedimentary rocks overlie these ophiolitic rocks (Almasco et al., 2000).

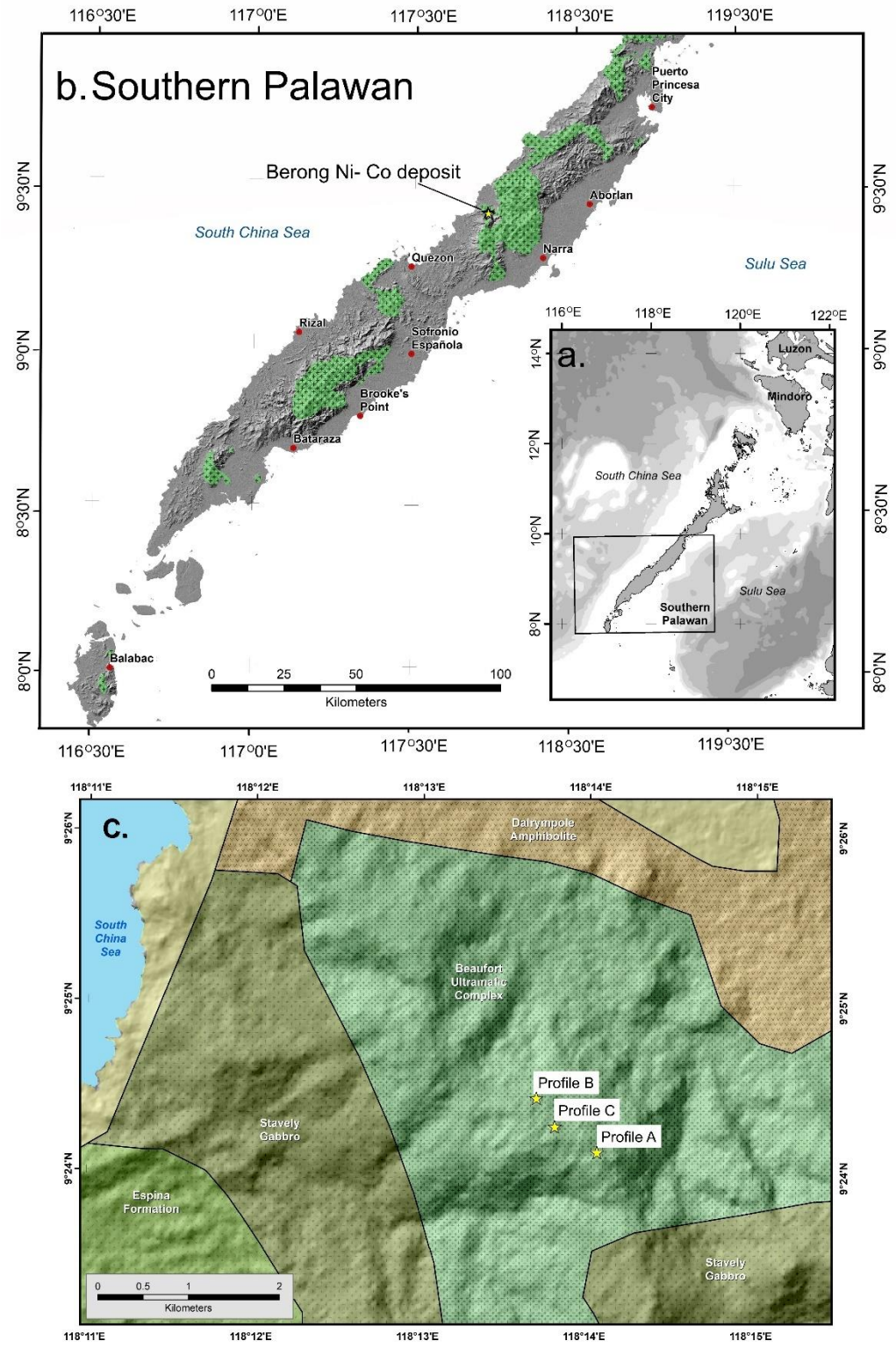

Fig. 11 a) Geologic map of the southern section of Palawan showing the b-c) location of the studied profiles within the 2,880,000 square meter portion of the Berong Nickel Corporation mine.

Akita University

3.3.2 Berong Ni-Co laterite deposit

The study area is in the southern block, particularly in Barangay Berong, Quezon, Palawan, Philippines. As shown in Figure 11c, three Ni laterite outcrops were investigated in the Berong deposit, which lie within the Beaufort Ultramafic Complex (Fig. 11c). The Berong Ni laterite project is operated by the Berong Nickel Corporation (BNC) with a Mineral Production Sharing Agreement (MPSA) no. 235-2007-IVB. The Berong deposit occupies a 2,880,000 m^2 area. In 2019, the mine production is 2,665,000 dry metric tonne with a material grade of 1.74% Ni.

The characteristic topography of the mining area spans from flatlands to high rolling mountains. The flatlands encompass the coastal areas, whereas small sandstone hills with gentle slope constitute a minor geomorphic feature. In those areas untouched by erosive processes, thick and diverse vegetation exists. The surface run-offs drift into dendritic and rectangular drainage systems.

The laterite profiles A, B and C occur in a limited area and have an elevation ranging from 524 to 642 m above sea level. These profiles are subdivided from bottom to top into: (i) the serpentinized peridotite bedrock, (ii) the saprolite horizon and (iii) the limonite horizon (Fig. 12a). The BNC project classifies each horizon based solely on the concentration of iron (Fe). The saprolite contains 10-30 wt% Fe, while the limonite consists of more than 30 wt% Fe. However, in this study, other characteristics such as

Akita University

rock texture, mineralogy and Ni concentration of the laterite samples were used to amend the classification of each horizon.

The only relatively fresh harzburgite bedrock was acquired from profile A (Fig. 12a), which is serpentinized and typically intensely fractured. The overlying saprolite and limonite horizons are characterized by lateral facies variations with an average depth of 14 m.

The thickness of the saprolite horizon ranges from two meters to five meters. It contains a mixture of saprock boulders (hard saprolite) up to 2 - 256 mm in diameter and earthy materials (soft saprolite) (Fig. 12b). Greenish and bluish garnierite commonly occurs as coatings on the surface of the saprock boulders with white patches of deweylite (Fig. 12c). A gradational change from weathered blocky rocks to fine-grained and reddish earthy materials is evident in the transition boundary between the saprolite and limonite (Fig. 12d). In profile C, garnierite occurs as fillings in the fractures (Fig. 12e). Millimeter- to centimeter-thick serpentine veins are visible in the saprock (Fig. 12e).

A three to 15 m thick limonite horizon is developed over the saprolite horizon. The limonite horizon is reddish-brown, loose, and friable Lateral and discontinuous exposures of millimeter- to centimeter-thick Mn-oxy-hydroxides coatings occur within the limonite (Fig. 12f). At a closer inspection, secondary silica is present in the upper section of the limonite horizon (Fig. 12g).

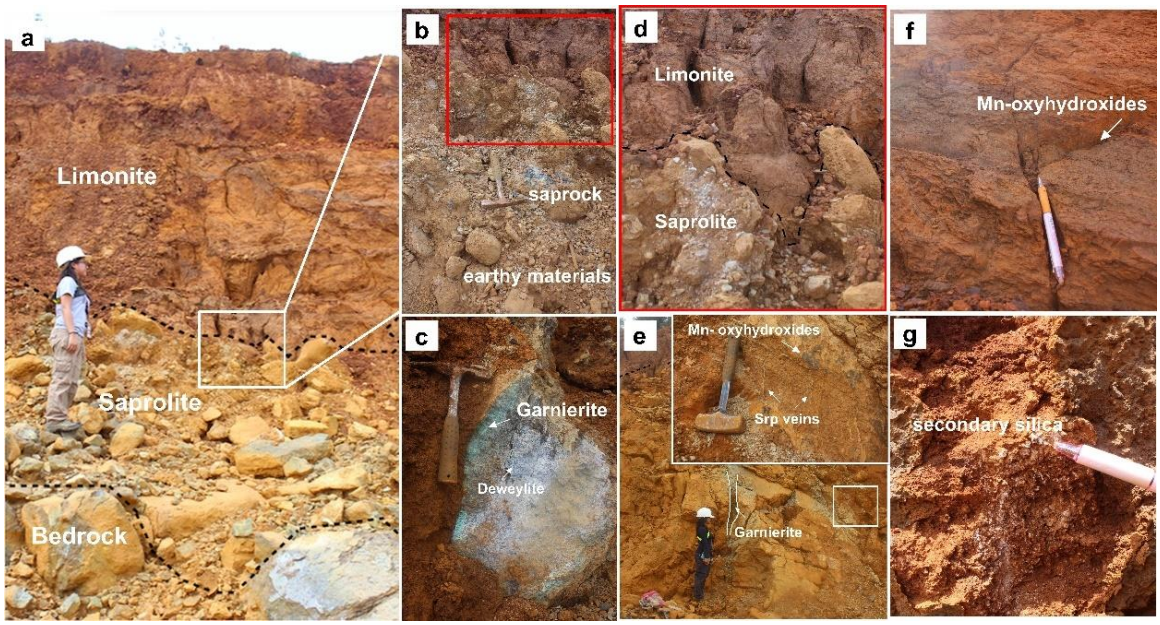

Fig. 12 a) Photos of the bedrock, saprolite and limonite horizons in profile A. b) The saprolite horizon consists mainly of saprock (hard saprolite) and earthy materials (soft saprolite). c) Bluish-green garnierite with deweylite cemented on the moderately weathered rock in the saprolite horizon. d) Closer image of the transition boundary between the saprolite and limonite horizons. e) In profile C, dark Mn-oxyhydroxides occur as coatings on the weathered saprock with millimeter thick serpentine (Srp) veins. f) Occurrence of discontinuous Mn-oxyhydroxides and g) secondary silica in the limonite horizon.

3.4 Material and Methods

3.4.1 Sampling

Forty-five samples were collected from the three different horizons of the laterite profiles. Approximately one kilogram of limonite and saprolite samples were sampled at an interval of one meter. In addition, garnierite and Mn-oxy-hydroxides samples were collected from the weathered horizons.

Akita University

3.4.2 Analytical techniques

All samples were air-dried at 20 ˚C to 30 ˚C for one to two weeks, quartered and powdered using mortar and pestle. Thirty air-dried samples were prepared for pH measurement. Twenty grams of each sample was weighed and was transferred in a 50 ml container. Then they were mixed with 20 ml of distilled water, and the contents were stirred every 10 minutes for over 30 minutes. The pH meter was calibrated using pH 4, 7, 10 standard solutions at 20˚C to 25˚C. The tip of the pH meter was dipped below the surface of the solution and was stirred gently for a few seconds until it was fully suspended. The pH reading was measured to the nearest 0.01 pH unit. The calibration was repeated after every ten samples. The electrode was rinsed with tap water and eventually with distilled water.

Bedrock, saprolite, and limonite samples were impregnated with petropoxy resin. A total of 24 polished thin sections were analyzed using transmitted and reflected light microscope. A detailed description was made on twelve thin sections. In addition, eleven polished sections containing Mn-oxy-hydroxides were prepared and examined under a reflected light microscope.

The mineralogical composition of the sample powders was analyzed by X-ray Powder Powder Diffraction (XRPD) Rigaku MultiFlex with a Cu Kα radiation source operating at 30 kV and 10mA. The XRPD patterns were scanned from 2˚ to 60˚ 2θ angle using copper (Cu) detector with a step size of 0.02, and scan speed maintained at 20˚ per minute. Mineralogy was

Akita University

determined using the COD reference database of MATCH! software. Both optical microscopy and XRPD analyses were carried out at Akita University, Japan.

Raman characterization was made on polished thin sections. The Raman spectra was obtained using an inVia Renishaw Raman microscope equipped with a 100mW 532 nm frequency-doubled Nd: YAG laser. The laser beam was attenuated to 10% power and focused using a 50x objective lens. A Si-based CCD detector was utilized for data collection. A 1800 lines/mm grating was used to dispersed the signal onto the CCD detector. Also, the spectrometer was calibrated using the Si-Au standard before analysis. The background fluorescence and noise were removed using the WiRE^{TM} software. Raman spectroscopy was utilized for accurate identification of the most common serpentine polymorph such as lizardite, chrysotile, and antigorite in the bedrock. This technique was also used to differentiate the various serpentine veins crosscutting the relict phases in the saprock. Spectra from low wavenumbers (100-500 cm^{-1}) and high wavenumbers (3000-4000 cm^{-1}) were collected for mineral identification. Spectral components of the low- and high-frequency domains were compared to rruff.info database and previous works by Auzende et al. (2004), Petriglieri et al. (2015), Muñoz et al. (2019), and Ulrich et al. (2019) (Appendix A).

Chemical compositions of the ore minerals were determined on a JEOL JXA-8530F Field Emission Electron Probe Microanalyzer (FE-EPMA) with

Akita University

operating conditions of 20kV voltage, 20nA probe current and spot size to 5µm beam diameter. Calibration was performed using JEOL reference standards: MgO (Mg, TAPH, Kα), SiO_2 (Si, TAP, Kα), Al_2O_3 (Al, TAPH, Kα), Fe_2O_3 (Fe, LIFH, Kα), MnO (Mn, LIFH, Kα), $CaSiO_3$ (Ca, PETH, Kα), NiO (Ni, LIFH, Kα), CoO (Co, LIFH, Kα), and Cr_2O_3 (Cr, LIFH, Kα). Raw counts were corrected using the ZAF procedure. Backscattered electron images and X-ray elemental maps were acquired at the facility of GSJ, AIST. The structural formula of olivine was calculated based on four oxygens, seven oxygens for serpentine and six oxygens both for pyroxene and brucite. Eleven oxygens were used for talc-like garnierites, 32 oxygens for sepiolite-falcondoite solid solution series, and two oxygens for Co-bearing Mn-oxy-hydroxides (lithiophorite and asbolane).

Thirty-six representative samples were powdered before whole-rock geochemical and loss on ignition (LOI) analyses. These samples were dried at 105°C in an oven for at least 30 minutes. A portion of 0.5 g of each sample was mixed with di-lithium tetraborate ($Li_2B_4O_7$, Spectromelt). The sample mixture was fused at 1250°C in a Pt crucible using a high-frequency fusion instrument (HERZOG HAG-M-HF) and cooled on a Pt disk. Major elements in the glasses were analyzed by XRF Spectrometry (Rigaku ZSX Primus III+) at a voltage of 50 kV and a current of 50 mA. Calibration curves for SiO_2, Al_2O_3, P_2O_5, TiO_2, Cr_2O_3, MnO, Fe_2O_3, Co_2O_3, and NiO were made using reference samples of OREAS. Calibration curves for the other major components including Na_2O, MgO, K_2O, and CaO, were made using the

Akita University

GSJ geochemical reference samples of igneous rock series (Imai et al., 1995; 1999). To evaluate the accuracy of the results, five international reference materials were used such as JP-1 (peridotite), JB-1b (basalt), JG-3 (granodiorite), OREAS 180 (Ni laterite ore), OREAS 184 (Ni laterite ore) and OREAS 401 (Fe ore). Furthermore, LOI determines the mass loss after strongly heating the sample. It represents the organic matter, carbon dioxide from carbonates, and structural water in minerals. The term "structural water" includes both the bonded H_2O molecules and OH units within the structure of the minerals (Klein and Dultrow, 2007).The Wavelength Dispersive X-ray Fluorescence (WDXRF) analysis and LOI determination were conducted at Geological Survey of Japan (GSJ), National Institute of Advanced Industrial Science and Technology (AIST) in Tsukuba, Japan.

3.5 Results

3.5.1 XRPD

Results of the XRPD analyses show that the harzburgite bedrock consists of olivine (forsterite), orthopyroxene (enstatite), and serpentine (Figs. 13a). Serpentine is identified based on its characteristic peaks at 7.25 Å, 3.64 Å, and 2.50 Å. It is also the dominant mineral in the saprolite horizon of profile A (Figs. 13a). Goethite is the main mineral, particularly in the lower and uppermost sections of the limonite horizon. While gibbsite typically occurs in the middle section of this horizon with minor to trace amounts of hematite, chromite, magnetite, magnesite and quartz (Figs. 13a).

Akita University

Garnierite samples mostly contain serpentine-like and talc-like phases with a minor amount of quartz. The XRPD pattern of pale green garnierite shows broad peaks at 7.31 Å and 9.93 Å, indicating the occurrence of both serpentine-like and talc-like phases (Fig. 13b). XRPD data of blue-green garnierite shows a broader peak at 9.78 Å, and the strong reflection at 12.4 Å suggests the occurrence of sepiolite (Fig. 13c).

The results of XRD analysis further confirm the occurrence of asbolane and lithiophorite. Lithiophorite is identified based on its reflections at 9.52 Å and 4.73 Å (Fig. 13d), while the broad peaks at 9.45 Å and 4.82 Å correspond to asbolane (Fig. 13e). The decoupling of peaks at 4.81 Å and 4.73 Å may indicate the presence of both lithiophorite and asbolane, but their identification only via XRPD can be misleading (Putzolu et al., 2018).

3.5.2 Mineral descriptions

3.5.2.1 Bedrock

Observation in thin section reveals that the harzburgite bedrock consists mainly of olivine (>20%), pyroxene (<10%) and serpentine (>70%) (Fig. 14a). Chromite is dark-red, euhedral- to subhedral-shaped and occurs as clusters surrounding serpentine (Fig. 14a).

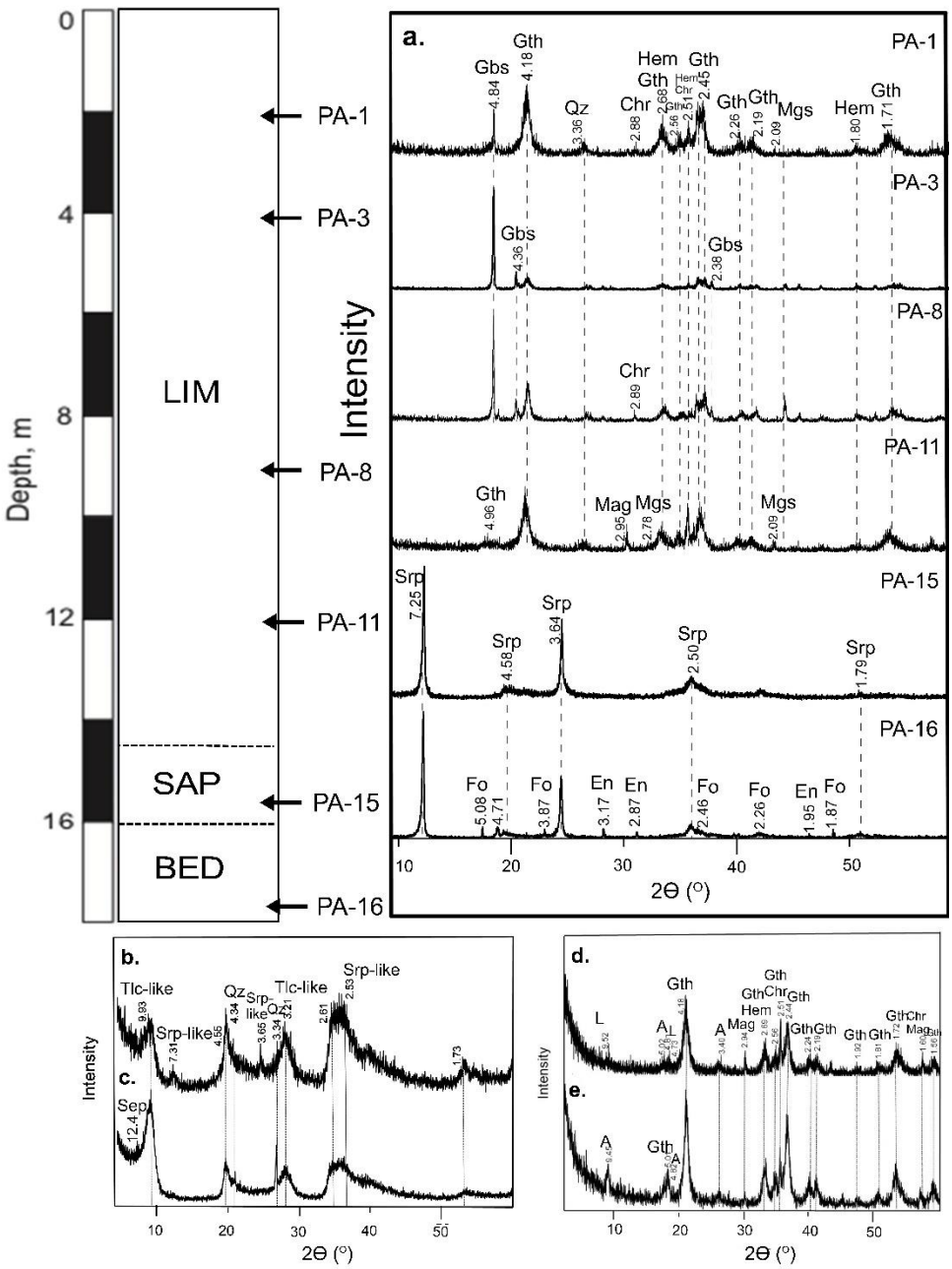

Fig. 13 XRPD patterns showing the mineralogy of a) the harzburgite bedrock (BED), saprolite (SAP) and limonite (LIM) samples from profile A, b) pale green garnierite and c) bluish-green garnierite, Mn-oxyhydroxides minerals (asbolane, lithiophorite) with goethite, hematite, magnetite and chromite obtained d) at 15m depth of laterite profile A and e) at 3 m depth of laterite profile C. *forsterite (Fo), enstatite (En), serpentine (Srp), goethite (Gth), magnetite (Mag), magnesite (Mgs), chromite (Chr), gibbsite (Gbs), hematite (Hem), quartz (Qz), talc-like (Talc-like), serpentine-like (Srp-like), sepiolite (Sep), asbolane (A), lithiophorite (L)*

Akita University

Three types of serpentine veins were identified in harzburgite bedrock based on their textures. Type I serpentine veins are irregular-shaped and are pseudomorph on the former primary olivine and pyroxene (Fig. 14b). The type II veins, on the other hand, cut through the type I veins and have magnetite- rich core (Fig. 14b). Brucite is observed to be associated with magnetite and serpentine by EPMA but was not detected on a diffractogram. Type III veins are hundreds of micrometers to millimeters wide and exhibit mesh texture (Fig. 14c). Although the cross-cutting relationship of the type III veins with the previous veins is ambiguous, the interlocking texture suggests that the type III veins formed after the narrower type I and type II veins.

3.5.2.2 *Saprolite horizon*

There are six types of serpentine veins in the saprock samples (Fig. 14d) and are classified based on their textural features. The type I veins mimic the relict primary minerals and have an interstitial amount of goethite at its rim (Fig. 14e). The type II veins are filled with a yellowish-orange colored mineral, most probably Fe-oxyhydroxides, whereas its core is seamed with fine-grained magnetite (Fig. 14e). Type I to type II veins were observed in all the studied laterite profiles (Table 1). The type III veins, on the other hand, have characteristic ribbon texture under cross-polarized light (Fig. 14f).

The type IV to type VI veins were only observed in profile A (Table 1). Type IV veins have distinct high birefringence and appear coarser than the

Akita University

previous veins (Fig. 14f). These are cut by type V veins, which are characterized by yellowish-white discontinuous veins (Fig. 14f) and are generally thin (< 10 micrometers). The banded veins, classified as type VI veins, contain multiple narrow bands, ranging from 10- 60 micrometers, which are parallel to the vein and occur near the voids (Fig. 14f). The thinner bands (< 20 um) in type VI veins may indicate multiple periods of crack-opening which eventually resulted in the authigenic formation of these veins.

Garnierite generally occurs as coatings and veins filling of the fractures of early- formed minerals in the saprolite. The collected samples have variable colors ranging from bluish-green to pale green and often occur as a mixture. The bluish-green garnierite shows banded and botryoidal

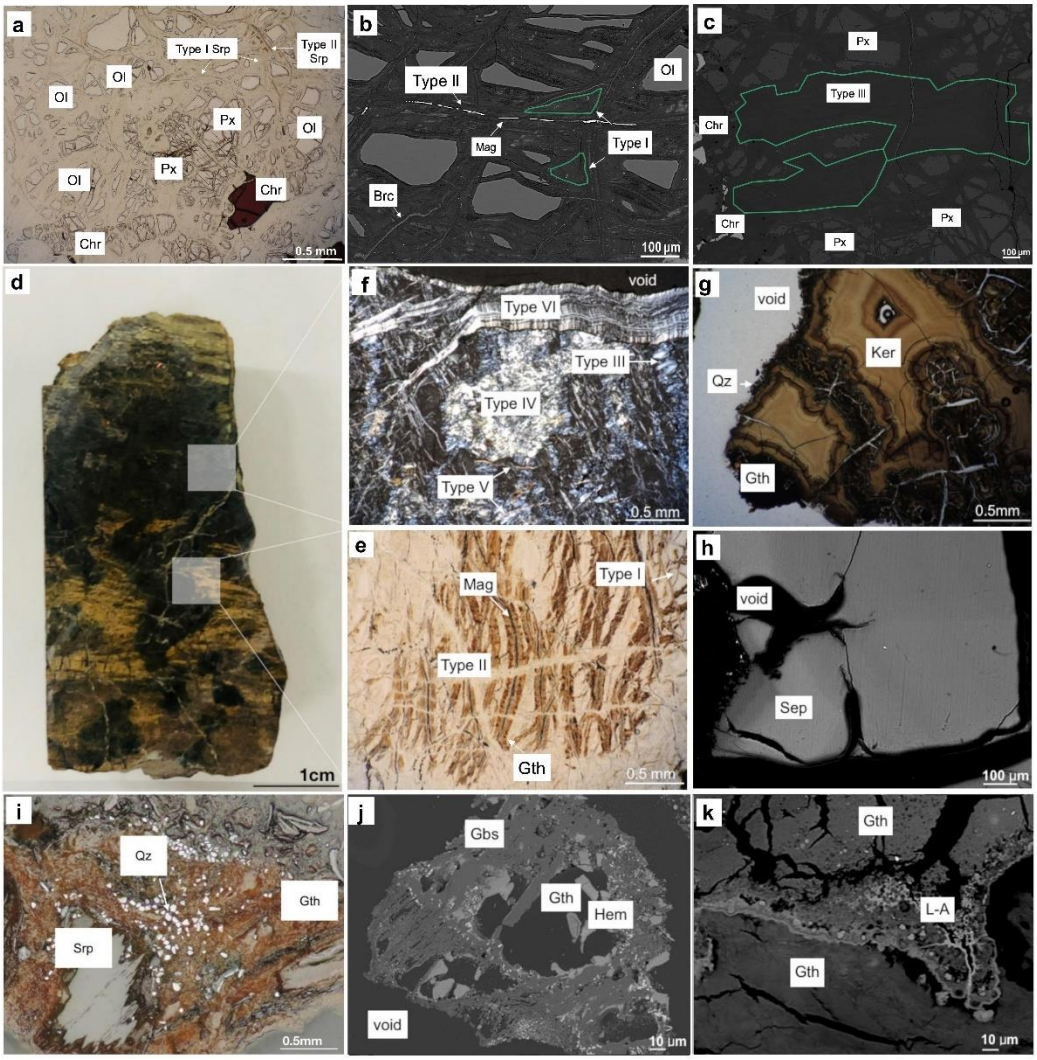

Fig. 14 Optical (a, e, g, i: plane-polarized light; f crossed polarized light), backscattered electron images (b, c, h, j, k) and d specimen photograph of moderately weathered rock in the saprolite. a- c) Type I, type II and type III serpentine (Srp) veins cutting olivine (Ol), pyroxene (Px) with chromite (Chr), fine-grained magnetite (Mag) and brucite (Brc); d-f) Type I to type VI serpentine veins formed in the saprock; g) botryoidal feature of talc-like (kerolite (Ker)) surrounded by quartz and goethite (Gth) h) fibrous characteristic of sepiolite (Sep); i) replacement of serpentine by goethite with disseminated quartz grain; j) gibbsite (Gbs) enveloping the porous goethite, which is intimately mixed with hematite (Hem) k) oscillation lamina of lithiophorite-asbolane (L-A) intermediate cemented by goethite.

Table 1 Summary of the different types of serpentine veins identified in the saprock of profile A (PA), profile B (PB), and profile C (PC).

Type	Samples	Description	Raman	NiO, wt%
Type I	PA-15, PB-10, PC-8	10 mm-wide, mesh-texture, disseminated fine-grained magnetite	low frequency domain: strong peaks at 232 cm^{-1}, 389 cm^{-1}, 690 cm^{-1}, minor peak at 655 cm-1, broad peak at 834 cm^{-1} ; high frequency domain: 3683 cm^{-1}	0.53 - 5.53 (0.01- 0.07 mol)
Type II- rim	PA-15, PB-10, PC-7	mm to cm-wide, mesh texture, yellowish-orange	low frequency domain: strong peaks at 228 cm^{-1}, 383 cm^{-1}, 686 cm^{-1}, broad peak at 823 cm-1 ; high frequency domain: 3678 cm^{-1}	0.95 - 6.65 (0.04- 0.11 mol)
Type II- core	PA-15, PB-10, PC-7	magnetite-rich core	low frequency domain: strong peaks at 228 cm^{-1}, 383 cm^{-1}, 686 cm^{-1}, broad peak at 832 cm-1 ; high frequency domain: 3678 cm^{-1}	0.58- 3.43 (0.01- 0.05 mol)
Type III	PA-15, PC-7	micrometer to mm-wide, ribbon texture, fewer amount of magnetite	low frequency domain: strong peaks at 234 cm^{-1}, 379 cm^{-1}, 688 cm^{-1}, broad peak at 832 cm-1 ; high frequency domain: 3696 cm-1	0.21- 1.06 (0.003- 0.014 mol)
Type IV	PA-15	massive texture, high birefringence	low frequency domain: strong peaks at 236 cm^{-1}, 389 cm^{-1}, 690 cm^{-1}, broad peak at 832 cm-1 ; high frequency domain: 3695 cm^{-1}	0.54- 0.81 (0.007 - 0.011 mol)
Type V	PA-15	<10 µm-wide, yellowish-white veins, appear disconnected	low frequency domain: strong peaks at 232 cm^{-1}, 389 cm^{-1}, 691 cm^{-1}, broad peak at 830 cm-1 ; high frequency domain: 3695 cm^{-1}	1.23- 1.81 (0.016- 0.024 mol)
Type VI	PA-15	contain several narrow bands (10- 60 micrometers) parallel to the vein	low frequency domain: strong peaks at 232 cm^{-1}, 389 cm^{-1}, 640 cm^{-1}, 686 cm^{-1}, broad peak at 830 cm-1 ; high frequency domain: 3695 cm^{-1}	0.55- 0.84 (0.007- 0.011 mol)

Akita University

features. Its boundary is typically cemented by quartz aggregates (Fig. 14g). The pale green garnierite is superimposed with Mn-oxyhydroxides and appears flaky. The backscattered electron image of this specimen reveals the existence of sepiolite marked by its fibrous texture (Fig. 14h).

3.5.2.3 Limonite horizon

Goethite shows fibrous to massive textures (Fig. 14i), while quartz is widely distributed and fills the voids of massive goethite (Fig. 14i). Tabular gibbsite grains are closely associated with goethite and hematite (Fig. 14j). The Mn-oxy-hydroxides minerals found in this horizon are mainly lithiophorite-asbolane intermediate (Fig. 14k). These are generally fine-grained and occur in a wide range of textures. Manganese-oxyhydroxides often occur as an oolitic form surrounded by goethite (Fig. 15a). These also appear as bands in a matrix of serpentine and goethite (Fig. 15b). In some specimens, the phases are either massive filling in the voids (Fig. 15c) or as fine aggregates superimposed on goethite (Fig. 15d).

3.5.3 Raman characterization

The Raman spectra of the different serpentine veins in the bedrock and saprolite horizon are shown in Figures 16 and 17. The Raman spectrum of type I veins is characterized by intense peaks at 230 cm^{-1}, 383 $cm^{-1,}$ and 690 cm^{-1} and weak peak at 627 cm^{-1} (Fig. 16).The spectra of type II- rim and type II- core veins are slightly shifted, but generally have a similar set of peaks. Only the sharp peaks were observed on type III serpentine veins. In

Akita University

the high-frequency domain, the Raman spectra of type I and type III veins generally reveal strong peaks at 3683 cm^{-1} and 3681 cm^{-1}, while the type II-rim and type II- core veins have minor Raman shifts at 3685 cm^{-1} and 3684 cm^{-1}. Nonetheless, the shape and Raman bands of type I, type II and type III veins correspond to lizardite.

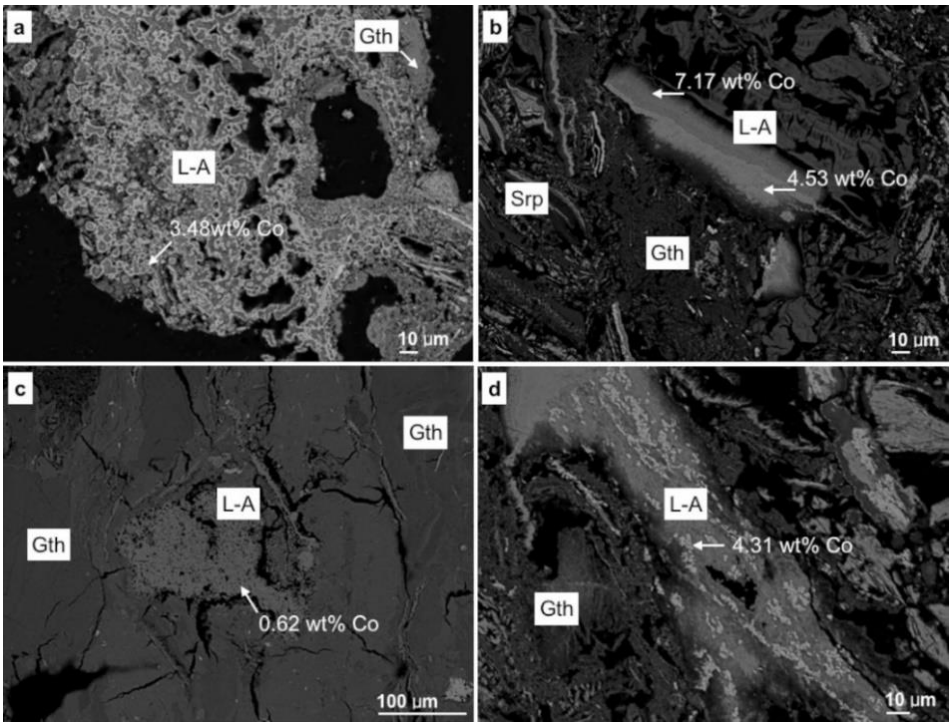

Fig. 15 Backscattered electron images of variable textural features of lithiophorite-asbolane intermediate with corresponding Co concentrations. Mn oxyhydroxides phases exhibiting an a) oolitic, b) banded or zoned, c) massive, and d) fibrous to dendritic forms.

For the six types of serpentine veins in the saprock, the Raman spectra in the low-frequency domain are generally characterized by strong peaks located at 232 cm^{-1}, 389 cm^{-1}, and 690 cm^{-1} with a broad peak at 832 cm^{-1} (Fig. 17). The additional broad band may belong to the poorly crystalline relict olivine. The type I and type II veins have similar strong peaks at 3683

cm^{-1} and 3678 cm^{-1} in the high-frequency domain, which resembles closely to lizardite. However, the type III, type IV, type V and type VI veins are characterized by different strong Raman bands at 3695 cm^{-1}, which corresponds to chrysotile.

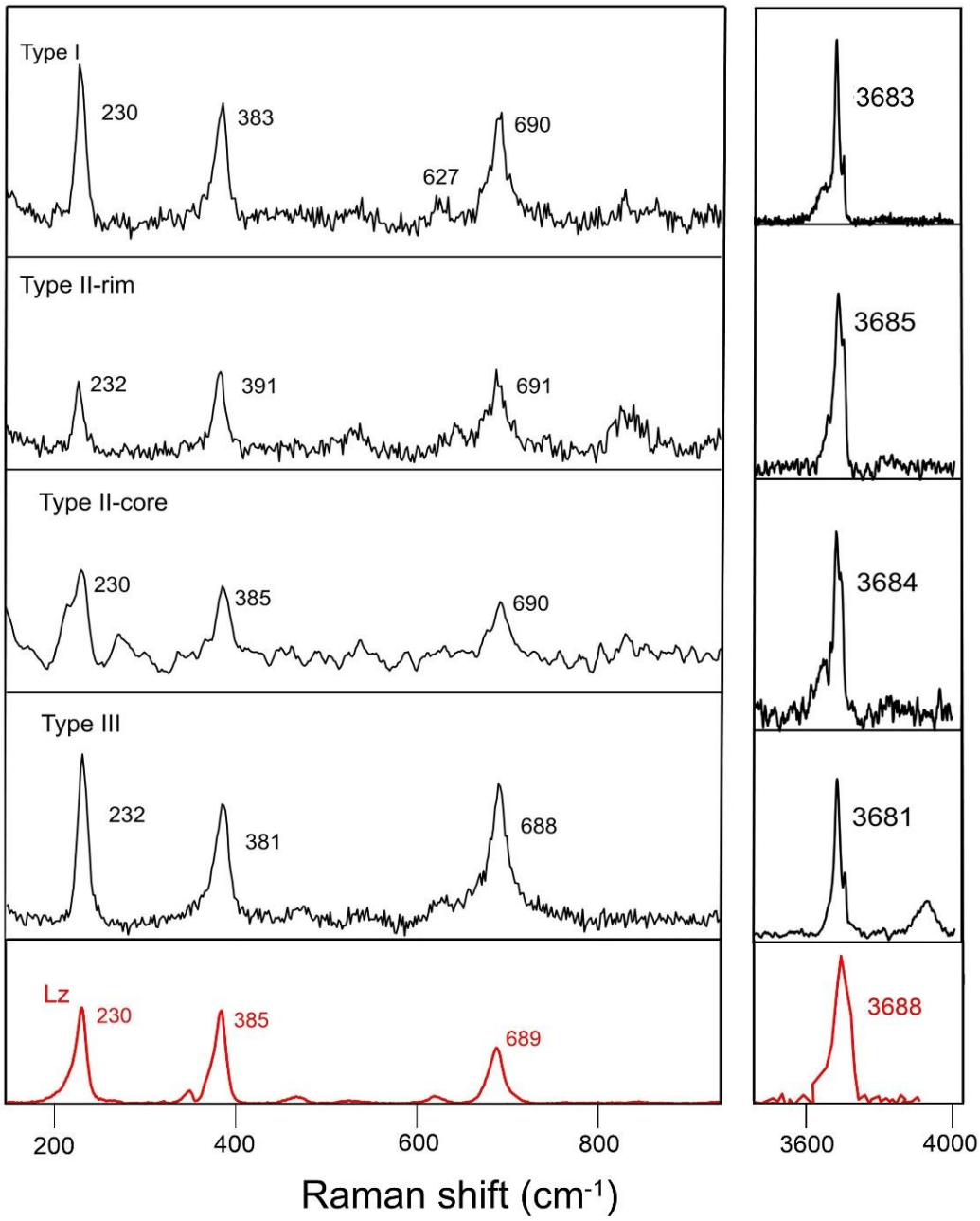

Fig. 16 Raman signatures of three types of serpentine veins identified in the bedrock. Raman data of lizardite (Lz) from rruff.info database.

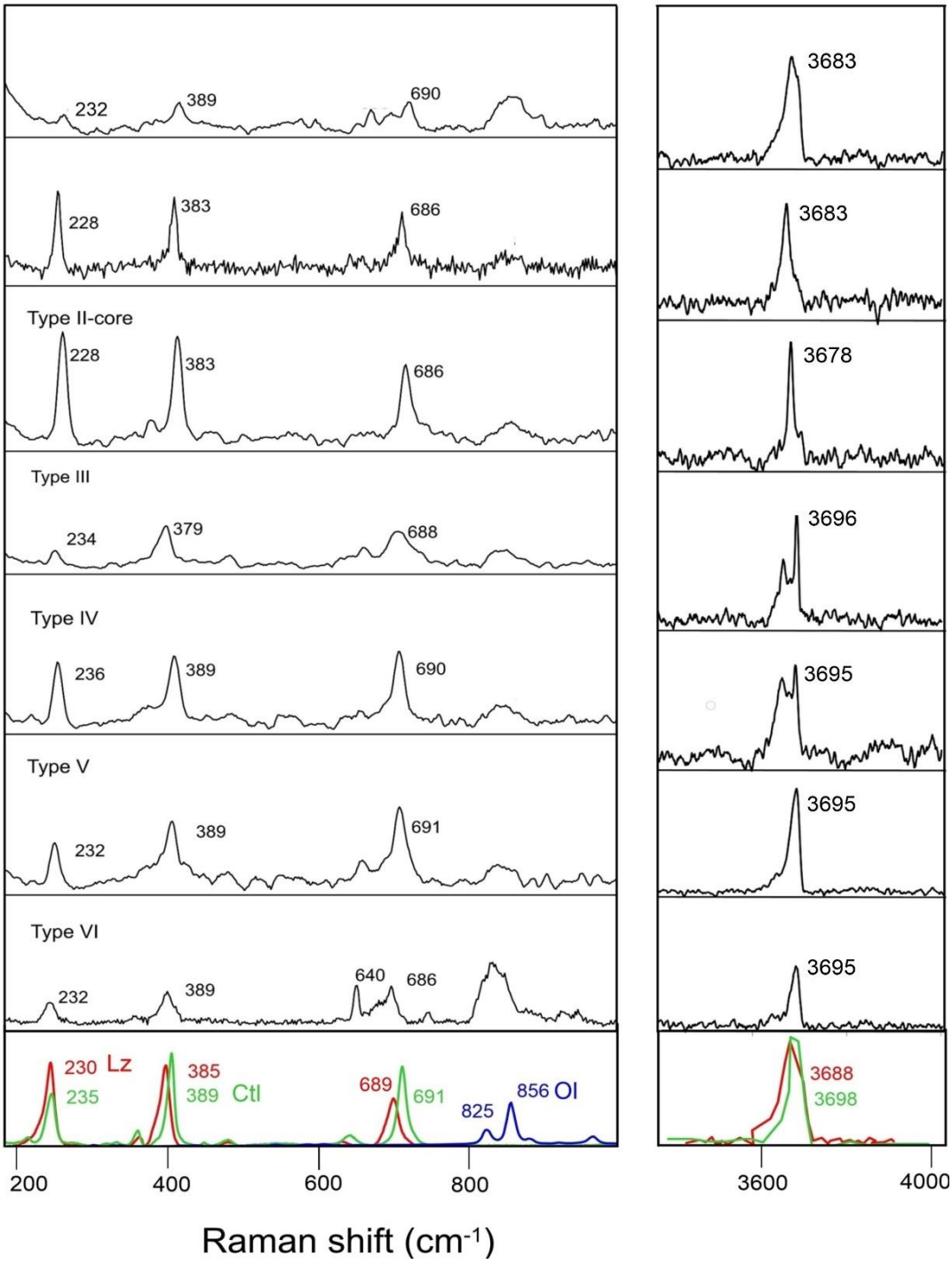

Fig. 17 Raman signatures of six types of serpentine veins identified in the saprocks. Raman data of lizardite (Lz), chrysotile (Ctl) and olivine (Ol) from rruff.info database.

Akita University

3.5.4 Mineral Chemistry

This section presents the chemical composition of the primary minerals in the bedrock and ore minerals in the weathered horizons.

3.5.4.1 *Primary and secondary minerals in the bedrock*

The average chemical composition of olivine, orthopyroxene, brucite and three types of serpentine veins in harzburgite is summarized in Table 2. Olivine contains significant amount of FeO (avg. 8.12 wt%, 0.168 apfu Fe) and NiO (avg. 0.38 wt%, 0.007 apfu Ni). Orthopyroxene, on the other hand, is enriched in FeO (avg. 5.28 wt%, 0.076 apfu Fe), Al_2O_3 (avg. 1.37 wt%, 0.028 apfu Al), CaO (avg. 1.12 wt%, 0.008 apfu Ca), and Cr_2O_3 (avg. 0.58 wt%, 0.021 apfu Cr). However, the concentration of CoO in olivine and orthopyroxene is low (0.02 wt% - 0.06 wt%). Since brucite is intimately mixed with serpentine, this may cause the increased SiO_2 content of brucite that ranges from 5- 8 wt%. The silica contents in brucite signifies a mixture of serpentine, which was interlayered at a fine scale (Frost et al., 2013). In addition, brucite has trace amounts of NiO (avg. 0.47 wt%, 0.021 apfu Ni) (Table 2).

The type I, type II (rim and core), and type III serpentines identified in the bedrock have variable NiO concentrations ranging from 0.05- 0.59 wt% (Fig. 18a). The mesh-textured type I and type II serpentines contain a relatively higher amount of NiO (avg. 0.30 wt%, 0.013 apfu Ni, and 0.27 wt%, 0.011 apfu Ni). However, the interlocking-textured type III serpentine contains a

Akita University

lower amount of NiO (avg. 0.08 wt%, 0.003 apfu Ni). Also, the MgO concentration of type III serpentine (avg. 31.33 wt%, 2.447 apfu) is relatively lower than type I (avg. 35.86 wt%, 2.789 apfu), type II- rim (avg. 36.02 wt%, 2.752 apfu) and type II- core (avg. 35.82 wt%, 2.840 apfu) serpentines (Fig. 18a). It is also worth noting that the core of type II serpentine has relatively higher FeO content (avg. 7.36 wt%, 0.329 apfu Fe) compared to its rim (avg. 5.65 wt% FeO, 0.243 apfu Fe). The CoO concentration of type I, type II and type III serpentines are low and ranges from 0.02-0.07 wt%.

3.5.4.2 *Ore minerals in the saprolite horizon*

3.5.4.2.1 Ni- bearing serpentine

Table 3 shows a summary of the average chemical composition of serpentine from the saprolite horizon. In all the studied profiles, the Ni concentration of type I (up to 5.33 wt%, 0.226 apfu Ni), type II- rim (up to 6.65 wt%, 0.288 apfu Ni), type II- core (up to 3.43 wt%, 0.152 apfu Ni) serpentines are relatively high (Fig. 18b, 19a, 19b) compared to those in the bedrock. Relatively lower Ni marks type III serpentine (up to 1.06 wt%, 0.042 apfu Ni) and Fe contents (up to 4.61 wt%, 0.188 apfu Fe) (Fig. 18b, 19a, 19b). The MgO concentration of type I, type II- rim, type II- core and type III serpentines is highly variable, ranging from 23.85 wt% to 35.84 wt%.

As mentioned in the previous section, all the six types of serpentine were only observed in profile A. Type IV serpentine contains a high amount of Al_2O_3 (up to 0.72 wt%, 0.041 apfu Al). The NiO and FeO concentrations

Akita University

increase from type IV (up to 0.81 wt%, 0.032 apfu Ni; 5.44 wt%, 0.228 apfu Fe), type V (up to 1.81 wt%, 0.080 Ni; 8.79 wt%, 0.387 apfu Fe) and to some extent, type VI serpentines (up to 0.84 wt%, 0.038 Ni; 7.69 wt%, 0.358 apfu Fe) (Fig. 18b). Furthermore, the MgO contents of type IV (up to 33.25 wt%, 2.411 apfu Mg), type V (up to 32.13 wt%, 2.533 apfu Mg) and type VI serpentines (up to 27.30 wt%, 2.210 apfu) are low. In profile A, the Mn content increases from type II- core (up to 0.046 wt%, 0.002 apfu Mn) to type VI serpentine (up to 0.085 wt%, 0.004 apfu Mn).

Table 2 Average chemical compositions and structural formula (apfu) of olivine, orthopyroxene, brucite, and serpentine in the peridotite bedrock (wt%) of profile A.

	Olivine		Orthopyroxene		Brucite		Serpentine							
		σ		σ		σ	Type I	σ	Type II- rim	σ	Type II-core	σ	Type III	σ
n	13		17		5		13		17		8		9	
SiO_2	40.71	0.31	57.21	0.56	7.40	1.14	37.26	3.10	38.84	1.27	35.81	2.62	39.37	1.70
MgO	49.26	0.37	34.06	0.43	49.51	1.19	35.86	1.07	36.02	1.06	35.82	0.84	31.33	1.40
FeO	8.12	0.11	5.28	0.08	22.24	2.25	6.98	1.90	5.65	0.88	7.36	2.46	7.13	0.88
NiO	0.38	0.03	0.08	0.01	0.47	0.10	0.30	0.15	0.27	0.06	0.27	0.08	0.08	0.02
CoO	0.03	0.02	0.01	0.01	0.04	0.01	0.04	0.05	0.02	0.01	0.04	0.03	0.01	0.01
Al_2O_3	0.04	0.03	1.37	0.07	0.03	0.02	0.05	0.02	0.10	0.09	0.04	0.03	0.74	0.11
Cr_2O_3	0.01	0.02	0.58	0.03	0.02	0.01	0.01	0.01	0.01	0.01	0.01	0.01	0.58	0.29
CaO	0.03	0.01	1.12	0.03	0.22	0.05	0.03	0.01	0.03	0.02	0.02	0.01	0.02	0.01
MnO	0.11	0.01	0.12	0.01	0.69	0.08	0.12	0.11	0.06	0.02	0.15	0.13	0.12	0.02
Total	98.69	0.64	99.83	0.94	80.61	2.46	80.64	1.00	80.99	1.06	79.51	1.03	79.38	3.11
Si	1.004	0.002	0.986	0.002	0.408	0.056	1.939	0.111	1.990	0.041	1.902	0.107	2.063	0.033
Al	0.001	0.001	0.028	0.001	0.002	0.001	0.000	0.001	0.006	0.005	0.003	0.002	0.045	0.006
Fe	0.168	0.003	0.076	0.001	1.028	0.098	0.306	0.092	0.243	0.041	0.329	0.119	0.313	0.037
∑ Tetr.	1.173	0.003	1.090	0.003	1.438	0.094	2.249	0.038	2.239	0.041	2.234	0.029	2.421	0.027
Mg	1.811	0.004	1.750	0.011	4.084	0.117	2.789	0.128	2.752	0.071	2.840	0.096	2.447	0.045
Ni	0.007	0.001	0.001	0.000	0.021	0.004	0.013	0.007	0.011	0.003	0.011	0.003	0.003	0.001
Co	0.001	0.000	0.000	0.000	0.002	0.000	0.000	0.002	0.001	0.001	0.002	0.001	0.001	0.000
Cr	0.000	0.000	0.021	0.001	0.001	0.000	0.000	0.000	0.000	0.000	0.000	0.000	0.024	0.013
Ca	0.001	0.000	0.008	0.000	0.013	0.003	0.000	0.001	0.002	0.001	0.001	0.000	0.001	0.001
Mn	0.002	0.000	0.002	0.000	0.032	0.003	0.000	0.005	0.003	0.001	0.007	0.006	0.005	0.001
∑ Oct.	1.823	0.004	1.782	0.011	4.152	0.119	2.810	0.138	2.768	0.072	2.862	0.100	2.482	0.047
Tetr./Oct.	0.643	0.739	0.611	0.266	0.346	0.790	0.800	0.276	0.809	0.572	0.781	0.285	0.976	0.585
Ni/Mg	0.004	0.0003	0.001	0.0001	0.005	0.0010	0.004	0.0022	0.004	0.0009	0.004	0.0012	0.001	0.0003

n total number of points acquired in polished thin section; σ standard deviation of the analyzed points; apfu atoms per formula unit

Table 3 Average chemical compositions and structural formula (apfu) of the different types of serpentine identified in the saprock.

Sample name	PA-15		PB-10		PA-15		PA-15		PA-15		PC-76		PA-15		PA-15		PA-15	
Depth, m	15.5		13		15.5		15.5		15.5				15.5		15.5		15.5	
	Type I	σ	Type I	σ	Type II-rim	σ	Type II-core	σ	Type III	σ	Type III	σ	Type IV	σ	Type V	σ	Type VI	σ
n	12		4		11		13		11		17		4		6		8	
SiO_2	41.00	0.68	42.59	1.04	40.98	2.14	41.26	1.60	45.04	1.03	42.88	1.36	44.29	0.63	39.61	0.71	40.642	0.33
MgO	33.63	1.43	28.26	4.35	35.84	1.88	35.05	1.64	34.14	1.18	36.38	1.81	32.13	0.88	29.26	2.40	26.149	1.16
FeO	7.45	1.11	7.69	0.98	6.14	3.29	4.50	2.89	3.11	0.47	3.02	1.17	3.27	1.45	7.12	1.27	7.08	0.53
NiO	1.70	0.77	3.88	1.58	1.33	0.22	0.90	0.19	0.38	0.13	0.87	0.11	0.66	0.12	1.40	0.23	0.638	0.11
CoO	0.02	0.01	0.07	0.04	0.02	0.01	0.02	0.02	0.01	0.01	0.06	0.01	0.01	0.01	0.02	0.01	0.017	0.01
Al_2O_3	0.26	0.17	0.05	0.01	0.06	0.05	0.05	0.02	0.26	0.32	0.69	2.54	0.56	0.17	0.12	0.07	0.028	0.02
Cr_2O_3	0.02	0.02	0.01	0.01	0.02	0.02	0.02	0.01	0.07	0.12	0.01	0.01	0.28	0.09	0.03	0.03	0.013	0.01
CaO	0.08	0.03	0.11	0.06	0.06	0.01	0.04	0.01	0.01	0.01	0.04	0.01	0.02	0.01	0.07	0.02	0.061	0.01
MnO	0.09	0.03	0.32	0.27	0.05	0.05	0.03	0.01	0.04	0.01	0.02	0.01	0.06	0.03	0.07	0.02	0.061	0.02
Total	84.25	1.06	82.98	3.39	84.49	0.93	81.85	1.53	83.08	1.93	83.97	1.89	81.27	1.06	77.70	1.83	74.69	0.95
Si	2.044	0.032	2.172	0.062	2.021	0.050	2.071	0.047	2.182	0.024	2.077	0.065	2.197	0.019	2.128	0.061	2.242	0.028
Al	0.015	0.010	0.003	0.000	0.003	0.003	0.003	0.001	0.015	0.018	0.038	0.140	0.032	0.010	0.008	0.005	0.002	0.001
Fe	0.311	0.045	0.329	0.050	0.257	0.149	0.191	0.126	0.126	0.018	0.123	0.049	0.136	0.062	0.320	0.058	0.327	0.025
∑ Tetr.	2.370	0.053	2.456	0.091	2.282	0.103	2.264	0.087	2.323	0.033	2.238	0.083	2.365	0.053	2.456	0.091	2.571	0.046
Mg	2.500	0.099	2.140	0.247	2.635	0.073	2.622	0.069	2.465	0.054	2.626	0.097	2.375	0.039	2.341	0.149	2.150	0.077
Ni	0.068	0.031	0.160	0.067	0.053	0.009	0.036	0.008	0.015	0.005	0.034	0.005	0.026	0.005	0.061	0.011	0.028	0.005
Co	0.001	0.000	0.003	0.002	0.001	0.000	0.001	0.001	0.000	0.000	0.002	0.000	0.001	0.000	0.001	0.001	0.001	0.000
Cr	0.001	0.001	0.001	0.000	0.001	0.001	0.001	0.001	0.003	0.005	0.000	0.001	0.011	0.004	0.001	0.001	0.001	0.001
Ca	0.004	0.002	0.006	0.003	0.003	0.001	0.002	0.000	0.001	0.000	0.002	0.000	0.001	0.000	0.004	0.001	0.004	0.001
Mn	0.004	0.001	0.014	0.012	0.002	0.002	0.001	0.000	0.002	0.001	0.001	0.000	0.003	0.001	0.003	0.001	0.003	0.001
∑ Oct.	2.578	0.078	2.411	0.146	2.695	0.064	2.663	0.061	2.486	0.052	2.665	0.096	2.416	0.043	2.411	0.146	2.186	0.072
Tetr./Oct.	0.919	0.684	1.019	0.624	0.847	1.603	0.850	1.427	0.934	0.636	0.840	0.864	0.979	1.245	1.019	0.624	1.176	0.632
Ni/Mg	0.028	0.013	0.026	0.005	0.020	0.004	0.014	0.003	0.006	0.002	0.013	0.002	0.011	0.002	0.026	0.005	0.013	0.003

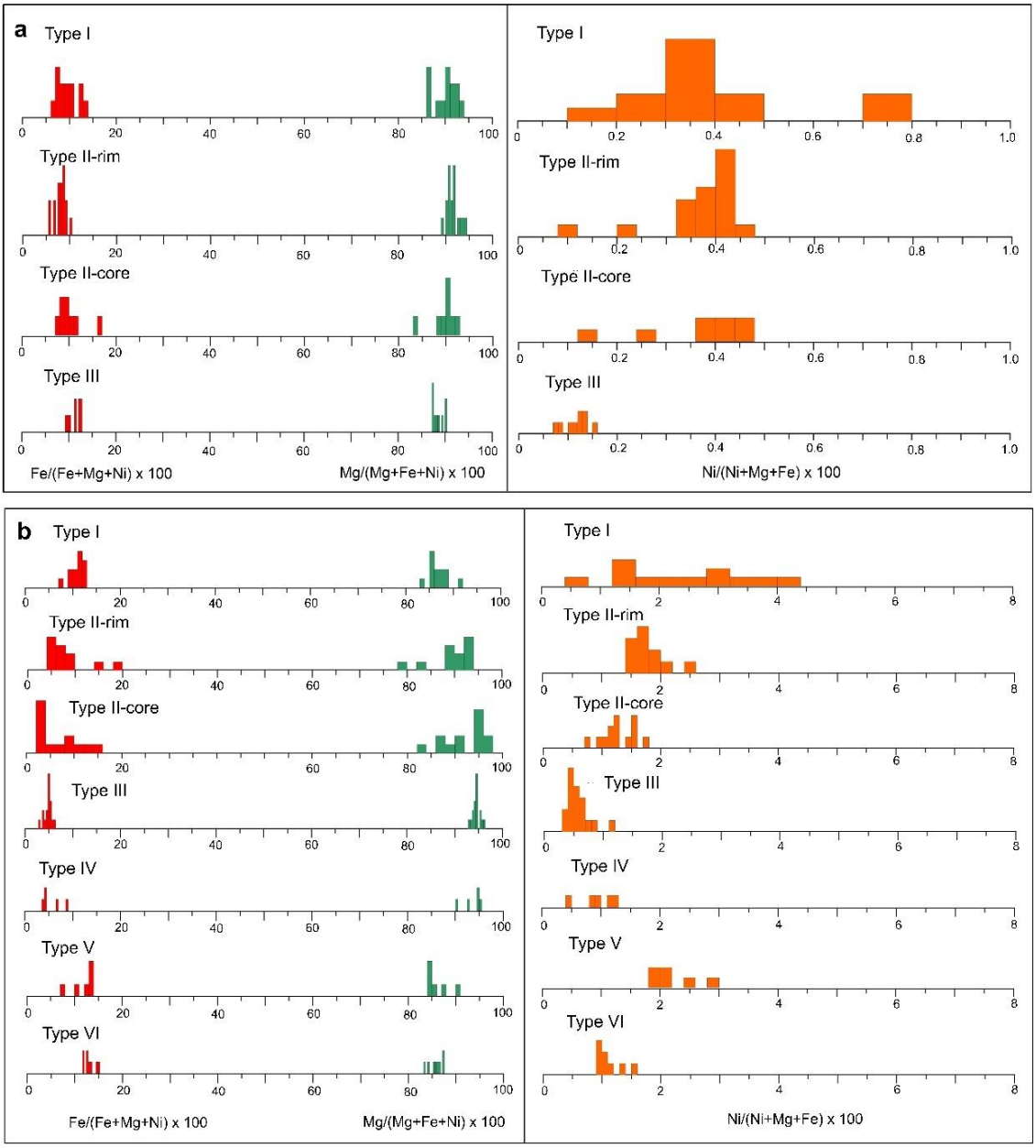

Fig. 18 Histogram of Fe- (red), Mg (green), and Ni (orange) ratio in the different types of serpentine identified in the a) bedrock and b) saprock of profile A.

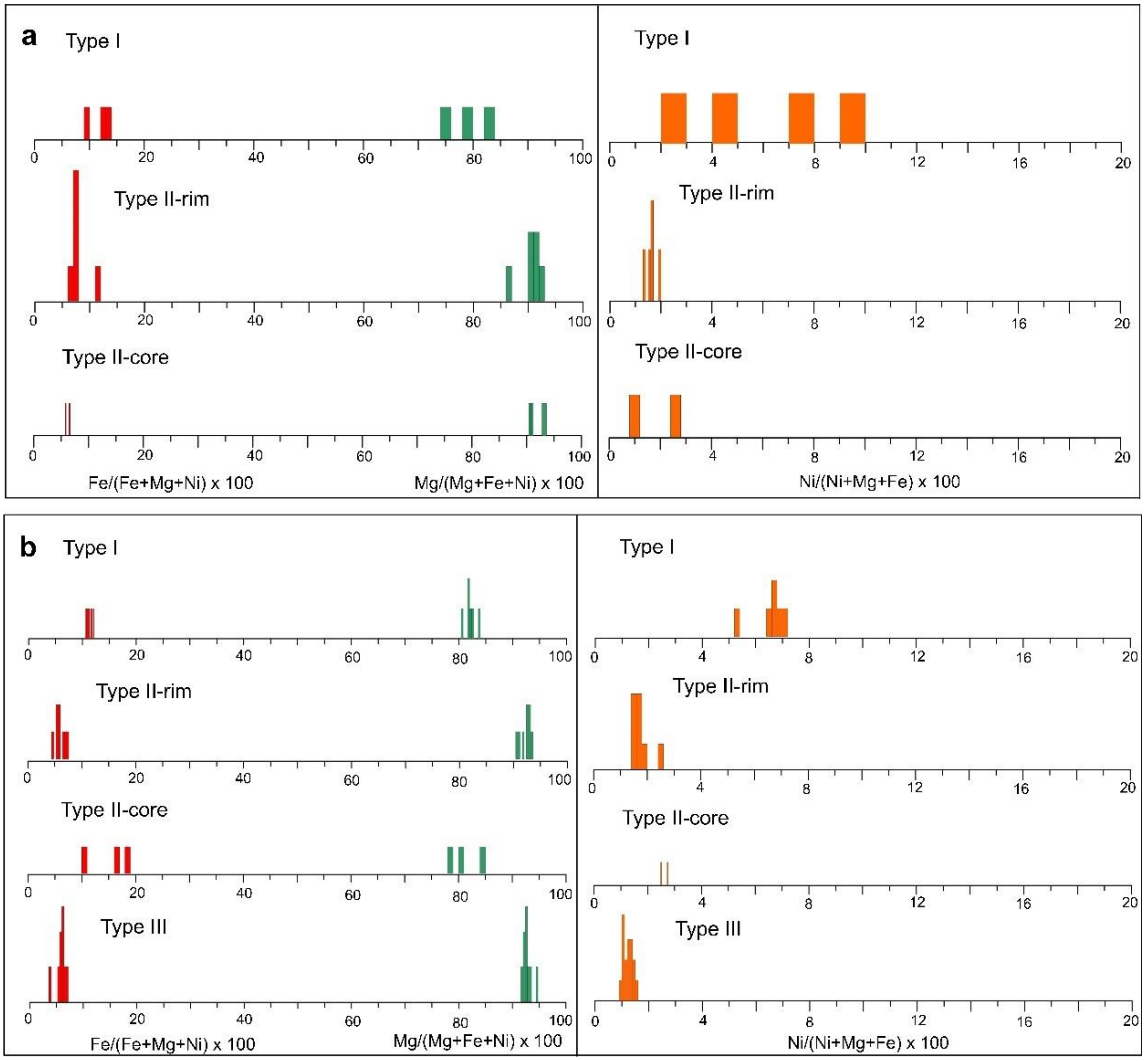

Fig. 19 Histogram of Fe- (red), Mg (green), and Ni (orange) ratio in the different types of serpentine identified in the saprock of a) profile B and b) profile C.

3.5.4.2.2 Garnierite

Microprobe chemical analysis of the two garnierite samples is summarized in Table 4. In general, the studied garnierite samples contain a high amount of SiO_2 up to 56.48 wt% (4.23 apfu Si), but with very low FeO and Al_2O_3 contents. The NiO content ranges from

Akita University

Table 4 Average compositions and structural formula (apfu) of selected talc-like (kerolite-Ker pimelite-Pim), serpentine-like (lizardite-Liz), and Ni-sepiolite-falcondoite (Sep-falc) in garnierite samples.

	Serpentine-like		Talc-like				Sepiolite-falcondoite	
Sample name	PB-9		PB-9		PB-9		PB-10	
Depth, m	12		12		12		13	
	Lizardite	σ	Keroite	σ	Pimelite	σ		σ
n	3		4		11		14	
MgO	8.51	3.96	14.04	0.60	9.53	1.89	16.43	3.41
SiO_2	24.96	2.98	55.32	1.61	52.47	2.12	50.38	6.35
NiO	5.32	2.86	19.78	0.60	28.34	4.14	17.56	1.24
CoO	0.08	0.03	0.01	0.00	0.01	0.01	0.01	0.01
FeO	25.74	9.32	0.03	0.03	0.06	0.13	0.06	0.12
Al_2O_3	5.72	3.43	0.03	0.02	0.03	0.03	0.02	0.01
Cr_2O_3	0.84	0.59	0.001	0.001	0.003	0.004	0.0004	0.001
CaO	0.03	0.05	0.08	0.03	0.08	0.03	0.10	0.06
MnO	0.06	0.02	0.01	0.01	0.01	0.01	0.01	0.01
Total	71.25	6.71	89.29	2.29	90.52	3.41	84.56	9.89
Si	1.794	0.061	4.229	0.009	4.134	0.048	11.926	0.040
Al	0.472	0.240	0.003	0.002	0.003	0.003	0.005	0.003
Fe	1.574	0.605	0.002	0.002	0.004	0.008	0.013	0.029
∑ Tetr.	3.839	0.316	4.234	0.008	4.141	0.051	11.944	0.047
Mg	0.579	0.085	1.312	0.039	0.918	0.178	4.710	0.437
Ni	0.413	0.046	1.217	0.035	1.797	0.258	3.390	0.457
Co	0.004	0.000	0.000	0.000	0.000	0.000	0.001	0.001
Cr	0.030	0.003	0.000	0.000	0.000	0.000	0.000	0.000
Ca	0.003	0.004	0.006	0.002	0.006	0.002	0.024	0.013
Mn	0.003	0.001	0.000	0.001	0.000	0.000	0.001	0.001
∑ Oct.	1.033	0.033	2.536	0.018	2.723	0.099	8.127	0.082
Tetr./Oct.	3.467	1.869	1.669	0.162	1.521	0.134	1.470	0.079
Ni/Mg	0.428		0.927		1.958		0.720	

n total number of points acquired in polished thin section
σ standard deviation of the analyzed points
apfu atoms per formula unit

2.25 to 34.86 wt% (0.12- 2.14 apfu Ni). Based on the mineral composition, the pale green garnierite is comparable to the Ni-sepiolite and falcondoite solid solution series reported by Tauler et al. (2009). The bluish-green

Akita University

garnierite sample matched the descriptions of type IV garnierite previously reported by Villanova-de-Benavent et al. (2014) (Fig. 20).

The Ni-sepiolite and falcondoite are marked by 2.66-4.19 apfu Ni and very low Al and Fe contents, with an average structural formula of $Mg_{4.71}Ni_{3.39}Si_{11.93}O_{15}(OH)_2 \cdot 6(H_2O)$. The high amount of Si in the plot of sepiolite and falcondoite could be due to the presence of quartz in the samples (Tauler et al., 2009). The talc-like phase is classified as kerolite or pimelite based on Ni (apfu)/ Mg (apfu) ratio (Nickel, 1992). The calculated average structural formula for pimelite is $Mg_{0.92}Ni_{1.80}Si_{4.13}O_{10}(OH)_2$ with Ni (apfu)/ Mg (apfu) > 1, while kerolite yielded Ni (apfu)/ Mg (apfu) < 1 and its structural formula is $Mg_{1.31}Ni_{1.22}Si_{4.23}O_{15}(OH)_2$.

3.5.4.2 Ore minerals in the limonite horizon

3.5.4.2.1 Goethite and hematite

Table 5 shows the average chemical composition and structural formula of the ore-bearing oxyhydroxides in the limonite horizon. Goethite contains a significant amount of NiO (up to 2.15 wt%, 0.025 apfu Ni) and Al_2O_3 (up to 13.02 wt%, 0.211 apfu Al). The CoO and MnO contents range from 0.09 -1.42 wt% (0.001-0.016 apfu Co) and 0.13- 8.76 wt% (0.002- 0.0135 apfu Mn), respectively. The average structural formula of goethite is $(Fe_{0.61}, Al_{0.08}, Ni_{0.01}, Mn_{0.02}, Co_{0.002})O(OH)$.

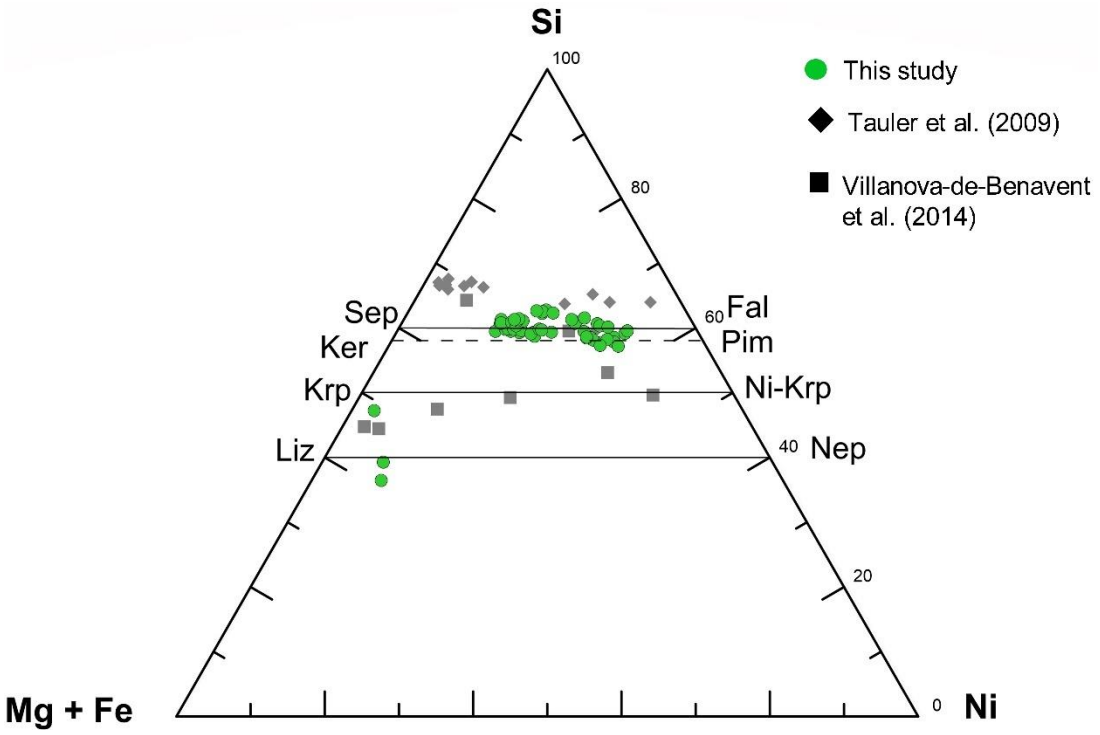

Fig. 20 Si-Ni-Mg-Fe ternary diagram illustrating the mineralogy and composition of garnierites from the Berong ore deposit.

The concentrations of NiO (up to 1.43 wt%, 0.032 apfu Ni), CoO (up to 1.13 wt%, 0.023 apfu Co), MnO (up to 1.86 wt%, 0.044 apfu Mn), and Al_2O_3 (up to 1.15 wt%, 0.036 apfu Al) are high in hematite with an average structural formula of hematite is $(Fe_{1.74}, Al_{0.02}, Ni_{0.02}, Mn_{0.02}, Co_{0.01})O_3$.

Table 5 Average compositions (wt%) and structural formula (apfu) of goethite and hematite in the limonite samples.

	Goethite								Hematite	
Sample name	PA-1		PA-11		PB-3		PB-4		PB-3	
Depth, m	2	σ	12	σ	3	σ	7	σ	3	σ
n	31		5		57		4		8	
SiO_2	1.63	0.4	1.75	1.02	2.43	2.76	2.45	0.36	1.51	0.43
MgO	0.6	0.41	0.08	0.02	0.44	0.73	0.09	0.09	2.78	1.7
Al_2O_3	6.15	1.86	10.68	3.08	3.35	1.39	3.91	0.27	0.51	0.39
FeO	62.84	3.43	56.92	2.48	64.19	3.15	58.04	4.53	77.22	4.13
NiO	0.86	0.19	0.75	0.38	1.36	0.33	1.71	0.34	0.85	0.47
CoO	0.11	0.02	0.12	0.02	0.12	0.02	0.65	0.54	0.49	0.39
Cr_2O_3	0.81	0.28	0.42	0.11	1.21	0.46	0.25	0.04	0.36	0.09
CaO	0.02	0.02	bdl	0.00	bdl	0.00	bdl	0.00	0.01	0.04
MnO	0.35	0.3	0.74	0.41	0.41	0.29	5.91	1.98	1.04	0.52
Total	73.37	3.87	71.46	2.16	73.51	3.03	73.01	6.11	84.77	3.03
Fe	0.810	0.030	0.660	0.040	0.840	0.030	0.760	0.040	1.740	0.070
Al	0.110	0.030	0.170	0.050	0.060	0.020	0.070	0.000	0.020	0.010
Mn	0.010	0.000	0.010	0.000	0.010	0.000	0.100	0.030	0.020	0.010
Ni	0.010	0.000	0.010	0.000	0.020	0.000	0.020	0.000	0.020	0.010
Co	0.000	0.000	0.000	0.000	0.000	0.000	0.010	0.010	0.010	0.010

n total number of points acquired in polished thin section
σ standard deviation of the analyzed points
apfu atoms per formula unit

Akita University

3.5.4.2.2 Mn-oxy-hydroxides

The microprobe chemical analysis of these phases is summarized in Table 6. The NiO and CoO concentrations in lithiophorite- asbolane is high (up to 23.89 wt%; 0.770 apfu Ni; up to 12.59 wt%, 0.465 apfu Co), respectively. Al_2O_3, FeO and MnO contents are found in variable proportions, ranging from 1.28- 21.14 wt% (0.069-0.960 apfu Al), 3.55-55.89 wt% (0.133- 1.990 apfu) and 11.59- 46.92 wt% (0.449- 1.980 apfu), whereas MgO content is relatively low (up to 2.88 wt%, 0.164 apfu Mg). Most of the analyzed Mn-hydroxides indicate that their compositions are spread between lithiophorite and asbolane end members (Fig. 21). The chemical composition of the lithiophorite-asbolane intermediates detected in this study is comparable with those presented by Dzemua et al. (2013) and Putzolu et al. (2018) The calculated average structural formula is $(Al_{0.42},Ni_{0.33},Co_{0.21})(Mn_{1.21},Fe_{0.52},Mg_{0.04})O_2(OH)_2$.

Akita University

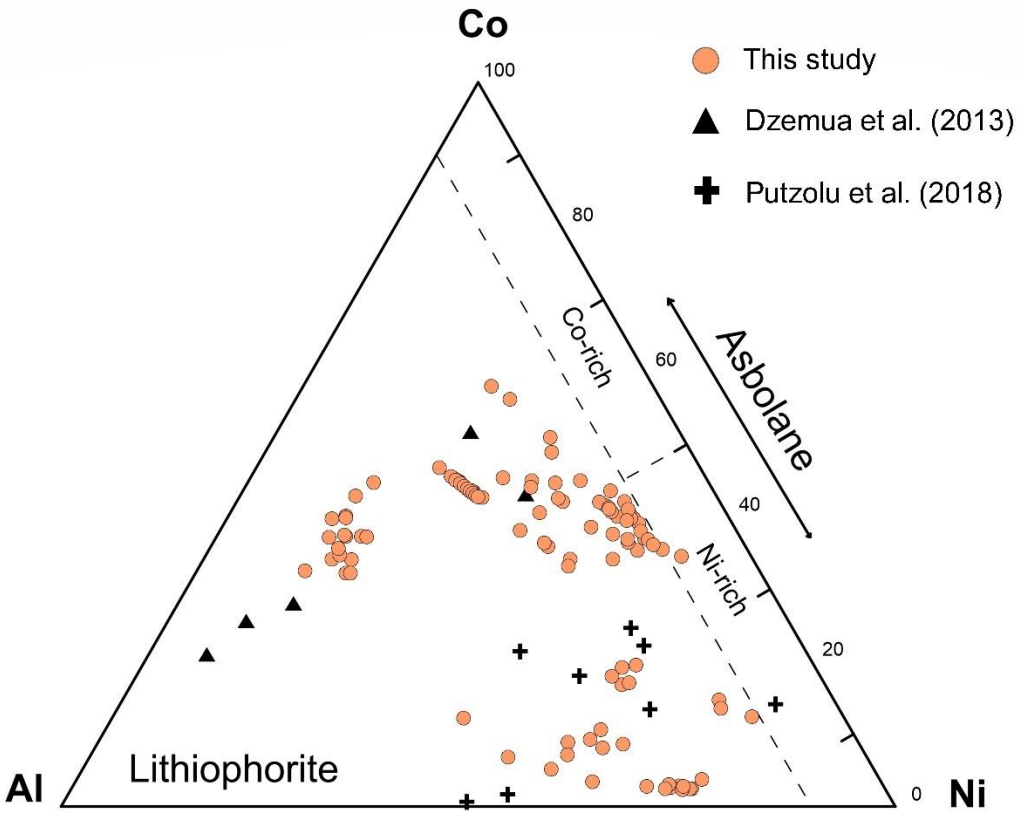

Fig. 21 Co-Ni-Al ternary diagram (wt%) displaying the mineralogy and composition of lithiophorite-asbolane intermediates from the Berong ore deposit.

3.5.5 pH and whole-rock geochemical analysis

Figures 22, 23 and 24 display the pH variations in the studied profiles. The pH of the samples ranges from 5.65 to 9.45. The pH gradient observed from the bedrock (pH 9.45) to the saprolite (pH 6.06 to 7.69) and the limonite (pH 5.65 to 7.09) indicates the transition from alkaline to mildly acidic conditions toward the uppermost sections of the weathering profiles.

Akita University

Table 6 Average chemical compositions (wt%) and structural formula (apfu) of the representative lithiophorite-asbolane intermediate from Berong deposit.

Sample name	PA-15		PA-14		PC-3		PA-11	
Depth, m	6	σ	15	σ	3	σ	12	σ
n	21		27		29		18	
SiO_2	0.41	0.15	0.71	0.57	0.54	0.79	0.70	0.12
MgO	0.48	0.50	0.60	0.23	0.91	1.04	0.35	0.06
Al_2O_3	13.37	6.18	4.12	1.81	5.99	1.68	12.08	1.59
FeO	11.72	3.06	20.10	17.25	12.02	5.81	9.39	5.22
NiO	5.23	3.10	9.87	3.14	3.66	2.83	19.49	3.35
CoO	7.57	1.09	8.06	2.76	5.85	3.20	1.32	0.81
Cr_2O_3	0.03	0.06	0.01	0.02	0.01	0.02	0.01	0.03
CaO	0.01	0.01	0.05	0.05	0.01	0.01	0.01	0.01
MnO	28.04	2.24	29.14	7.99	36.50	4.72	30.34	3.47
Total	66.88	3.67	72.68	4.01	65.52	3.27	73.75	1.90
Ni	0.194	0.126	0.366	0.119	0.142	0.108	0.641	0.116
Al	0.663	0.249	0.224	0.101	0.344	0.092	0.580	0.064
Co	0.267	0.048	0.298	0.103	0.226	0.120	0.043	0.026
Mn	1.044	0.128	1.138	0.323	1.515	0.217	1.049	0.120
Fe	0.433	0.124	0.761	0.638	0.495	0.248	0.321	0.182
Mg	0.028	0.030	0.034	0.013	0.053	0.060	0.018	0.003
Co/Ni	1.374	0.386	0.814	0.866	1.595	1.110	0.067	0.223

n total number of points acquired in polished thin section; σ standard deviation of the analyzed points; apfu atoms per formula unit

Akita University

The total major oxides of the three Ni laterite profiles by XRF are shown in Tables 7, 8, and 9. The geochemical trend of the representative samples from profiles A, B and C are displayed in Figures 22, 23 and 24.

The bedrock of profile A is characterized by high concentrations of MgO (41.06 wt%) and SiO_2 (37.74 wt%), and low amounts of Fe_2O_3 (6.49 wt%) and NiO (0.31 wt%) (Fig. 22). The MgO and SiO_2 contents decrease significantly near the transition boundary between the saprolite and limonite. In contrast, high Fe_2O_3 and Al_2O_3 concentrations are observed in the limonite (up to 74.5 wt% and 6.68 wt%). It is interesting to note the opposing trends of Fe_2O_3 and Al_2O_3 in profile A. Higher amounts of Al_2O_3 are associated with the gibbsite-dominant zone, while high contents of Fe_2O_3 correspond to goethite-dominant zone (Fig. 22).

The saprolite horizon of all the studied profiles displays high NiO concentration (up to 7.77 wt%). In general, the vertical trend of Co_2O_3 mimics that of MnO from the bedrock to the uppermost horizon. In profile A, slight enrichment is observed near the transition boundary between the saprolite and limonite with concentrations of 0.27 wt% Co_2O_3 and 2.15 wt% MnO, respectively (Fig. 22).

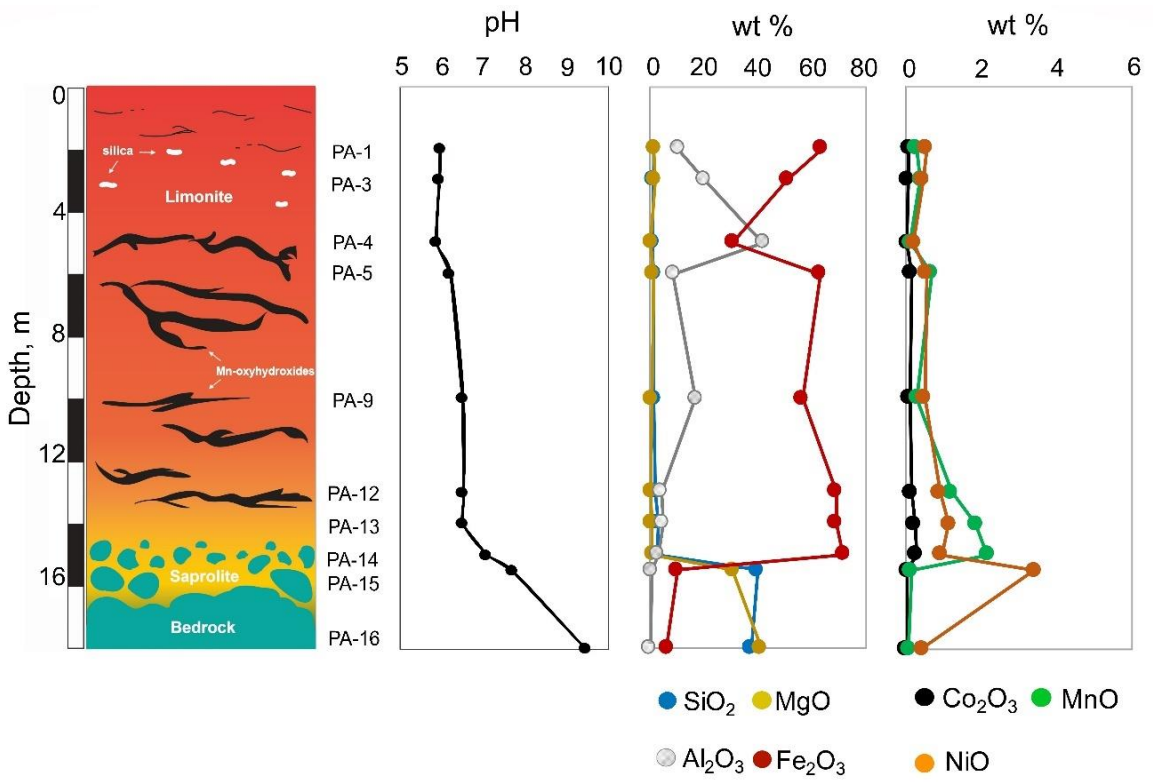

Fig. 22 pH and element distribution with depth along laterite profile A (PA).

However, in profile B, the highest Co_2O_3 (> 0.2 wt%) and MnO concentrations (> 1 wt%) were observed within the limonite horizon, particularly at 9 m depth (Fig. 23). The Cr_2O_3, TiO_2, K_2O, CaO, and P_2O_5 contents are generally low throughout the profiles (up to 0.25 wt%, 0.29 wt%, 0.08 wt%, 0.05 wt%, 0.04 wt%, respectively).

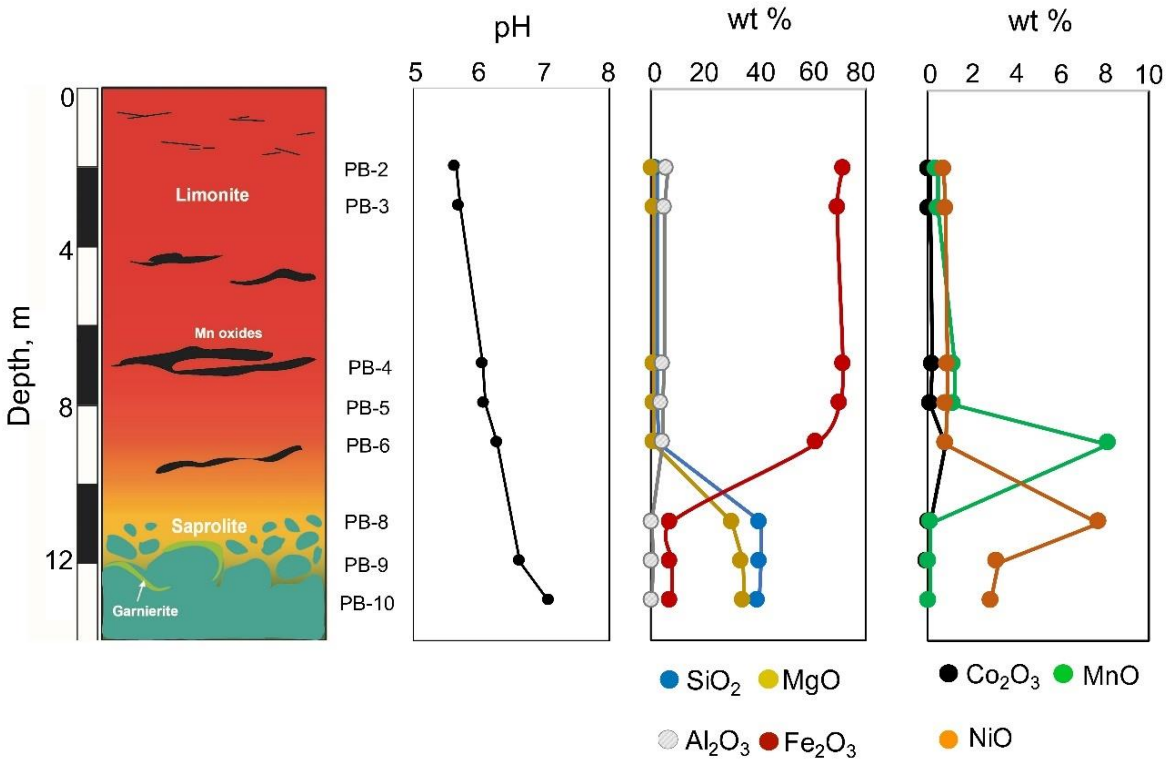

Fig. 23 pH and element distribution with depth along laterite profile B (PB).

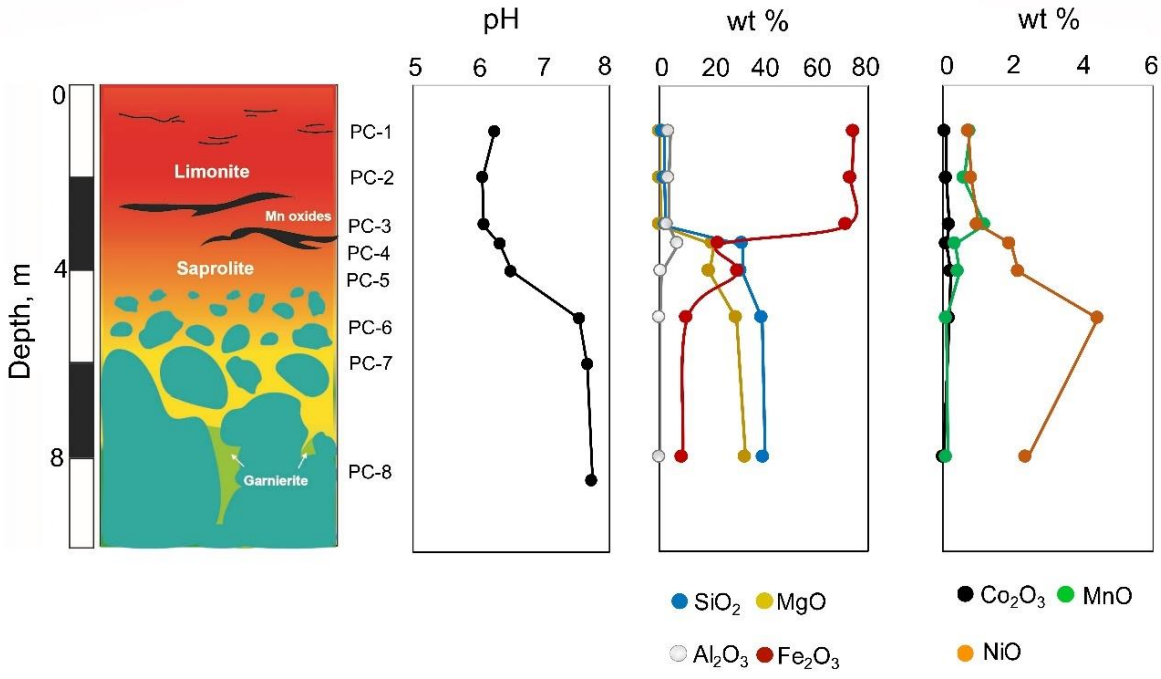

Fig. 24 pH and element distribution with depth along laterite profile C (PC).

Table 7 Whole-rock chemical analyses (wt%) of the bedrock (BED), saprolite (SAP), and limonite (LIM) samples along profile A.

Sample name	PA-1	PA-2	PA-3	PA-4	PA-5	PA-6	PA-7	PA-8	PA-9	PA-10	PA-11	PA-12	PA-13	PA-14	PA-15	PA-16
Horizon	LIM	LIM	LIM	LIM	LIM	LIM	LIM	LIM	LIM	LIM	LIM	LIM	LIM	LIM	SAP	BED
Depth, m	2	3	4	5	6	7	9	9.8	10	11	12	13	14	15	15.5	18
Na_2O	bdl	bdl	bdl	bdl	bdl	0.04	bdl	bdl	bdl	bdl	bdl	bdl	bdl	bdl	bdl	bdl
MgO	1.66	2.07	0.91	0.51	1.47	0.20	1.58	0.95	1.01	0.92	0.95	0.62	1.00	1.14	30.77	41.06
SiO_2	1.69	1.36	1.25	1.07	1.68	1.10	1.00	1.62	1.82	2.40	2.05	2.49	3.22	2.88	40.10	37.74
Al_2O_3	10.79	20.38	34.16	42.19	8.84	56.33	30.93	6.86	17.19	4.87	5.51	4.55	5.11	3.38	0.79	0.26
P_2O_5	0.017	0.011	0.016	0.011	0.006	0.006	0.016	0.006	0.008	bdl	0.005	bdl	bdl	0.006	bdl	bdl
K_2O	bdl	bdl	bdl	bdl	bdl	0.004	0.004	bdl	0.001	bdl	bdl	0.005	bdl	0.001	0.001	0.001
CaO	bdl	0.03	0.03	0.03	bdl	0.04	0.03	0.03	bdl	bdl	bdl	bdl	bdl	bdl	bdl	0.28
TiO_2	0.12	0.11	0.15	0.08	0.06	0.05	0.29	0.05	0.14	0.01	0.02	0.01	0.02	0.03	bdl	bdl
Cr_2O_3	4.46	6.71	3.31	2.73	6.68	0.96	6.45	4.35	4.32	3.91	4.61	4.32	2.91	3.11	0.75	0.25
MnO	0.26	0.38	0.24	0.12	0.67	bdl	0.04	0.14	0.29	0.69	0.93	1.20	1.86	2.15	0.13	0.07
Fe_2O_3	63.86	50.88	39.25	30.79	63.27	14.14	39.94	73.07	56.62	69.58	69.68	69.01	69.09	71.61	10.36	6.49
Co_2O_3	0.06	0.06	0.05	0.03	0.15	0.01	0.04	0.07	0.08	0.13	0.15	0.15	0.24	0.27	0.02	0.01
NiO	0.54	0.45	0.33	0.22	0.55	0.14	0.23	0.37	0.50	0.91	0.94	0.90	1.14	0.95	3.40	0.43
LOI	12.96	14.06	20.71	23.61	10.28	28.73	18.67	8.62	14.38	13.50	11.23	13.50	12.65	11.57	12.90	12.30
Total	96.42	96.03	100.39	101.38	93.65	101.73	99.23	96.13	95.88	96.01	96.07	96.75	97.23	97.10	99.23	98.88

Table 8 Whole-rock chemical analyses (wt%) of the bedrock (BED), saprolite (SAP), and limonite (LIM) samples along profile B.

Sample name	PB-1	PB-2	PB-3	PB-4	PB-5	PB-6	PB-7	PB-8	PB-9	PB-10
Horizon	LIM	LIM	LIM	LIM	LIM	LIM	LIM	SAP	SAP	SAP
Depth, m	1	2	3	7	8	9	10	11	12	13
Na_2O	bdl	bdl	bdl	bdl	bdl	bdl	bdl	bdl	bdl	bdl
MgO	0.97	0.60	1.00	0.86	0.93	1.01	0.88	30.07	34.13	34.81
SiO_2	2.56	2.02	2.14	2.21	2.29	2.50	2.46	40.68	40.69	40.23
Al_2O_3	6.68	6.01	5.15	4.79	3.87	4.26	4.12	0.38	0.45	0.31
P_2O_5	0.04	0.02	0.02	0.01	0.01	0.01	0.01	bdl	bdl	bdl
K_2O	0.02	bdl	bdl	bdl	0.01	0.08	bdl	bdl	bdl	bdl
CaO	0.05	bdl	bdl	bdl	bdl	0.03	bdl	bdl	bdl	bdl
TiO_2	0.17	0.13	0.10	0.05	0.04	0.02	0.02	bdl	bdl	bdl
Cr_2O_3	5.07	3.11	4.70	3.32	4.10	3.38	2.99	0.25	0.35	0.29
MnO	0.24	0.42	0.48	1.19	1.20	8.17	3.77	0.12	0.06	0.09
Fe_2O_3	64.12	71.74	69.69	71.82	70.71	61.87	68.42	7.50	7.43	7.46
Co_2O_3	0.07	0.07	0.09	0.19	0.11	0.81	0.45	0.08	0.01	0.03
NiO	0.64	0.74	0.83	0.91	0.85	0.80	1.03	7.77	3.18	2.87
LOI	16.12	12.71	12.32	12.21	13.01	12.47	13.01	12.57	12.97	13.12
Total	96.74	97.57	96.51	97.55	97.12	95.41	97.16	99.42	99.27	99.20

bdl- below the detection limit

Table 9 Whole-rock chemical analyses (wt%) of the bedrock (BED), saprolite (SAP), and limonite (LIM) samples along profile C.

Sample name	PC-1	PC-2	PC-3	PC-4	PC-5	PC-6	PC-7	PC-8
Horizon	LIM	LIM	LIM	LIM-SAP	LIM-SAP	SAP	SAP	SAP
Depth, m	1	2	3	3.4	4	5	6	8.5
Na_2O	bdl	bdl	bdl	bdl	bdl	bdl	bdl	bdl
MgO	0.70	0.71	0.85	20.85	19.52	29.88	31.58	33.26
SiO_2	2.11	2.35	2.87	32.19	31.81	39.62	39.38	40.35
Al_2O_3	4.32	4.01	3.76	7.44	1.26	0.62	0.55	0.58
P_2O_5	0.007	0.008	0.003	bdl	0.003	0.004	bdl	bdl
K_2O	bdl	bdl	bdl	bdl	bdl	bdl	bdl	bdl
CaO	bdl	bdl	bdl	bdl	bdl	bdl	bdl	bdl
TiO_2	0.04	0.04	0.01	0.09	0.01	bdl	bdl	0.01
Cr_2O_3	2.63	2.76	3.54	1.11	1.31	0.48	0.59	0.59
MnO	0.78	0.62	1.21	0.36	0.47	0.12	0.12	0.13
Fe_2O_3	74.50	73.55	71.44	23.35	30.39	11.15	10.46	9.48
Co_2O_3	0.09	0.11	0.21	0.12	0.24	0.20	0.07	0.03
NiO	0.74	0.83	1.01	1.94	2.17	4.43	3.58	2.40
LOI	12.28	12.63	12.21	11.44	11.82	12.87	13.18	12.63
Total	98.18	97.63	97.09	98.89	99.00	99.37	99.51	99.45

bdl- below the detection limit

Akita University

3.6 Discussion

3.6.1 Geochemical and mineralogical evolution of the profiles

The results from the mineralogical, petrographic and geochemical analyses of the Berong deposit revealed the alteration pathway from the serpentinized harzburgite bedrock to the weathered horizons of the laterite profiles. The alteration from primary to secondary mineralogical assemblages is reported in Figure 25.

3.6.1.1 Hydrothermal alteration of the ultramafic suite

Lizardite is the dominant phase produced by the hydration of primary minerals in the Berong ultramafic bedrock (i.e., olivine and pyroxene). This observation is in good agreement with previous works related to the serpentinization of peridotite (Hyndman and Peacock, 2003; Bach et al., 2006; Frost et al., 2013). The primary olivine contains a significant amount of Ni (up to 0.4 wt% NiO), indicating that olivine is the source of ore in the serpentinized peridotite.

Type I, II, and III serpentine veins are developed in the harzburgite bedrock of profile A. The typical mesh texture of type I veins indicates the onset of serpentinization starting from the rims of olivine and pyroxene. The core zone of type II veins is formed later than the rim zone. During the formation of a moderately iron-rich type II-core vein,

Akita University

part of Fe was extracted from the rim of type II serpentine and brucite to form magnetite in the core of the type II veins. This interpretation is consistent with the findings of Oufi et al. (2002), who suggested that as serpentinization proceeds, the FeO content of serpentine decreases due to the increased formation of secondary magnetite. Additionally, the NiO concentration decreases from type II-core serpentine to type III serpentine, indicating an incipient (and Mg) leaching from the core of type II veins.

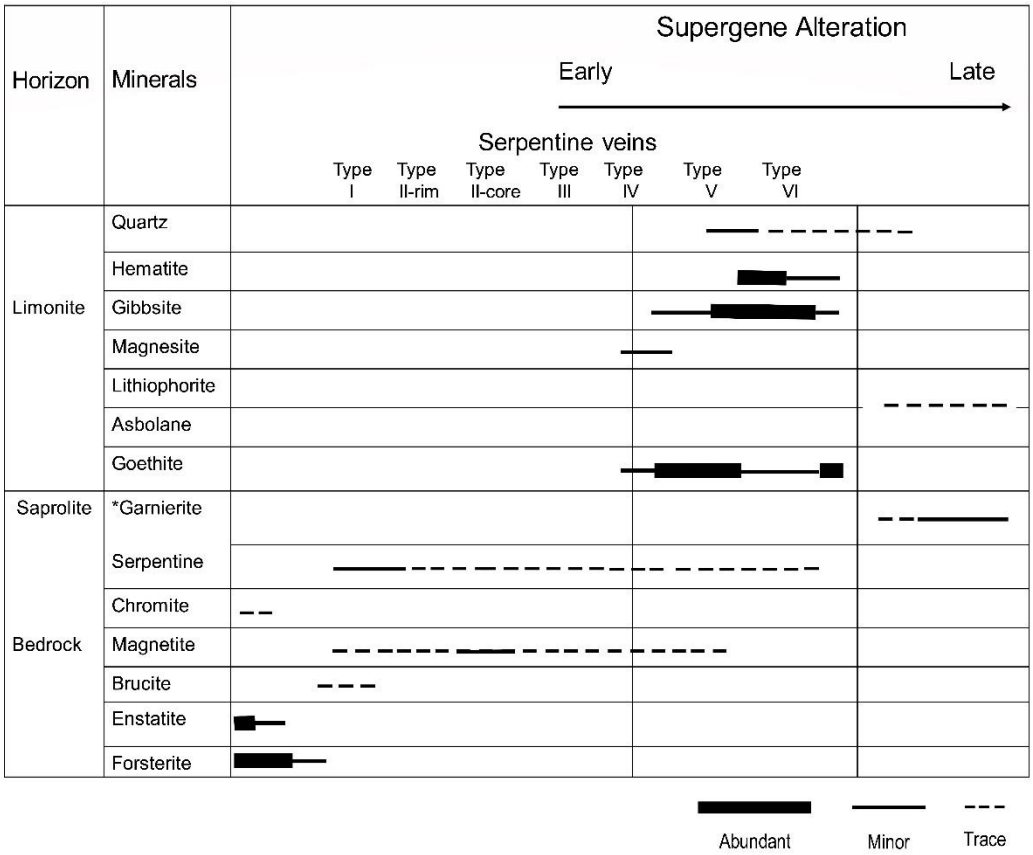

Fig. 25 Paragenesis and mineral abundance of primary and alteration minerals with Ni-bearing serpentine veins developed in the bedrock and saprock of the Berong Ni-Co laterite profiles.

Akita University

To describe the genesis of serpentine in the Berong deposit, two models of serpentinization can be considered: (A) the first model involves a two-step process whereby brucite and serpentine develop after the hydration of olivine (Eq. 1) and later forms magnetite from the breakdown of primary brucite (Eq. 2) and serpentine (Eq. 3).

$$2(Mg,Fe)_2SiO_4 + 3H_2O = (Mg,Fe)_3Si_2O_5(OH)_4 + (Mg,Fe)(OH)_2 \quad (1)$$
olivine water serpentine brucite

$$9FeOH_2 + 4SiO_2 = 2Fe_3Si_2O_5(OH)_4 + Fe_3O_4 + 4H_2O + H_2 \quad (2)$$
brucite silica serpentine magnetite water hydrogen

$$Fe_3Si_2O_5(OH)_4 = Fe_3O_4 + 2SiO_2 + H_2O + H_2 \quad (3)$$
serpentine magnetite silica water hydrogen

In contrast, (B) the second model consists of only one- step process (Eq. 4) where the serpentinization of olivine yields serpentine, brucite, and magnetite. However, both models require development of brucite during serpentinization (Toft et al., 1990; Oufi et al., 2002; Bach et al., 2006; Beard et al., 2009; Frost et al., 2013).

$$8(Mg,Fe)_2SiO_4 + 10H_2O = 4(Mg,Fe)_3Si_2O_5(OH)_4 + (Mg,Fe)(OH)_2 + Fe_3O_4 + H_2 \quad (4)$$
olivine water serpentine brucite magnetite hydrogen

From the data, a significant amount of magnetite was found in the mesh core of type II veins. The formation of magnetite in type II- core veins may have formed in an oxidizing fluid-dominated system (Frost et al. 2013). The serpentine type sequence and mineral composition of type II serpentines (rim and core), combined with the formation of

Akita University

brucite in type I veins, support the two-stage model for serpentinization above (Toft et al., 1990; Oufi et al., 2002, Bach et al., 2006; Beard et al., 2009; Frost et al., 2013).

The recrystallization of mesh-textured type I and II serpentines into interlocking-textured type III serpentine was observed. According to O'Hanley (1996), changes in the fluid composition or temperature are possible factors that lead to recrystallization and replacement of serpentine. The change in texture from type I and II to type III is accompanied by an increase in grain size of the serpentine. The Raman analysis showed that lizardite is the principal component in both mesh (type I and II) and interlocking serpentine (type III). The absence of talc in the harzburgite bedrock is explained by the relatively low amount of orthopyroxene (20%), which is fundamental for the talc development from brucite during the serpentinization stage (Sonzogni et al., 2017).

3.6.1.2 Ni-enriched serpentine in the saprolite horizon

Progressive weathering led to the development of the saprolite horizon and the limonite horizon. The saprolite horizon primarily consists of Ni-enriched serpentine and garnierite. Goethite, magnetite, chromite, and quartz occur in minor to trace amounts. The bulk Ni concentration in the saprolite was found to be nine times higher than the bedrock.

Akita University

Type I and type II serpentines in the saprock resemble that of lizardite in all the studied profiles. However, these serpentines in the saprock contain a significant amount of NiO in contrast to the two types of serpentines in the harzburgite bedrock. Type I and II serpentines are the Ni-richest serpentine types in the saprock. This indicates the addition of Ni from the limonite horizon (Dublet et al., 2015). The Raman peak of the interlocking type III veins located at 3696 cm^{-1} corresponds to chrysotile. As shown by previous authors (Moody, 1976; O'Hanley, 1996; Evans, 2004), the lizardite-to-chrysotile transformation is due either to contamination of meteoritic-hydrothermal waters or meteoric waters.

As serpentinization process continues, type IV serpentines are formed, and subsequently by type V and type VI serpentines in the saprock. Type IV serpentines may have undergone some extent of recrystallization owing to its coarser grained texture (O'Hanley, 1996). The EPMA results of type V and VI serpentines show a relatively lower sum of oxides which could be due to the occurrence of 'deweylite'. Deweylite is a mixture of poorly crystalline serpentine and talc-like minerals, which are assumed to have additional H_2O in their structure (Speakman and Majumdar, 1971; Bish and Brindley, 1978; Fritsch et

Akita University

al., 2016). Type VI serpentine veins cut the previous type I to type V veins, suggesting it formed last in the paragenetic sequence (Fig. 25).

3.6.1.3 Formation of Fe-oxyhydroxides, garnierite, Mn-oxy-hydroxides, and silica

The alteration of serpentine to goethite was observed in the limonite horizon of the studied profiles. It is widely recognized that Fe-oxyhydroxides are a typical alteration product of the ultramafic rocks (Golightly, 1981; Dublet et al., 2012; Fu et al., 2014). High concentration of NiO (> 1.5 wt%) in goethite is observed in the lower section of the limonite horizon. Samples from this section have pH values ranging from 5.91 to 7.09, suggesting favorable conditions for sorption of Ni onto goethite. This is consistent with previous works of (i.e. Trivedi and Axe, 2001; Ponthieu et al., 2006), which observed the control of the pH of the soil solutions during the sorption of Ni onto goethite. These above-mentioned works suggest that sorption capability is approximately 10% in acid conditions (pH = 5), while it is higher where slightly neutral to neutral conditions are attained (i.e. about 40% at pH = 6 and up to 80% at pH = 7).

In the studied laterite profiles, the mineralogical assemblage, as well as the geochemical tendencies, are generally complex and heterogeneous. The limonite horizon of profile A reveals an inverse trend of Fe and Al, with sections of high concentration of Fe reflecting

Akita University

the goethite-rich zone, while the Al-bearing facies within the limonite corresponds to the gibbsite-rich pods.

In the gibbsite-rich zone, the pH of the limonite samples occurs nearly at pH 6, while at higher pH, Al minerals becomes more soluble than Fe minerals resulting in a relatively higher stability of goethite and hematite (Norton, 1973; Taylor and Eggleton, 2001). In contrast, the other profiles have higher concentrations of Fe and lower Al. Our data show that the pH values of the Fe-rich limonite samples are generally mildly acidic (pH ≥ 6). This corroborates the existence of a strong control of the pH of the system during the formation of the Fe- and Al-oxy-hydroxides facies of the limonite ore.

Garnierite generally occurs as coatings and veins filling of the fractures of early-formed minerals in the saprolite, and this suggests that it formed last in the paragenetic sequence. In the Berong deposit, the composition of the garnierite mainly displays the kerolite-pimelite and sepiolite-falcondoite stoichiometries. However, few garnierites show a serpentine-like characteristic. The results of XRD and mineral chemistry indicate a mixture of serpentine-like and talc-like phases in the garnierite samples, similar to the observations reported by Galí et al. (2012) and Villanova-de-Benavent et al. (2014). The above-mentioned works suggested that the genesis of garnierite ores is due

Akita University

to the formation of Ni- and Si-saturated solutions during the lateritization process. In all the studied profiles, garnierite occurs in the saprolite horizon with pH values between 6.63 and 7.77, suggesting that slightly alkaline conditions favour their formation.

Various factors control the precipitation of Mn-oxy-hydroxides from soil solutions such as oxidation, the catalytic action of other mineral grains, evaporative dehydration, and interaction with microorganisms (Cornell, 1979). The physicochemical conditions of the environment and the soil solutions convey the type of Mn-oxy-hydroxides formed in supergene settings (McKenzie, 1989). In the Berong Ni-Co laterites, the most common Mn-oxy-hydroxides mineral is the lithiophorite-asbolane intermediate. Bulk XRF data of Co and Mn display parallel behavior in all the investigated laterite profiles, which is consistent with previous works (e.g. Dublet et al., 2017; Putzolu et al., 2019) highlighting the high Co-Mn geochemical affinity in laterite systems. The EPMA results reveal that Mn-oxy-hydroxides are generally higher grade (up to 12.59 wt% CoO). Loganathan et al. (1977) observed that there is a sudden increase in adsorption for Co and Zn between pH 5 and pH 7 from the solution, which is consistent with the pH values recorded (i.e. pH 6.08 to 7.09) in the Mn(Co)-bearing layers in the lower limonite zone of the presented Berong deposit.

Akita University

The presence of lithiophorite-asbolane intermediates have been observed in other Ni-Co laterites including Lomié region, south-east Cameroon (Yongue-Fouateu et al., 2006), Moa Bay Cuba (Roqué-Rosell et al., 2010), Nkamouna, Cameroon (Dzemua et al., 2011), and Wingellina, Western Australia (Putzolu et al., 2018). Previous works have proposed that their occurrence is associated with the oxidation of other Mn-oxy-hydroxide minerals, including birnessite, todorokite, cryptomelane, buserite, vernadite and hollandite (Taylor et al., 1964; McKenzie, 1989; Dowding and Fey, 2007). In this study, no direct evidence indicating which primary mineral influences the formation of lithiophorite- asbolane intermediate was found. According to Golden et al. (1993) and Cui et al. (2009), a high amount of Al is needed for the formation of lithiophorite. Since that the serpentinized ultramafic bedrock in the Berong region contains quite low amounts of Al (< 1 wt% Al_2O_3), an external source of this element has been considered. Yongue-Fouateu et al. (2006) and Dzemua et al. (2011) proposed that the high amount of lithiophorite is attributed to the sialic and acidic nature of ferricrete.

3.6.2 Laterization Model of the Berong Ni-Co laterite profiles

The formation and evolution of the Berong Ni-Co laterite deposit are consistent with the genetic models proposed by Freysinnet et al.

Akita University

(2005), Cluzel and Vigier (2008), Butt and Cluzel (2013), Villanova-de-Benavent et al. (2014) and Quesnel et al. (2017). The studied deposit formed under seasonally humid savannas with an annual rainfall of 900-1800 mm (Butt and Cluzel, 2013). Such conditions allow the intensive weathering of peridotite bedrock and subsequently resulted in the formation of the saprolite and limonite horizons (Fig. 26a). In acidic to alkaline groundwater (pH 5 to 9), the ferromagnesian minerals in the bedrock are easily dissolved, which leads to the removal of the more soluble elements, Mg and Si, whereas Al and Fe are retained. The high concentration of Al and Fe in the limonite horizon reflects the abundance of gibbsite and goethite in this horizon (Robb, 2004).

Goethite in the lower section of the limonite horizon contains a significant amount of Ni (Fig. 16b). In the near-surface environment, oxidation of ferrous (Fe^{2+}) to the ferric (Fe^{3+}) valence state occurs which leads to the formation of goethite and hematite, respectively (Robb, 2004).

Tectonic uplift affects the topography by lowering formerly high water-tables, which may cause the strong leaching of Ni from the

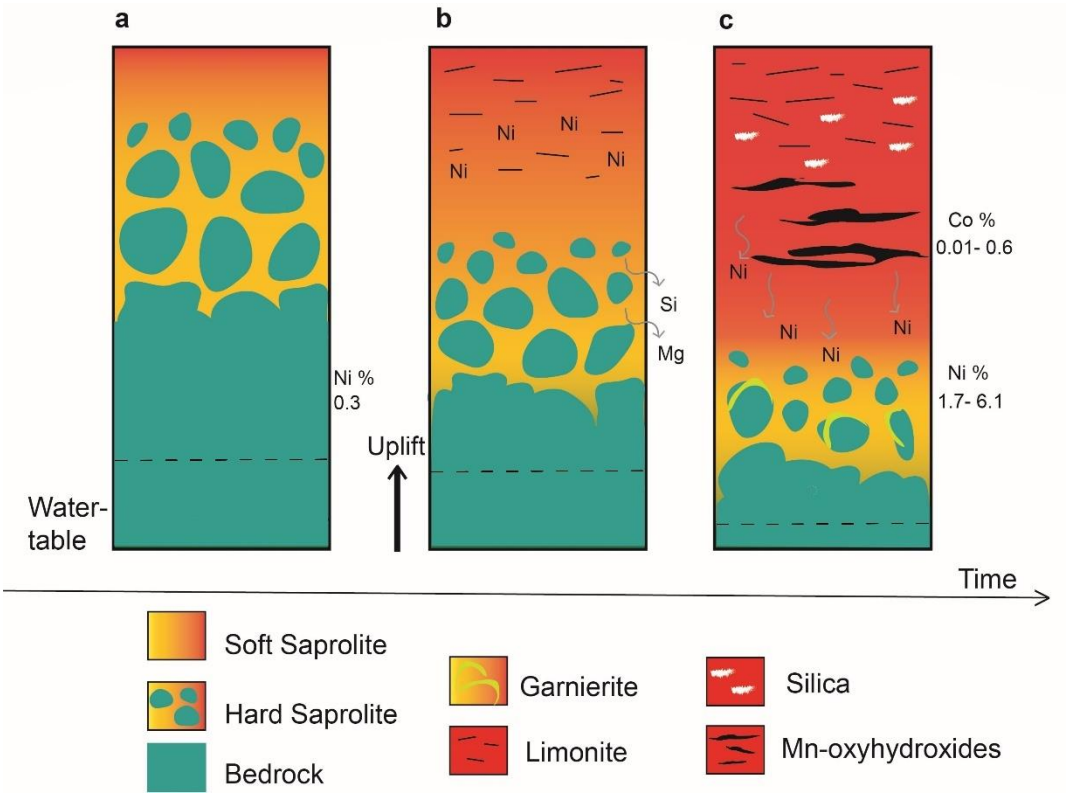

Fig. 26 The evolution stages of the Berong Ni-Co laterite deposit. Long and pervasive chemical weathering of the serpentinized bedrock resulted in the development of the a) saprolite and limonite horizons, b) the effect of uplift under humid wet savannas intensifies the leaching of Mg and Si and in turn, c) Ni is re-mobilized and transported to the deeper section of the profiles leading to hydrous Mg silicate formation in the saprolite, and subsequently Mn oxyhydroxides minerals with secondary silica are formed in the limonite horizon.

limonite horizon and its absolute enrichment in the saprolite horizon. The released Ni may be adsorbed by goethite or may substitute for Mg in serpentine (Golightly, 1979a). The weathering solution supersaturated with Ni and Si results in the precipitation of garnierite in the saprolite horizon (Freysinnet et al., 2005). The favorable pH conditions (pH 5.08- 7.09) and composition of the weathering solutions may have instigated the formation of Mn-oxy-hydroxides in the limonite

Akita University

horizon (Fig. 16c). Also, silica is accumulated in this horizon, which is most likely due to a poor drainage condition (Butt and Cluzel, 2013). Based on geological evidence combined with mineralogical and geochemical data, the Berong Ni-Co laterite deposit evolved through two weathering processes; (i) the formation of the saprolite and the limonite horizons, and (ii) the late precipitation of secondary phyllosilicates (i.e. garnierite), Mn-oxy-hydroxides and silica.

3.7 Conclusions

The Berong Ni laterite deposit is formed by long and intense weathering of the serpentinized dunite bedrock under tropic humid conditions. The olivine in the bedrock contains a significant amount of Ni, indicating that this the primary source of the ore in the saprolite and limonite horizons.

In the saprolite, Ni is principally associated with serpentine and garnierite. Six types of serpentine have a distinct texture with variable Ni contents. Garnierite is a sepiolite-falcondoite and pimelite-kerolite series. Goethite and Mn-oxy-hydroxides, on the other hand, are the principal Ni ore minerals in the limonite horizon. Cobalt is mainly hosted by lithiophorite-asbolane intermediate with a strikingly high Co/Ni ratio (up to 1.60).

The saprolite horizon contains nine times higher Ni content compared to the bedrock, and the bulk Ni concentration reaches up to

Akita University

6.11wt%. In contrast, the limonite horizon contains up to 0.90 wt% Ni. Additionally, the highest Co content generally occurs in the lower section of the limonite (up to 0.90 wt%).

The studied laterite profiles exhibit depletion of Mg and Si near the surface, and preferential enrichment of Fe, Al, Ni, Co and Mn in the weathered horizons. There is an apparent redistribution of Ni and, to some extent Co to the lower section of the limonite and saprolite horizons, which is attributed to the change in pH, oxidation state and tectonic uplift. The transportation of Ni to the deeper part of the studied profiles resulted in the formation of the hydrous Mg silicates. Therefore, supergene Ni enrichment occurred in the Berong laterite deposit, which is comparable to other Ni-laterite deposits in New Caledonia, Indonesia, northeastern Australia, and the Caribbean. Geological evidence correlated with mineralogical and geochemical data suggest that the Berong Ni-Co laterite deposit evolved through two weathering processes; (i) the formation of the saprolite and the limonite horizons, and (ii) the late precipitation of secondary phyllosilicates (i.e. garnierite), Mn-oxy-hydroxides and silica.

Akita University

3.8 References

Almasco, J.N., Rodolfo, K., Fuller, M., Frost, G., 2000. Paleomagnetism of Palawan, Philippines. J. Asian Earth Sci. 18, 369-389.

Andreani, M., Baronnet, A., Boullier, A.M., Gratier, J.P., 2004. A microstructural study of a “crack-seal” type serpentine vein using SEM and TEM techniques. Eur. J. Mineral. 16, 585-595.

Aurelio, M., Peña, R., 2004. (eds.) Geology and Mineral Resources of the Philippines. Geol. 1, 27-30.

Auzende, A.L., Daniel, I., Reynard, B., Lemaire, C., Guyot, F., 2004. High-pressure behavior of serpentine minerals: A Raman spectroscopic study. Phys. Chem. Miner. 31, 269-277.

Bach, W., Paulick, H., Garrido, C.J., Ildefonse, B., Meurer, W.P., Humphris, S.E., 2006. Unraveling the sequence of serpentinization reactions: Petrography, mineral chemistry, and petrophysics of serpentinites from MAR 15°N (ODP Leg 209, Site 1274). Geophys. Res. Lett. 33, 1-4.

Beard, J.S., Frost, B.R., Fryer, P., McCaig, A., Searle, R., Ildefonse, B., Zinin, P., Sharma, S.K., 2009. Onset and progression of serpentinization and magnetite formation in Olivine-rich troctolite from IODP hole U1309D. J. Petrol. 50, 387-403.

Bish, D.L., Brindley, G.W., 1978. Deweylites, mixtures of poorly crystalline hydrous serpentine, and talc-like minerals. Mineral. Mag. 42, 75-79.

Brand, N.W., Butt, C.R.M., Elias, M., 1998. Nickel laterites: classification and features. AGSO J. Aust. Geol. Geophys. 17, 81-88.

Butt, C.R.M., Cluzel, D., 2013. Nickel laterite ore deposits: Weathered serpentinites. Elements. 9, 123-128.

Chassé, M., Griffin, W.L., O’Reilly, S.Y., Calas, G., 2017. Scandium speciation in a world-class lateritic deposit. Geochemical Perspect. Lett. 31, 105-114.

Akita University

Cluzel, D., Vigier, B., 2008. Syntectonic mobility of supergene nickel ores of new caledonia (Southwest Pacific). Evidence from garnierite veins and faulted regolith. Resour. Geol. 58, 161-170.

Cui, H., You, L., Feng, X., Tan, W., Qiu, G., Liu, F., 2009. Factors governingthe formation of lithiophorite at atmospheric pressure. Clays Clay Miner. 57, 353-360.

Dowding, C.E., Fey, M. V., 2007. Morphological, chemical and mineralogical properties of some manganese-rich oxisols derived from dolomite in Mpumalanga province, South Africa. Geoderma. 141, 23-33.

Dublet, G., Juillot, F., Morin, G., Fritsch, E., Fandeur, D., Ona-Nguema, G., Brown, G.E., 2012. Ni speciation in a New Caledonian lateritic regolith: A quantitative X-ray absorption spectroscopy investigation. Geochim. Cosmochim. Acta. 95, 119-133.

Dublet, G., Juillot, F., Morin, G., Fritsch, E., Fandeur, D., Brown, G.E., 2015. Goethite aging explains Ni depletion in upper units of ultramafic lateritic ores from New Caledonia. 160, 1-15. Geochim. Cosmochim. Acta. 160, 1-15.

Dublet, G., Juillot, F., Brest, J., Noël, V., Fritsch, E., Proux, O., Olivi, L., Ploquin, F., Morin, G., 2017. Vertical changes of the Co and Mn speciation along a lateritic regolith developed on peridotites (New Caledonia). Geochim. Cosmochim. Acta. 217, 1-15.

Dzemua, G.L., Mees, F., Stoops, G., Van Ranst, E., 2011. Micromorphology, mineralogy, and geochemistry of lateritic weathering over serpentinite in south-east Cameroon. J. African Earth Sci. 60, 38-48.

Dzemua, G.L., Gleeson, S.A., Schofield, P.F., 2013. Mineralogical characterization of the Nkamouna Co-Mn laterite ore, southeast Cameroon. Miner. Depos. 48, 155-171.

Elias, M., 2002. Nickel laterite deposits – geological overview, resources and exploitation. Giant Ore Depos. Charact. Genes. Explor. CODES Spec. Publ. 4, 205-220.

Eliopoulos, D.G., Economou-Eliopoulos, M., Apostolikas, A., Golightly, J.P., 2012. Geochemical features of nickel-laterite deposits from

Akita University

the Balkan Peninsula and Gordes, Turkey: The genetic and environmental significance of arsenic. Ore Geol. Rev. 48, 413-427.

Encarnacion, J.P., Essene, E.J., Mukasa, S.B., Hall, C.H., 1995. High-pressure and-temperature subophiolitic kyanite—garnet amphibolites generated during initiation of mid-Tertiary subduction, Palawan, Philippines. J. Petrol. 36, 1481-1503.

Fan, R., Gerson, A.R., 2015. Synchrotron micro-spectroscopic examination of Indonesian nickel laterites. Am. Mineral. 100, 926-934.

Faure, M., Marchadier, Y., Rangin, C., 1989. Pre-Eocene Synmetamorphic Structure in the Mindoro-Romblon-Palawan Area, West Philippines, and implications for the history of southeast Asia. Tectonics. 8, 963-979.

Faust, G.T., 1966. The hydrous nickel-magnesium silicates—the garnierite group. Am. Mineral. 51, 279-298.

Freyssinet, P., Butt, C.R.M., Morris, R.C., Piantone, P., 2005. Ore-forming processes related to lateritic weathering. Econ. Geol. 100, 681-722.

Fritsch, E., Juillot, F., Dublet, G., Fonteneau, L., Fandeur, D., Martin, E., Caner, L., Auzende, A.L., Grauby, O., and Beaufort, D., 2016. An alternative model for the formation of hydrous Mg/Ni layer silicates (“deweylite”/“garnierite”) in faulted peridotites of New Caledonia: I. Texture and mineralogy of a paragenetic succession of silicate infillings. Eur J Mineral. 28, 295–311.

Frost, B.R., Evans, K.A., Swapp, S.M., Beard, J.S., Mothersole, F.E., 2013. The process of serpentinization in dunite from New Caledonia. Lithos. 178, 24-39.

Fu, W., Yang, J., Yang, M., Pang, B., Liu, X., Niu, H., Huang, X., 2014. Mineralogical and geochemical characteristics of a serpentinite-derived laterite profile from East Sulawesi, Indonesia: Implications for the lateritization process and Ni supergene enrichment in the tropical rainforest. J. Asian Earth Sci. 93, 74-88.

Akita University

Fuller, M., Haston, R., Lin, J.L., Richter, B., Schmidtke, E., Almasco, J., 1991. Tertiary paleomagnetism of regions around the South China Sea. J. Southeast Asian Earth Sci. 6, 161-184.

Galí, S., Soler, J.M., Proenza, J.A., Lewis, J.F., Cama, J., Tauler, E., 2012. Ni enrichment and stability of Al-free garnierite solid-solutions: A thermodynamic approach. Clays Clay Miner. 60, 121-135.

Gleeson, S.A., Herrington, R.J., Durango, J., Velásquez, C.A., Koll, G., 2004. The mineralogy and geochemistry of the Cerro Matoso S.A. Ni Laterite deposit, Montelíbano, Colombia. Econ. Geol. 99, 1197-1213.

Golden, D.C., Dixon, J.B., Kanehiro, Y., 1993. The manganese oxide mineral, lithiophorite, in an oxisol from Hawaii. Aust. J. Soil Res. 31, 51-66.

Golightly, J.P., Arancibia, O.N., 1979. The chemical composition and infrared spectrum of nickel-and iron-substituted serpentine from a nickeliferous laterite profile, Soroako, Indonesia. The Can Mineral. 17, 719-728.

Golightly, J.P., 1981. Nickeliferous laterite deposits. Econ Geol 75th Anniv. 75, 710-735.

Holloway, N.H., 1981. The North Palawan block, Philippines: its relation to the Asian Mainland and its role in the evolution of the South China Sea. Bull. Geol. Soc. Malaysia. 14, 19-58.

Hyndman, R.D., Peacock, S.M., 2003. Serpentinization of the forearc mantle. Earth Planet. Sci. Lett. 2003, 417-432.

Imai, N., Terashima, S., Itoh, S., and Ando, A., 1995. 1994 compilation of analytical data for minor and trace elements in seventeen GSJ geochemical reference samples, “Igneous rock series.” Geostandard Newslett. 19, 135-213.

Imai, N., Terashima, S., Itoh, S., and Ando, A., 1999. 1998 compilation of analytical data for five GSJ geochemical reference samples: The “Instrumental analysis series.” Geostandard Newslett. 23, 223-250.

Akita University

Klein, C., Dutrow, B., 2007. Mineral science. John Wiley and Sons, Inc., Hoboken, NJ. 23, 675.

Kuhnel, R.A., Roorda, H.J., Steensma, J.J.S., 1978. Distribution and partitioning of elements in nickeliferous laterites. Bull Bur Rech Geol Minieres Deux. Ser Sect 2, 191-206.

Loganathan, P., Burau, R.G., Fuerstenau, D.W., 1977. Influence of pH on the Sorption of Co2+, Zn2+, and Ca2+ by a Hydrous Manganese Oxide1. Soil Sci. Soc. Am. J. 1, 57-62.

Manceau, A., Schlegel, M.L., Musso, M., Sole, V.A., Gauthier, C., Petit, P.E., Trolard, F., 2000. Crystal chemistry of trace elements in natural and synthetic goethite. Geochim. Cosmochim. Acta. 21, 3643-3661.

Marsh, E., Anderson, E., Gray, F., 2011. Ni-Co laterites–a deposit model. US Geol Surv.1, 1-9.

McKenzie, R.M., 1989. Manganese oxides and hydroxides. In: Minerals in Soil Environment (J.B. Dixon & S.B. Weed editors). SSSA. 1, 439-465.

Mitchell, A.H.G., Hernandez, F., dela Cruz, A.P., 1986. Cenozoic evolution of the Philippine archipelago. J. Southeast Asian Earth Sci. 1, 3-22.

MMAJ-JICA, 1987. Report on the Mineral Exploration, Mineral Deposits, and Tectonics of Two Contrasting Geologic Environments in the Philippines, Phase 3, Northern Sierra Madre Area. 1, 1-24.

Muñoz, M., Ulrich, M., Cathelineau, M., Mathon, O., 2019. Weathering processes and crystal chemistry of Ni-bearing minerals in saprock horizons of New Caledonia ophiolite. J. Geochemical Explore. 198, 82-99.

Nickel, E.H., 1992. Solid solutions in mineral nomenclature. Eur. J. Mineral. 46, 49-53.

Norton, S.A., 1973. Laterite and bauxite formation. Econ. Geol. 68, 353-361.

Akita University

O'Hanley, D.S., 1996. Serpentinites: records of tectonic and petrological history. Oxford University Press on Demand. 135, 143-158.

Oufi, O., 2002. Magnetic properties of variably serpentinized abyssal peridotites. J. Geophys. Res. 107, 1-19.

Petriglieri, J.R., Salvioli-Mariani, E., Mantovani, L., Tribaudino, M., Lottici, P.P., Laporte-Magoni, C., Bersani, D., 2015. Micro-Raman mapping of the polymorphs of serpentine. J. Raman Spectrosc. 46, 953-958.

Ponthieu, M., Juillot, F., Hiemstra, T., Van Riemsdijk, W.H., Benedetti, M.F., 2006. Metal ion binding to iron oxides. Geochim. Cosmochim. Acta. 70, 2679-2698.

Power, I. M., Wilson, S. A., Dipple, G. M., 2013. Serpentinite carbonation for CO_2 sequestration. Elements. 9, 115-121.

Putzolu, F., Balassone, G., Boni, M., Maczurad, M., Mondillo, N., Najorka, J., Pirajno, F., 2018. Mineralogical association and Ni-Co deportment in the Wingellina oxide-type laterite deposit (Western Australia). Ore Geol. Rev. 196, 282-296.

Quesnel, B., de Veslud, C. L. C., Boulvais, P., Gautier, P., Cathelineau, M., & Drouillet, M., 2017. 3D modeling of the laterites on top of the Koniambo Massif, New Caledonia: refinement of the per descensum lateritic model for nickel mineralization. Miner Deposita. 52, 961-978.

Raschka, H., Nacario, E., Rammlmair, D., Samonte, C., Steiner, L., 1985. Geology of the ophiolite of central Palawan Island, Philippines. Ofioliti (Italy). 10, 375-390.

Ratié, G., Jouvin, D., Garnier, J., Rouxel, O., Miska, S., Guimarães, E., Cruz Vieira, L., Sivry, Y., Zelano, I., Montarges-Pelletier, E., Thil, F., Quantin, C., 2015. Nickel isotope fractionation during tropical weathering of ultramafic rocks. Chem. Geol. 402, 68-76.

Ratié, G., Garnier, J., Calmels, D., Vantelon, D., Guimarães, E., Monvoisin, G., Nouet, J., Ponzevera, E., Quantin, C., 2018. Nickel distribution and isotopic fractionation in a Brazilian lateritic regolith: Coupling Ni isotopes and Ni K-edge XANES. Geochim. Cosmochim. Acta. 230, 137-154.

Akita University

Roqué-Rosell, J., Mosselmans, J.F.W., Proenza, J.A., Labrador, M., Galí, S., Atkinson, K.D., Quinn, P.D., 2010. Sorption of Ni by “lithiophorite-asbolane” intermediates in Moa Bay lateritic deposits, eastern Cuba. Chem. Geol. 275, 9-18.

Samama, J. C., 1986. Ore fields and continental weathering. New York: Van Nostrand Reinhold Company. 224-249.

Soler, J. M., Cama, J., Gali, S., Meléndez, W., Ramírez, A., Estanga, J., 2008. Composition and dissolution kinetics of garnierite from the Loma de Hierro Ni-laterite deposit, Venezuela. Chem. Geol. 249, 191-202.

Sonzogni, Y., Treiman, A.H., Schwenzer, S.P., 2017. Serpentinite with and without brucite: A reaction pathway analysis of natural serpentinite in the Josephine ophiolite, California. J. Mineral. Petrol. Sci. 112, 59-76.

Speakman, K., Majumdar, A.J., 1971. Synthetic ‘deweylite.’ Mineral. Mag. 38, 225-234.

Tarling, M.S., Rooney, J.S., Viti, C., Smith, S.A.F., Gordon, K.C., 2018. Distinguishing the Raman spectrum of polygonal serpentine. J. Raman Spectrosc. 49, 1978-1984.

Tauler, E., Proenza, J.A., Galí, S., Lewis, J.F., Labrador, M., García-Romero, E., Suarez, M., Longo, F., Bloise, G., 2009. Ni-sepiolite-falcondoite in garnierite mineralization from the Falcondo Ni-laterite deposit, Dominican Republic. Clay Miner. 44, 435-454.

Tauler, E., Lewis, J. F., Villanova-de-Benavent, C., Aiglsperger, T., Proenza, J. A., Domènech, C., Galí, S., 2017. Discovery of Ni-smectite-rich saprolite at Loma Ortega, Falcondo mining district (Dominican Republic): geochemistry and mineralogy of an unusual case of “hybrid hydrous Mg silicate–clay silicate” type Ni-laterite. Miner. Deposita. 52, 1011-1030.

Taylor, R.M., McKenzie, R.M., Norrish, K., 1964. The mineralogy and chemistry of manganese in some Australian soils. Aust. J. Soil Res. 2, 235-248.

Taylor, R.M., McKenzie, R.M., 1966. The association of trace elements with manganese minerals in Australian soils. Aust. J. Soil Res. 4, 29-39.

Akita University

Taylor, B., Hayes, D.E., 1983. Origin and history of the South China Sea basin. Tecton. Geol. Evol. Southeast Asian seas islands. Part 2. 27, 23-56.

Toft, P.B., Arkani-Hamed, J., Haggerty, S.E., 1990. The effects of serpentinization on density and magnetic susceptibility: a petrophysical model. Phys. Earth Planet. Inter. 65, 137-157.

Trescases, J. J., 1973. Weathering and geochemical behavior of the elements of ultramafic rocks in New Caledonia. Bureau of Mineral Resources, Geology and Geophysics, Canberra, Extract from Bulletin. 141, 149-161.

Trescases JJ (1997). The lateritic nickel-ore deposits. J Soil Sediment. 125-138.

Trivedi, P., Axe, L., 2001. Predicting divalent metal sorption to hydrous Al, Fe, and Mn oxides. Environ. Sci. Technol. 35, 1779-1784.

Trolard, F., Tardy, Y., 1989. A model of Fe 3+-kaolinite, Al 3+-goethite, Al 3+-hematite equilibria in laterites. Clay Miner. 24, 1-21.

Ulrich, M., Cathelineau, M., Muñoz, M., Boiron, M.C., Teitler, Y., Karpoff, A.M., 2019. The relative distribution of critical (Sc, REE) and transition metals (Ni, Co, Cr, Mn, V) in some Ni-laterite deposits of New Caledonia. J. Geochemical Explor. 197, 93-113.

United Nations Development Programme, 1985. Geology of Central Palawan. Technical Report No. 6, United Nations Development Programme, New York. 45.

Villanova-de-Benavent, C., Proenza, J.A., Galí, S., García-Casco, A., Tauler, E., Lewis, J.F., Longo, F., 2014. Garnierites and garnierites: Textures, mineralogy, and geochemistry of garnierites in the Falcondo Ni-laterite deposit, Dominican Republic. Ore Geol. Rev. 58, 91-109.

Villanova-de-Benavent, C., Domènech, C., Tauler, E., Galí, S., Tassara, S., & Proenza, J. A., 2017. Fe–Ni-bearing serpentines from the saprolite horizon of Caribbean Ni-laterite deposits: new insights from thermodynamic calculations. Miner Deposita. 52, 979-992.

Akita University

Wolfart, R., Čepek, P., Gramann, F., Kemper, E., Porth, H., 1986. Stratigraphy of Palawan Island, Philippines. Newsletters Stratigr. 16, 19-48.

Yongue-Fouateu, R., Ghogomu, R.T., Penaye, J., Ekodeck, G.E., Stendal, H., Colin, F., 2006. Nickel and cobalt distribution in the laterites of the Lomié region, south-east Cameroon. J. African Earth Sci. 45, 33-47.

Yumul, G.P., Dimalanta, C.B., Marquez, E.J., Queaño, K.L., 2009. Onland signatures of the Palawan microcontinental block and Philippine mobile belt collision and crustal growth process: A review. J. Asian Earth Sci. 34, 610-623.

Akita University

CHAPTER 4

Ni-Co mineralization in the Intex laterite deposit, Mindoro, Philippines

Abstract

The Intex laterite deposit in Mindoro, Philippines is derived from the weathering of the ultramafic rocks under a tropical climate. This study investigates the several types of serpentines and the effect of the degree of chemical weathering of ultramafic rocks and laterites on the enrichment of Ni in the deposit. The five types of serpentines are differentiated based on their textural features and Raman spectral data. Type I, type II, type III, and type IV serpentines contain a low amount of NiO (avg. 0.15 wt%), and their formation is linked to the previous exhumation of the ultramafic body. Conversely, type V serpentines show the highest NiO contents (avg. 1.42 wt%) and have the composition of serpentine-like garnierites, indicating a supergene origin. In the limonite horizon, goethite is the main ore mineral and shows high NiO contents of up to 1.68 wt%, whereas the Mn-oxyhydroxides (i.e. asbolane and lithiophorite-asbolane intermediate) display substantial amounts of CoO (up to 11.3 wt%) and NiO (up to 15.6 wt%). The Ultramafic Index of Alteration (UMIA) and Index of Lateritization (IOL) are used to characterize the different stages of weathering of rocks and laterites. The calculated index values correspond to a less advanced stage of weathering of the Intex laterites compared with the Berong laterites. The Berong deposit is a

Akita University

Ni-Co laterite deposit in the Philippines, which is formed from the weathering of the serpentinized peridotite. The less extreme degree of weathering of the Intex laterites indicates less advanced leaching, and thereby the re-distribution of Ni, Si, and Mg from the limonite towards the saprolite horizon may have resulted in the poor precipitation of talc-like (kerolite-pimelite) and sepiolite-like (sepiolite-falcondoite) phases in the studied saprolite horizon. Nickel in the Intex deposit has undergone supergene enrichment similar to other humid tropical laterite deposits.

4.2 Introduction

Nickel laterite deposits are derived from chemical weathering of ultramafic rocks, and contain a significant amount of Ni, and to some extent, Co and Sc (Butt and Cluzel, 2013). Most Ni laterite deposits occur in the present humid tropics, and tectonically active collision zones, including New Caledonia, Indonesia, the Philippines, and Cuba, but some are situated in cratonic areas in Australia, Brazil, and West Africa (Elias, 2002). Nickel laterite deposits are commonly divided into three types based on the main Ni hosting minerals such as oxide deposits, hydrous Mg silicates, and clay silicate deposits (Brand et al., 1998; Freyssinet et al., 2005). Each of these categories has implications on the assessment of resource and mineral processing (Gleeson et al., 2004; Butt and Cluzel, 2013). A typical Ni laterite profile consists from the bottom to top: (i) unaltered or serpentinized ultramafic rocks, (ii) saprolite horizon and (iii) limonite horizon. This

Akita University

profile is often covered by goethite-rich ferricrete (Fontanaud and Meunier, 1983).

An increasing number of studies focus on the distribution of Ni, Co, and Sc in laterite deposits developed above serpentinite or peridotite bedrock (Fontanaud and Meunier, 1983; Yongue-Fouateu et al., 2006; Thorne et al., 2012; Fu et al., 2014). Earlier work reported that understanding the sorption mechanism of Ni in the limonite horizon, pH conditions, and soil porosity give further insight into the mobility of Ni within the laterite profiles (Roqué-Rosell et al., 2010). Another study investigated the Ni content of laterites with contrasting mineralogy and crystallinity to understand the enrichment or depletion of Ni upon weathering (Dublet et al., 2015). Recent work utilized geochemical transport modeling to explain the conditions and processes crucial for Ni mineralization (Myagkiy, 2017). Despite the numerous works towards understanding the behavior of Ni in laterites, there is a gap of knowledge about the behavior of Ni in serpentine in the bedrock and saprolite horizon (Cluzel and Vigier, 2008; Villanova-de-Benavent et al., 2014; Muňoz et al., 2019).

This study investigates the different types of serpentine found in the bedrock and the saprolite horizon. The chemistry and textures of the serpentines are used to determine the spatial relations between the previous serpentinization and the Ni-bearing serpentines in the saprolite horizon. Emphasis is also given on examining the main Co-hosting minerals in the limonite horizon of the Intex deposit. Based on the mineralogical and geochemical studies of the studied deposit, this

Akita University

work explores the effect of the degree of chemical weathering of ultramafic rocks and laterites on the enrichment of Ni in the profiles. Two weathering indexes, namely Ultramafic Index of Lateritization (UMIA) and Index of Lateritization (IOL), are utilized to show the degree of chemical weathering of rocks and laterites in the Intex deposit. We then compare the index results of this study with another tropical laterite deposit, which is the Berong Ni-Co laterite deposit in Palawan, Philippines.

4.3 Geological setting and Topographic features

4.3.1 Regional geology

The Mindoro island, situated in the western-central Philippines (Figure 27a), exhibits the imprints of the Miocene-age arc-continent collision event involving the Palawan Continental Block (PCB) and the Philippine Mobile Belt (PMB) (Hamilton, 1979). There are opposing suggestions on whether the whole island is continentally derived (Holloway, 1982; Rangin et al., 1985; Bird et al., 1993) or only the southwest portion is associated with Palawan (Karig, 1973; Mitchell et al., 1986; Sarewitz and Karig, 1986).

The Mindoro island is separated into two blocks: (i) the southwest block, which is comparable to continental-derived PCB, and (ii) the northeast block, which has PMB island-arc affinity (Karig, 1973; Sarewitz and Karig, 1986). The two blocks are separated by the northwest-southeast steeply dipping lithospheric boundary, known as the Mindoro Suture Zone, which is cut by the more recent transcurrent

Akita University

fault; East Mindoro Fault Zone (Sarewitz and Karig, 1986). Three ophiolite belts are found in the Mindoro Suture Zone; the Cretaceous Manyan Complex, Eocene Puerto Galera Complex and mid-Oligocene Amnay Complex (Figure 27b) (Hashimoto and Sato, 1968; Rangin et al., 1985; Karig and Sarewitz, 1986). The multiphase collisions that occurred from Early to Middle Miocene along this suture zone result in the exposure of the various ophiolites in the island (Yumul et al., 2003; Yumul et al., 2005).

In northwestern Mindoro, the basement rocks are composed of metamorphic rocks and minor amounts of ophiolitic fragments of the Mangyan ophiolitic complex, which are designated as the Halcon Metamorphics (Faure et al., 1989; Concepcion et al., 2012). The Halcon Metamorphics consist mainly of chlorite, graphite schist, quartz mica with phyllite, slate and amphibolites. This metamorphic complex was initially a mélange, which was subjected to regional metamorphism after the Cretaceous period (Faure et al., 1989).

The study area in northeastern Mindoro Suture Zone encompasses the Mangyan Ophiolitic Complex and Lasala Formation. The Intex exploration project area lies in the Mangyan Ophiolitic Complex in the north-central part of the island, which is 40 km south of Calapan. A total of three drill cores, namely BB2515, PG1500, and BB2406, were examined at Victoria drill core house in Mindoro, Philippines (Figure 27c).The Mangyan Ophiolitic Complex comprises of mafic rocks such as gabbro, sheeted dike complex, pillow lavas, but ultramafic rocks are scarce (Hashimoto and Sato, 1968; Karig and Sarewitz, 1986).

Akita University

The Late Eocene Lasala Formation consists dominantly of interbedded sandstone and shale with mudstone, conglomerate, limestone, basalt flows, and dikes. The clasts of conglomerate contain mostly of basalt and chert (Hashimoto and Sato, 1968). Earlier works (Concepcion et al., 2012; Mitchell et al., 1986; Boudier et al., 1988) proposed that the Cretaceous Mangyan Ophiolitic Complex was emplaced immediately after its formation based on the occurrence of amphibolite sole below the ultramafic rock complex.

4.3.2 Topography

The Ni-laterite ore deposits of Mindoro are in the mountainous interior of the island, and the three highest peaks in this area are Mt. Halcon (2582 m), Mt. Baco (2488 m) and Mt. Iglit (2364 m). The Intex project area lies in the north-central part of the island, which is 40 km south of Calapan. The Intex's concession area covers an elevation area, which ranges from 135 m in the north-east section to 1460 m near the southwestern part (Figure 28) (Petersen et al., 2010).

The topography varies from rolling hills and moderate relief with elevation up to 300 m to high plateaus and sharp-crested ridges at an altitude of more than 1200 m. The intermediate plateaus mainly divided by incised V-shaped stream valleys. It is found that the terrain with a

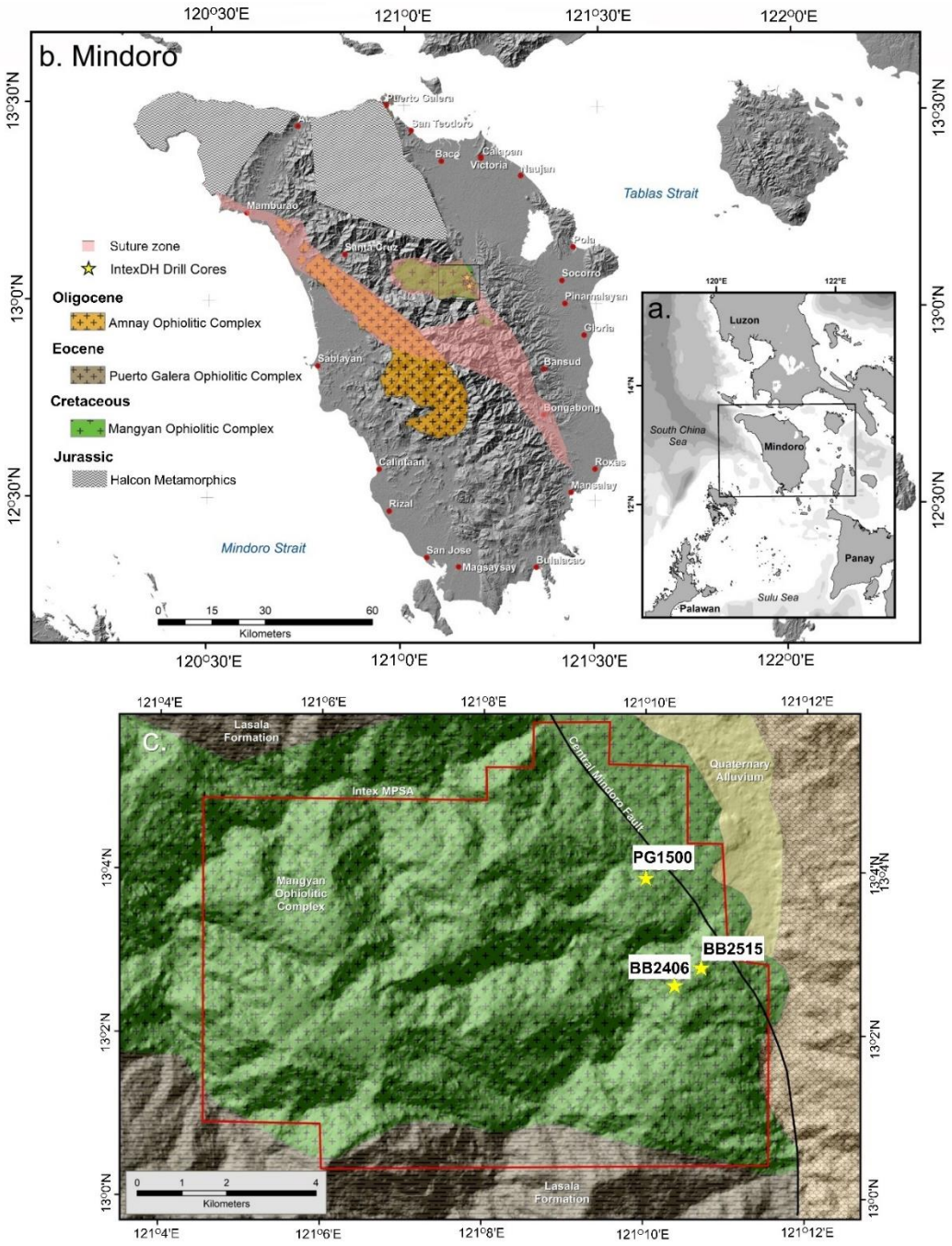

Fig. 27 Location map of a) Mindoro b) three ophiolitic complexes on the island, c) three drill cores used in this study.

slope less than 30˚ has a well-developed laterite profile above the ultramafic rocks. The laterite profile is typically thin or absent when the slope is steeper (Petersen et al., 2010).

Akita University

4.3.3 Intex Ni-Co laterite profiles

The laterite profiles observed in the drill cores are divided from bottom to top into: (i) serpentinized ultramafic rocks, (ii) saprolite horizon, and (iii) limonite horizon. The bulk Fe concentration, texture and mineralogy of the rock and laterite were used to distinguish each horizon. The thickness of the laterite ranges from 13 m to 16 m. The ultramafic rocks in the studied cores are characterized by mm-wide serpentine veins. In this study, lherzolite (BB2515 core), clinopyroxenite (PG1500 core) and harzburgite-dunite bedrock (BB2406 core) are examined (Figure 29a – 29c).

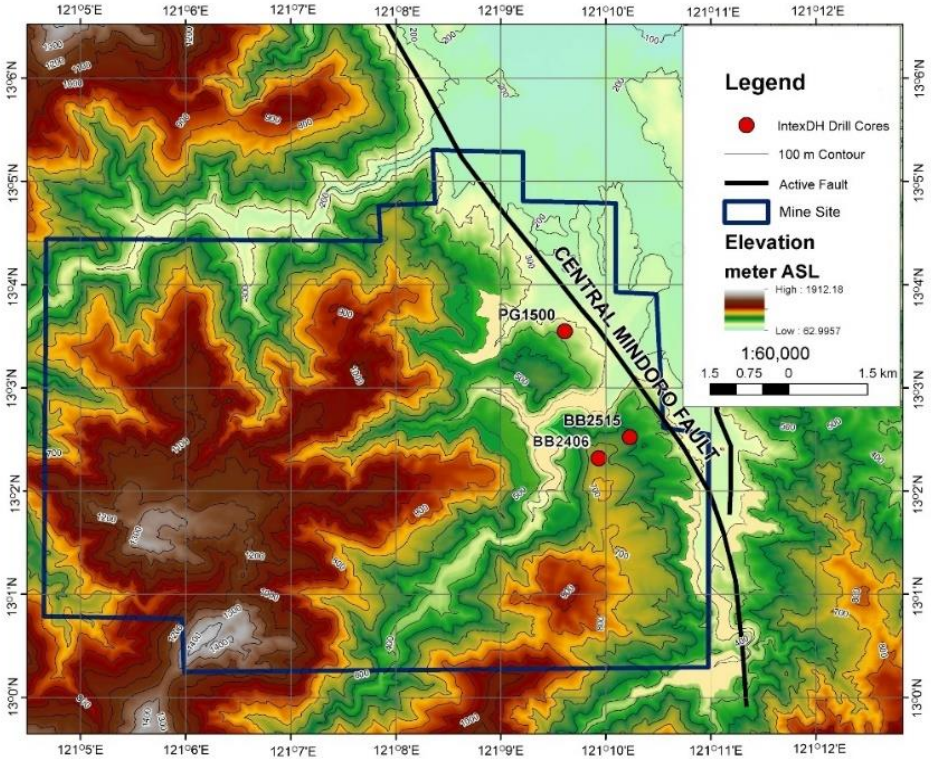

Fig. 28. Relief map showing the studied drill cores within the Intex's exploration project area.

Overlying the serpentinized bedrock is the saprolite horizon, which is generally yellow-brown, and porous. The saprolite horizon is well developed in all studied cores with thickness ranging from 3 m to 8 m.

Akita University

This horizon contains a combination of earthy materials and coarse-grained to gravel size rocks remnants (Figure 29d). Residual silica and Mn-oxyhydroxides often occur as coatings on the surface of moderately weathered rocks. A thick layer of residual silica marks the saprolite horizon of PG1500 core derived from clinopyroxenite bedrock in contrast to other cores.

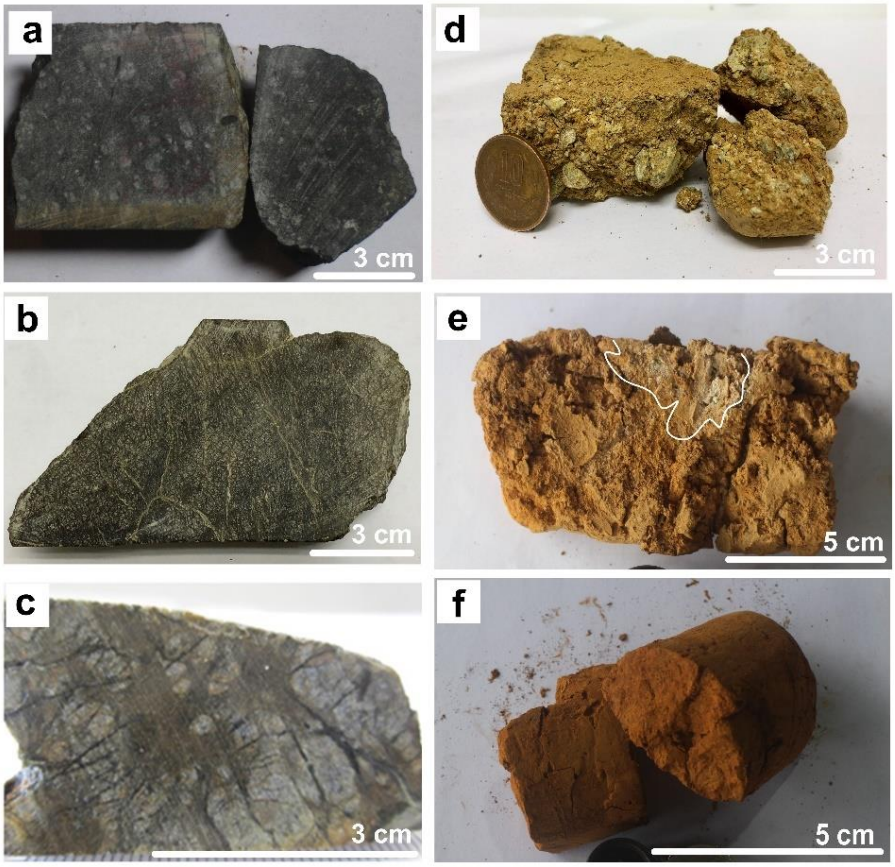

Fig. 29 Photos of (**a**) serpentinized lherzolite (BB2515 core), (b) harzburgite-dunite (BB2406 core), and (**c**) clinopyroxenite (PG1500 core),(**d**) earthy material including pebble-sized rock remnants (**e**) dark orange highly weathered materials and (**f**) silica-bearing limonite sample from the limonite horizon.

Approximately 3 m to 4.5 m of the limonite horizon is developed above the saprolite horizon. Irregular patches of residual silica are occasionally found on the upper section of the limonite horizon (Figure

Akita University

29e). Figure 29f displays an example of dark orange colored and friable limonite.

4.4 Sampling and analytical methods

Samples from the bedrock, saprolite and limonite horizons were collected from the three drill cores mentioned above. These samples were air-dried at 20 ˚C to 30 ˚C for one to two weeks. Then these were quartered and powdered using mortar and pestle.

The pH measurement of 26 representative samples was conducted. Twenty grams of powdered sample and 20 ml of distilled water were transferred in a 50 ml container and were mixed. The mixed solution was continuously stirred for one minute and at a 10-minute interval for 30 minutes. The pH meter was calibrated using pH 4, 7, and 10 standard solutions under 20 ˚C to 25 ˚C temperature conditions. The pH meter was then dipped into the solution, and a pH measurement to the nearest 0.01 pH unit was acquired. Lastly, the electrode was rinsed with tap and distilled water.

Twenty polished thin sections and polished samples were prepared. The modal proportions of olivine, orthopyroxene, clinopyroxene, talc, and serpentine in the bedrock were determined by point-counting method under an optical microscope. A total of 2,500 points were covered for each polished thin section. The saprolite and limonite samples were impregnated with petropoxy resin prior to sectioning and polishing.

The bulk mineralogy of the sample was analyzed using X-ray Powder Diffraction (XRPD) at Akita University, Japan. The Rigaku

Akita University

MultiFlex XRD with Cu Kα radiation source is operated at 30 kV and 10 mA with a step size of 0.02 and a scan step of 20° per minute. Mineral identification was accomplished using the COD reference database of MATCH! software-based on 'figure-of-merit" values and visual inspection relative to the experimental diffraction pattern.

The polymorphs of serpentine were distinguished using an inVia Renishaw Raman microscope of Akita University. This instrument is equipped with a 100 mW 532 nm frequency-doubled Nd: YAG laser and a CCD detector. A 1800 lines/mm grating was used to disperse the signal onto the CCD detector. Before the analysis of polished thin sections, the analyzer was calibrated using the Si-Au standard. Ten percent to 50% laser power was used, and the minerals were observed under a 50x objective lens. Both the spectra from low wavenumbers (100-500 cm^{-1}) and high wavenumbers (3600-4000 cm^{-1}) were collected for mineral identification. The background fluorescence and noise were removed using the WiRE™ software. The Raman signatures of the serpentine polymorphs from this study were compared to rruff.info database and previous results (Auzende et al., 2002; Petriglieri et al., 2015; Ulrich et al., 2019) (Appendix A).

The chemical composition of the silicate and oxide minerals was acquired by the JEOL JXA-8530F Field Emission Electron Probe Microanalyzer (FE-EPMA) of the Geological Survey of Japan (GSJ), National Institute of Advanced Industrial Science and Technology (AIST) in Tsukuba, Japan. The operation conditions were 20 kV voltage, 20 nA probe current and spot size to 5 µm beam diameter.

Akita University

Various JEOL reference standards were utilized to calibrate the instrument including MgO (Mg, TAPH, Kα), SiO_2 (Si, TAP, Kα), Al_2O_3 (Al, TAPH, Kα), Fe_2O_3 (Fe, LIFH, Kα), MnO (Mn, LIFH, Kα), $CaSiO_3$ (Ca, PETH, Kα), NiO (Ni, LIFH, Kα), CoO (Co, LIFH, Kα) and Cr_2O_3 (Cr, LIFH, Kα). The raw counts were corrected through the ZAF procedure.

The whole-rock composition of representative samples was obtained by Rigaku ZSX Primus III+ X-ray Fluorescence (XRF) Spectrometer. Forty powdered samples were oven-dried at 105˚C for over 30 minutes. The mixture of 0.5 g sample and di-lithium tetraborate was fused at 1250˚C in a Pt crucible using a high-frequency fusion instrument (HERZOG HAG-M-HF). Then this mixture was cooled on a Pt disk, and the fused glass beads were analyzed using the XRF spectrometer. The voltage used is 50 kV and a current of 50 mA. Two calibration curves were prepared using a different set of OREAS reference standards for SiO_2, Al_2O_3, P_2O_5, TiO_2, Cr_2O_3, MnO, Fe_2O_3, Co_2O_3, and NiO, whereas GSJ standards for Na_2O, MgO, K_2O, and CaO (Imai et al., 1995; 1999). Five international standards, including JP-A (peridotite), JB-1b (basalt), JG-3 (granodiorite), OREAS 401 (Fe ore), OREAS 180 and OREAS 184 (Ni laterite ore) were used to evaluate the accuracy of the analytical results. The loss-on-ignition (LOI) of each representative sample was obtained. Both XRF and LOI were done at GSJ, AIST in Tsukuba.

Akita University

4.5 Results

4.5.1 XRPD analyses

Figures 30 and 31 show the XRPD pattern of the bedrock and laterite samples, and corresponding d-spacing values of each mineral. The interplanar spacing between the atoms in the crystal (d-spacing) was calculated using Bragg's equation ($n\lambda = 2d\sin\theta$), where n is a positive integer (first order Bragg diffraction peak), and lambda λ is the wavelength of the incident wave. Serpentine, olivine, pyroxene are the dominant minerals in the bedrock with a trace amount of chromite (Figure 30). The strong reflection at 7.25 Å and weaker reflections at 4.60 Å and 3.60 Å are characteristics of serpentine. In the saprolite horizon, serpentine is the major mineral, whereas chromite, goethite, talc, quartz, actinolite, relict olivine, and pyroxene occur as accessory constituents (Figure 30). The minor peaks at 3.12 Å and 8.40 Å belong to actinolite (Figure 31a). The limonite horizon consists mainly of goethite. Hematite, talc, chromite, magnetite, asbolane, and quartz occur in minor to trace amounts. XRPD analysis of the limonite samples shows the occurrence of talc of which reflections are at 9.36 Å (d_{001}), 4.67 Å (d_{002}) and 3.12 Å (d_{003}) (Figure 31a). The 9.44 Å and 4.74 Å peaks belong to asbolane (Figure 31b).

4.5.2 Mineral descriptions

Based on modal proportions of the primary olivine (> 50-72%), orthopyroxene (20-36%) and clinopyroxene (8-13%), two bedrock

samples from BB2515 core are identified as lherzolite (Fig. 32). On the other hand, the BB2406 core has two differing bedrock types,

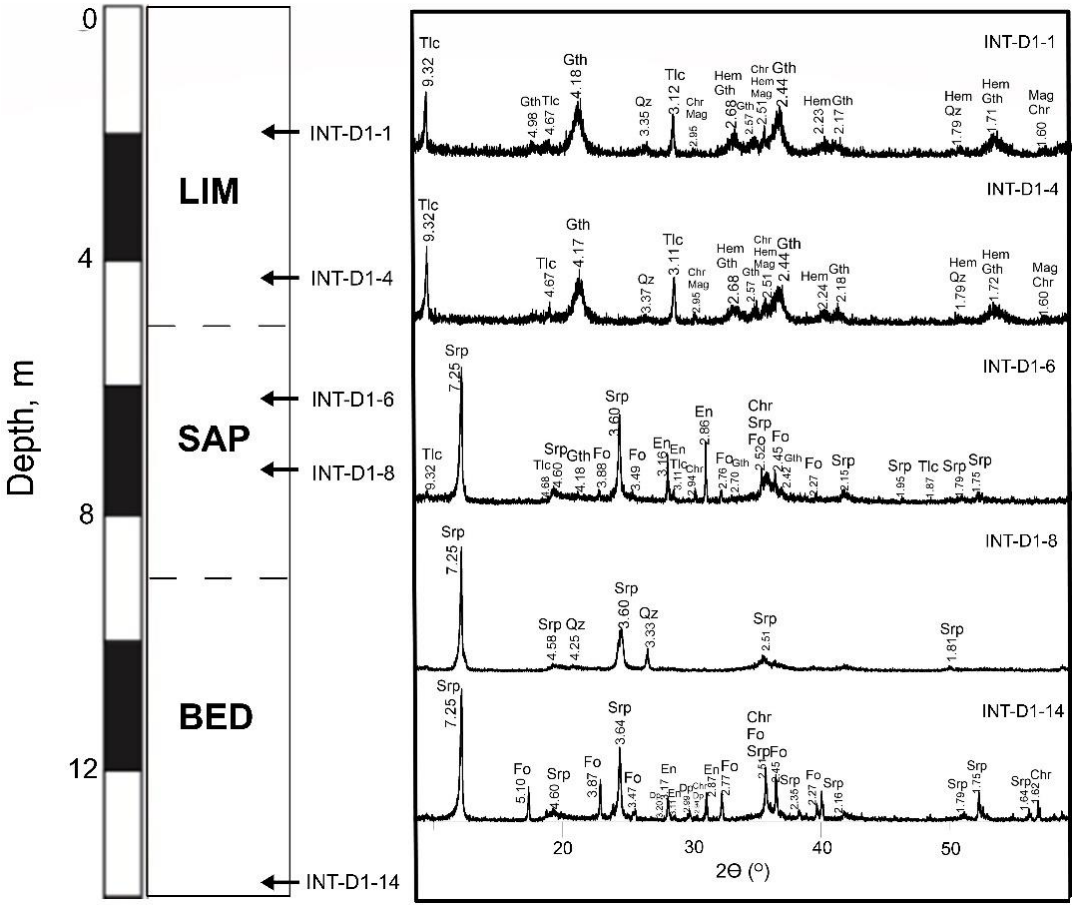

Fig. 30 Stacked XRPD patterns of bedrock, saprolite and limonite representative samples from BB2515 drill core. *Fo- forsterite, En- enstatite, Srp- serpentine, Tlc- talc, Qz- quartz, Chr- chromite, Mag- magnetite, Gth- goethite, Hem- hematite*

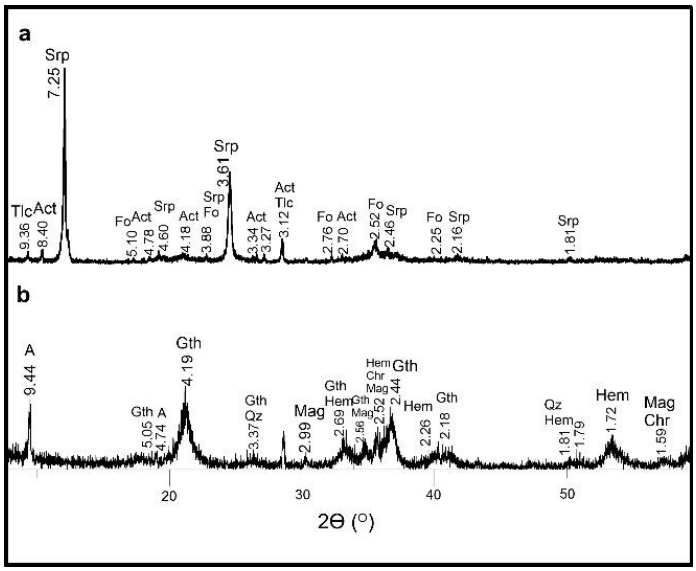

Fig. 31 XRPD patterns of samples showing the (a) occurrence of serpentine, actinolite, talc and relict olivine and (b) presence of asbolane with goethite, hematite, magnetite, chromite, and quartz. *Srp- serpentine, Act- actinolite, Fo- forsterite, Tlc- talc, A- asbolane, Gth- goethite, Mag- magnetite, Hem- hematite, Chr- chromite, Qz- quartz*

namely dunite and harzburgite. Dunite contains 99% olivine, whereas harzburgite consists of 85% olivine, 11% orthopyroxene, and 4% clinopyroxene (Fig. 32). No fresh bedrock sample was retrieved from the PG1500 drill core. However, the petrographic results from the previous work of Ferrer et al. (2013) showed that the bedrock type is clinopyroxenite.

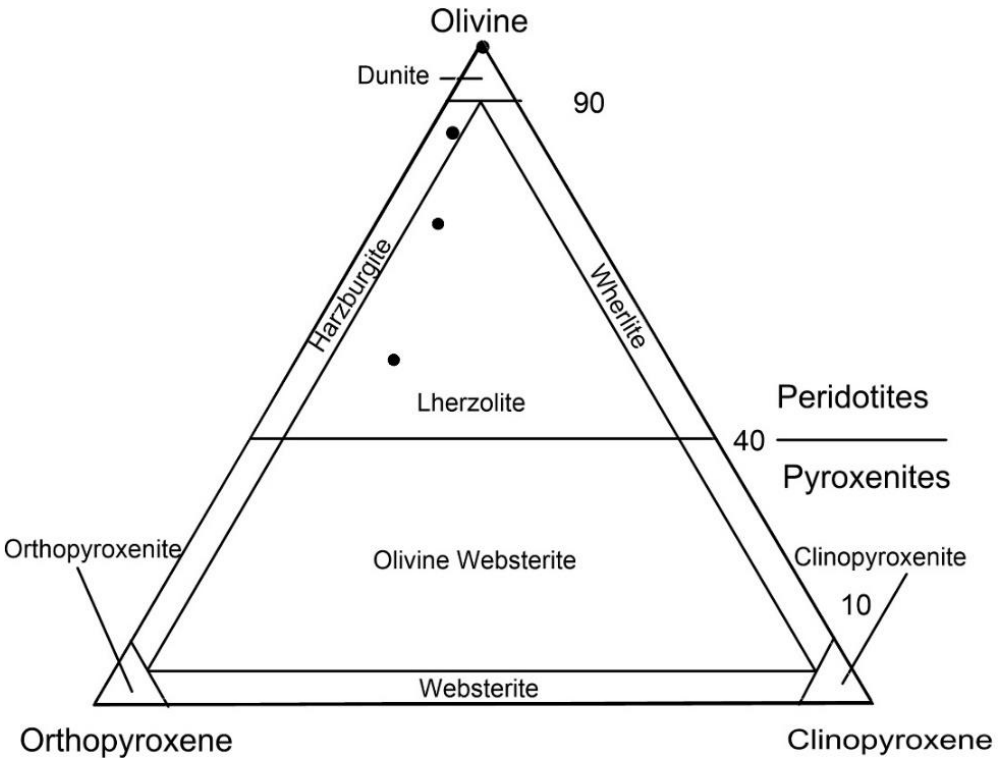

Fig. 32 Plot of the petrographic composition of the bedrock samples, which are investigated at Intex deposit, Mindoro, Philippines.

A network of serpentine cuts the primary minerals in all the studied bedrock. The serpentine veins contain discontinuous strings of magnetite (Figure 33a). The peridotite bedrock from BB2515 and BB2406 cores are characterized by three types of serpentine veins including mesh-textured type I and type II veins and the interlocking-textured type III veins. Fine- to coarse-grained magnetite outlines the core of type II veins, whereas the rim is free from magnetite (Figure 33a). The type III veins are wider, generally hundred in micrometers to a millimeter in width. Talc has a characteristic high birefringence under cross-polarized light. Figure 33b shows that fine-grained talc replaces type III serpentines. Microscopic observations show that talc is more dominant in lherzolite in contrast to harzburgite-dunite bedrock.

Akita University

Chromite occurs in various shapes and sizes but is typically subhedral in form (Figure 33b).

Three types of serpentine veins are identified in the saprock derived from lherzolite bedrock (Figure 33c). The textural features of these veins are analogous to the previous veins identified in the bedrock. Type I veins contain disseminated magnetite and pseudomorph the former primary olivine and pyroxene. Type II veins have distinct magnetite rich core and cut through the type I veins. Type III veins are characterized by interlocking texture (Figure 33c). Similarly, the saprock derived from harzburgite-dunite bedrock shows type I to type III serpentine veins, and these are subsequently cut by yellow-orange, discontinuous type IV veins, which are often associated with magnetite (Figure 33d). The saprock developed above clinopyroxenite is marked by type I and type V veins. Type I veins are characterized by interpenetrating texture (Figure 33e) and are cut by type V serpentine veins (Figure 33f). Hematite is widely distributed within type V veins (Figure 33f).

Akita University

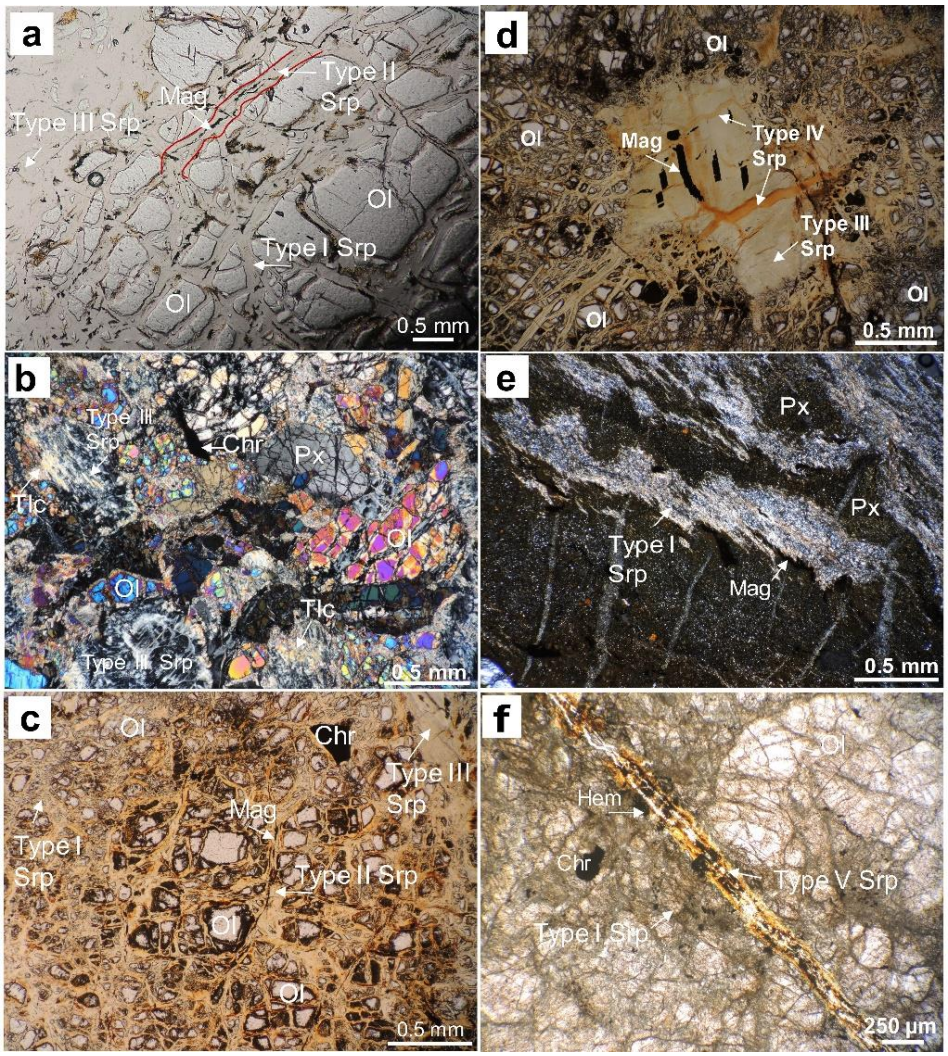

Fig. 33. Photomicrographs of (**a-b**) type I, II and III serpentine veins cutting primary olivine, pyroxene, chromite, and Fe-oxide in lherzolite (BB2515 core); serpentine veins in the saprock (**c**) developed above lherzolite (BB2515 core), (**d**) harzburgite-dunite (BB2406 core), and (**e-f**) clinopyroxenite (PG1500 core). *Ol- olivine, Px- pyroxene, Srp- serpentine, Tlc- talc, Chr- chromite, Gth- goethite*

4.5.3 Raman characterization of serpentine in the bedrock and saprolite

Figure 34 displays the Raman peaks of different types of serpentine formed in the studied bedrock. The Raman peaks of type I serpentines exhibit strong peaks at 228 cm^{-1}, 381 cm^{-1}, and 688 cm^{-1}. Type II and type III serpentines show a comparable set of bands as type I serpentines. The high-frequency domains display sharp peaks

Akita University

at 3684 cm^{-1}, 3685 cm^{-1}, and 3682 cm^{-1}. The Raman signatures of the three types of serpentine in the lherzolite bedrock belong to lizardite.

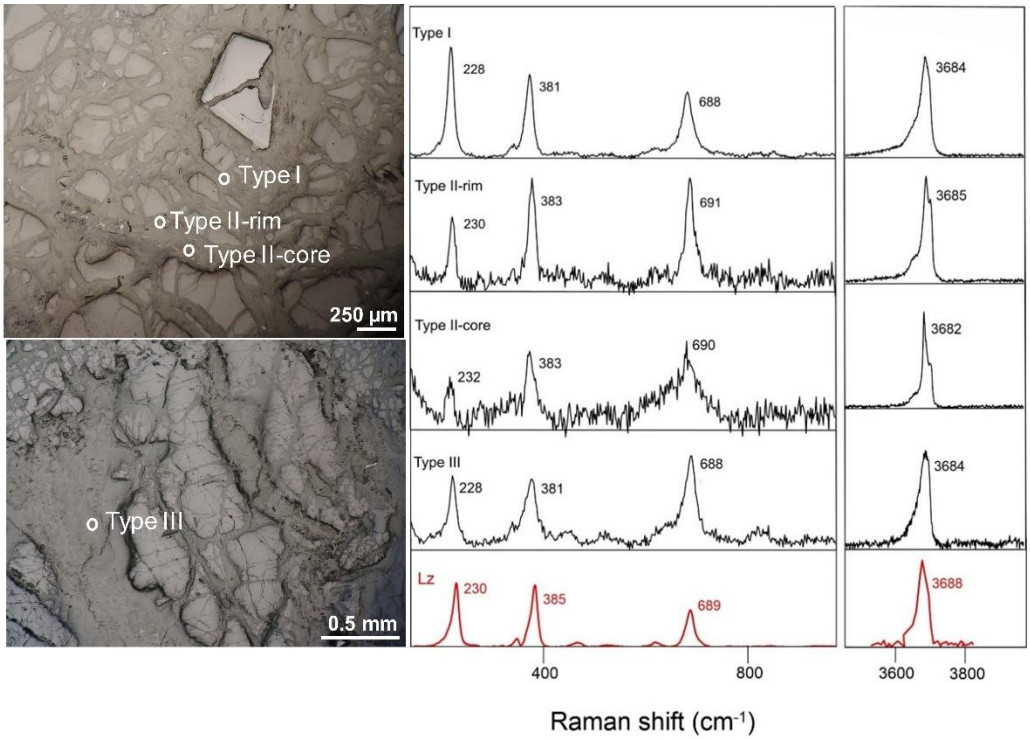

Fig. 34 Raman signatures of type I, type II and type III vein serpentines in the lherzolite bedrock. Raman data of lizardite (Lz) from rruff.info database.

The saprolite horizon developed above lherzolite and harzburgite-dunite is characterized by the frequent presence of type I, type II-rim, type II-core, and type III serpentines with the addition of type IV serpentines (Figure 35a). The main peaks of type I serpentines are positioned at 228 cm^{-1}, 383 cm^{-1}, and 688 cm^{-1}. The extra reflections at 827 cm^{-1} and 857 cm^{-1} correspond to the relict phase of olivine. The high-frequency-domains reveal sharp peaks at 3682 cm^{-1}, 3683 $cm^{-1}$and 3684 cm^{-1}. Both the low-frequency and high-frequency domains of type I to type IV serpentines in the saprock derived from harzburgite-dunite match the signature of lizardite (Figure 35a). However, the Raman peaks of type I in the saprock derived from clinopyroxenite

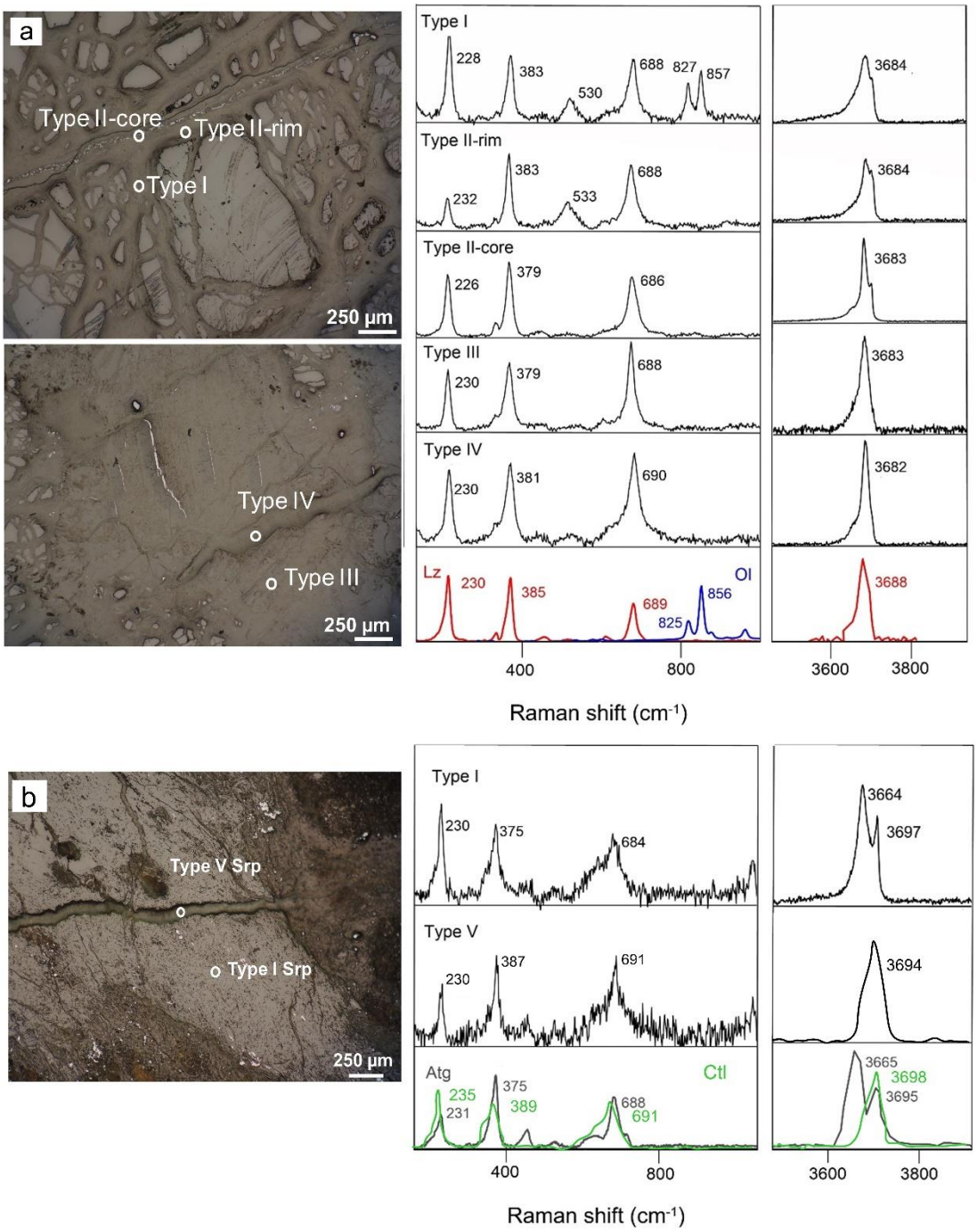

Fig. 35 Raman signatures of type I, type II, type III and type IV vein serpentines identified in the saprock derived from (**a**) harzburgite- dunite (BB2406 core) and (**b**) type I and type V vein serpentines in the saprock formed above clinopyroxenite bedrock (PG1500 core). Raman data of lizardite (Lz), antigorite (Atg), chrysotile (Ctl) and olivine (Ol) from rruff.info database.

belong to antigorite. Here the low-frequency domains show intense peaks at 230 cm^{-1}, 375 cm^{-1}, and 684 cm^{-1}, whereas in the high-

Akita University

frequency domain, the strong peak is at 3664 cm^{-1} (Figure 35b). Conversely, the Raman bands of type V serpentines in the saprock developed above clinopyroxenite are identified as chrysotile (Figure 35b). The Raman signatures of lizardite (3679 cm^{-1} to 3684 cm^{-1}) are differentiated from antigorite (3667 cm^{-1}) and chrysotile (3694 cm^{-1}) based on the strong peaks in the high-frequency domain.

4.5.4 Mineral Chemistry

The bedrock samples show that the highest NiO concentration is measured in primary olivine (avg. 0.37 wt%; 0.01 apfu Ni) with a considerable amount of FeO (avg. 8.42 wt%) (Figure 36a). Orthopyroxene and clinopyroxene are marked by relatively higher FeO concentrations (avg. 5.56 wt%, avg. 1.78 wt%) (Table 10). Talc commonly occurs as fine aggregates in the bedrock and it contains a substantial amount of FeO (avg. 1.75 wt%) and Al_2O_3 (avg. 1.24 wt%), but with low NiO concentration (avg. 0.07 wt%). The average structural formula of talc is $Mg_{2.93}Si_{3.89}O_{10}(OH)_2$.

The FeO content of type I, type II-rim and type II-core serpentines (avg. 6.30 wt%, avg. 5.85 wt%, avg. 8.17 wt%) is higher than type III serpentines (avg. 5.13 wt%) in the lherzolite and harzburgite-dunite bedrock (Table 11). The MgO concentration of type I and type II-rim serpentines (avg. 37.56 wt%, avg. 38.37 wt%) is generally higher in contrast to type II-core and type III serpentines (avg. 36.48 wt%, avg. 36.26 wt%) in both the bedrock. The sudden decrease of the Mg/(Mg+Fe+Ni) ratio from type II-rim to type II-core and type III serpentines are clearly shown in Figure 9a. The NiO contents of type I

Akita University

and type II serpentines in the bedrock are similar (avg. 0.22 wt%, 0.009 apfu), but type III serpentines are distinctively lower (0.06 wt%, 0.002 apfu) (Table 11). The Ni/(Ni+Mg+Fe) ratio from type I to type III serpentines decreases in the bedrock (Figures 36a, 36b).

In the saprock developed above lherzolite and harzburgite-dunite, the FeO content of type I, type II-rim, and type II-core serpentines (avg. 5.62 wt%, avg. 7.01 wt%, avg. 7.75 wt%) continuously increases (Tables 12). Then the concentration of FeO in type III serpentines (avg. 6.42 wt%) drops in the saprock. However, the amount of FeO in type IV serpentines (avg. 9.65 wt%) increases again and finally decreases in type V serpentines (avg. 5.47 wt%). Figures 37a and 37b show that the Fe/(Fe+Mg+Ni) ratio increases from type I to type II serpentines and decreases in type III serpentines, but rises again in type IV serpentines. Finally, the Fe/(Fe+Mg+Ni) ratio declines in type V serpentines (Figure 37c). The MgO concentration from type I to type II serpentines (avg. 32.2 wt%, avg. 33.68 wt%, avg. 33.09 wt.%) increases, and subsequently decreases in type III and type IV serpentines (avg. 31.06 wt%, avg. 29.84 wt%). A similar trend is observed in Mg/(Mg+Fe+Ni) ratio from type I to type III serpentines except this time, there is a significant decrease in the Mg/(Mg+Fe+Ni) ratio of type IV serpentines (Figure 37b).

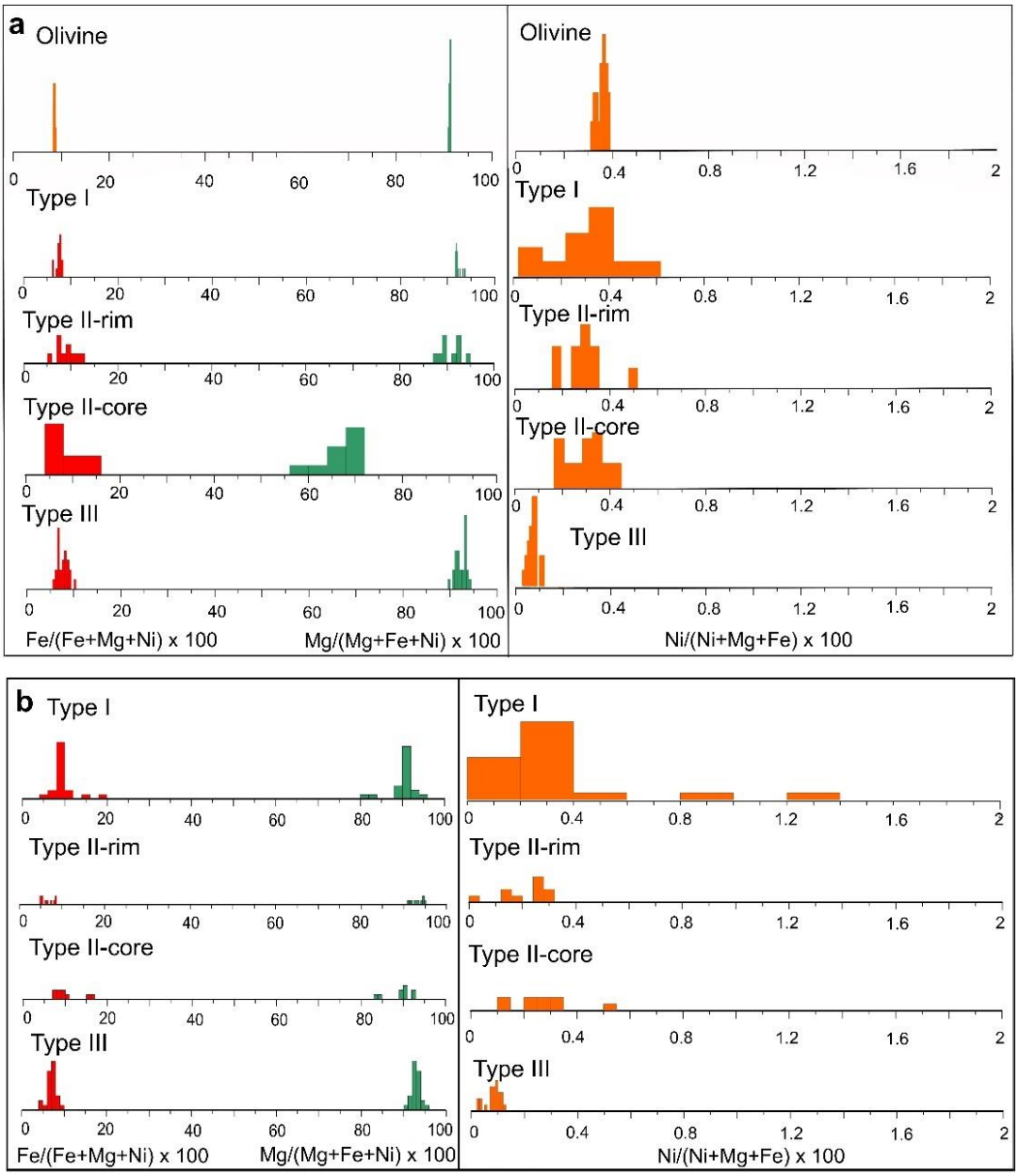

Fig. 36. Histogram of Mg (green), Fe (red) and Ni (orange) mol ratio in olivine and different types of serpentines found in the (**a**) lherzolite and (**b**) harzburgite-dunite bedrock.

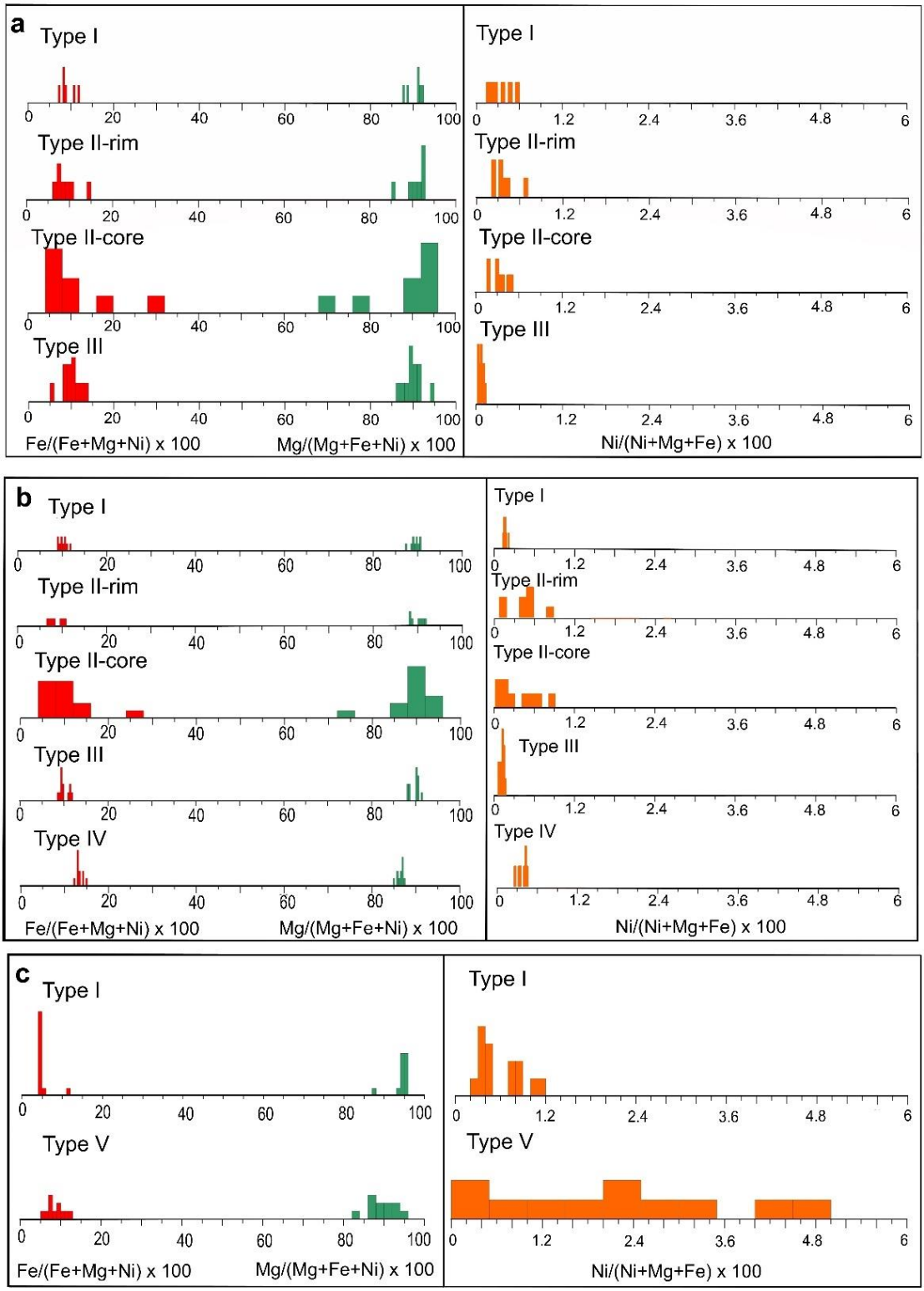

Fig. 37. Histogram of Mg (green), Fe (red) and Ni (orange) mol ratio in the different types of serpentines identified in the saprock derived from (**a**) lherzolite(**b**) clinopyroxenite, and (**c**) harzburgite-dunite bedrock.

Akita University

However, a significant amount of NiO is observed in type V serpentines (avg. 1.42 wt%), particularly in the saprock derived from clinopyroxenite (Appendix B). Among the different types of serpentines in the saprock, a high Ni/(Ni+Mg+Fe) ratio is observed in type V serpentines (Figure 37c). The chemical composition of type V serpentines observed in the saprock plot near the serpentine-like garnierite of the Si-Mg(+Fe)-Ni ternary diagram (Figure 38). The average O/T ratio (Mg+Fe+Ni)/Si) of type V serpentines is 0.94, which is less than the ideal value (O/T = 1.5) of the serpentine group minerals.

Goethite contains a significant amount of Al_2O_3 (avg. 6.63 wt%), NiO (avg. 0.77 wt%), MnO (avg. 1.09wt%) and CoO (avg. 0.27 wt%) (Table 13). In Figure 39a, the NiO concentration of goethite reaches up to 1.68 wt%. The average structural formula of goethite is $(Fe_{0.72}, Al_{0.11}, Ni_{0.01}, Mn_{0.01}, Co_{0.003})O(OH)$. Hematite is characterized by a considerable amount of NiO (avg. 0.26 wt%), CoO (avg. 0.31 wt%), Al_2O_3 (avg. 0.55 wt%) and MnO (avg. 0.46 wt%) (Table 13). Hematite is intimately mixed with goethite containing up to 0.38 wt% NiO (Figure 39b). The average structural formula of hematite is $(Fe_{2.81}, Al_{0.03}, Ni_{0.01}, Mn_{0.02}, Co_{0.01})O_3$. The EPMA results show that residual talc contains a trace amount of NiO (0.10 wt%, 0.006 apfu Ni) (Table 13). The average structural formula of the residual talc is $Mg_{2.56}Si_{3.92}O_{10}(OH)_{2.}$

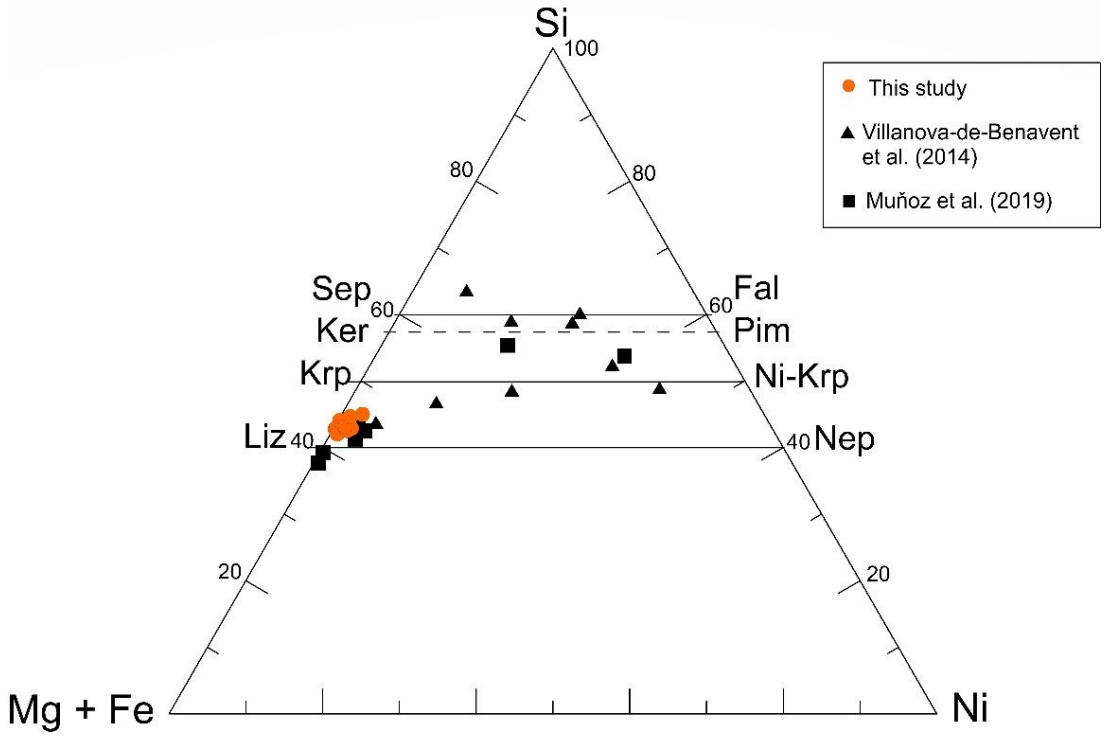

Fig. 38 Si-Mg-(+Fe)-Ni plot showing the composition of serpentine-like garnierite in this study and previous works. *Lz- lizardite, Nep- nepouite, Krp- karpinskite, Ni-Krp- Ni-karpinskite, Ker- kerolite, Pim- pimelite, Sep- sepiolite, Fal- falcondoite*

Figures 39c and Figure 39d show the occurrence of asbolane and lithiophorite-asbolane intermediate in the limonite. Based on the Ni-Co-Al ternary plot, these two phases are the major Co-bearing Mn-oxyhydroxides in the limonite samples (Figure 40). Asbolane is marked by high NiO and CoO concentrations of up to 12.89 wt% and 3.82 wt%. Also, it contains a high amount of FeO and MnO (12.89 wt%, 0.29 apfu Fe; 32.17 wt%, 5.82 apfu Mn) (Table 14). The structural formula of asbolane is $(Al_{0.02}Ni_{0.30}Co_{0.09})(Mn_{0.80}Fe_{0.23}Mg_{0.26})O_2(OH)_2$.Lithiophorite-asbolane intermediate is characterized by high amounts of NiO (avg. 3.00 wt%), CoO (avg. 10.07 wt%), FeO (avg. 10.72 wt%), and MnO (avg. 39.21 wt%). The

calculated average formula is $(Al_{0.20},Ni_{0.08},Co_{0.26})(Mn_{1.06},Fe_{0.29},Mg_{0.02})O_2(OH)_2$.

Table 10 Average chemical compositions and structural formula (apfu) of olivine, orthopyroxene, clinopyroxene and talc the peridotite bedrock (wt%).

	Olivine		Orthopyroxene		Clinopyroxene		Talc	
		σ		σ		σ		σ
n	18		12		6			
SiO_2	39.99	0.44	55.75	0.48	53.22	1.37	58.28	2.17
Al_2O_3	0.01	0.02	1.69	0.22	0.97	0.41	1.24	0.78
FeO	8.42	0.37	5.56	0.09	1.78	0.15	1.75	0.33
MgO	50.70	2.18	35.39	0.38	20.03	2.89	28.87	0.60
NiO	0.37	0.03	0.07	0.01	0.04	0.02	0.07	0.01
CoO	0.02	0.01	0.01	0.01	0.00	0.00	0.01	0.02
CaO	0.01	0.03	0.54	0.23	24.41	1.37	0.02	0.01
Cr_2O_3	0.00	0.00	0.48	0.09	0.30	0.21	0.30	0.16
MnO	0.12	0.01	0.13	0.01	0.07	0.02	0.02	0.01
Total	99.66	2.73	99.66	0.39	100.85	0.31	90.56	2.09
Si	0.981	0.021	1.931	0.010	1.922	0.048	3.915	0.080
Al	0.000	0.001	0.069	0.009	0.041	0.017	0.098	0.062
Fe	0.173	0.004	0.161	0.003	0.054	0.005	0.099	0.019
∑ Tetr.	1.154	0.018	2.161	0.005	2.017	0.054	4.113	0.039
Mg	1.854	0.040	1.827	0.017	1.079	0.157	2.893	0.077
Ni	0.007	0.001	0.002	0.000	0.001	0.000	0.004	0.001
Co	0.000	0.000	0.000	0.000	0.000	0.000	0.001	0.001
Cr	0.000	0.000	0.013	0.002	0.009	0.006	0.016	0.008
Ca	0.000	0.001	0.020	0.009	0.945	0.052	0.001	0.001
Mn	0.003	0.000	0.004	0.000	0.002	0.001	0.001	0.001
∑ Oct.	1.864	0.039	1.867	0.011	2.035	0.105	2.915	0.082
Tetr./Oct.	0.620	0.025	1.158	0.009	0.994	0.072	1.412	0.052
Ni/Mg	0.004	0.000	0.001	0.000	0.001	0.000	0.001	0.000

n total number of points acquired in polished thin section; σ standard deviation of the analyzed points

Table 11 Average chemical compositions and structural formula (apfu) of the different serpentine veins in the bedrock (wt%).

	BB2515 Type I	σ	BB2406 Type I	σ	BB2515 Type II-rim	σ	BB2406 Type II-rim	σ	BB2515 Type II-core	σ	BB2406 Type II-core	σ	BB2515 Type III	σ	BB2406 Type III	σ
n	14		20		10		10		11		9		26		25	
SiO_2	38.65	1.58	37.27	2.60	37.14	2.98	39.43	1.33	35.51	4.95	36.67	1.85	39.55	0.63	40.40	1.47
Al_2O_3	0.32	0.37	0.11	0.10	0.05	0.05	0.03	0.02	0.04	0.03	0.02	0.02	1.93	0.62	2.34	1.66
FeO	5.43	0.47	7.16	2.28	6.91	2.01	4.79	1.05	8.74	7.28	7.59	2.41	5.35	0.79	4.88	0.90
MgO	37.40	1.94	37.71	1.99	38.95	1.94	37.79	0.75	36.45	5.10	36.50	1.71	36.59	0.86	35.92	0.99
NiO	0.22	0.10	0.27	0.25	0.24	0.06	0.16	0.07	0.23	0.06	0.20	0.09	0.05	0.01	0.06	0.02
CoO	0.01	0.01	0.02	0.02	0.01	0.01	0.01	0.01	0.02	0.01	0.04	0.04	0.01	0.01	0.01	0.01
CaO	0.22	0.19	0.10	0.05	0.14	0.07	0.04	0.02	0.12	0.04	0.05	0.02	0.11	0.13	0.04	0.03
Cr_2O_3	0.13	0.24	0.01	0.01	0.00	0.00	0.01	0.01	0.01	0.01	0.01	0.01	0.47	0.13	0.73	0.65
MnO	0.09	0.04	0.11	0.04	0.10	0.03	0.09	0.04	0.08	0.02	0.13	0.11	0.08	0.03	0.09	0.03
Total	82.48	1.34	82.76	1.24	83.53	1.09	82.36	1.01	81.19	2.61	81.20	1.78	84.17	1.02	84.51	1.16
Si	1.949	0.062	1.898	0.098	1.874	0.119	1.978	0.036	1.858	0.144	1.908	0.073	1.945	0.021	1.969	0.070
Al	0.019	0.022	0.006	0.006	0.003	0.003	0.002	0.001	0.002	0.002	0.001	0.001	0.112	0.036	0.135	0.095
Fe	0.229	0.021	0.307	0.106	0.293	0.090	0.202	0.047	0.416	0.436	0.331	0.105	0.220	0.034	0.199	0.037
∑ Tetr.	2.197	0.069	2.211	0.092	2.170	0.067	2.181	0.028	2.276	0.311	2.240	0.106	2.277	0.037	2.303	0.036
Mg	2.812	0.148	2.866	0.158	2.934	0.171	2.826	0.043	2.844	0.213	2.833	0.148	2.683	0.045	2.610	0.050
Ni	0.009	0.004	0.011	0.010	0.010	0.003	0.007	0.003	0.010	0.002	0.008	0.004	0.002	0.001	0.002	0.001
Co	0.001	0.000	0.001	0.001	0.000	0.000	0.000	0.000	0.001	0.001	0.002	0.002	0.001	0.000	0.000	0.000
Cr	0.005	0.009	0.000	0.000	0.000	0.000	0.000	0.000	0.000	0.000	0.000	0.000	0.018	0.005	0.028	0.025
Ca	0.012	0.011	0.006	0.003	0.007	0.004	0.002	0.001	0.007	0.002	0.003	0.001	0.006	0.007	0.002	0.001
Mn	0.004	0.002	0.005	0.002	0.004	0.001	0.004	0.002	0.004	0.001	0.006	0.005	0.003	0.001	0.004	0.001
∑ Oct.	2.843	0.138	2.888	0.161	2.955	0.171	2.840	0.043	2.865	0.212	2.852	0.150	2.713	0.046	2.647	0.042
Tetr./Oct.	0.776	0.061	0.769	0.072	0.737	0.063	0.768	0.019	0.806	0.187	0.789	0.080	0.840	0.028	0.871	0.027
Ni/Mg	0.003	0.001	0.004	0.003	0.003	0.001	0.002	0.001	0.003	0.001	0.003	0.001	0.001	0.000	0.001	0.000

Table 12 Average chemical compositions (wt%) and structural formula (apfu) of the different vein serpentines in the saprock derived from lherzolite and clinopyroxenite.

Sample name	BB2515		PG1500		BB2515		PG1500		BB2515		PG1500	
Depth, m	7.4		8.5		7.4		7.4		7.4		8.5	
	Type I	σ	Type I	σ	Type II-rim	σ	Type II-core	σ	Type III	σ	Type V	σ
n	6		14		7		8		11		11	
SiO_2	39.49	2.44	42.08	1.67	39.41	2.79	39.84	3.31	44.28	4.75	40.92	1.25
Al_2O_3	0.69	1.37	1.40	1.09	0.01	0.02	0.01	0.01	0.89	0.38	0.04	0.03
FeO	5.90	1.46	3.19	1.32	6.23	1.78	8.06	5.86	5.71	1.28	5.47	1.16
MgO	32.21	1.63	32.86	0.95	34.27	1.87	32.77	2.63	28.56	1.52	31.81	2.21
NiO	0.23	0.12	0.39	0.19	0.26	0.12	0.23	0.09	0.05	0.02	1.42	0.95
CoO	0.02	0.01	0.01	0.01	0.02	0.01	0.03	0.03	0.01	0.01	0.02	0.02
CaO	0.02	0.01	0.01	0.00	0.01	0.01	0.03	0.03	0.05	0.02	0.03	0.02
Cr_2O_3	0.03	0.04	0.21	0.28	0.00	0.01	0.01	0.01	0.29	0.13	0.02	0.01
MnO	0.08	0.02	0.03	0.01	0.10	0.03	0.16	0.19	0.09	0.05	0.10	0.03
Total	78.69	1.03	80.18	1.76	80.32	3.43	81.14	2.08	79.97	3.99	79.84	1.55
Si	2.070	0.112	2.121	0.045	2.035	0.072	2.052	0.093	2.240	0.114	2.119	0.030
Al	0.043	0.085	0.083	0.064	0.001	0.001	0.001	0.001	0.054	0.025	0.003	0.002
Fe	0.259	0.067	0.135	0.060	0.272	0.088	0.356	0.275	0.243	0.055	0.238	0.054
∑ Tetr.	2.372	0.055	2.339	0.038	2.307	0.040	2.409	0.191	2.538	0.090	2.359	0.074
Mg	2.519	0.149	2.469	0.062	2.640	0.071	2.518	0.130	2.168	0.189	2.453	0.128
Ni	0.010	0.005	0.016	0.008	0.011	0.005	0.010	0.004	0.002	0.001	0.060	0.041
Co	0.001	0.001	0.000	0.000	0.001	0.001	0.001	0.001	0.001	0.000	0.001	0.001
Cr	0.001	0.002	0.008	0.011	0.000	0.000	0.000	0.000	0.012	0.006	0.001	0.001
Ca	0.001	0.001	0.000	0.000	0.001	0.000	0.002	0.002	0.003	0.001	0.002	0.001
Mn	0.004	0.001	0.001	0.000	0.004	0.002	0.007	0.009	0.004	0.002	0.005	0.001
∑ Oct.	2.536	0.151	2.495	0.052	2.657	0.077	2.538	0.118	2.189	0.192	2.521	0.098
Tetr./Oct.	0.939	0.080	0.938	0.032	0.869	0.034	0.954	0.122	1.171	0.143	0.938	0.067
Ni/Mg	0.004	0.002	0.006	0.003	0.004	0.002	0.004	0.002	0.001	0.000	0.025	0.018

Table 13 Average compositions (wt%) and structural formula (apfu) of goethite, hematite, and supergene talc in the limonite samples acquired from the Intex deposit.

	Goethite				Hematite						Supergene Talc
Sample name	INT-D1-1		INT-D2-1		INT-D1-1		INT-D2-1		INT-D3-2		
Depth, m	1	σ	1	σ	1	σ	1	σ	2.4	σ	
n	8		10		12		5		11		1
SiO_2	2.81	0.42	3.30	0.90	1.32	0.64	0.89	0.52	0.41	0.65	55.04
MgO	0.37	0.24	0.62	0.50	0.50	0.25	0.56	0.60	0.27	0.09	24.07
Al_2O_3	6.47	2.48	6.79	2.30	1.46	0.60	0.10	0.12	0.08	0.12	1.53
FeO	62.58	3.70	62.66	1.89	77.61	3.49	80.72	2.32	82.50	3.92	6.55
NiO	0.79	0.38	0.76	0.35	0.24	0.08	0.41	0.76	0.13	0.08	0.10
CoO	0.43	0.28	0.10	0.04	0.14	0.02	0.64	0.68	0.16	0.02	0.02
Cr_2O_3	0.34	0.24	0.96	0.68	0.89	0.35	0.08	0.05	0.10	0.09	0.17
CaO	0.07	0.06	0.00	0.00	0.00	0.00	0.00	0.01	0.01	0.03	0.00
MnO	1.78	1.22	0.39	0.30	0.15	0.06	1.04	0.95	0.19	0.24	0.04
Total	75.69	3.22	75.81	3.16	82.34	3.45	84.46	2.52	83.88	3.86	87.56
Fe	0.72	0.06	0.71	0.06	2.69	0.09	2.81	0.11	2.92	0.06	
Al	0.10	0.04	0.11	0.03	0.07	0.03	0.01	0.01	0.00	0.01	
Mn	0.02	0.01	0.00	0.00	0.01	0.00	0.04	0.03	0.01	0.01	
Ni	0.01	0.00	0.01	0.00	0.01	0.00	0.01	0.02	0.00	0.00	
Co	0.00	0.00	0.00	0.00	0.00	0.00	0.02	0.02	0.01	0.00	

ntotal number of points acquired in polished thin section
σ standard deviation of the analyzed points
apfu atoms per formula unit

Akita University

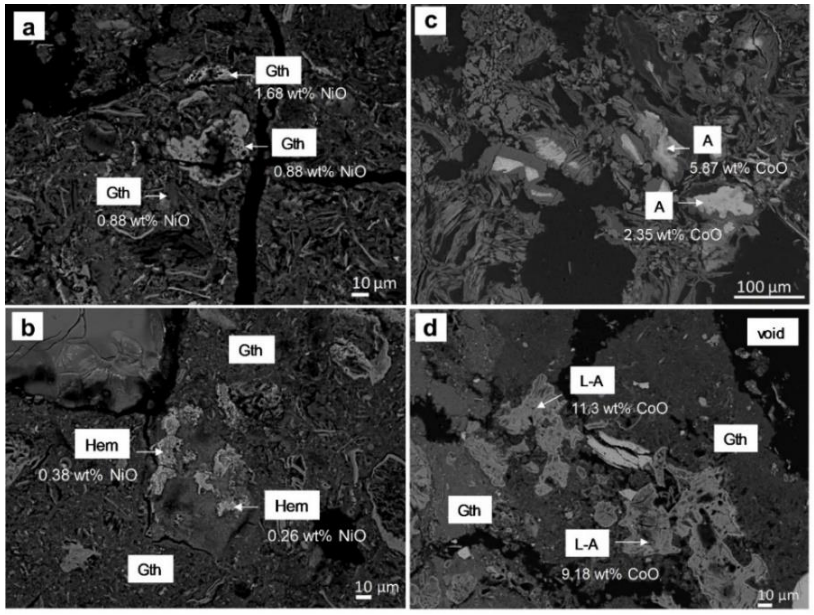

Fig. 39. Backscattered electron images of (**a**) massive goethite (Gth) (**b**) an intimate mixture of hematite (Hem) and goethite, irregular aggregates of (**c**) asbolane in a serpentine (Srp) matrix (A) and (**d**) lithiophorite-asbolane intermediate (L-A) in a goethite matrix.

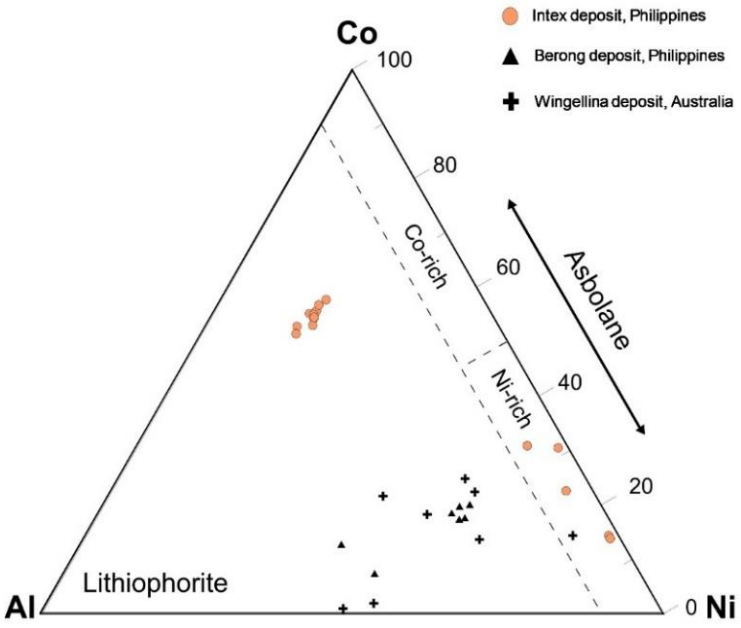

Fig. 40. Co-Ni-Al ternary diagram (wt%) displaying the mineralogy and composition of asbolane and lithiophorite-asbolane intermediates from the Intex ore deposit.

Table 14 Average chemical compositions (wt%) and structural formula (apfu) of the representative asbolane and lithiophorite-asbolane intermediate from the Intex deposit.

	Asbolane			Lithiophorite-asbolane		
Sample name	INT-D1-4		INT-D2-1		INT-D3-2	
Depth, m	4	σ	1	σ	2.4	σ
n	5		8		3	
SiO_2	5.95	8.92	0.03	0.02	0.04	0.05
MgO	6.68	3.15	0.33	0.07	0.43	0.07
Al_2O_3	0.50	0.31	5.60	0.40	4.88	0.34
FeO	9.64	1.97	8.66	2.36	12.79	11.00
NiO	12.89	3.22	3.14	0.34	2.85	0.61
CoO	3.82	1.53	10.43	1.07	9.72	2.20
Cr_2O_3	0.11	0.09	0.02	0.02	0.01	0.01
CaO	0.95	1.69	0.06	0.02	0.08	0.03
MnO	32.17	5.82	39.41	4.07	39.01	9.65
Total	72.70	4.45	67.68	3.85	69.82	1.83
Ni	0.305	0.108	0.081	0.005	0.072	0.014
Al	0.016	0.010	0.213	0.009	0.182	0.008
Co	0.089	0.046	0.269	0.014	0.245	0.050
Mn	0.796	0.251	1.074	0.061	1.040	0.235
Fe	0.230	0.063	0.237	0.079	0.343	0.304
Mg	0.265	0.056	0.016	0.003	0.020	0.003
Co/Ni	0.316	0.152	3.317	0.161	3.388	0.062

n total number of points acquired in polished thin section; σ standard deviation of the analyzed points; apfu atoms per formula unit

5.5. pH, petrographic and whole-rock geochemical analysis

Figures 41, 42, and 43 illustrate the relative amount of olivine, variations of pH and elements in representative bedrock, saprolite, and limonite samples. The pH of the bedrock, saprolite and limonite samples is between 6.14 and 8.75. A pH gradient displays the shift from alkaline condition (pH 8.75) in the bedrock to neutral condition (pH 7.32) in the saprolite horizon to mildly acidic condition (pH 6.14) in the limonite horizon.

The different types of bedrock contain high amounts of MgO (up to 41.96 wt%) and SiO_2 (up to 42.73 wt%), and low content of Fe_2O_3 (6.63 wt%) (Tables 15, 16, 17). It is evident from Figures 41, 42 and 43, the sudden decrease in MgO and SiO_2 concentrations (2.09 wt%, 5.49 wt%) in the transition boundary between the saprolite and limonite horizons. In contrast, the Fe_2O_3 content sharply increases from this boundary towards the limonite horizon (up to 67.58 wt%). In this horizon, relatively high concentrations of Al_2O_3 and Cr_2O_3 (up to 9.29 wt%, 3.93 wt%) are observed.

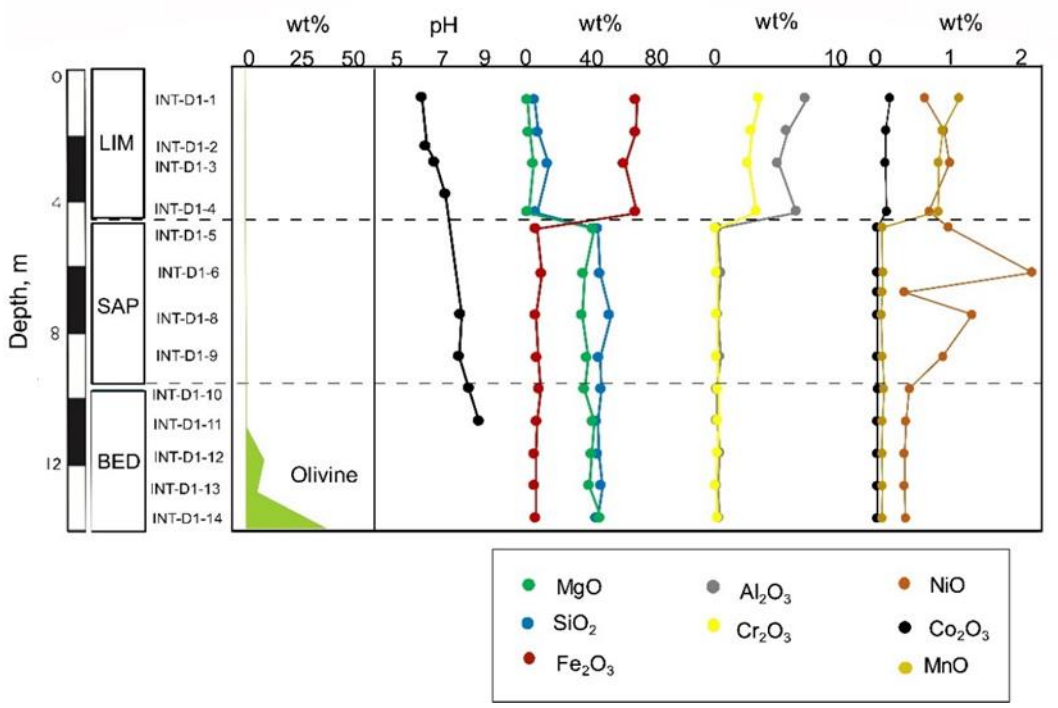

Fig. 41 Distribution of olivine, pH and elements with depth in the laterite derived from lherzolite bedrock (BB2515 core).

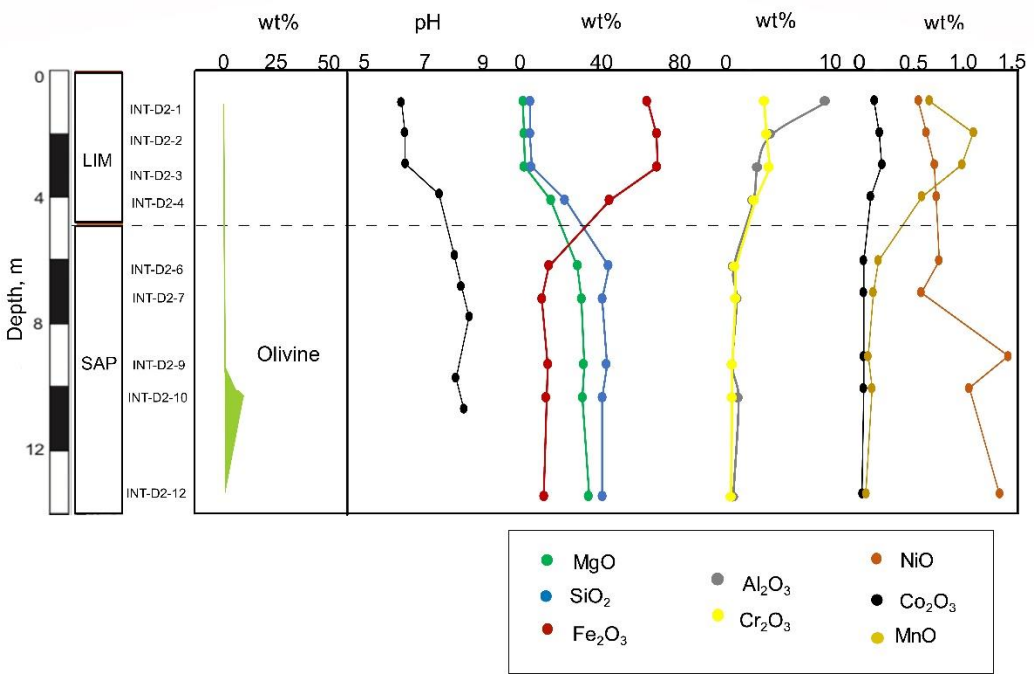

Fig. 42 Distribution of olivine, pH and elements with depth in the laterite derived from clinopyroxenite bedrock (PG1500 core).

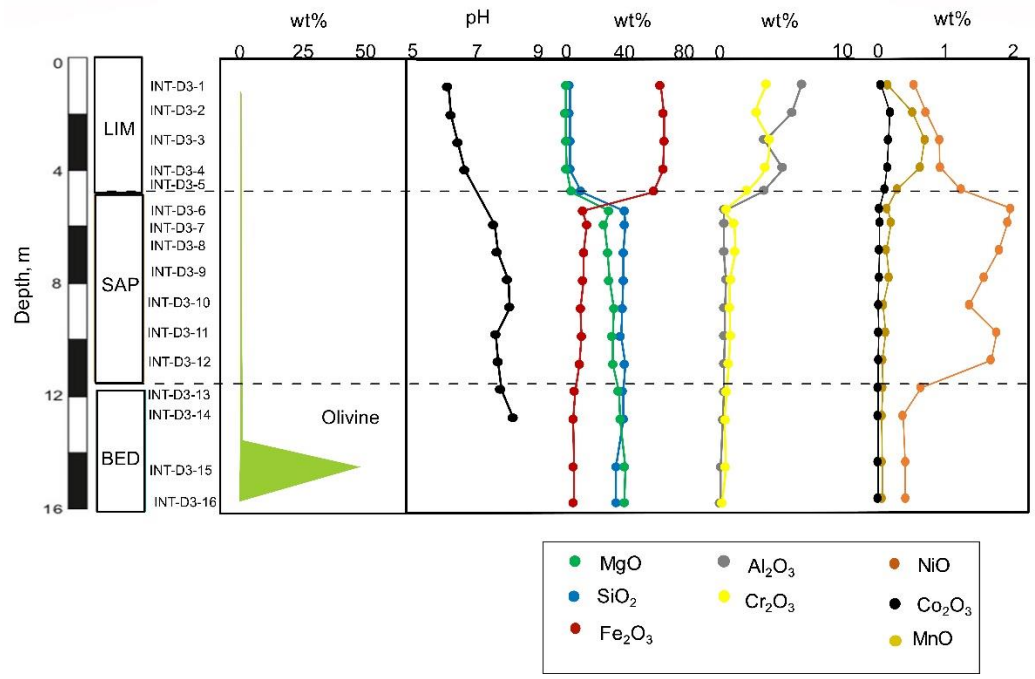

Fig. 43 Distribution of olivine, pH and elements with depth in the laterite derived from harzburgite-dunite bedrock (BB2406 core).

Table 15 Whole-rock chemical analyses (wt%) of the bedrock (BED), saprolite (SAP), and limonite (LIM) samples through BB2515 core.

Drill core	BB2515	BB2515	BB2515	BB2515	BB2515	BB2515	BB2515	BB2515	BB2515	BB2515	BB2515	BB2515	BB2515	BB2515
Depth, m	1	2	3	5	5	6	7	8	9	10	11	12	13	14
Horizon	LIM	LIM	LIM	LIM-SAP	HSAP	HSAP	BED	HSAP	HSAP	BED	BED	BED	BED	BED
Na_2O	bdl	bdl	bdl	bdl	bdl	bdl	bdl	bdl	bdl	bdl	bdl	bdl	bdl	bdl
MgO	2.63	3.72	5.86	3.03	38.14	33.15	40.65	32.00	35.13	33.56	38.25	37.21	35.85	41.96
SiO_2	6.41	8.54	13.76	7.56	40.59	41.82	40.65	47.07	41.57	42.39	40.13	40.72	42.73	39.99
Al_2O_3	7.36	5.91	5.20	6.63	0.49	0.78	0.61	0.49	0.72	0.41	0.47	0.68	0.47	0.64
P_2O_5	0.01	0.01	0.01	0.01	bdl	bdl	bdl	bdl	bdl	bdl	bdl	bdl	bdl	bdl
K_2O	0.01	0.01	0.01	0.01	0.00	0.00	0.01	0.01	0.00	0.00	0.01	0.00	0.00	0.00
CaO	0.03	0.05	1.15	0.07	0.37	0.50	0.76	0.09	0.24	0.13	0.32	0.27	0.12	0.62
TiO_2	0.12	0.09	0.08	0.12	bdl	bdl	0.01	0.01	0.01	0.01	0.01	bdl	bdl	bdl
Cr_2O_3	3.73	3.15	2.87	3.54	0.38	0.46	0.39	0.44	0.46	0.55	0.55	0.51	0.37	0.49
MnO	1.15	0.92	0.86	0.86	0.08	0.09	0.09	0.07	0.09	0.11	0.08	0.08	0.08	0.08
Fe_2O_3	61.28	60.97	54.81	61.33	7.29	10.42	7.36	7.04	8.05	9.27	7.85	6.88	6.68	7.00
Co_2O_3	0.19	0.13	0.13	0.14	0.01	0.01	0.01	0.01	0.01	0.02	0.01	0.01	0.01	0.01
NiO	0.68	0.94	1.01	0.73	1.00	2.15	0.39	1.33	0.92	0.46	0.41	0.39	0.39	0.41
LOI	12.55	11.48	10.61	12.18	10.55	9.37	7.86	10.32	11.58	11.96	11.31	12.20	12.05	7.06
Total	96.10	95.83	96.37	96.18	98.86	98.73	98.74	98.83	98.75	98.84	99.42	98.90	98.76	98.21

bdl- below detection

Akita University

The saprolite horizon is marked by a high NiO concentration, which reaches up to 2.15 wt%. The bedrock shows low CoO and MnO contents (0.01 wt%, 0.07 wt%), whereas significant amounts of these elements are found in the limonite horizon (up to 0.19 wt%, 1.15 wt%). The concentrations of TiO_2, K_2O, CaO, and P_2O_5 in the bedrock are either low or below the detection limits. However, the limonite horizon contains a considerable amount of TiO_2 and CaO contents (up to 0.35 wt%, 1.15 wt%).

Table 16 Whole-rock chemical analyses (wt%) of the bedrock (BED), saprolite (SAP), and limonite (LIM) samples through PG1500 core.

Drill core	PG1500	PG1500	PG1500	PG1500	PG1500	PG1500	PG1500	PG1500	PG1500	PG1500
Horizon	1	2	3.0	3.8	4	6	7	9	10	13.3
Depth, m	LIM	LIM	LIM	LIM	LIM-SAP	HSAP	HSAP	HSAP	HSAP	HSAP
Na_2O	0.05	bdl	bdl	bdl	0.05	bdl	0.04	0.08	bdl	-0.05
MgO	1.35	2.02	2.09	24.02	14.92	28.10	29.92	31.11	30.47	32.94
SiO_2	4.88	4.86	5.49	29.86	21.96	43.27	40.01	42.23	40.07	40.06
Al_2O_3	9.29	4.21	2.97	1.60	2.59	0.76	1.05	0.65	1.22	0.71
P_2O_5	0.015	0.005	bdl	0.003	0.009	bdl	bdl	bdl	bdl	0.003
K_2O	0.043	0.012	0.009	0.005	0.042	0.006	0.010	0.018	0.006	0.002
CaO	0.04	bdl	bdl	0.08	0.12	0.32	0.34	0.91	1.29	0.15
TiO_2	0.35	0.08	0.06	0.02	0.05	0.01	0.01	0.01	0.01	0.01
Cr_2O_3	3.60	3.81	4.08	1.55	2.70	0.87	0.92	0.60	0.61	0.69
MnO	0.69	1.14	1.02	0.43	0.62	0.18	0.13	0.08	0.11	0.05
Fe_2O_3	62.08	66.60	66.98	30.11	43.81	14.07	10.71	13.43	12.78	12.22
Co_2O_3	0.14	0.19	0.21	0.07	0.10	0.03	0.03	0.03	0.03	0.01
NiO	0.58	0.66	0.74	0.70	0.77	0.79	0.61	1.49	1.10	1.41
LOI	13.66	11.89	11.94	11.29	10.89	10.12	18.05	9.23	8.77	11.46
Total	96.76	95.51	95.61	99.76	98.62	98.54	101.82	99.86	96.50	99.66

bdl- below detection limit

Table 17 Whole-rock chemical analyses (wt%) of the bedrock (BED), saprolite (SAP), and limonite (LIM) samples through BB2406 core.

Horizon	1	2	3	4	4.8	5.5	6	7	8	9	10	11	12	13	15	16
Depth, m	LIM	LIM	LIM	LIM	LIM-SAP	SAP	SAP	SAP	SAP	SAP	SAP	SAP	SAP	BED	BED	BED
Na_2O	bdl	bdl	bdl	bdl	bdl	bdl	bdl	bdl	bdl	bdl	bdl	bdl	bdl	bdl	bdl	bdl
MgO, %	1.66	1.40	1.71	1.85	5.18	30.75	27.17	29.58	30.73	33.97	32.81	33.33	37.13	38.06	41.39	40.78
SiO_2, %	4.06	4.13	4.26	4.36	11.91	40.76	41.22	40.12	40.07	39.35	38.47	41.34	40.02	40.25	35.33	35.31
K_2O,%	0.01	bdl	bdl	bdl	0.01	0.01	0.01	bdl	bdl	bdl	bdl	bdl	bdl	bdl	bdl	bdl
CaO,%	0.02	0.02	0.01	0.02	0.37	0.00	0.04	0.01	0.16	0.18	0.09	0.23	0.15	0.35	0.06	0.05
Al_2O_3, %	6.77	6.00	3.75	5.26	3.69	0.46	0.48	0.47	0.63	0.49	0.52	0.44	0.47	0.37	0.20	0.14
P2O5, %	0.01	0.01	0.00	0.01	0.01	0.01	0.00	0.00	0.00	0.00	0.00	0.00	0.00	0.00	0.00	0.00
TiO2, %	0.13	0.08	0.08	0.07	0.11	0.01	0.01	0.01	0.01	0.01	bdl	0.01	bdl	bdl	bdl	bdl
Cr_2O_3	3.93	3.14	4.13	3.84	2.37	0.68	1.28	1.36	0.97	0.95	0.97	0.86	0.69	0.53	0.61	0.29
MnO, %	0.15	0.52	0.71	0.64	0.30	0.15	0.21	0.14	0.18	0.09	0.13	0.08	0.09	0.07	0.08	0.08
Fe_2O_3, %	65.21	67.09	67.58	66.79	60.43	12.92	15.69	13.69	13.11	11.52	12.10	10.77	7.69	6.63	7.03	6.83
Co_2O_3, %	0.05	0.19	0.17	0.16	0.11	0.03	0.04	0.03	0.03	0.02	0.02	0.02	0.01	0.01	0.02	0.02
NiO, %	0.55	0.73	0.93	0.94	1.25	1.99	1.94	1.81	1.58	1.37	1.78	1.69	0.66	0.38	0.42	0.42
LOI	13.83	13.31	11.77	11.49	10.99	11.49	11.06	11.79	11.45	11.13	12.43	10.38	12.45	12.49	13.89	15.38
Total	96.35	96.59	95.08	95.38	96.71	99.15	99.05	98.99	98.88	99.08	99.31	99.12	99.30	99.10	98.99	99.26

bdl- below detection limit

Akita University

4.6 Discussion

4.6.1. Mineralogical evolution of the laterite profiles

The NiO concentration of olivine (0.37 wt%), orthopyroxene (0.07 wt%), clinopyroxene (0.04 wt%), and talc (0.07 wt%) (Table 1) indicates that olivine is the major source of Ni in the saprolite and limonite horizons. The initial serpentinization of peridotite and pyroxenite results in the formation of type I serpentines. Continuous serpentinization leads to the formation of type II-rim serpentine veins, which is followed by type II-core and later by type III veins in the studied bedrock (Figure 44). This sequence is identical in the bedrock and saprock suggesting a similar generation of serpentinization.

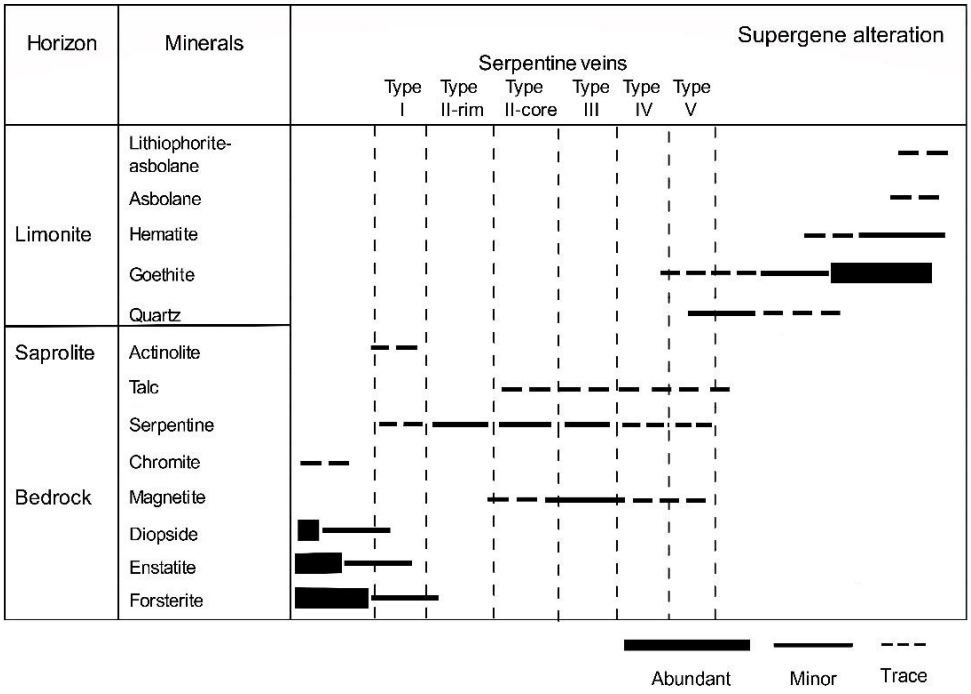

Fig. 44. Mineral paragenesis and abundance of primary and alteration minerals with Ni-bearing serpentine veins in the bedrock and saprock of the Intex laterite deposit in Mindoro, Philippines.

Akita University

The Raman characterization of type I, type II, and type III serpentines in the lherzolite and harzburgite- dunite identified the types as lizardite, whereas type I serpentines in the clinopyroxenite were identified as antigorite. The serpentine variety can be explained by the difference in the pressure and temperature conditions to which they were subjected. Lizardite and chrysotile form predominantly in a low-temperature (< 300 °C)-pressure condition, whereas antigorite forms in a high-temperature (> 320 °C)- pressure condition (Schwartz et al., 2013; Auzende et al., 2004). Type I to type III serpentines found in the ultramafic bedrock are of hydrothermal origin, which is formed before its settlement and exposure on the surface. Although we have not confirmed the replacement texture of lizardite by antigorite, the formation of lizardite in type I veins can be explained by the reaction of olivine and water (Eq. 1), and then magnetite develops after the breakdown of brucite (Eq. 2) and serpentine (Eq. 3) (Toft et al., 1990; Beard et al., 2009; Frost and Beard, 2007).

$$2(Mg, Fe)_2SiO_4 + 3H_2O = (Mg,Fe)_3Si_2O_5(OH)_4 + (Mg,Fe)(OH)_2 \quad (1)$$
olivine water serpentine brucite

$$9Fe(OH)_2 + 4SiO_2 = 2(Mg,Fe)_3Si_2O_5(OH)_4 + Fe_3O_4 + 4H_2O + H_2 \quad (2)$$
brucite silica serpentine magnetite water hydrogen

$$Fe_3Si_2O_5(OH)_4 = Fe_3O_4 + 2SiO_2 + H_2O + H_2 \quad (3)$$
serpentine magnetite silica water hydrogen

The further reaction of silica-rich fluid with brucite leads to the formation of type II lizardite. The absence of brucite in the samples may be attributed to

Akita University

the dissolution of brucite during serpentinization. The iron from the rim of type II serpentines is consumed to precipitate magnetite in the core of type II serpentines. The depletion of Ni and Mg from type II-core to type III serpentines suggests the removal of these elements from the core of the type II veins. The transformation from mesh textured type I and type II veins to the interlocking textured type III veins is due to the change in the temperature or the composition of the fluid which leads to the recrystallization of serpentines (O'Hanley, 1996).

The NiO content of type III lizardite in the bedrock is lower than type I and type II lizardite indicating a local redistribution of the element in the serpentines. It is possible that this element was transported with the serpentinizing fluid and homogenizes in the late-stage type serpentines. Type IV serpentines in the saprock are typically associated with magnetite and contain low amount of NiO (avg. 0.11 wt%). Earlier work reported that magnetite is formed between 200 °C and 300 °C during serpentinization (Klein et al., 2014). The composition of type IV serpentines and conditions related to its formation, suggest that these serpentines are also formed prior to the exhumation of the ultramafic body. In contrast, type V serpentines show the highest NiO content (avg. 1.42 wt%). These serpentines are comparable to serpentine-like phases reported by previous works, which are more likely formed at low-temperature conditions (Tauler et al., 2009; Villanova-de-Benavent et al., 2014; Muňoz et al., 2019).

Akita University

During progressive weathering, Ni is leached from the limonite horizon and then transported downwards to the saprolite horizon. The leached Ni is accommodated in type V serpentines owing to the increased amount of Ni in these serpentines (Trescases et al., 1973; Dublet et al., 2015). Therefore, the composition of type V serpentines indicates that it precipitated last in the paragenetic sequence. Despite type V serpentines only occuring in the saprock derived from clinopyroxenite, we posit that the enrichment of Ni in the saprolite horizon above lherzolite and harzburgite-dunite is contributed to by other minerals including goethite and talc.

Observations under the microscope show that pyroxene crystals are not only altered to serpentine but also talc. The hydration of orthopyroxene-bearing rock primarily produces talc and can be explained by the reaction below (Frost and Beard, 2007).

$$\underset{\text{orthopyroxene}}{3\,MgSiO_3} + \underset{\text{fluid}}{SiO_2} + H_2O = \underset{\text{talc}}{Mg_3Si_4O_{10}(OH)_2} \quad (4)$$

Replacement of serpentine by talc is common in the studied bedrock. The prolonged interaction of serpentine with fluid leads to the development of talc. Since carbonates (e.g. magnesite) were not detected in the samples, this observation implies that carbonatization is not responsible for the formation of talc. Thus, talc formation (eqn. 5) is possible if the silica activity of the fluid is increased or if the water activity is decreased (Bach et al., 2004).

$$\underset{\text{serpentine}}{Mg_3Si_2O_5(OH)_4} + \underset{\text{fluid}}{2SiO_2(aq)} = \underset{\text{talc}}{Mg_3Si_4O_{10}(OH)_2} + H_2O \quad (5)$$

Akita University

Talc is typically fine-grained in the bedrock samples. Based on XRPD data, talc is also present in the saprolite and limonite samples. The accumulation of talc in the weathered horizon is most likely due to residual enrichment under supergene process. In this horizon, the pH is between 6.14 and 6.82 indicating this is the right condition for the stability of residual talc. Earlier studies have reported that talc could form under near-neutral conditions (Trescases, 1973; Fontanaud and Meunier, 1983) and is stable under low-temperature conditions (Bricker et al., 1973).

A minor amount of goethite is present in the saprolite horizon with pH ranges from 7.53 to 8.13. However, at pH values between 6.24 and 6.46, there is an increased amount of goethite in the limonite horizon. Goethite is the main host of Ni in the limonite horizon, which contains significant amount of NiO of up to 1.68 wt%. Hematite is also found in this horizon, particularly more hematite is formed when the pH is above pH 6.46. This is consistent with the fact that hematite is more stable at the pH condition closer to neutral than goethite (Schwertmann and Murad, 1983). The transformation of goethite to hematite depends mainly on temperature, composition of goethite and physico-chemical parameters of the solution (Schwertmann and Murad, 1983; Gualtieri and Venturelli, 1999).

Asbolane and lithiophorite-asbolane intermediate are the typical Co-bearing Mn-oxyhydroxides in the laterites from the Intex deposit in Mindoro, Philippines. Based on the XRF results, the trends of Co and Mn are similar throughout the three profiles, suggesting the strong association of Co with

Akita University

Mn oxyhydroxides minerals. The occurrence of these minerals is linked to the oxidation of other Mn-oxyhydroxide minerals such as buserite, cryptomelane, birnessite, hollandite and todorokite (Taylor et al., 1964; McKenzie, 1989). However, we currently don't have definitive evidence in which primary minerals affect the formation of asbolane and lithiophorite-asbolane intermediate.

The mineral chemistry data reveal that both of these minerals contain significant amounts of CoO (up to 11.3 wt%) and NiO (up to 15.6 wt%). The sorption of Ni by Mn oxyhydroxides depends on structural and physicochemical parameters (Peacock, 2009), and the presence of Al in the solution at pH above 6 (Roberts et al., 1999). In this study, asbolane commonly found in the limonite horizon with a pH value above 7.29, whereas lithiophorite-asbolane intermediate occurs around pH 6.32. The results suggest that around pH 6, it allows the formation of lithiophorite-asbolane intermediate and then at higher pH (pH above 7), asbolane is precipitated. Asbolane shows a lower Co/Ni ratio (0.32) in contrast to lithiophorite-asbolane intermediate which has a higher Co/Ni ratio of 3.35. Taking into account the difference in pH and Co/Ni ratio of these minerals, these results, therefore, show that under slightly acidic conditions (pH 6), Co is more closely associated with lithiophorite-asbolane intermediate.

The limonite horizon exhibits abundant silica mainly quartz, particularly in the limonite derived from clinopyroxenite. Since pyroxenes have 15% more SiO_2 than olivine, this reflects a higher amount of silica in pyroxene-

Akita University

dominated rocks. The precipitation of silica is generally attributed to the poorly drained environment. With this environmental condition, silica may not be fully leached resulting in its accumulation in the upper horizon (Butt and Cluzel, 2013).

4.6.2. Degree of weathering on ultramafic rocks and laterites

Two weathering indexes namely Ultramafic Index of Alteration (UMIA) (Babechuk et al., 2014; Aiglsperger et al., 2016) and the Index of Lateritization (IOL) are utilized to determine the degree of chemical weathering of ultramafic rocks and laterites (Babechuk et al., 2014). Then the index values of this study are compared with the results from Berong deposit in Palawan, Philippines. Similarly, the Berong laterite ores are product of intensive weathering of ultramafic rocks under humid tropical conditions (Tupaz et al., 2019).

The Berong deposit in Palawan, Philippines is also divided from bottom to top into: (i) bedrock, (ii) saprolite and (iii) limonite horizon. The different horizons are classified based on Fe concentration, texture and mineralogy of the rock and laterite samples (Tupaz et al., 2019). Both the studied samples from Berong and Intex deposits were acquired from topmost ridges and on uneroded areas. The bedrock in the Berong deposit is mainly peridotite (i.e. harzbugite and dunite). The summer rainfall in these two deposits is between 900 and 1800 mm (Butt and Cluzel, 2013). The major differences between the two deposits are the ore minerals in the saprolite, bulk Ni concentration in the saprolite horizon and thickness of the

Akita University

weathered horizons. The saprolite horizon of the Berong deposit shows higher Ni contents of up to 6.11 wt%, and the main ore minerals are talc-like (kerolite-pimelite) and sepiolite-like (sepiolite-falcondoite) phases. The profiles in the Berong deposit have thinner saprolite (2 m to 5 m) and thicker limonite (3 m to 15m).

The UMIA values are calculated using the equation below and are expressed in molar ratios (Duzgoren et al., 2002).

$$UMIA = 100 \times ((Al_2O_3 + Fe_2O_{3(T)}) / (SiO_2 + MgO + Al_2O_3 + Fe_2O_{3(T)})) \quad (6)$$

The UMIA values of the bedrock samples from Intex deposit range from 3 to 5, the saprolite between 3 and 14, and the limonite from 16 to 82. The low UMIA values of the bedrock and saprolite samples indicate that these samples are not intensely altered. In Figure 45a, the bedrock and saprolite samples have high amounts of MgO and SiO_2. However, as weathering progresses, Mg and Si are leached from the bedrock and saprolite resulting in an increased Fe_2O_3 in the samples. The sample acquired from the transition boundary between the saprolite and limonite horizons exhibits a relatively higher UMIA value of 29 compared to the bedrock and saprolite samples (Figure 45a). On the other hand, the limonite samples are characterized by higher UMIA values (more than 50), which plot near the apex of Al_2O_3 and Fe_2O_3. This observation is consistent with the fact that limonite samples from Intex deposit contain a high amount of Fe_2O_3 indicating the abundance of Fe-oxyhydroxides (e.g. goethite and hematite) in the samples.

Akita University

The UMIA values of the bedrock and saprolite from Intex deposit are comparable to that of the Berong deposit in Palawan, Philippines. Based on Figure 45a, the two deposits have a similar weathering trend. However, the limonite samples from the Berong deposit show the highest UMIA values suggesting that these samples are strongly altered.

The different stages of advanced chemical weathering are not sufficiently quantified if only UMIA is utilized. To supplement these results, IOL is applied. This index is a quantitative approach to determine the stages of advanced chemical weathering (weakly, moderately, and strongly), and is typically expressed in wt% (Babechuk et al., 2014).

$$IOL = 100 \times ((Al_2O_3 + Fe_2O_{3(T)}) / (SiO_2 + Al_2O_3 + Fe_2O_{3(T)})) \quad (7)$$

The IOL values of the bedrock samples are in the range of 14 to 19, and the saprolite samples up to 17. However, the limonite samples from the Intex deposit exhibit higher IOL values reaching up to 94 (Figure 45b). Earlier studies reported that unweathered rocks have IOL values of less than 40 (Bach et al., 2004). Even though the IOL values of the saprolite samples are low, these suggest weak weathering based on observations under the microscope. Conversely, the sample from the transition boundary has a higher IOL value (46), corresponding to the point in the middle section of the SiO_2-Al_2O_3-Fe_2O_3 (SAF) ternary diagram, which indicate a significant loss of silica. As lateritization progresses, more silica is leached resulting

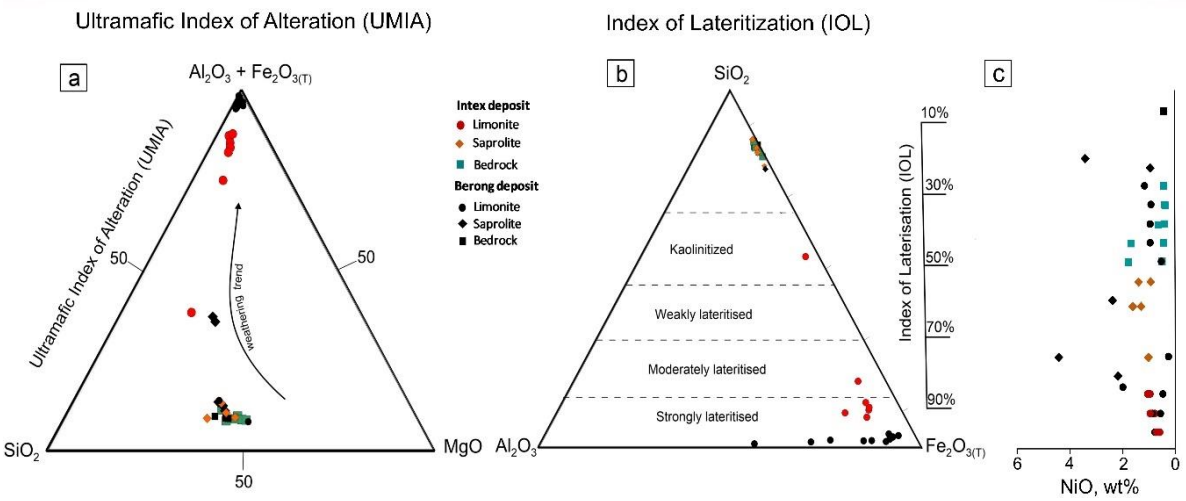

Fig. 45. Molar ternary plot of (a) Al_2O_3+Fe_2O_3+-SiO_2-MgO showing the weathering of ultramafic bedrock from Intex deposit with the depletion of SiO_2 and MgO and relative enrichment of Al_2O_3 and Fe_2O_3. (b) Mass ternary plot of SiO_2-Al_2O_3-Fe_2O_3 displaying the Index of Lateritization (IOL) for Intex deposit and the Berong deposit. (c) Bulk Ni contents in the bedrock and weathered horizons of the Intex and Berong deposits.

on the enrichment of Fe. Samples from the saprolite and limonite horizons show an apparent increase in Ni (Figure 45c).

The calculated IOL values of the Intex profiles correspond to a less advanced stage of weathering or moderately to strongly “laterized” profiles, which leads to the development of thicker saprolite (3 m to 8 m) and thinner limonite (3 m to 4.5 m). In contrast, the profiles in the Berong deposit experienced a more advanced stage of weathering or strongly “laterized” profiles and subsequently yielded thinner saprolite (2 m to 5 m) and thicker limonite (3 m to 15m). Concerning the Ni contents between the two deposits, the Intex deposit exhibit lower bulk Ni in the saprolite (up to 1.69 wt%) and limonite (up to 0.79 wt%) compared with the Berong deposit (up to 6.11 wt%; up to 0.90 wt%) (Figure 45c). Thus, the difference in Ni

Akita University

concentration between the Intex and Berong deposits may be the result of different degrees of weathering of the laterites.

Since the limonite from the Intex deposit experienced a less advanced degree of weathering, this affected the leaching and re-mobilization of Ni from the limonite horizon towards the saprolite horizon. The weathering solution is not supersaturated with Ni, Si, and Mg, which may have resulted in poor precipitation of talc-like (kerolite- pimelite) or sepiolite-like (sepiolite-falcondoite) phases in the studied saprolite horizon. Nevertheless, the combined mineralogical and geochemical data suggest that Ni in the Intex deposit has undergone supergene enrichment similar to other humid tropical laterite deposits in New Caledonia, the Caribbean, and northeastern Australia (Cluzel and Vigier, 2008; Villanova-de-Benavent et al., 2014; Aiglsperger et al., 2016; Chassé et al., 2017).

4.6.3 Formation of Intex laterite deposit, Mindoro, Philippines

The Intex laterite deposit evolved from the weathering of the peridotite and pyroxenite bedrock under a humid tropical climate. These rocks were fractured and sheared during the tectonic activity in the Miocene. The effect of uplift also results in the change of the topography, where the regolith is freely drained (Golightly, 1979a). Such conditions allow the percolation of mildly acidic meteoric water which intensifies the leaching of MgO and SiO_2. The removal of these oxides leads to the residual enrichment of Fe_2O_3 and NiO, which mainly hosted by goethite in the limonite. The degree of

Akita University

weathering in the Intex laterites is less extreme compared with the Berong laterites in Palawan, Philippines. The Intex profiles formed thicker saprolite between 3.4 and 8.2 m, and thinner limonite that ranges from 3 to 4.5 m only. The less advanced chemical weathering of the Intex laterites affected the leaching and re-mobilization of Ni, Mg and Si from the upper horizon towards the saprolite horizon and may have led to poor precipitation of talc-like and sepiolite-like phases in the studied saprolite. The genesis of the Intex deposit is analogous to the Berong deposit and models proposed by previous workers (Freysinnet et al., 2005; Cluzel and Vigier, 2008; Butt and Cluzel, 2013). The Intex laterite deposit evolved from two distinct stages: (i) the development of the saprolite and the limonite horizons, and (ii) the formation of Ni- bearing serpentine, Mn-oxyhydroxides and silica in the limonite (Figure 46).

Akita University

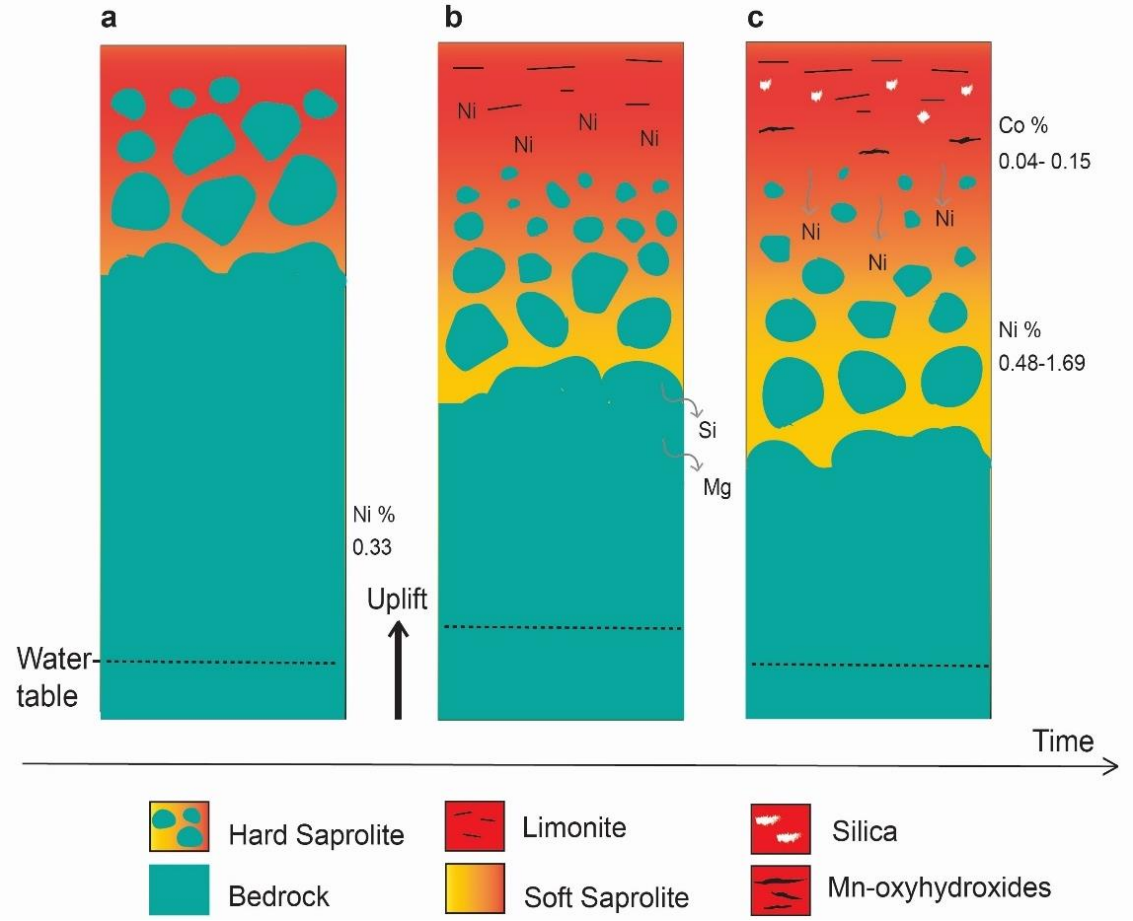

Fig. 46. The evolution stages of the Intex Ni-Co laterite deposit. The strong chemical weathering of the peridotite and pyroxenite bedrock resulted in the development of the a) saprolite and limonite horizons, b) with the effect of uplift and change in pH environmental condition, the Mg and Si in the bedrock is leached excessively which caused the c) re-distribution and mobilization of Ni to the saprolite leading to the formation of Ni-bearing serpentine in the saprolite and Mn-oxyhydroxides with secondary in the limonite horizon.

4.7 Conclusions

The weathering of the serpentinized ultramafic rocks resulted in the formation of the Intex laterite deposit. In the bedrock, olivine is the main source of ore in the saprolite and limonite horizons. The early stages of serpentinization leads to the development of type I, type II, type III, and type

Akita University

IV serpentines. The results of this study show that these serpentines are of hydrothermal origin. The late-stage type V serpentines cut the early-stage type I to type IV serpentines. Type V serpentines are the serpentine-like garnierites and display the highest amount of NiO (avg. 1.42 wt%).

The UMIA and IOL values of the Intex laterites are in agreement with the less advanced stage of weathering compared with Berong laterites. The difference in bulk Ni concentration between the Intex and Berong deposits may be the result of different degrees of weathering of the laterites. The less extreme degree of weathering of Intex profiles indicates less advanced leaching, and thus re-distribution of Ni, Si, and Mg from the limonite towards the saprolite horizon may have resulted in the poor precipitation of talc-like (kerolite-pimelite) and sepiolite-like (sepiolite-falcondoite) phases in the studied saprolite horizon.

Supergene enrichment of Ni occurred in the Intex laterite deposit, which is comparable to the Ni laterite deposits in New Caledonia, the Caribbean, and northeastern Australia. The main difference between the Intex deposit and other tropical laterite deposits is the composition of garnierites. In this study, garnierites consist mainly of serpentine-like minerals, whereas talc-like and sepiolite-like phases are often found in other laterite deposits. Another similarity of the studied deposit with other classic deposits is the occurrence of goethite and Mn-oxyhydroxides (i.e. asbolane and lithiophorite-asbolane intermediate) in the limonite horizon. Ni is mainly hosted by goethite, and Mn-oxyhydroxides contain significant amounts of

Akita University

CoO (up to 11.3 wt%) and NiO (up to 15.6 wt%). Our results show that the Intex laterite deposit evolved from two distinct stages: (i) the development of the saprolite and the limonite horizons, and (ii) the formation of Ni-bearing serpentines, Mn-oxyhydroxides and silica.

4.8 References

Aiglsperger, T., Proenza, J. A., Lewis, J. F., Labrador, M., Svojtka, M., Rojas-Puron, A., Ďurišová, J., 2016. Critical metals (REE, Sc, PGE) in Ni laterites from Cuba and the Dominican Republic. Ore Geol Rev. 73, 127-147.

.

Auzende, A.L., Devouard, B., Guillot, S., Daniel, I., Baronnet, A., Lardeaux, J.M., 2002. 465 Serpentinites from Central Cuba: petrology, and HRTEM study. European Journal of 466 Mineralogy 14, 905-914.

Auzende, A.L., Daniel, I., Reynard, B., Lemaire, C., Guyot, F., 2004. High-pressure behaviour of serpentine minerals: A Raman spectroscopic study. Phys. Chem. Miner. 31, 269-277.

Babechuk, M.G., Widdowson, M., Kamber, B.S., 2014. Quantifying chemical weathering intensity and trace element release from two contrasting basalt profiles, Deccan Traps, India. Chem. Geol. 103, 1645-1680.

Bach, W., Garrido, C. J., Paulick, H., Harvey, J., Rosner, M., 2004. Seawater-peridotite interactions: First insights from ODP Leg 209, MAR 15 N. Geochem Geophys. 5, 1-22.

Beard, J.S., Frost, B.R., Fryer, P., McCaig, A., Searle, R., Ildefonse, B., Zinin, P., Sharma, S.K., 2009. Onset and progression of serpentinization and magnetite formation in Olivine-rich troctolite from IODP hole U1309D. J. Petrol. 50, 387-403.

Bird, P.R., Quinton, N.A., Beeson, M.N., Bristow, C., 1993. Mindoro: a rifted microcontinent in collision with the Philippine Island arc: basin evolution and hydrocarbon potential. J Southeast Asian Earth Sci. 8, 449-468.

Akita University

Brand, N.W., Butt, C.R.M., Elias, M. 1998. Nickel laterites: classification and features. AGSO J. Aust. Geol. Geophys. 17, 81-88.

Boudier, F., Ceuleneer, G., Nicolas, A., 1988. Shear zones, thrusts and related magmatism in the Oman ophiolite: initiation of thrusting on an oceanic ridge. Tectonophysics. 151, 275-296.

Bricker, O.P., Wayne, Nesbitt, H., Gunter, W.D., 1973. The stability of talc. Am Miner. 58, 64-72.

Butt, C.R.M., Cluzel, D., 2013. Nickel laterite ore deposits: Weathered serpentinites. Elements. 9, 123-128.

Cluzel, D., Vigier, B., 2008. Syntectonic mobility of supergene nickel ores of new caledonia (Southwest Pacific). Evidence from garnierite veins and faulted regolith. Resour. Geol. 58, 161-170.

Concepcion, R.A.B, Dimalanta, C.B., Yumul, G.P., Faustino-Eslava, D.V., Queaño, K.L., Tamayo, R.A., Imai, A., 2012. Petrography, geochemistry, and tectonics of a rifted fragment of Mainland Asia: evidence from the Lasala Formation, Mindoro Island, Philippines. Int J Earth Sci. 101, 273-290.

Dublet, G., Juillot, F., Morin, G., Fritsch, E., Fandeur, D., Brown Jr., G.E., 2015. Goethite aging explains Ni depletion in upper units of ultramafic lateritic ores from New Caledonia. Geochim. Cosmochim. Acta. 160, 1-15.

Duzgoren-Aydin, N.S., Aydin, A., Malpas, J., 2002. Distribution of clay minerals along a weathered pyroclastic profile, Hong Kong. Catena. 50, 17-41.

Elias, M., 2002. Nickel laterite deposits – geological overview , resources and exploitation. Giant Ore Depos. Charact. Genes. Explor. CODES Spec. Publ. 4, 205-220.

Ferrer, C., 2013. Laterites from Different Ultramafic Rocks in Mindoro, Philippines: Effect of Bedrock Mineralogy on the Mineralogy and Geochemistry of Laterites. Unpublished M.S. Thesis, NIGS, UP Diliman. 41-47.

Freyssinet, P., Butt, C.R.M., Morris, R.C., Piantone, P., 2005. Ore-forming processes related to lateritic weathering. Econ. Geol. 100th Anniv. 681-722.

Akita University

Frost, R.B., Beard, J.S., 2007. On silica activity and serpentinization. J. Petrol. 48, 1351-1368.

Fontanaud, A., Meunier, A., 1983. Mineralogical facies of a weathered serpentinized lherzolite from the Pyrenees, France. Clay Miner. 18, 77-88.

Fu, W., Yang, J., Yang, M., Pang, B., Liu, X., Niu, H., Huang, X., 2014. Mineralogical and geochemical characteristics of a serpentinite-derived laterite profile from East Sulawesi, Indonesia: Implications for the lateritization process and Ni supergene enrichment in the tropical rainforest. J. Asian Earth Sci. 93, 74-88.

Gleeson, S.A., Herrington, R.J., Durango, J., Velásquez, C.A., Koll, G., 2004. The mineralogy and geochemistry of the Cerro Matoso S.A. Ni Laterite deposit, Montelíbano, Colombia. Econ. Geol. 99, 1197-1213.

Golightly, J.P., Arancibia, O.N., 1979. The chemical composition and infrared spectrum of nickel-and iron-substituted serpentine from a nickeliferous laterite profile, Soroako, Indonesia. The Can Mineral. 17, 719-728.

Golightly, J.P., 1981. Nickeliferous laterite deposits. Econ Geol 75th Anniv. 710-735.

Hamilton, W., 1979. Tectonics of the Indonesian Region. U.S. Geol. Surv. Prof. Paper. 1078, 345.

Hashimoto, W., Sato, T., 1968. Contribution to the geology of Mindoro and neighboring islands, the Philippines. Geology and Paleontology of Southeast Asia. 5, 192-210.

Holloway, N.H., 1982. North Palawan block, Philippines - its relation to Asian mainland and role in evolution of South China Sea. Am. Assoc. Pet. Geol. Bull. 14, 19-58.

Karig, D.E., 1973. Plate convergence between the Philippines and the Ryukyu islands. Mar. Geol. 14, 153-168.

Karig, D.E., Sarewitz, D.R., 1986. Processes of allochthonous terrane evolution, Mindoro, Island, Philippines. Tectonics. 5, 525-552.

Akita University

Klein, F., Bach, W., Humphris, S. E., Kahl, W. A., Jöns, N., Moskowitz, B., Berquó, T. S., 2014. Magnetite in seafloor serpentinite—Some like it hot. Geol. 42, 135-138.

Ilyas, A., Kashiwaya, K., Koike, K., 2016. Ni grade distribution in laterite characterized from geostatistics, topography and the paleo-groundwater system in Sorowako, Indonesia. J. Geochemical Explor. 165, 174-188.

Marsh, E., Anderson, E., Gray, F., 2011. Ni-Co laterites–a deposit model. US Geol Surv. 1, 1-9.

McKenzie, R.M., 1989. Manganese oxides and hydroxides. Minerals in Soil Environments. 1, 439-465.

Mitchell, A.H.G., Hernandez, F., dela Cruz, A.P., 1986. Cenozoic evolution of the Philippine archipelago. J. Southeast Asian Earth Sci. 1, 3-22.

Muñoz, M., Ulrich, M., Cathelineau, M., Mathon, O., 2019. Weathering processes and crystal chemistry of Ni-bearing minerals in saprock horizons of New Caledonia ophiolite. J. Geochemical Explor. 198, 82-99.

Myagkiy, Truche, L., Cathelineau, M., Golfier, F., 2017. Revealing the conditions of Ni mineralization in the laterite profiles of New Caledonia: Insights from reactive geochemical transport modelling. Chem. Geol. 466, 274-284.

O'Hanley, D.S., 1996. Serpentinites: records of tectonic and petrological history. Oxford University Press on Demand. 1, 42-58.

Peacock, C.L., 2009. Physiochemical controls on the crystal-chemistry of Ni in birnessite: genetic implications for ferromanganese precipitates. Geochim. Et Cosmochim Acta. 73, 3568-3578.

Petersen, J.S., Jensen, S.M., Blomsterberg, J., Audet, MA., 2010. Mineral Resources of the Mindoro Nickel-Laterite Project, the Philippines: Ni 43-101 Technical Report, Unpublished Technical Report. 1-10.

Petriglieri, J.R., Salvioli-Mariani, E., Mantovani, L., Tribaudino, M., Lottici, P.P., Laporte-Magoni, C., Bersani, D., 2015. Micro-Raman mapping of the polymorphs of serpentine. J. Raman Spectrosc. 46, 953-958.

Akita University

Rangin, C., Stephan, J.F., Müller, C., 1985. Middle Oligocene oceanic crust of South China Sea jammed into Mindoro collision zone (Philippines). Geology. 13, 425-428.

Roberts, D.R., Scheidegger, A.M., Sparks, D.L., 1999. Kinetics of mixed Ni-Al precipitate formation on a soil clay fraction. Environ Sci Technol. 33, 3749-3754.

Roqué-Rosell, J., Mosselman, J.F.W., Proenza, J.A., Labrador, M., Gali, S., Atkinson, K.D., Quinn, P.D. 2010. Sorption of Ni by'lithiophorite-asbolane' intermediates in Moa Bay lateritic deposits, eastern Cuba. Chem. Geol. 275, 9-18.

Sarewitz, D.R., Karig, D.E., 1986. Stratigraphic framework of western Mindoro Island, Philippines. Journal of the Geological Society Philippines. 40, 3-51.

Schwertmann, U., Murad, E., 1983. Effect of pH on the formation of goethite and hematite from ferrihydrite. Clays Clay Miner. 31, 277-284.

Schwartz, S., Guillot, S., Reynard, B., Lafay, R., Debret, B., Nicollet, C., Lanari, P., Auzende, A.L., 2013. Pressure-temperature estimates of the lizardite/antigorite transition in high pressure serpentinites. Lithos. 178, 197-210.

Taylor, R.M., McKenzie, R.M., Norrish, K., 1964. The mineralogy and chemistry of manganese in some australian soils. Aust. J. Soil Res. 2, 235-248.

Toft, P.B., Arkani-Hamed, J., Haggerty, S.E., 1990. The effects of serpentinization on density and magnetic susceptibility: a petrophysical model. Phys. Earth Planet. Inter. 65, 137-157.

Thorne, R.L., Roberts, S., Herrington, R., 2012. Climate change and the formation of nickel laterite deposits. Geology. 40, 331-334.

Trescases, J. J., 1973. Weathering and geochemical behaviour of the elements of ultramafic rocks in New Caledonia. Bureau of Mineral Resources, Geology and Geophysics, Canberra, Extract from Bulletin. 141, 149-161.

Tupaz, C.A.J, Watanabe, Y., Sanematsu, K., Echigo, T., 2019. Mineralogy and geochemistry of the Berong Ni-Co laterite deposit, Palawan, Philippines. Manuscript submitted for publication.

Akita University

Ulrich, M., Cathelineau, M., Muñoz, M., Boiron, M.C., Teitler, Y., Karpoff, A.M., 2019. The relative distribution of critical (Sc, REE) and transition metals (Ni, Co, Cr, Mn, V) in some Ni-laterite deposits of New Caledonia. J. Geochemical Explor. 197, 93-113.

Yongue-Fouateu, R., Ghogomu, R.T., Penaye, J., Ekodeck, G.E., Stendal, H., Colin, F., 2006. Nickel and cobalt distribution in the laterites of the Lomié region, south-east Cameroon. J. African Earth Sci. 45, 33-47.

Villanova-de-Benavent, C., Proenza, J.A., Galí, S., García-Casco, A., Tauler, E., Lewis, J.F., Longo, F., 2014. Garnierites and garnierites: Textures, mineralogy, and geochemistry of garnierites in the Falcondo Ni-laterite deposit, Dominican Republic. Ore Geol. Rev. 58, 91-109.

Yumul Jr, G. P., Dimalanta, C. B., Tamayo Jr, R. A., Maury, R. C., 2003. Collision, subduction and accretion events in the Philippines: a synthesis. Island Arc. 12, 77-91.

Yumul, G. P., Dimalanta, C. B., Tamayo, R. A., 2005. Indenter-tectonics in the Philippines: Example from the Palawan Microcontinental Block-Philippine Mobile Belt Collision. Resour Geol. 55, 189-198.

Akita University

CHAPTER 5

Trace element (Sc, REE) distribution in Ni laterite from Berong, Palawan and Intex, Mindoro, Philippines

Abstract

Ni laterite deposits contain a significant amount of Ni and, to a lesser extent, Co and Sc, which are vital for sustainable energy development. In this study, the trace element composition (Sc, REE) in laterites from Berong, Palawan and Intex, Mindoro, Philippines are investigated. The mobility diagrams exemplify the depletion of the major elements (Mg, Si) and enrichment of Ni, Co, Mn, Sc and REE in laterites with respect to the bedrock during weathering. The limonite horizon is marked by increased concentrations of Sc and REE (up to 67 ppm and 357 ppm). The positive correlations of Sc with Fe and Mn suggest that it is likely associated with Fe- or Mn-oxyhydroxides minerals such as goethite, asbolane or lithiophorite-asbolane intermediate. The maximum amount of REE typically occurs either at the transition boundary between the saprolite and limonite horizons or at the lower section of the limonite. The trend of REE mimics the trend of Fe, indicating that Fe-oxyhydroxides phases could also host these elements. The occurrence of the positive and negative Ce anomalies between the upper section of the limonite and the lower section of the limonite or saprolite may reflect the redox boundary where REE can accumulate.

Akita University

5.2 Introduction

The global production of Ni comes from laterite ores, accounting for about 40% of the total production, and the rest comes from sulfide ores. Nickel laterite ores also contain Co and scandium (Sc) (Butt and Cluzel, 2013). Since the report published by the European Commission (2014) about the list of critical raw materials, several studies and projects have been commenced to determine the concentration of Sc and REE in various deposits, including laterite deposits. The raw materials were considered critical based on their economic significance and relative risk of supply. Over the past few years, there has been an increasing demand to produce permanent magnets, wind turbines, electric cars, and others. These materials are commonly utilized to produce green technologies, which are essential to lessen greenhouse gases and obtain efficient energy supply (Chakhmouradain and Wall, 2012). Scandium is mostly used to alloy with Al and to produce Solid Oxide Fuel Cells (SOFCs), whereas REE are used in catalytic converters, ceramics and glass, polishing, and associated metallurgical applications (USGS, 2019). In 2017, an updated version of the report highlighted the supply of REE because China restricted the exportation of these metals. Nevertheless, China is the leading supplier of REE, producing approximately 95% of REE globally (EC, 2017).

Several studies were devoted to determine the occurrence of Sc and REE along the laterite profiles in Cuba and the Dominican Republic (Villanova-de-Benavent et al., 2014; Aiglsperger et al., 2016), Australia

Akita University

(Chasśe et al., 2017) and in New Caledonia (Ulrich et al., 2019; Teitler et al., 2019). It has been determined that these elements displayed low mobility, thus may concentrate locally in oxides, neoformed silicates, and phosphates (Eliopoulos and Economu-Eliopoulus, 2000; Chakhmouradain and Wall, 2012). The enrichment of Sc in the weathered horizon, particularly in oxide deposits, is controlled mainly by the initial amount of Sc in the bedrock. Chasśe et al. (2017) showed that oxide type laterites derived from clinopyroxenite containing Sc concentrations up to 800 ppm locally, whereas oxide-type laterites developed above peridotites may hold up to 100 ppm (Audet 2008; Aiglsperger et al., 2016). To date, few studies have been conducted to determine the Sc and REE contents in Philippine laterite deposits.

This work presents mainly the trace elements, including Sc and REE, in laterites developed above ultramafic rocks in the Berong deposit, Palawan and Intex deposit, Mindoro, Philippines. The aim is to understand their geochemical behavior and enrichment in the laterite profiles. The mobility of the major, minor, and trace elements in the weathered horizons with respect to the bedrock is also explained.

5.3 Study areas

The Sc and REE contents in two Philippine laterite deposits are investigated, particularly in Palawan and Mindoro, Philippines (Fig. 47). In Palawan, the samples were collected from three outcrops at the open pit

mine of Berong Nickel Corporation (BNC), whereas drill core samples were acquired at the core house of Intex in Victoria, Mindoro, Philippines.

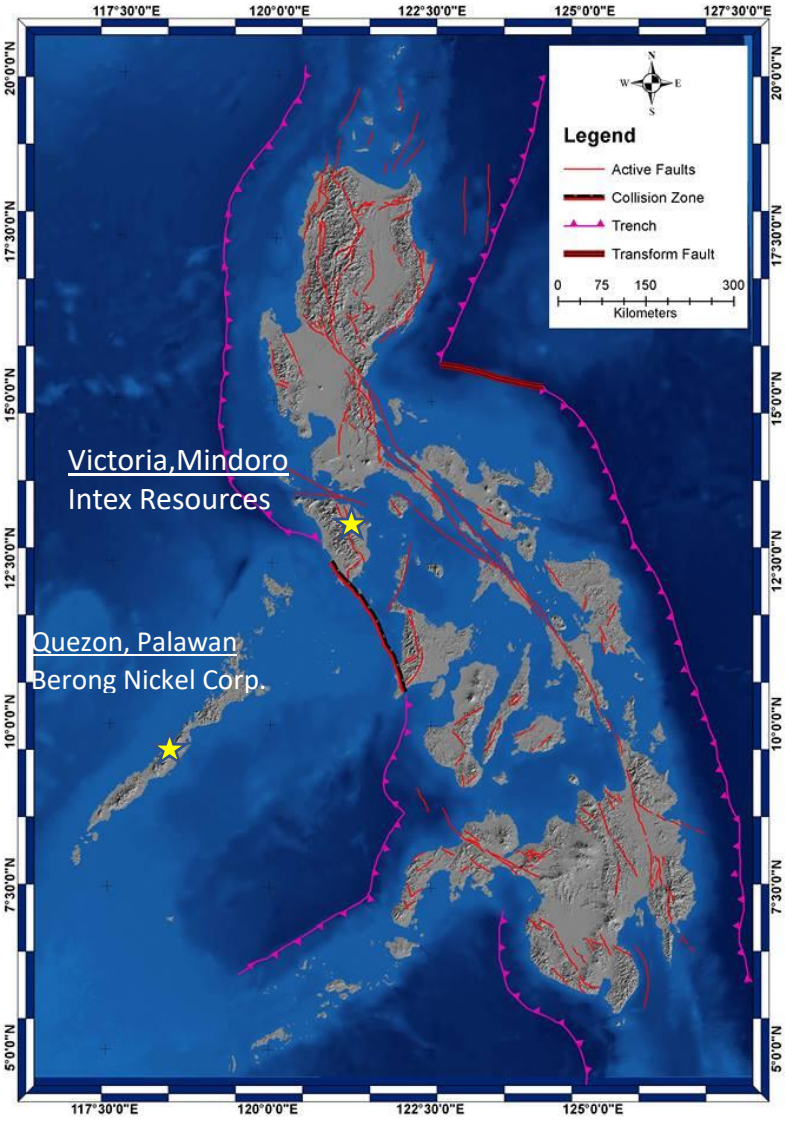

Fig. 47 Location map of the studied laterite deposits in the Philippines.

5.4 Material and analytical methods

Thirty-three samples were collected from the different horizons of the laterite profile at Berong deposit, Palawan (Table 18), whereas 23 samples

from the drill cores at Intex deposit, Mindoro, Philippines (Table 19). A total of 56 samples were air-dried at 20°C to 30°C for up to two weeks, quartered, and then powdered using mortar and pestle.

Table 18 List of samples collected from three laterite outcrops at Berong deposit in Palawan, Philippines.

Profile A	Profile B	Profile C
PA-2 m	PB- 1 m	PC- 1 m
PA-3 m	PB- 2 m	PC- 2 m
PA-4 m	PB- 3 m	PC- 3 m
PA-5 m	PB- 7 m	PC- 3.4 m
PA-6 m	PB- 8 m	PC- 4 m
PA-9 m	PB- 9 m	PC- 5 m
PA-10 m	PB- 10 m	PC- 6 m
PA-12 m	PB- 11 m	PC- 8 m
PA-13 m	PB- 12 m	
PA-14 m	PB- 13 m	
PA-15 m		
PA-15.5 m		
PA-18 m		

Table 19 Summary of drill core samples collected at Intex deposit in Mindoro, Philippines.

BB2515 core	PG1500 core	BB2406 core
DC1- 1 m	DC2- 1 m	DC3- 2 m
DC1- 2 m	DC2- 3 m	DC3- 3 m
DC1- 4.5 m	DC2- 3.8 m	DC3- 4.8 m
DC1- 5 m	DC2- 4 m	DC3- 6 m
DC1- 7 m	DC2- 6 m	DC3- 8 m
DC1- 9 m	DC2- 9 m	DC3- 10 m
DC1- 12 m	DC2- 13 m	DC3- 12 m
DC1- 14 m		DC3- 16 m

Akita University

5.4.1 Open acid digestion for ICP-MS analysis

Laterite samples and reference materials of 0.1000 g were weighed and transferred into 5-ml PTFE beakers. Then these were added with 1 ml of 23M hydrofluoric acid (HF) and 1 ml of 7M perchloric acid ($HClO_4$) (Fig. 48a). The tightly capped beakers were covered with aluminum foil and were heated on a hotplate at 100˚C. The decomposed samples were dried at 120˚C for 12 hours, followed by 165˚C for 12h and 195˚C until dryness. The dried residues were dissolved in 1ml of 7M $HClO_4$, heated and evaporated again in a similar set of temperatures. One ml of concentrated HNO_3 was added to the dried samples and were heated at 90˚C for 30 minutes. Also, 3 ml of H_2O were added, and the capped beaker was heated again at 90^0C for 4 hours. The final solutions were added with 4 ml HNO_3 and were diluted using ultrapure H_2O to 100 ml volumetric flask (Fig. 48b). The sample solutions were filtered using a 0.45 µm filter and were analyzed using Agilent 7500 ICP-MS at a dilution of 1:10000.

5.4.2 Instrumentation, spectral lines and interferences

In this study, $HClO_4$ acid was used because it has been reported to effectively remove insoluble REE fluoride interferences from oxide ions of dysprosium (Dy) and holmium (Ho) to low levels (Makishima et al., 1999; Nagaishi and Ishikawa 2009). The sample solutions were carried out at higher power (1550 W) using the Agilent 7700 ICP-MS instrument (Agilent Technologies), which is available at Akita University (Fig. 48c). Makishima et al. (1999) and Nagaishi and Ishikawa (2009) reported that a higher power

(> 1100 W) is needed to reduce the occurrence of matrix effects. Every after analysis, the system is washed with 2% HNO_3 to remove the remaining samples from the previous samples. Operating conditions and measurement parameters are shown in Table 20. The recommended spectral lines available in the software was used in this work. Rhenium (Re) was used as an internal standard to eliminate common problems encountered in ICP-MS analysis, such as differences in solution parameters (e.g., density, viscosity, or surface tension), power fluctuations, changes in temperature and sample introduction system (Sivakumar et al., 2006).

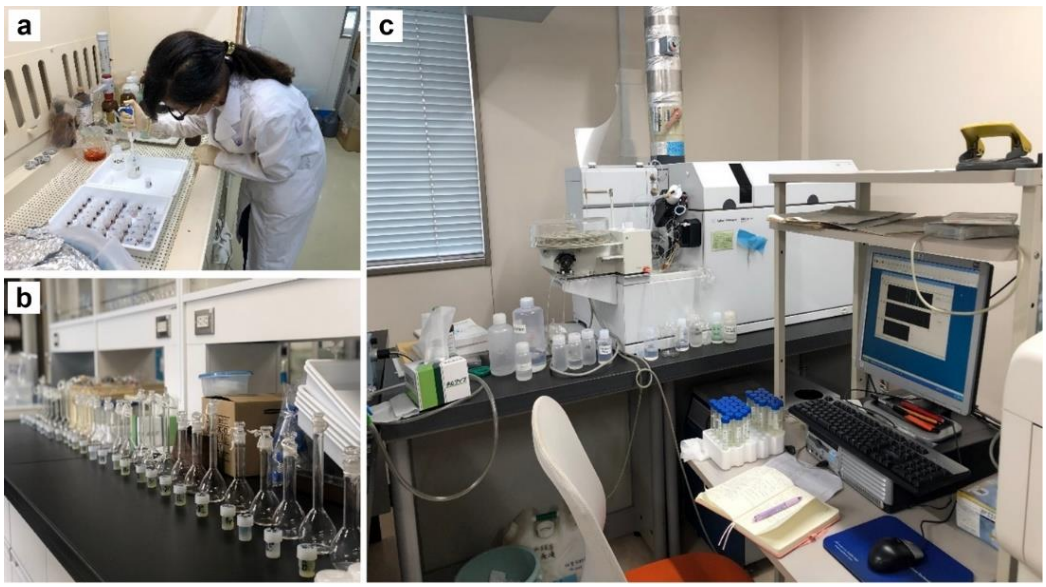

Fig. 48 Photos of a) transferring of HF and $HClO_4$ acids to the samples b) batch of final solutions ready for analysis c) set-up of Inductively Coupled Plasma – Mass Spectrometer (ICP-MS) taken at the facility of the Graduate School of International Resource Sciences, Akita University.

Akita University

Table 20 Instrumental operating conditions for ICP-MS.

Agilent 7500 ICP-MS	
RF power	1550 W
	1.78 V
RF Matching	8 mm
Sample Depth	0.2 mm
Torch-H	0.2 mm
Torch-V	0.9 L/min
Carrier Gas	0.22 L/min
Make-up Gas	0.1 rps
Nebulizer Pump	2 mins.
Sample uptake time	2 mins.
Total measurement time	3 mins.
Wash time	2^0C
S/C Temp	Electron Multiplier
Detector type	^{45}Sc, ^{89}Y, , ^{139}La, ^{140}Ce, ^{141}Pr, ^{146}Nd, ^{147}Sm, ^{151}Eu, ^{157}Gd, ^{159}Tb, ^{163}Dy, ^{165}Ho, ^{166}Er, ^{169}Tm, ^{172}Yb, ^{175}Lu, ^{232}Th
Isotopes quantified	

5.5 Results

5.5.1 Geochemistry

5.5.1.1 Berong Ni-Co laterite deposit, Palawan, Philippines

Figures 49, 50 and 51 display the geochemical trends of the major (SiO_2, MgO, Al_2O_3, Fe_2O_3), minor (NiO, Co_2O_3, MnO), and trace elements (Sc and total REE) chemical analyses of the bedrock, saprolite and limonite samples at Berong, Palawan, Philippines. The total REE consists of elements from lanthanum (La) to lutetium (Lu). Tables 21, 22, and 23 show the concentrations of Sc and REE present in the samples. Since the geochemical trends for the major and minor elements were already explained in the previous chapters, only the distribution of trace elements is described in detail. In general, the variations show a progressive loss of Mg

Akita University

and Si from the saprolite to the uppermost horizon and an upward enrichment of Fe and Al. In all the studied profiles, the highest Ni concentration is observed in the saprolite horizon, and Co and Mn are enriched in the limonite horizon.

5.5.1.1.1 Profile A

The harzburgite bedrock of profile A contains a low amount of Sc (6 ppm) but shows an increasing trend towards the limonite horizon with concentrations of up to 55 ppm. It is apparent from Figure 49a the irregular pattern of Sc in this horizon, and interestingly, it mimics the behavior of Fe_2O_3. Even though the total REE contents of the bedrock and saprolite samples are below the detection limit, significant enrichment (up to 82 ppm) is observed between the transition boundary of the saprolite and limonite horizons. However, the trend subsequently decreases as it reaches the surface.

The chondrite normalized patterns show that the lower limonite samples are one order magnitude higher than the upper limonite samples (Fig. 49b). A strong negative Ce anomaly is observed between the transition boundary, whereas positive Ce anomalies are evident at 12 m and 14 m depth, which are both parts of the lower limonite section. The zigzag patterns indicate low REE contents in the samples.

Akita University

5.5.1.1.2 Profile B

Profile B shows an increasing trend of Sc from the saprolite horizon (3 ppm) until the uppermost section of the limonite horizon (55 ppm). The total amount of REE are low in the saprolite samples, but with a remarkable increase of up to 357 ppm in the lower limonite. The concentration of these elements decreases towards the surface (Fig. 50a).

Both the total REE contents of the saprolite and the lower limonite samples are one to two order magnitude higher compared to the contents of the upper limonite samples. Also, strong negative Ce anomalies are observed in these sections. The bedrock is marked by very low REE concentrations and is below the detection limit of the ICP-MS machine (Fig. 50b).

5.5.1.1.3 Profile C

The behavior of Sc in profile C is similar to the previous profiles, where the saprolite horizon is marked by the relatively lower amount of Sc (7 to 18 ppm). The amount of Sc increases towards the uppermost horizon with a concentration of up to 61 ppm. Among the studied profiles at Berong, profile C exhibits the lowest amount of total REE (up to 15 ppm) (Fig. 51a).

The low contents of REE are reflected in the chondrite normalized REE patterns. Figure 51b shows highly irregular patterns, and often disconnected points are noticeable, indicating the occurrence of very low REE concentrations in the limonite and saprolite samples.

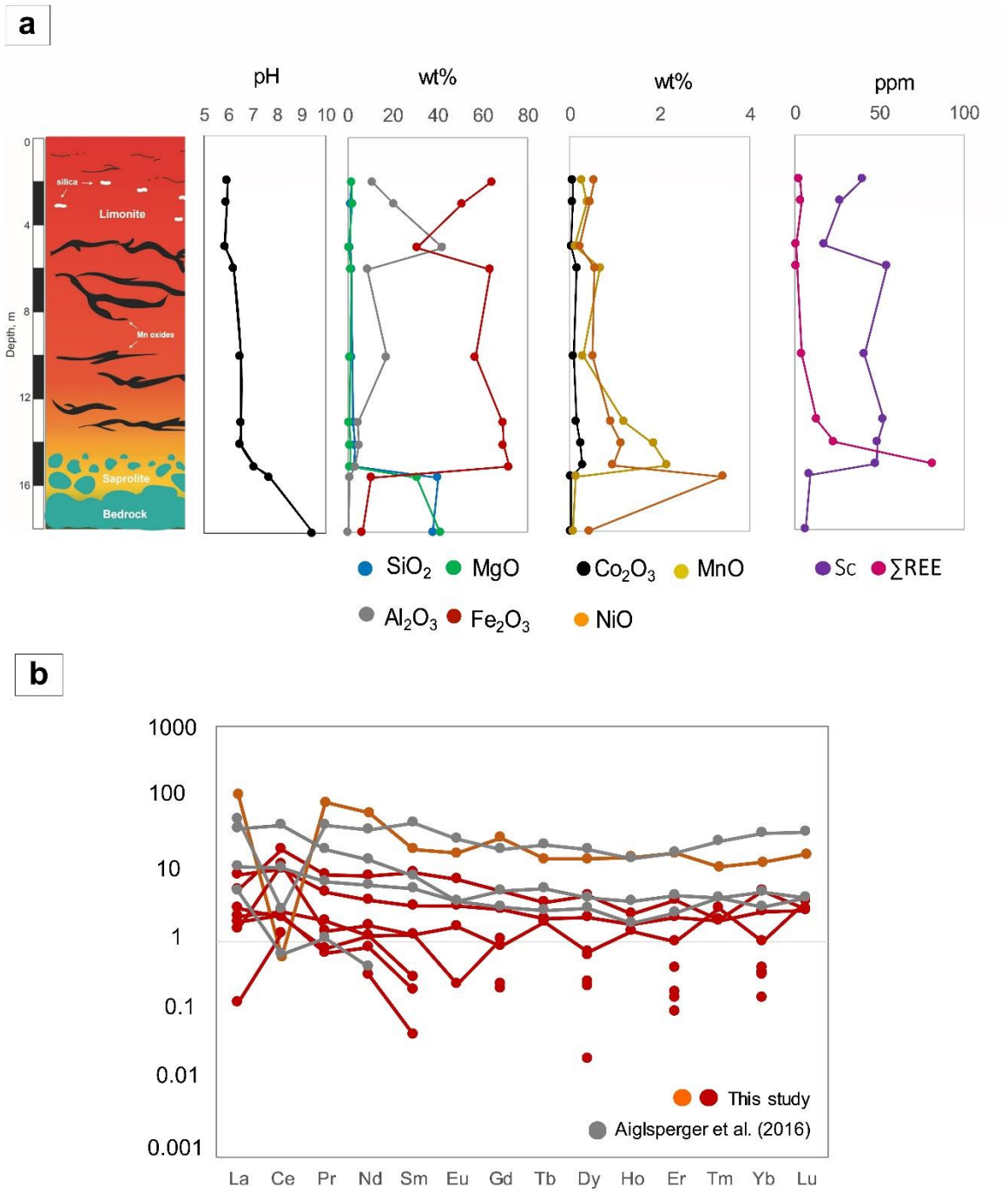

Fig. 49 a) Variation in concentration of major, minor, and trace elements with depth. b) Chondrite normalized REE patterns of the saprolite (orange) and limonite (red) samples from profile A. Normalization (chondrite) values from Anders and Grevesse (1989).

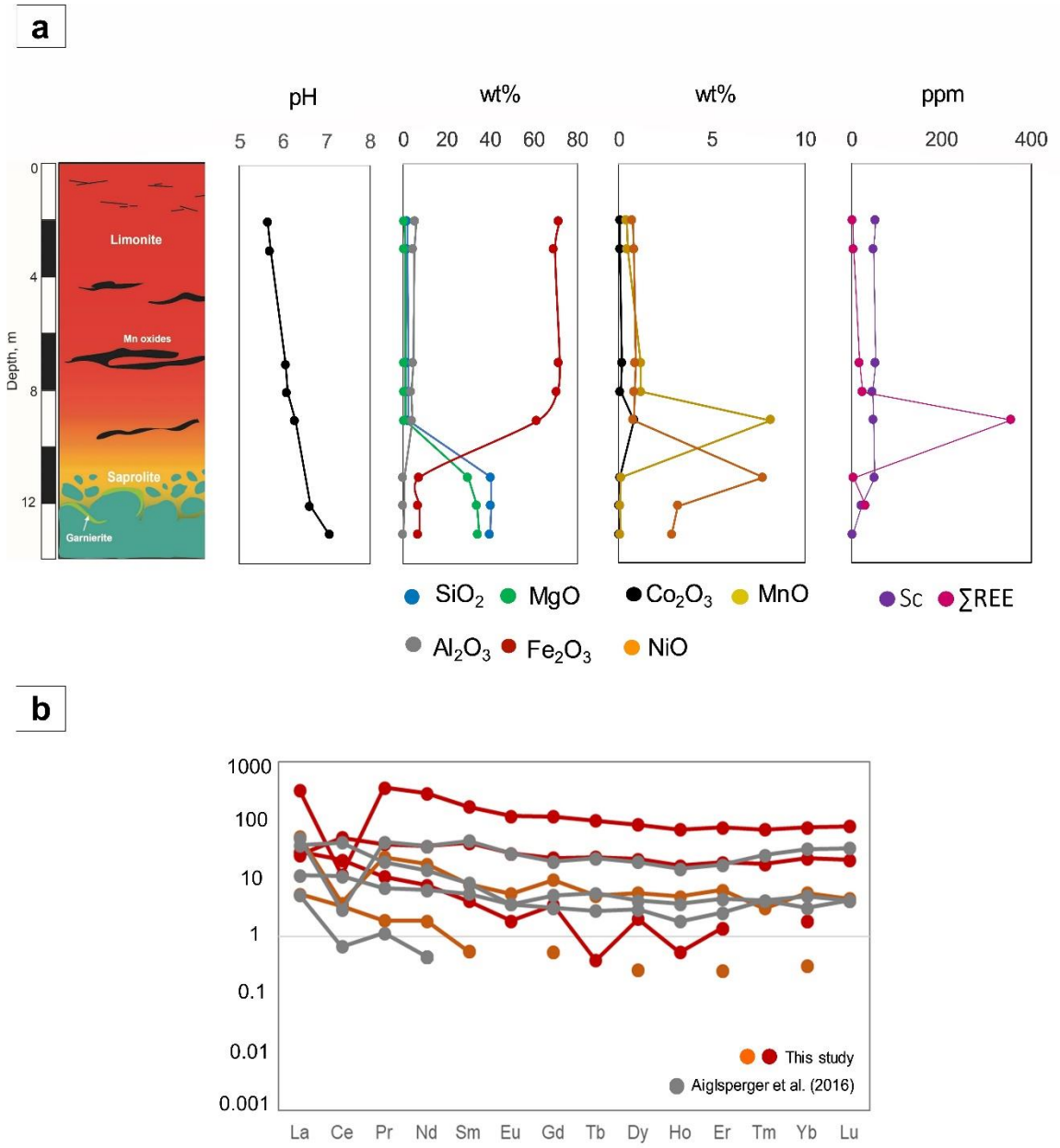

Fig. 50 a) Variation in concentration of major, minor, and trace elements with depth. b) Chondrite normalized REE patterns of the saprolite (orange) and limonite (red) samples from profile B. Normalization (chondrite) values from Anders and Grevesse (1989).

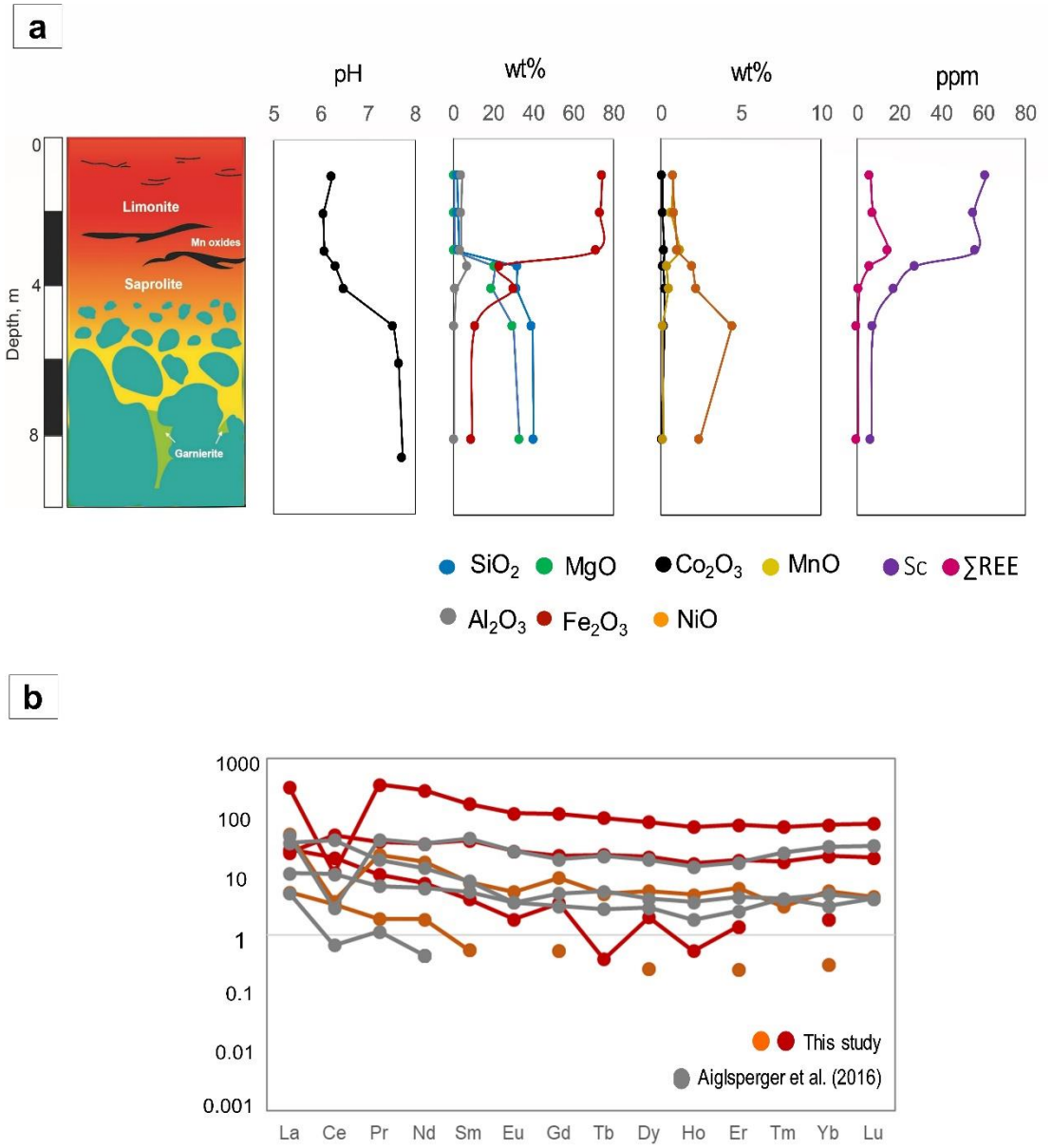

Fig. 51 a) Variation in concentration of major, minor, and trace elements with depth. b) Chondrite normalized REE patterns of the saprolite (orange) and limonite (red) samples from profile C. Normalization (chondrite) values from Anders and Grevesse (1989).

Table 21 Sc and REE contents in bedrock, saprolite and limonite samples from Profile A, Berong deposit, Palawan, Philippines.

Depth, m	2	3	4	5	6	9	10	12	13	14	15	16	18
Horizon	LIM	LIM	LIM	LIM	LIM	LIM	LIM	LIM	LIM	LIM	LIM	SAP	BED
Sc	40.31	27.26	24.00	17.31	54.63	20.84	41.30	51.39	52.68	49.07	48.26	8.95	6.48
La	0.69	0.36	0.44	0.16	0.03	1.26	0.53	0.35	2.01	1.24	26.32	bdl	bdl
Ce	1.31	3.16	1.40	0.67	0.78	2.34	1.57	7.19	6.20	11.70	0.37	bdl	bdl
Pr	0.07	0.01	0.06	bdl	bdl	0.19	0.17	0.12	0.43	0.77	7.72	bdl	bdl
Nd	0.54	0.31	0.37	0.12	0.15	0.84	0.54	0.75	1.73	3.76	28.20	bdl	bdl
Sm	0.05	bdl	0.03	bdl	0.01	0.07	0.18	0.18	0.46	1.36	2.84	bdl	bdl
Eu	bdl	bdl	bdl	bdl	bdl	bdl	0.09	0.01	0.18	0.42	0.96	bdl	bdl
Gd	0.05	0.04	0.04	bdl	bdl	0.07	0.17	0.21	0.56	1.01	5.46	bdl	bdl
Tb	bdl	bdl	bdl	bdl	bdl	bdl	0.07	bdl	0.08	0.13	0.52	bdl	bdl
Dy	0.06	0.01	0.07	bdl	0.01	0.09	0.17	0.16	0.53	1.08	3.43	bdl	bdl
Ho	bdl	bdl	bdl	bdl	bdl	bdl	0.08	bdl	0.10	0.14	0.82	bdl	bdl
Er	0.03	bdl	0.03	bdl	0.02	0.06	0.16	0.07	0.35	0.60	2.68	bdl	bdl
Tm	bdl	bdl	bdl	bdl	bdl	bdl	0.07	bdl	0.05	0.05	0.26	bdl	bdl
Yb	0.03	0.01	0.05	bdl	0.06	0.08	0.16	0.07	0.42	0.83	2.04	bdl	bdl
Lu	bdl	bdl	bdl	bdl	bdl	bdl	0.09	bdl	0.07	0.07	0.39	bdl	bdl
∑REE	2.83	3.89	2.50	0.94	1.06	4.99	4.04	9.12	13.13	23.14	82.02	nd	nd
LREE	2.72	3.88	2.34	0.94	0.98	4.76	3.25	8.83	11.55	20.24	71.87	nd	nd
HREE	0.11	0.01	0.15	nd	0.08	0.22	0.80	0.29	1.58	2.90	10.15	nd	nd
LREE/HREE	24.89	274.65	15.33	nd	11.86	21.36	4.07	30.08	7.32	6.99	7.08	nd	nd

bdl – below the detection limit

Table 22 Sc and REE contents in bedrock, saprolite and limonite samples from Profile B, Berong deposit, Palawan, Philippines.

Depth, m	1	2	3	7	8	9	10	12	13
Horizon	LIM	LIM	LIM	LIM	LIM	LIM	LIM	SAP	SAP
Sc	40.6	54.7	49.8	55.0	46.7	50.3	55.9	23.8	3.4
La	1.25	0.78	1.77	0.88	6.67	77.64	5.85	12.23	bdl
Ce	2.01	2.23	1.91	15.02	12.32	6.79	29.88	2.24	bdl
Pr	0.17	0.10	0.23	0.25	0.94	32.20	3.44	2.06	bdl
Nd	0.83	0.57	0.93	1.31	3.41	130.6	16.04	7.95	bdl
Sm	0.08	0.04	0.07	0.34	0.60	24.83	5.99	1.15	bdl
Eu	bdl	bdl	bdl	0.05	0.10	6.52	1.49	0.30	bdl
Gd	0.11	0.08	0.12	0.39	0.68	22.73	4.41	1.85	bdl
Tb	bdl	bdl	bdl	bdl	0.01	3.55	0.83	0.18	bdl
Dy	0.06	0.05	0.08	0.31	0.48	20.24	5.12	1.35	bdl
Ho	bdl	bdl	bdl	bdl	0.03	3.86	0.91	0.27	bdl
Er	0.04	0.03	0.04	0.19	0.22	11.82	2.96	0.98	bdl
Tm	bdl	bdl	bdl	bdl	bdl	1.67	0.43	0.07	bdl
Yb	0.05	0.04	0.05	0.20	0.30	12.22	3.57	0.91	bdl
Lu	bdl	bdl	bdl	bdl	bdl	1.91	0.50	0.11	bdl
∑REE	4.60	3.92	5.20	18.93	25.76	356.6	81.4	31.64	nd
LREE	4.45	3.80	5.03	18.24	24.72	301.3	67.1	27.78	nd
HREE	0.15	0.12	0.17	0.70	1.04	55.26	14.32	3.87	nd
LREE/HREE	28.96	31.99	30.20	26.13	23.68	5.45	4.69	7.18	nd

bdl – below detection limit

Table 23 Sc and REE contents in bedrock, saprolite and limonite samples from Profile C, Berong deposit, Palawan, Philippines.

Depth, m	1	2	3	3.4	4	5	6	8
Horizon	LIM	LIM	LIM	LIM-SAP	SAP	SAP	SAP	SAP
Sc	61	55	57	28	18	8	6	7
La	0.41	0.53	1.97	2.14	0.68	0.07	0.13	bdl
Ce	4.34	5.34	5.24	1.74	0.29	bdl	bdl	bdl
Pr	0.11	0.16	0.70	0.18	bdl	bdl	bdl	bdl
Nd	0.71	0.90	3.21	0.99	0.03	bdl	0.06	bdl
Sm	0.14	0.22	1.11	0.17	bdl	bdl	bdl	bdl
Eu	bdl	0.01	0.21	0.01	bdl	bdl	bdl	bdl
Gd	0.17	0.20	0.67	0.21	bdl	bdl	bdl	bdl
Tb	bdl	bdl	0.05	bdl	bdl	bdl	bdl	bdl
Dy	0.12	0.12	0.71	0.20	bdl	bdl	bdl	bdl
Ho	bdl	bdl	0.04	bdl	bdl	bdl	bdl	bdl
Er	0.05	0.04	0.34	0.14	bdl	bdl	bdl	bdl
Tm	bdl	bdl	bdl	bdl	bdl	bdl	bdl	bdl
Yb	0.07	0.07	0.36	0.15	bdl	bdl	bdl	bdl
Lu	bdl	bdl	bdl	bdl	bdl	bdl	bdl	bdl
∑REE	6.12	7.61	14.60	5.93	1.00	0.07	0.19	bdl
LREE	5.89	7.38	13.11	5.44	1.00	0.07	0.19	bdl
HREE	0.24	0.23	1.49	0.49	bdl	0.00	0.00	bdl
LREE/HREE	25	32	9	11	nd	nd	nd	nd

bdl – below the detection limit

Akita University

5.5.1.2 Intex Ni laterite deposit, Mindoro, Philippines

The trends of major, minor, and trace elements in the saprolite and limonite samples of the Intex deposit are shown in Figures 52, 53, and 54. The summary of the Sc and REE contents in this deposit is listed on Tables 24, 25, and 26. In all the studied cores, the concentrations of Mg and Si are decreasing from the bedrock towards the surface. While Fe, Al, and Cr have opposite trends. The maximum Ni concentration is observed in the saprolite horizon, while Co and Mn are enriched in the limonite horizon.

5.5.1.2.1 BB2515 core

The Sc contents of the lherzolite bedrock (6 ppm) and saprolite samples are low (7 ppm) but increase significantly in the limonite horizon, particularly at 1 m depth (up to 67 ppm). The total REE concentrations are below the detection limit of the ICP-MS machine. However, a considerable gain of REE are contained in the limonite horizon (up to 38 ppm) (Fig. 52a).

A moderately strong positive Ce anomaly is apparent between the transition boundary and the limonite sample at 1 m depth, whereas the limonite sample at 2 m depth is characterized by a negative Ce anomaly (Fig. 52b). All the saprolite and bedrock samples have deficient REE concentrations which were not detected by the machine.

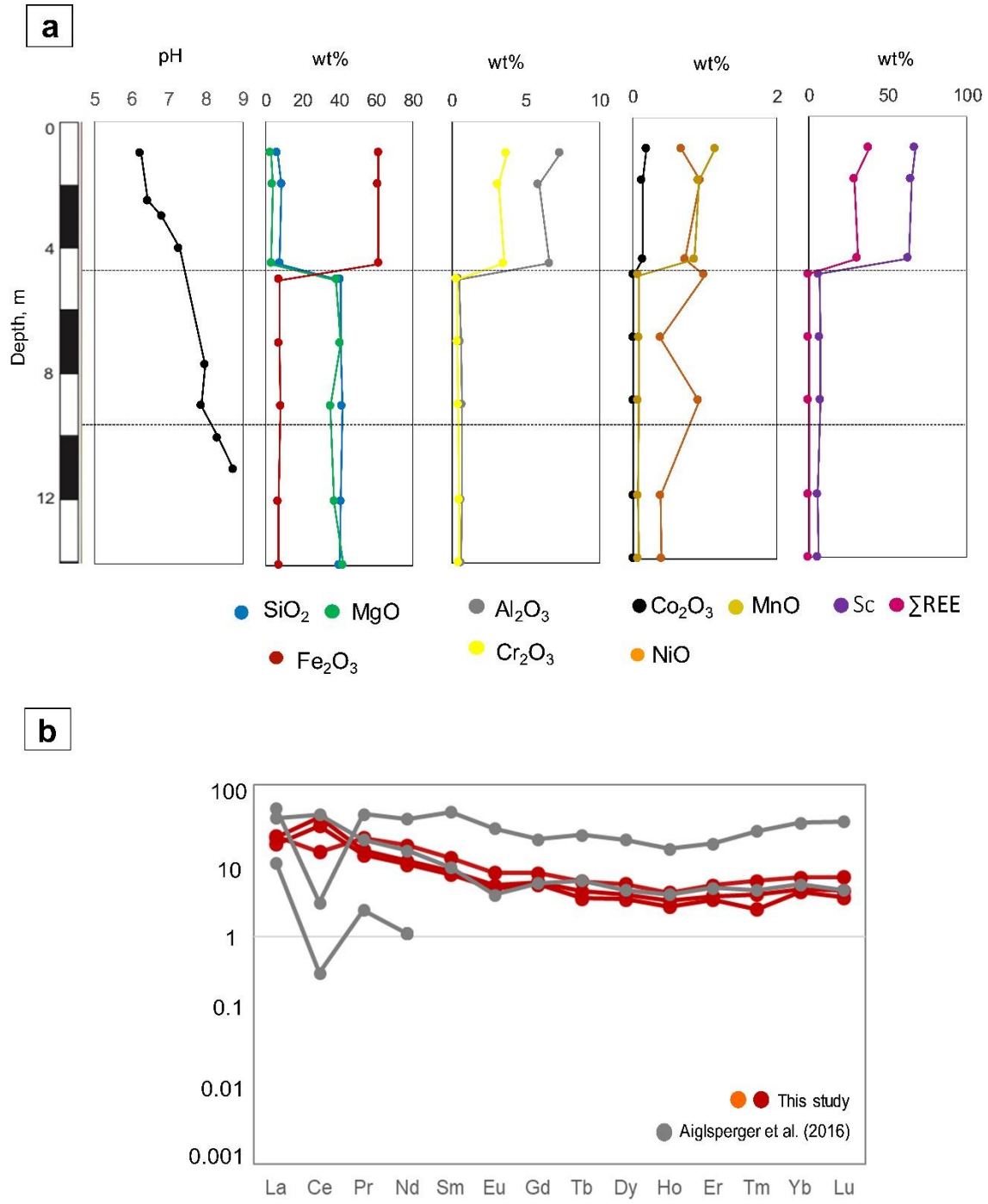

Fig. 52 a) Variation in concentration of major, minor, and trace elements with depth. b) Chondrite normalized REE patterns of the limonite (red) samples from BB2515 core. Normalization (chondrite) values from Anders and Grevesse (1989).

Akita University

5.5.1.2.2 PG1500 core

Similarly, the PG1500 core shows an upward increase of Sc from the saprolite horizon (8- 15 ppm) to the limonite horizon (34- 49 ppm). The maximum amount of Sc (49 ppm) is observed at 3 m depth. The total REE contents, on the other hand, are low in the saprolite (0.02- 3 ppm) but show 50 times enrichment in the limonite horizon (up to 55 ppm) (Fig. 53a).

Most of the samples from the saprolite horizon and the lower limonite display pronounced negative Ce anomalies. Only the limonite sample at 1 m depth shows a positive Ce anomaly. Although, the REE contents of the saprolite samples are low as reflected by the disconnected points (Fig. 53b).

5.5.1.2.3 BB2406 core

The harzburgite-dunite bedrock and saprolite samples exhibit low Sc contents (up to 2 ppm and 10 ppm) and further increases as it reaches near the surface (59 ppm). The REE contents of the bedrock and saprolite samples are very low and were not detected by the machine. The limonite samples from BB2406 core are relatively enriched in total REE (up to 55 ppm) compared to the bedrock (Fig. 54a).

The chondrite-normalized patterns of the bedrock and saprolite samples are no longer discernable because of the very low REE contents. However, the sample from the transition boundary between the saprolite and limonite horizon illustrates a strong negative Ce anomaly. The upper limonite sample, particularly at 1 m depth, illustrates a slight positive Ce anomaly,

and generally, the patterns of the limonite samples are moderately enriched in LREE compared to HREE (Fig. 54b).

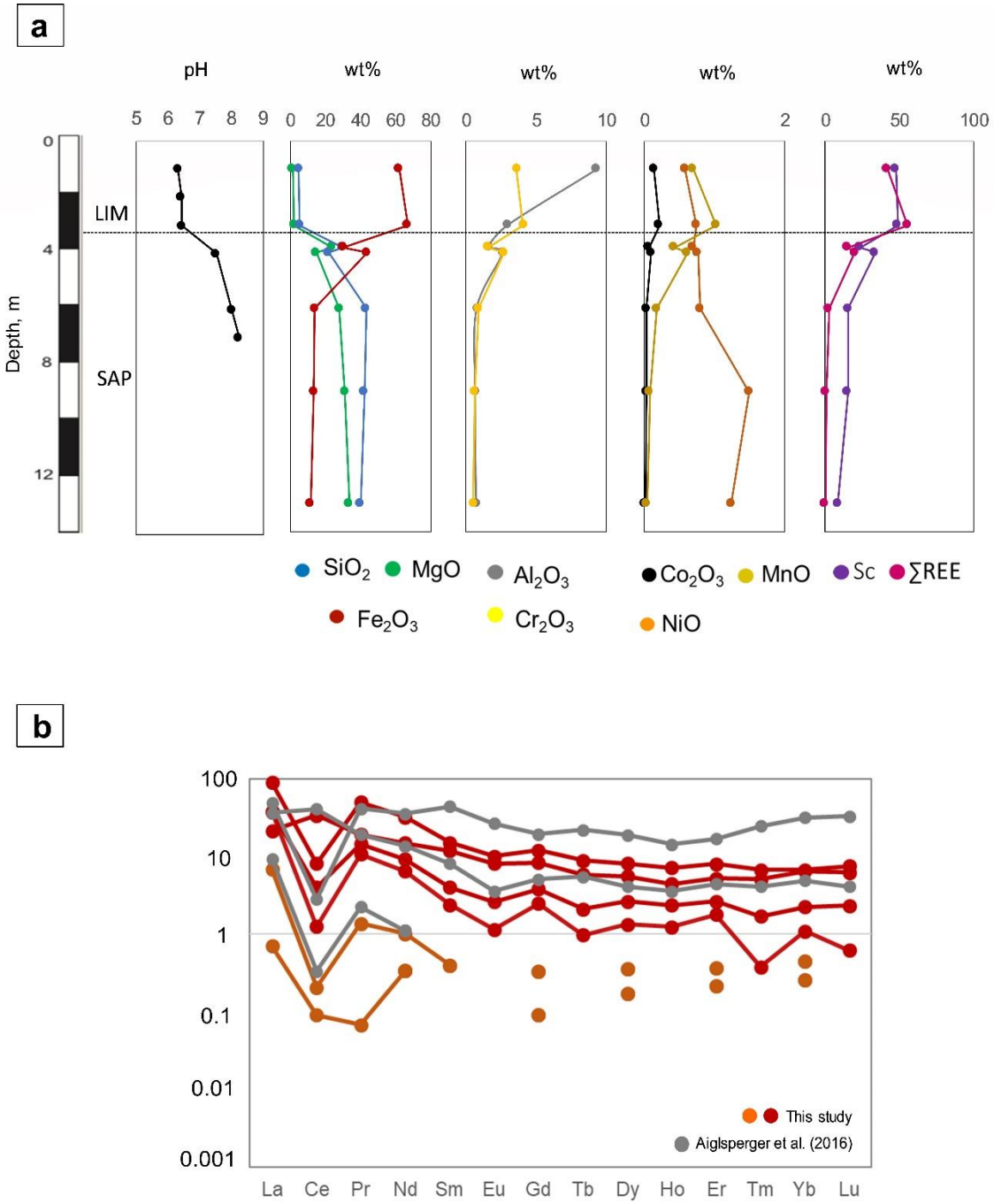

Fig. 53 a) Variation in concentration of major, minor, and trace elements with depth. b) Chondrite normalized REE patterns of the saprolite (orange) and limonite (red) samples from PG1500 core. Normalization (chondrite) values from Anders and Grevesse (1989).

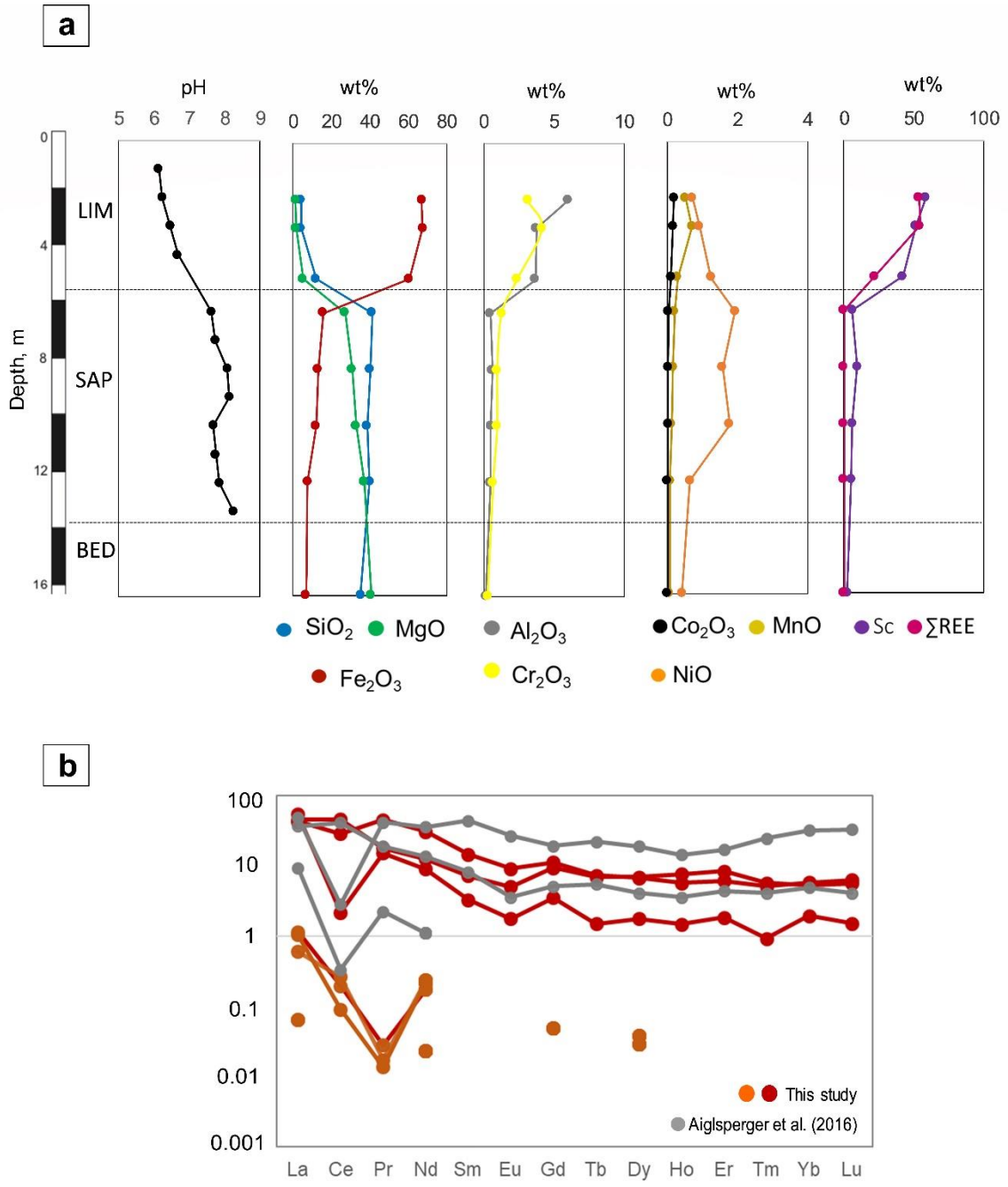

Fig. 54 a) Variation in concentration of major, minor, and trace elements with depth. b) Chondrite normalized REE patterns of the saprolite (orange) and limonite (red) samples from BB2406 core. Normalization (chondrite) values from Anders and Grevesse (1989).

Table 24 Sc and REE contents in bedrock, saprolite and limonite samples from BB2515 core, Berong deposit, Palawan, Philippines.

Depth, m	1	2	4.5	5	7	9	12	14
Horizon	LIM	LIM	LIM-SAP	HSAP	BED	HSAP	BED	BED
Sc	67.20	64.78	62.99	6.62	7.27	7.36	5.58	5.99
La	4.79	4.98	3.92	bdl	bdl	bdl	bdl	bdl
Ce	22.52	7.96	17.47	bdl	bdl	0.01	bdl	bdl
Pr	1.23	1.80	1.07	bdl	bdl	bdl	bdl	bdl
Nd	4.53	7.22	4.08	bdl	bdl	0.002	bdl	bdl
Sm	1.06	1.60	0.97	bdl	bdl	bdl	bdl	bdl
Eu	0.27	0.39	0.24	bdl	bdl	bdl	bdl	bdl
Gd	1.03	1.36	0.96	bdl	bdl	bdl	bdl	bdl
Tb	0.14	0.20	0.12	bdl	bdl	bdl	bdl	bdl
Dy	0.88	1.21	0.76	bdl	bdl	bdl	bdl	bdl
Ho	0.17	0.21	0.14	bdl	bdl	bdl	bdl	bdl
Er	0.55	0.75	0.49	bdl	bdl	bdl	bdl	bdl
Tm	0.09	0.13	0.06	bdl	bdl	bdl	bdl	bdl
Yb	0.69	0.99	0.63	bdl	bdl	bdl	bdl	bdl
Lu	0.10	0.15	0.08	bdl	bdl	bdl	bdl	bdl
∑REE	38	29	31	nd	nd	nd	nd	nd
LREE	35	25	29	nd	nd	nd	nd	nd
HREE	3	4	2	nd	nd	nd	nd	nd
LREE/HREE	14	7	13	nd	nd	nd	nd	nd

bdl – below detection limit

Table 25 Sc and REE contents in bedrock, saprolite, and limonite samples from PG1500 core, Berong deposit, Palawan, Philippines.

Depth, m	1	3	3.8	4	6	9	13
Horizon	LIM	LIM	LIM	LIM-SAP	HSAP	HSAP	HSAP
Sc	47.55	48.89	23.31	33.73	15.40	15.22	8.48
La	5.06	20.99	8.83	8.95	1.59	0.16	0.001
Ce	20.43	4.91	0.75	2.43	0.12	0.05	bdl
Pr	1.72	4.46	0.95	1.30	0.12	0.01	bdl
Nd	6.78	14.50	2.93	4.15	0.46	0.15	0.01
Sm	1.75	2.23	0.35	0.59	0.06	bdl	bdl
Eu	0.46	0.56	0.06	0.15	bdl	bdl	bdl
Gd	1.64	2.37	0.49	0.75	0.07	0.02	bdl
Tb	0.21	0.32	0.04	0.08	bdl	bdl	bdl
Dy	1.35	1.97	0.32	0.64	0.09	0.04	0.004
Ho	0.25	0.40	0.07	0.13	bdl	bdl	bdl
Er	0.83	1.27	0.28	0.42	0.06	0.03	bdl
Tm	0.12	0.16	0.01	0.04	bdl	bdl	bdl
Yb	1.05	1.09	0.18	0.36	0.07	0.04	bdl
Lu	0.15	0.18	0.02	0.06	bdl	bdl	bdl
∑REE	41.8	55.4	15.3	20.0	2.64	0.51	0.02
LREE	37.8	50.0	14.4	18.3	2.42	0.40	0.01
HREE	4.0	5.4	0.9	1.7	0.22	0.12	0.00
LREE/HREE	9.5	9.3	15.7	10.6	11.10	3.37	3.26

bdl – below the detection limit

Table 26 Sc and REE contents in bedrock, saprolite, and limonite samples from BB2406 core, Berong deposit, Palawan, Philippines.

Depth, m	2	3	4.8	6	8	10	12	16
Horizon	LIM	LIM	LIM-SAP	SAP	SAP	SAP	SAP	BED
Sc	58.90	51.68	42.05	5.87	9.51	5.84	5.30	2.48
La	10.58	10.04	12.83	0.27	0.24	0.14	0.02	bdl
Ce	27.72	17.24	1.30	0.12	0.05	0.16	bdl	bdl
Pr	1.60	4.06	1.37	0.00	0.001	0.002	bdl	bdl
Nd	5.68	13.90	4.10	0.08	0.10	0.11	0.01	bdl
Sm	1.07	2.15	0.49	bdl	bdl	bdl	bdl	bdl
Eu	0.28	0.51	0.10	bdl	bdl	bdl	bdl	bdl
Gd	1.85	2.22	0.69	0.01	bdl	bdl	bdl	bdl
Tb	0.25	0.27	0.05	bdl	bdl	bdl	bdl	bdl
Dy	1.68	1.64	0.43	bdl	0.01	0.01	bdl	bdl
Ho	0.42	0.32	0.08	bdl	bdl	bdl	bdl	bdl
Er	1.34	0.97	0.29	bdl	bdl	bdl	bdl	bdl
Tm	0.14	0.12	0.02	bdl	bdl	bdl	bdl	bdl
Yb	0.87	0.94	0.32	bdl	bdl	bdl	bdl	bdl
Lu	0.14	0.15	0.04	bdl	bdl	bdl	bdl	bdl
∑REE	53.6	54.5	22.1	0.48	0.41	0.41	0.03	0.00
LREE	48.8	50.1	20.9	0.48	0.40	0.41	0.03	0.00
HREE	4.8	4.4	1.2	0.00	0.01	0.01	0.00	0.00
LREE/HREE	10.1	11.3	16.9	nd	43	58	nd	nd

bdl – below the detection limit

Akita University

5.5.2 Mass gains and losses of elements

As a result of the intense weathering of the ultramafic bedrock in the Berong, Palawan, and Intex, Mindoro, Philippines, the rock-forming elements are re-distributed in the laterite profiles. The behavior of these elements is controlled by various processes such as oxidation, hydrolysis and dissolution (Golightly, 1981; Gleeson et al., 2004). Mass balance calculation was utilized to examine the loss and gain of elements during weathering (Schellmann, 1989; Braun et al., 1998). These calculations were only applied to those studied profiles with fresh parent rock and concentrations above the detection limit of the ICP-MS machine, including profile A from Berong laterite deposit in Palawan, and two drill cores (BB2515 and BB2406) from Intex laterite deposit in Mindoro, Philippines. The mass transport coefficient (tau, T) by Brimhall and Dietrich (1987) and Anderson et al. (2012) is calculated using the equation below. In this model, C refers to the concentration of elements (j) in the parent rock (p), while w pertains to the altered rock with respect to that of an immobile element (i). Then the T values are plotted vs. depth (Fig. 54, 55, 56).

$$T_{i,j} = \{ [(C_{j,w}) / (C_{j,p})] / [(C_{i,w}) / (C_{i,p})] \} -1$$

If the result has a negative value, it signifies that the element (j) is loss during weathering, while a positive value indicates that there is a gain of an element. A zero value suggests that the element is not mobilized relative to the parent rock. The most common immobile elements being considered in

Akita University

this type of environment include Cr, Ti, Hf, Zr (Schellmann, 1989; Fu et al., 2014), Nb and Sc (Rivera et al., 2018). In this study, Ti is used as the immobile element. On the other hand, Hf, Zr, Nb and Sc were not considered because their concentrations are very low in the bedrock.

5.5.2.1 Profile A – Berong laterite deposit, Palawan, Philippines

It is important to note here that profile A has a thicker limonite (~15 meters) and a thin saprolite (~0.5 meters). The T values for Mg and Si are consistently negative from the saprolite horizon up to the limonite horizon.

In contrast, there is an apparent gain of Al in the profile. The T values for Fe and Cr generally show negative values in the upper section of the limonite horizon, but additional gains in the lower limonite, particularly at 13 m depth. Similarly, Co, Mn, Sc, and V are enriched at this depth with progressive loss towards the surface. Nickel is significantly enriched in the saprolite horizon (Fig. 55).

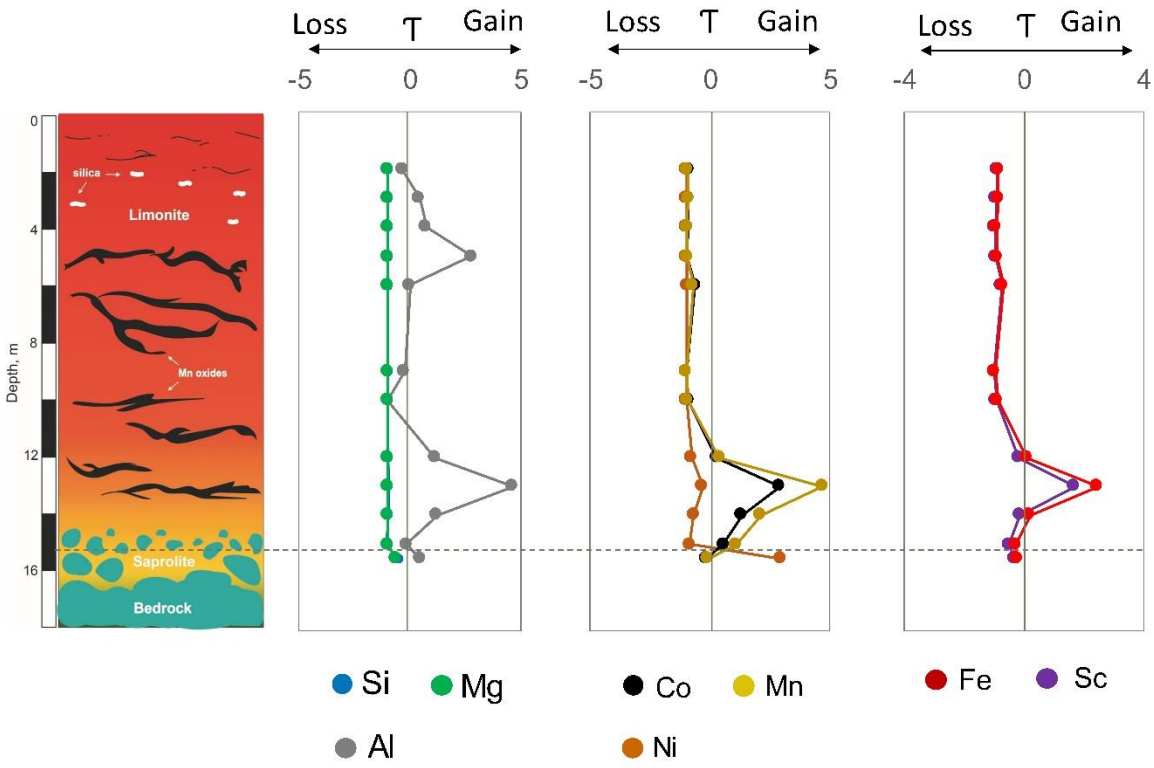

Fig. 55 Mass balance profiles of the major, minor, and trace elements for the Berong weathering profile A.

5.5.2.2 BB2515 core – Intex laterite deposit, Mindoro, Philippines

The interesting feature of this profile is that all the elements, including Si, Mg, Fe, Al, Cr, Ni, Co, Mn, Sc, and V show gains in the transition boundary between the saprolite and limonite horizon, particularly at 5m depth. At this depth, a significant enrichment of Ni is evident. The limonite horizon is characterized by negative T values indicating the progressive loss of these elements (Fig. 56).

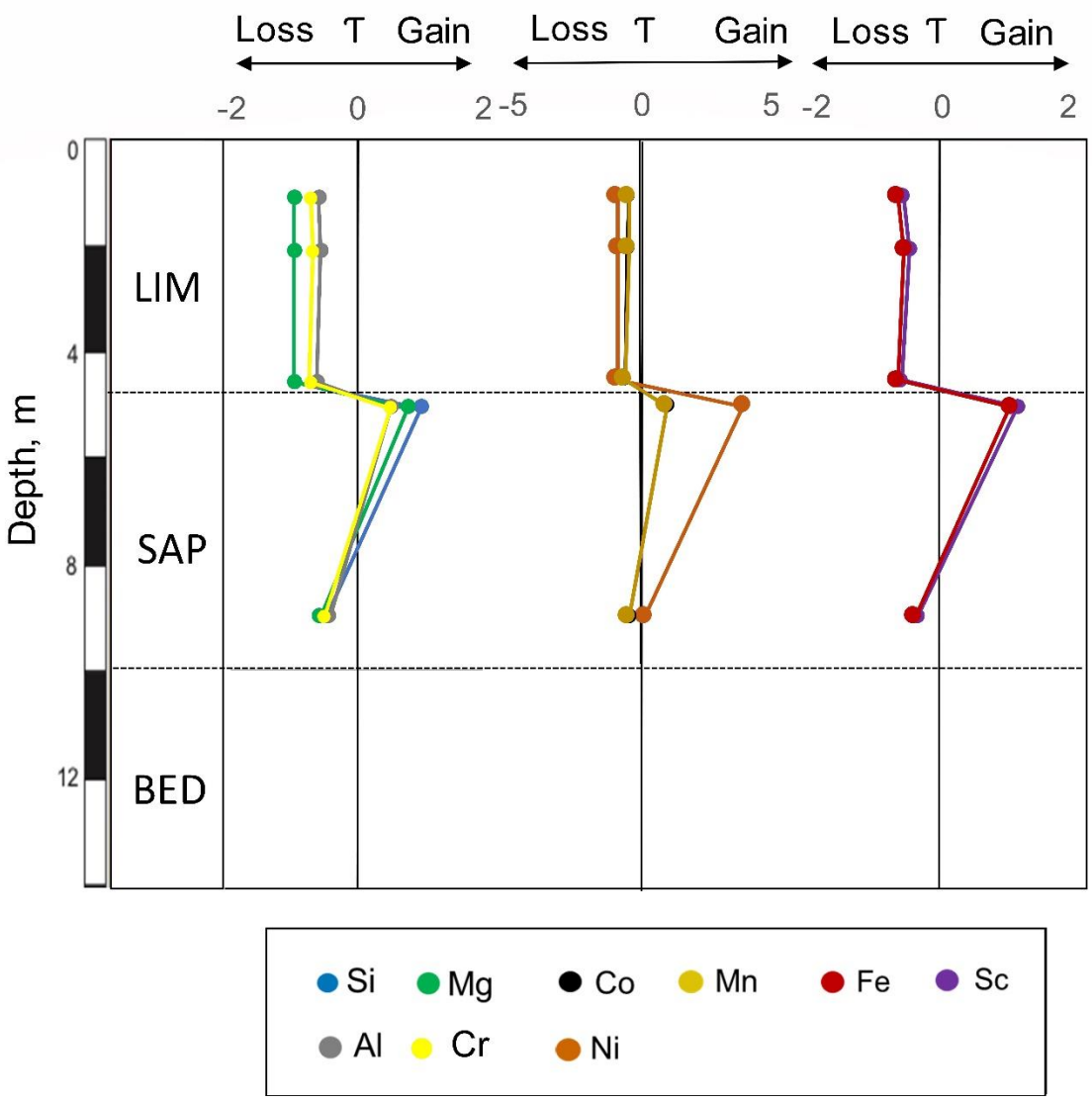

Fig. 56 Mass balance profiles of the major, minor, and trace elements for the Intex weathering BB2515 core.

5.5.2.3 BB2406 core – Intex laterite deposit, Mindoro, Philippines

Most of the elements, except Ni, have negative T values towards the limonite horizon. There is a minimal gain of Ni in the saprolite horizon indicating that low amount of Ni is remobilized or redistributed from the limonite to the saprolite horizon. This could be attributed to the less

advanced stage of weathering of the limonite, which results in the formation of a thick saprolite (~8 meters) and a thin limonite (~3.5 meters) horizon (Fig. 57).

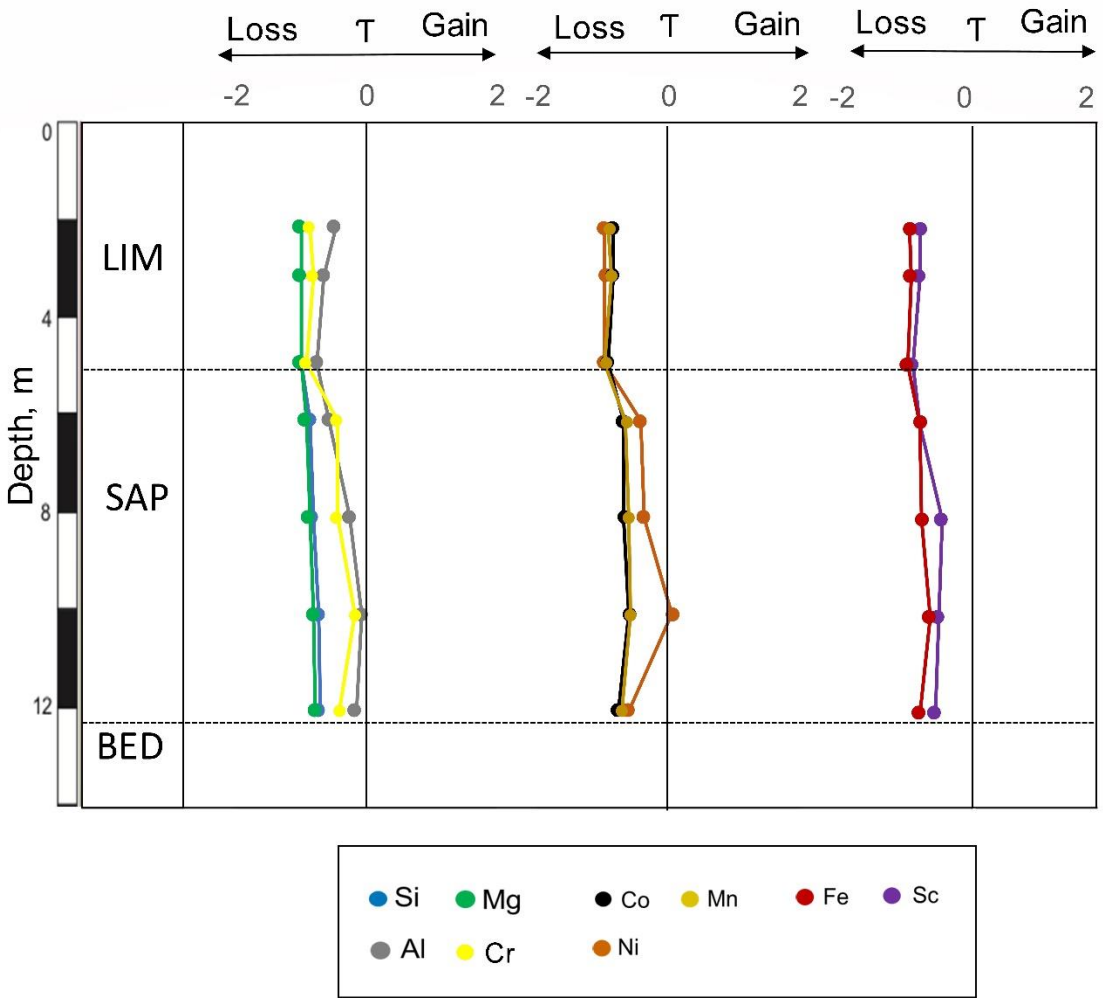

Fig. 57 Mass balance profiles of the major, minor, and trace elements for the Intex weathering BB2406 core.

Akita University

5.6 Discussion

5.6.1 Enrichment of Sc in laterites

The estimated worldwide consumption and supply of Sc ranges from 10 to 15 tons per year. Even though the market for this is minor contrary to other metals, there is an expected rise in demand primarily to produce clean energy technologies (USGS, 2019). Scandium-rich minerals are scarce, but Sc is typically found in various minerals including fluoride, hydroxides, phosphate, silicate, and sulfates (Rudnick and Gao, 2013). Furthermore, Sc is often recovered as a by-product from mine tailings and waste liquors in the manufacturing of other metals (Wang et al., 2011). Numerous Sc projects are being established; for example, the Scandium-Cobalt- Nickel (SCONI) project in Queensland is expected to produce approximately 12 million tons comprising 3,000 tons of scandium oxide with a cut-off grade of 162 ppm. The commercial plant of Taganito in the Philippines is expected to produce 7.5 tons per year of scandium oxide through high-pressure acid leach (HPAL) process (USGS, 2019). Another significant source of scandium oxide is the residual nickel ores in Australia with an average grade between 76 and 370 ppm, and these could be produced in massive amounts (Wang et al., 2011).

In this study, the fresh harzburgite bedrock of profile A from Berong, Palawan, Philippines, is marked by Sc content of 6 ppm. The saprolite samples yield Sc concentration that reaches up to 24 ppm. Moreover, the limonite samples show concentrations between 17 ppm and 61 ppm Sc.

Akita University

There is an apparent gain of Sc in the studied limonite samples, which dominantly consist of goethite (14 to 86 wt%). Similarly, the lherzolite bedrock of BB2515 core reveals 6 ppm of Sc and 2 ppm for the harzburgite-dunite bedrock of BB2406 core. However, a higher amount of Sc can be observed in the limonite samples derived from lherzolite bedrock (up to 67 ppm) compared to the laterites developed above harzburgite- dunite bedrock (up to 59 ppm). The enrichment of Sc in the weathered horizons is controlled mainly by its initial amount in the parent rock. The results from this study are consistent with the previous work by Teitler et al. (2019), they reported that the highest concentration of Sc is contained in lherzolite and harzburgite, followed by dunite, which correlates to the increasing proportion of enstatite and diopside over olivine. Previous studies have shown a significant amount of Sc up to 100 ppm in Fe-oxyhydroxides-rich horizons derived from ultramafic-mafic rocks (Aiglsperger et al., 2016; Chasse et al., 2017; Teitler et al., 2019; Ulrich, 2019). Chasse et al. (2017) presented that Sc in laterite samples from Eastern Australia are mainly adsorbed on goethite (ca. 80%) and the rest is incorporated in the structure of hematite using the combination of X-ray absorption near-edge spectroscopy (XANES), XRD, microscopic and chemical analyses. They also reported that crystal chemistry plays a vital role in Sc enrichment in lateritic deposits derived from ultramafic-mafic rocks. In this study, a positive correlation is apparent between Fe versus Sc in the laterites of the Berong and Intex deposits suggesting that Sc is associated with Fe-oxyhydroxides

Akita University

(Fig. 58a, 58d). Furthermore, the linear relationship between Mn and Sc indicates that Sc could also be hosted by Mn-oxyhydroxides minerals (Fig. 58b, 58e).

5.6.2 Behaviour of REE during lateritization

The abundance of REE in the Earth's crust ranges from 130 ppm to 240 ppm (Zepf, 2013). The resources of REE are mainly associated with alkaline igneous systems, ion-adsorption clay deposits, carbonatite or granite, monazite-xenotime -bearing placer deposits (USGS, 2019). REEs are redistributed and mobile during weathering processes (Nesbitt, 1979; Braun et al., 1993; 1998; Sanematsu et al., 2011).

Despite the deficient REE concentrations of the ultramafic bedrock samples from Berong, Palawan, and Intex, Mindoro, Philippines, a moderate enrichment is evident at the transition boundary between the saprolite and limonite horizons and at the lower section of the limonite horizon. This observation is more likely associated with the abundance of goethite in these sections. Although the correlation plots do not clearly show their linear association, the distribution trends with depth suggest that REE are associated with Fe-oxyhydroxides (Fig. 58c, 58f). Nesbitt (1979) and Mongelli (1993) investigated the enrichment and the occurrence of LREE in phyllosilicates and in general, REE could substitute or adsorb with Fe-oxyhydroxides (Aide and Aide, 2012). LREE are re-mobilized from the upper section of the limonite but are retained towards the lower part or to

Akita University

the transition boundary. Another important observation is the negative and positive Ce anomalies found in the laterites. Cerium is commonly utilized to track redox fractionation in lateritic environments (Braun et al., 1998). Negative Ce anomalies are common in the lower section of the limonite horizon while positive Ce anomalies typically found in the upper part of the limonite which is attributed to the formation of cerianite in oxidizing solutions (Braun et al., 1998; Aide and Aide, 2012). However, the present work does not have solid evidence of the occurrence of cerianite. According to Braun et al. (1998), the precipitation of cerianite is highly dependent on the change of Eh-pH conditions in the profiles. The pronounced positive Ce anomalies have pH values ranging from 6.24 to 6.52. In alluvial Albaqualfs, Missouri, the transition from acidic soil environment (pH 5) to alkaline conditions play a significant role in the enrichment of Ce (Aide and Aide, 2012). Fendorf and Fendorf (1996) reported that the behavior of REE depends on the mineralogy in soils, for example, the sorption of La on the surface of Fe-oxyhydroxides (goethite), Mn-oxides (birnessite) and Ti (rutile) occur from pH 3 to pH 8. The mineralogy and pH conditions of the solutions are important factors to determine the geochemical behavior of REE in laterites.

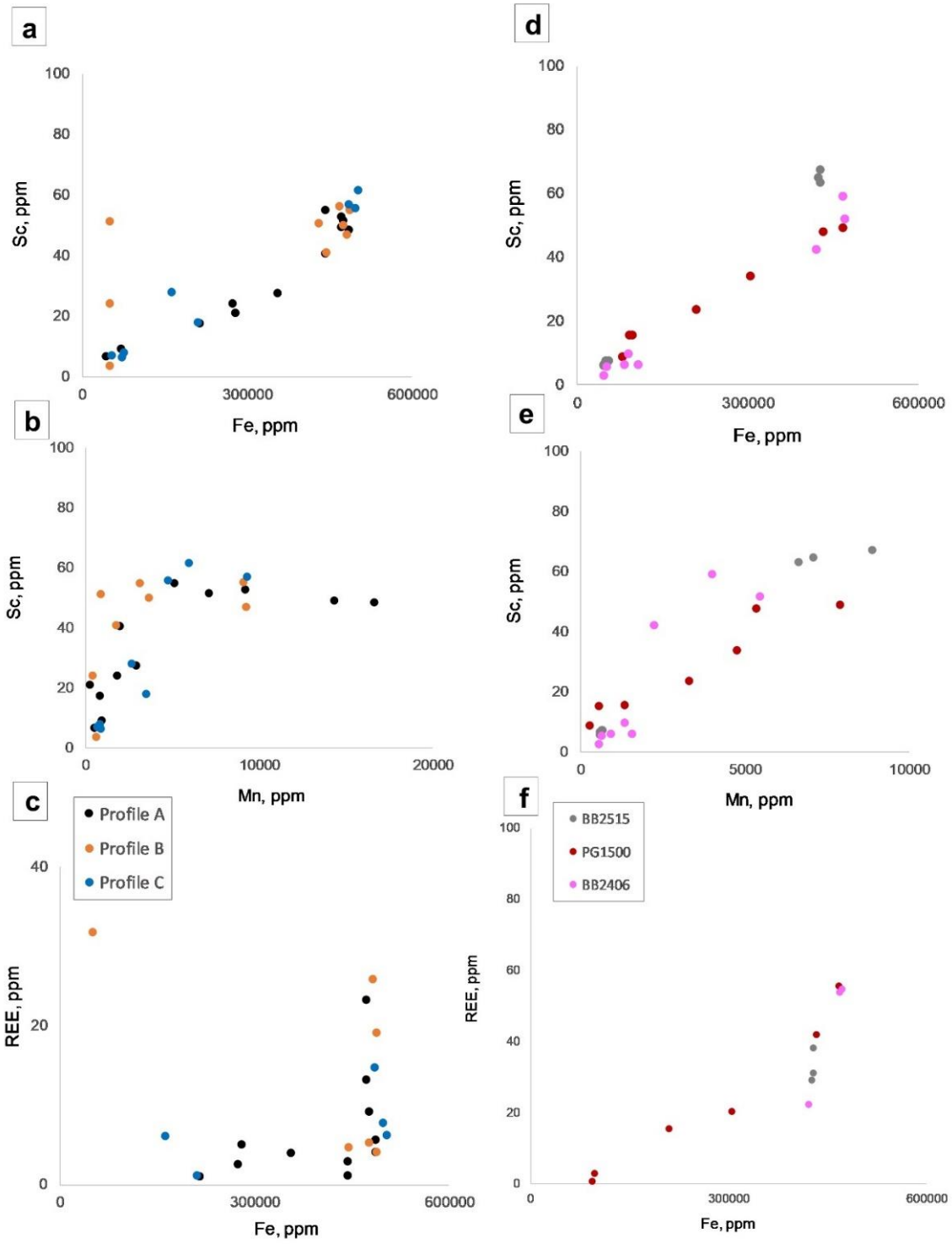

Fig. 28 Correlational plots of Sc versus a-d) Fe and b-e) Mn and REE versus c) Fe and f) Mn.

Akita University

5.7 Conclusions

Six laterite profiles from Berong deposit and Intex deposit in the Philippines were examined to understand the geochemical behavior of Sc and REE. The long and pervasive chemical weathering of ultramafic bedrock resulted in the removal of Mg and Si, while the other elements, including Fe, Al, Ni, Co, Mn, and to some extent, Sc and REE are retained in the specific horizon of the laterite profiles. In all the studied profiles, there is a pronounced enrichment of Sc and REE in the limonite horizon with concentrations of up to 67 ppm and 357 ppm. The highest bulk amount of Sc is found in the limonite developed above lherzolite, followed by harzburgite and dunite, indicating that the mineralogy of the parent rock can affect the enrichment of Sc in the weathered horizon. The behavior of Sc and, to some extent, REE are closely associated with the occurrence of Fe- and Mn-oxyhydroxides in the limonite horizon. This observation is illustrated by the positive correlational plots between Sc and REE with Fe and Mn and mobility diagrams used in this study.

REE displays specific enrichment either at the transition boundary between the saprolite and limonite horizons or at the lower section of the limonite. Its trend is generally similar to Fe, indicating the association with Fe-oxyhydroxides. However, their relationship is not apparent in the correlational plots, which may imply that REE are hosted or associated with other minerals. The results from chondrite normalized REE patterns reveal the positive and negative Ce anomalies developed during weathering

Akita University

processes. The positive Ce anomalies in the upper limonite and negative Ce anomalies in the lower limonite and saprolite horizon may demonstrate the redox boundary where REE could accumulate.

5.8 References

Aide, M.T., Smith, C.C., 2001. Soil genesis on peralkaline felsics in Big Bend National Park, Texas. Soil Sci. 166, 209-221.

Aiglsperger, T., Proenza, J. A., Lewis, J. F., Labrador, M., Svojtka, M., Rojas-Puron, A., Ďurišová, J., 2016. Critical metals (REE, Sc, PGE) in Ni laterites from Cuba and the Dominican Republic. Ore Geol Rev. 73, 127-147.

Anders, E., Grevesse, N., 1989. Abundances of the elements: Meteoritic and solar. Geochim. Cosmochim. Acta. 53, 197-214.

Anderson, S. P., Dietrich, W. E., Brimhall Jr, G. H., 2002. Weathering profiles, mass-balance analysis, and rates of solute loss: Linkages between weathering and erosion in a small, steep catchment. Geol Soc Am Bull. 114, 1143-1158.

Audet, M. A., 2008. Le massif du Koniambo-Nouvelle Calédonie: Formation et obduction d'un complexe ophiolitique de type SSZ. Enrichissement en nickel, cobalt et scandium dans les profils résiduels (Doctoral dissertation), 199- 221.

Braun, J.J., Pagel, M., Herbilln, A., Rosin, C., 1993. Mobilization and redistribution of REEs and thorium in a syenitic lateritic profile: A mass balance study. Geochim. Cosmochim. Acta. 57, 4419-4434.

Braun, J. J., Viers, J., Dupré, B., Polve, M., Ndam, J., Muller, J. P., 1998. Solid/liquid REE fractionation in the lateritic system of Goyoum, East Cameroon: the implication for the present dynamics of the soil covers of the humid tropical regions. Geochim. Cosmochim. Acta. 62, 273-299.

Akita University

Brimhall, G.H., Dietrich, W.E., 1987. Constitutive mass balance relations between chemical composition, volume, density, porosity, and strain in metasomatic hydrochemical systems: Results on weathering and pedogenesis. Geochim. Cosmochim. Acta. 51, 567-587.

Butt, C.R.M., Cluzel, D., 2013. Nickel laterite ore deposits: Weathered serpentinites. Elements. 9, 123-128.

Chakhmouradian, A. R., & Wall, F. (2012). Rare earth elements: minerals, mines, magnets (and more). Elements. 8, 333-340.

Chassé, M., Griffin, W.L., O'Reilly, S.Y., Calas, G., 2017. Scandium speciation in a world-class lateritic deposit. Geochemical Perspect. Lett. 3, 105-113.

EC., 2017. Communication from the Commission on the 2017 list of Critical Raw Materials for the EU. European Commission, Brussels. 1-8

Eliopoulos, D.G., Economou-Eliopoulos, M., 2000. Geochemical and mineralogical characteristics of Fe-Ni- and bauxitic-laterite deposits of Greece. Ore Geol. Rev. 16, 41-58.

Fendorf, S., Fendorf, M., 1996. Sorption mechanisms of lanthanum on oxide minerals. Clays Clay Miner. 44, 220-227.

Fu, W., Yang, J., Yang, M., Pang, B., Liu, X., Niu, H., Huang, X., 2014. Mineralogical and geochemical characteristics of a serpentinite-derived laterite profile from East Sulawesi, Indonesia: Implications for the lateritization process and Ni supergene enrichment in the tropical rainforest. J. Asian Earth Sci. 93, 74-88.

Gleeson, S.A., Herrington, R.J., Durango, J., Velásquez, C.A., Koll, G., 2004. The mineralogy and geochemistry of the Cerro Matoso S.A. Ni Laterite deposit, Montelíbano, Colombia. Econ. Geol. 99, 1197-1213.

Golightly, J.P., 1981. Nickeliferous laterite deposits. Econ Geol 75th Anniv. 710-735.

Makishima, A., Nakamura, E., 1997. Suppression of matrix effects in ICP-MS by high power operation of ICP: Application to precise determination of Rb, Sr, Y, Cs, Ba, REE, Pb, Th and U at ng g-1 levels in milligram silicate samples. Geostand. Newsl. 21, 307-319.

Akita University

Mongelli, G., 1997. Ce-anomalies in the textural components of Upper Cretaceous karst bauxites from the Apulian carbonate platform (southern Italy). Chem. Geol. 140, 69-79.

Nagaishi, K., Ishikawa, T., 2009. A simple method for the precise determination of boron, zirconium, niobium, hafnium and tantalum using ICP-MS and new results for rock reference samples. Geochem. J. 43, 133-141.

Nesbitt, H.W., 1979. Mobility and fractionation of rare earth elements during weathering of a granodiorite. Nature. 279, 206-210.

Rivera, J., Reich, M., Schoenberg, R., González-Jiménez, J. M., Barra, F., Aiglsperger, T., Carretier, S., 2018. Platinum-group element and gold enrichment in soils monitored by chromium stable isotopes during weathering of ultramafic rocks. Chem Geol, 499, 84-99.

Rudnick, R.L., Gao, S., 2013. Composition of the Continental Crust, in: Treatise on Geochemistry: Second Edition. 3, 1-64.

Sanematsu, K., Moriyama, T., Sotouky, L., Watanabe, Y., 2011. Mobility of Rare Earth Elements in Basalt-Derived Laterite at the Bolaven Plateau, Southern Laos. Resour. Geol. 61, 140-158.

Schellmann, W., 1989. Composition and origin of lateritic nickel ore at Tagaung Taung, Burma. Miner. Depos. 24, 161-168.

Sivakumar, V., Ernyei, L. and Obenauf, R.H., 2006. Guide for determining ICP/ICPMS method detection limits and instrument performance. SPEX CertiPrep, Inc. 21, 13.

Teitler, Y., Cathelineau, M., Ulrich, M., Ambrosi, J.P., Munoz, M., Sevin, B., 2019. Petrology and geochemistry of scandium in New Caledonian Ni-Co laterites. J. Geochemical Explor. 196, 131-155.

Ulrich, M., Cathelineau, M., Muñoz, M., Boiron, M.C., Teitler, Y., Karpoff, A.M., 2019. The relative distribution of critical (Sc, REE) and transition metals (Ni, Co, Cr, Mn, V) in some Ni-laterite deposits of New Caledonia. J. Geochemical Explor. 197, 93-113.

U.S. Geological Survey, 2019, Mineral commodity summaries 2019: U.S.G.S.1-200.

Akita University

Villanova-de-Benavent, C., Proenza, J.A., Galí, S., García-Casco, A., Tauler, E., Lewis, J.F., Longo, F., 2014. Garnierites and garnierites: Textures, mineralogy, and geochemistry of garnierites in the Falcondo Ni-laterite deposit, Dominican Republic. Ore Geol. Rev. 58, 91-109.

Wang, W., Pranolo, Y., Cheng, C. Y., 2011. Metallurgical processes for scandium recovery from various resources: A review. Hydrometallurgy. 108, 100-108.

Zepf, V., 2013. Rare Earth Elements: What and where they are. In Rare Earth Elements. Springer, Berlin, Heidelberg. 11-39.

Akita University

Chapter 6

Similarities and differences between the Berong and Intex Ni-Co laterite deposits, Philippines

Several factors affect the enrichment of Ni and Co in the Berong and Intex laterite deposits in the Philippines. This study investigated the various factors and processes crucial for Ni and Co mineralization. Based on the mineralogy and geochemistry of the samples, the distribution of Ni and Co is complex in the studied profiles. The laterite profiles in the Berong deposit are characteristically distinct from Intex deposit. Nevertheless, there are similar features how these deposits evolved and formed over long periods of time. Table 27 shows the summary of the similarities and differences between the Berong and Intex laterite deposits.

Serpentinization is a major process affecting the peridotite and pyroxenite bedrock when these rocks react with hydrous fluids. Type I, type I, type II and type III serpentines formed in the bedrock of the Berong and Intex deposits. Type I serpentines developed after the hydration of primary olivine and pyroxene. Continuous serpentinization leads to the generation of type II and type III serpentines in the bedrock.

Table 27 Similarities and differences of the Berong and Intex deposits in the Philippines.

Processes/ Characteristics	Similarities	Differences
Serpentinization	The different serpentines in the bedrock contain low amount of NiO. Serpentine is an important Ni ore in the saprolite horizon.	Type I to type VI serpentines contain significant amount of Ni in the saprock of the Berong deposit. Type V serpentines only contain considerable amount of Ni in the saprock of the Intex deposit.
Dissolution	Mg and Si are leached from the ultramafic bedrock, whereas Fe, Al, Ni are retained in the weathered horizons. Goethite is the dominant Ni ore in the limonite horizon.	
Hydrolysis		Residual accumulation of goethite and gibbsite in the limonite horizon of the Berong deposit. Only goethite is formed in the limonite horizon of the Intex deposit after the hydrolysis of Fe.
Oxidation	The oxidation of Fe^{2+} to Fe^{3+} results in the formation of goethite and hematite in the upper section of the limonite horizon.	
Degree of weathering		Higher UMIA and IOL values of the Berong laterite samples indicating a more advanced degree of weathering. Relatively low UMIA and IOL values of the Intex laterites suggesting a less advanced degree of weathering.
Leaching	Ni (Si and Mg) is leached from the limonite towards the saprolite horizon.	Precipitation of garnierite (serpentine-like, talc-like and sepiolite-like) is observed in the Berong deposit. Poor precipitation of talc-like and sepiolite-like in the Intex deposit.
Change in pH conditions and composition of the weathering solutions	Favorable pH conditions lead to the formation of Mn-oxyhydroxides	

The intensive chemical weathering of the bedrock results in the formation of the saprolite and limonite horizons. In both deposits, the highest Ni

Akita University

content (> 2 wt%) were found in the samples from the saprolite horizon. The main difference is the formation of the different types of serpentines in the said horizon. In the Berong deposit, type I to type VI serpentine veins are developed, whereas type I to type V veins are formed in the Intex deposit. The chemistry of the serpentines in the Berong deposit shows higher Ni concentration compared with the serpentines in the Intex deposit.

As a consequence of the dissolution of rock-forming minerals in the ultramafic bedrock during weathering, the more soluble elements, Mg and Si, are removed while Al, Fe and Ni are concentrated in the weathered horizons. The hydrolysis of Al and Fe results in the concentration of gibbsite and goethite in the limonite horizon. In both deposits, goethite is the dominant mineral that host significant amount of Ni in the limonite horizon. In the near-surface environment, the oxidation of ferrous (Fe^{2+}) to the ferric (Fe^{3+}) valence state occurs which leads to the formation of goethite and hematite. All the laterite profiles from the Berong and Intex deposits contain minor amount of hematite in the upper section of the limonite horizon.

Another major difference of the two deposits is the result of the Ultramafic Index of Alteration (UMIA) and Index of Lateritisation (IOL). The Berong laterites show higher UMIA values indicating a more advanced weathering stage, which subsequently yielded a thicker (mature) limonite. On the other hand, Intex laterites have relatively low UMIA and IOL values suggesting a less advanced degree of weathering. Since few Ni, Mg, and Si are remobilized and redistributed from the limonite horizon towards the

Akita University

saprolite horizon, this most likely affected the poor precipitation of talc-like and sepiolite-like phases in the Intex deposit.

The change in pH condition play an important role in the remobilization and leaching of Ni from the limonite to the lower section of the profiles. Precipitation of talc-like and sepiolite-like is observed only in the saprolite horizon of the Berong deposit. The favorable pH conditions (pH 5.08-7.09) and composition of the weathering solutions may have instigated the formation of Mn-oxyhydroxides in the limonite horizon in both deposits.

Akita University

CHAPTER 7

Conclusions

The strong weathering of the peridotite and pyroxenite bedrock under a tropical climate resulted in the formation of the Berong and Intex Ni-Co laterite deposits. In this study, the laterite profile is divided from bottom to top into (i) serpentinized ultramafic bedrock (ii) saprolite horizon and (iii) limonite horizon. The ultramafic rocks consist mainly of primary olivine, orthopyroxene, and clinopyroxene with minor to trace amounts of serpentine, brucite, magnetite, talc, and chromite. The primary olivine in the bedrock contains a considerable amount of Ni, suggesting this is the main source of the ore in the weathered horizons. There are three types of serpentine veins identified in the peridotite bedrock. Type I and type II veins have mesh texture and are cut by interlocking-textured type III veins. The results of Raman spectroscopy show that the mesh- and interlocking textured- serpentines correspond to lizardite, which indicates that there is no replacement of serpentine. Moreover, antigorite is the main serpentine in the clinopyroxenite bedrock and is marked by an interpenetrating texture. The serpentine in the bedrock is either partially or completely altered to talc. This primary talc contains a low amount of NiO with a concentration of up to 0.07 wt%.

The Ni-bearing minerals in the saprolite horizon are serpentine and garnierite. Six types of serpentine veins are determined in the Berong

Akita University

deposit (Palawan, Philippines), and five types of these veins are identified in the Intex deposit (Mindoro, Philippines). All these veins possess distinct texture and contain variable amounts of Ni. The texture of type I and II serpentine veins in the saprock from the Berong deposit resemble that of lizardite. However, the Raman signatures of type III to type VI serpentines correspond to chrysotile. The lizardite- chrysotile serpentinization could either formed in the occurrence of meteoritic-hydrothermal waters or meteoritic waters. The Ni concentration of type I to type VI serpentines in the saprock from the Berong and Intex deposit varies unpredictably. Therefore, the local enrichment of Ni in these serpentines is a complex process. Only in the Berong deposit that talc-like and sepiolite-like garnierites are found, which contain a significant amount of Ni (up to 34.86 wt%).

In the limonite horizon, Ni is mainly hosted by goethite and Mn-oxyhydroxides (up to 2.15 wt% NiO and 23.89 wt% NiO). Lithiophorite-asbolane intermediate occurs in wide-ranging morphologies such as fibrous, dendritic, oolitic, banded, and massive forms. Both lithiophorite-asbolane intermediate and asbolane occur at Intex deposit. However, it is apparent in the field that Mn-oxyhydroxides in the limonite horizon occurs extensively in the Berong deposit compared to Intex deposit.

The amount of primary olivine in the bedrock influence the enrichment of Ni in the weathered horizons. The highest amount of Ni is found in laterite derived from harzburgite- dunite, followed by lherzolite and clinopyroxenite

Akita University

bedrock. Nevertheless, there is no significant difference of Ni contained in the saprolite and limonite horizons among the various bedrock types. Through UMIA and IOL plots, it has been shown that the laterites in the Berong deposit experienced a strong degree of weathering in contrast to the moderately weathered laterites of the Intex deposit.

Irrespective of bedrock types, olivine, and pyroxene, are the primary minerals in the peridotite and pyroxenite, which dominantly contain Mg and Si. As weathering progresses, these elements are easily leached out from the profiles leading to the relative enrichment of Ni, Co, Mn, Fe in the weathered horizons. Using the results from XRF analysis, the following geochemical trends of the major and minor elements are observed through the laterite profiles: (i) Mg and Si are depleted towards the surface, (ii) Fe, Al, Cr, Co, and Mn are enriched in the limonite horizon and (iii) high amount of Ni is retained in the saprolite horizon. There is a change in pH conditions from the bedrock to the weathered horizons. It is mildly acidic in the upper horizon of the profile and then shifts to alkaline condition at the bottom of the profile. The acidic solutions percolate through the rocks which augment the remobilization of Ni and, to lesser extent, Co, from the upper limonite to the upper section of the saprolite horizon during weathering. These results are supported by the mobility diagrams presented in Chapter 4.

Ni laterite deposits are vital targets for the exploration of critical metals including Sc and REE. The studied profiles show a marked enrichment of Sc and REE in the limonite horizon with concentrations of up to 67 ppm and

Akita University

357 ppm. The highest amount of Sc is observed in the limonite developed above lherzolite, owing to the abundance of pyroxene in the bedrock and its close association with Fe-oxyhydroxides and to some extent, Mn-oxyhydroxides in the limonite horizon. The enrichment of REE are evident at the transition boundary or the lower section of the limonite. The element distribution plots of REE with depth show that it mimics the trend of Sc, implying Fe-oxyhydroxides could host REE in the limonite. The chondrite normalized REE patterns show positive and negative Ce anomalies at the transition boundary between the limonite and saprolite horizons. It is likely that REE could accumulate in this redox boundary.

The thickness of the weathered horizons varies laterally and vertically. The profiles of the Berong deposit is characterized by a thinner saprolite (2 m to 5m) and thicker limonite (3.4m to 15m). In contrast, the laterite profiles of the Intex deposit is marked by a thicker saprolite (3.4m to 8.2 m) and thinner limonite (3m to 4.5 m). The genesis of the Berong and Intex laterite deposits are consistent with the per descendum model proposed by previous authors, where weathering of ultramafic rocks initially resulted in the formation of the saprolite and limonite horizons. The effect of the tectonic uplift augmented the percolation of acidic meteoric water through cracks and fractures that enable the intense leaching of Mg and Si and residual enrichment of Ni in goethite. With the change in the pH conditions of the horizon, Ni is re-distributed and transported to the deeper section of the saprolite leading to the formation of hydrous Mg silicate, Mn-

Akita University

oxyhydroxides and secondary silica albeit these stages overlapped and interacted in the time sequence of laterization. However, in the Intex deposit, the weathering solution is not supersaturated with Ni, Mg and Si hindering the formation of talc-like and sepiolite-like garnierites in the studied saprolite. Integrating field observations, mineralogical and geochemical data, the Berong and Intex deposits in the Philippines evolved in two distinct processes: (i) the development of the saprolite and limonite horizons and (ii) formation of secondary silicate minerals, Mn-oxyhydroxides and silica.

There are additional analyses that can be considered for the improvement of this study, including the determination of Co content in the primary minerals and concentration of Sc and REE in pyroxene, goethite and Mn-oxyhydroxides (i.e., asbolane, lithiophorite-asbolane intermediate) using EPMA and Laser Ablation- Inductively Coupled Plasma Mass Spectrometer (LA-ICP-MS). The quantification of these elements in the minerals mentioned above could help determine the source of the ore in the limonite horizon. Furthermore, a quantitative approach in the analysis of the mobility of the elements through the profiles can accurately determine the behavior (i.e., enrichment or depletion) of the elements in the weathered horizons with respect to the bedrock during weathering.

Appendix A

Raman data from rruff.info database and previously published results.

	Lizardite wavelength, cm^{-1}	Chyrsotile wavelength, cm^{-1}	Antigorite wavelength, cm^{-1}
rruff. info	230 385 688 3688	232 386 688 3686	236 378 688 3695
Auzende et al., 2004	238 393 695 3683	235 391 694 3694	235 377 685 3698
Tarling et al., 2018	231 385 690 3681	230 389 690 3697	230 377 685 3696
Muňoz et al., 2019	Lizardite-mesh 227 381 687 3685 Lizardite-weathered 227 381 687 3686		

Appendix B

Average chemical compositions (wt%) and structural formula (apfu) of the different vein serpentines in the saprock (Intex deposit) derived from lherzolite and clinopyroxenite.

Drill core	BB2515		PG1500		BB2515		BB2515		BB2515		PG1500	
Sample name	INT-D1-7		INT-D2-8		INT-D1-7		INT-D1-7		INT-D1-7		INT-D2-8	
	Type I	σ	Type I	σ	Type II-rim	σ	Type II-core	σ	Type III	σ	Type IV	σ
n	6		14		7		8		11		11	
SiO_2	39.49	2.44	42.08	1.67	39.41	2.79	39.84	3.31	44.28	4.75	40.92	1.25
Al_2O_3	0.69	1.37	1.40	1.09	0.01	0.02	0.01	0.01	0.89	0.38	0.04	0.03
FeO	5.90	1.46	3.19	1.32	6.23	1.78	8.06	5.86	5.71	1.28	5.47	1.16
MgO	32.21	1.63	32.86	0.95	34.27	1.87	32.77	2.63	28.56	1.52	31.81	2.21
NiO	0.23	0.12	0.39	0.19	0.26	0.12	0.23	0.09	0.05	0.02	1.42	0.95
CoO	0.02	0.01	0.01	0.01	0.02	0.01	0.03	0.03	0.01	0.01	0.02	0.02
CaO	0.02	0.01	0.01	0.00	0.01	0.01	0.03	0.03	0.05	0.02	0.03	0.02
Cr_2O_3	0.03	0.04	0.21	0.28	0.00	0.01	0.01	0.01	0.29	0.13	0.02	0.01
MnO	0.08	0.02	0.03	0.01	0.10	0.03	0.16	0.19	0.09	0.05	0.10	0.03
Total	78.69	1.03	80.18	1.76	80.32	3.43	81.14	2.08	79.97	3.99	79.84	1.55
Si	2.070	0.112	2.121	0.045	2.035	0.072	2.052	0.093	2.240	0.114	2.119	0.030
Al	0.043	0.085	0.083	0.064	0.001	0.001	0.001	0.001	0.054	0.025	0.003	0.002
Fe	0.259	0.067	0.135	0.060	0.272	0.088	0.356	0.275	0.243	0.055	0.238	0.054
∑ Tetr.	2.372	0.055	2.339	0.038	2.307	0.040	2.409	0.191	2.538	0.090	2.359	0.074
Mg	2.519	0.149	2.469	0.062	2.640	0.071	2.518	0.130	2.168	0.189	2.453	0.128
Ni	0.010	0.005	0.016	0.008	0.011	0.005	0.010	0.004	0.002	0.001	0.060	0.041
Co	0.001	0.001	0.000	0.000	0.001	0.001	0.001	0.001	0.001	0.000	0.001	0.001
Cr	0.001	0.002	0.008	0.011	0.000	0.000	0.000	0.000	0.012	0.006	0.001	0.001
Ca	0.001	0.001	0.000	0.000	0.001	0.000	0.002	0.002	0.003	0.001	0.002	0.001
Mn	0.004	0.001	0.001	0.000	0.004	0.002	0.007	0.009	0.004	0.002	0.005	0.001
∑ Oct.	2.536	0.151	2.495	0.052	2.657	0.077	2.538	0.118	2.189	0.192	2.521	0.098
Tetr./Oct.	0.939	0.080	0.938	0.032	0.869	0.034	0.954	0.122	1.171	0.143	0.938	0.067